Poloidal CX visible light plasma rotation diagnostics in TCV

PAR

Claudio MARINI

acceptée sur proposition du jury:

Prof. F. Mila, président du jury
Dr B. Duval, Dr A. Karpushov, directeurs de thèse
Dr N. Conway, rapporteur
Dr Y. Camenen, rapporteur
Dr J. Graves, rapporteur

EPFL

ÉCOLE POLYTECHNIQUE
FÉDÉRALE DE LAUSANNE

Suisse
2017

I always think that
the chances of finding out
what really is going on in the universe are so absurdly remote,
that the only thing to do is to say hang the sense of it
and just keep yourself occupied.

— D. Adams

To my family.

Abstract

Controlled thermonuclear fusion for large scale energy production is one of the main goals of plasma physics. At the Swiss Plasma Center (SPC) in Lausanne, Switzerland, the institute that supported this thesis' research, the *Tokamak à Configuration Variable* (TCV) constitutes the main experiment on fusion research. In a tokamak, one of the most promising concepts for fusion, high temperature toroidal-shaped plasmas are confined by means of magnetic fields. The confinement of plasma energy and particles, which is necessary for a net energy gain, is limited by transport, collisional or turbulent, naturally arising from the gradients between the hot-dense plasma core and the cold-rarefied plasma edge, and by instabilities, driven by gradients and plasma current.

Due to the geometrical topology, plasma can rotate in the toroidal and poloidal directions. Plasma rotation has a strong influence on confinement and stability, which makes its understanding one of the priorities in fusion, where prediction on a reactor relevant scenario are demanded. There are many open issues and discrepancies between the theoretical rotation description and experiments, which stimulated active research in the field. In this context this work provided experimental results of unprecedented accuracy in TCV, where plasma rotation and impurity parameters are measured with the charge exchange recombination spectroscopy (CXRS) diagnostic. CXRS exploits the active CX signal induced by a low power diagnostic neutral beam injector (DNBI), which applies negligible torque to the plasma, permitting localised measurements of "intrinsic" rotation. Impurity, either Carbon or Boron, density and temperature are also measured by CXRS, resulting in a complete set of kinetic profiles.

During this work, the CXRS diagnostic was extended with the development of a new high-spatial (<3 mm) and temporal (≥2 ms) resolution system, termed CXRS-EDGE, devoted to the study of edge profiles. The accuracy improvements with respect to the legacy systems were obtained through an expressly designed high throughput lens spectrometer and numerical-aperture matching optics, resulting in rotation uncertainties <1 km/s, required for significant poloidal flow characterisation.

The upgraded CXRS diagnostic was used in the study of the impact of the sawtooth (ST) magneto-hydrodynamic (MHD) instability on rotation in L-mode limited plasmas and on the changes in edge impurity parameters at the onset of the H-mode in diverted discharges. The EDGE spectrometer was also exploited for the characterisation of the spectral (H and D)

Abstract

Balmer and molecular emission in the resonant antenna ion device (RAID) and for a survey fast ion D_α (FIDA) diagnostic in TCV.

The evolution of rotation and kinetic profiles during a "canonical" ST were studied with a 2 ms time resolution for ST periods ranging from 8 to 36 ms, obtained by locking the ST period with the electron cyclotron heating (ECRH) modulation. Rotation profiles suddenly change at the ST crash, with a more complex dynamic than a simple flattening expected from an augmented transport, passing from peaking counter-current to hollow co-current in the core, showing evidence of a co-current torque at the crash of increasing magnitude with the ST period. This explains the $1/I_p$ scaling observed in TCV L-mode plasmas, where the maximum rotation is limited by ST dynamics. This effect must be included in realistic theoretical models and might be exploited in tailoring rotation using ST period and radius as actuators. The crash is also characterised by expulsion of impurity from the core, resulting in hollow post-crash profiles, that can be exploited in a reactor scenario for avoiding impurity accumulation and for ash removal, the process being more efficient for short ST periods.

The first accurate measurement of the changes in impurity flow across the transition to ELM-free H-mode were performed in this work. A narrow ($\simeq 5.5$ mm) and deep ($|u_\theta| \geq 20$ km/s) poloidal rotation well develops at the last closed flux surface (LCFS) at the transition, together with a density pedestal <15 mm wide and an uniform increase of the impurity temperature of $\simeq 100$ eV, lacking a clear evidence of a pedestal. From the kinetic profiles the radial electric field E_r was computed, revealing the development in TCV of the well characteristic of H-mode as observed in other devices, whose width agrees with inter-machine scaling. The evolution of E_r components suggests involvement of the poloidal rotation in the triggering of the transition, although the time resolution is insufficient to prove the causality. Estimates of the main ion flow suggests that the E_r well main contributor is the main ion pressure gradient term. This is consistent with the reasonable agreement found in the comparison of the impurity rotation with neoclassical analytical and numerical predictions.

The observations reported in this work constitute a strong constrain for theoretical models, demonstrate the strong influence that fast MHD events have on transport and set more stringent conditions for edge impurity behaviours.

ii

Sinossi

La fusione termonucleare controllata per la produzione di energia su larga scala è uno degli obiettivi principali della fisica del plasma. Il *Tokamak à Configuration Variable* (TCV) costituisce il principale esperimento nella ricerca sulla fusione al Swiss Plasma Center (SPC), l'istituto che ha sostenuto questo progetto di ricerca, con sede a Losanna, in Svizzera. In un tokamak, uno dei più promettenti design per la fusione, plasmi ad alta temperatura e di forma toroidale sono confinati per mezzo di campi magnetici. Il confinamento dell'energia e delle particelle del plasma, che è necessario per un guadagno netto di energia, è limitato dal trasporto, sia esso collisionale o turbolento, che sorge spontaneamente dai gradienti tra il centro del plasma, caldo e denso, e il plasma al bordo esterno, freddo e rarefatto, oltre che dalle varie instabilità, causate da gradienti e dalla corrente del plasma.

Il plasma può ruotare nella direzione toroidale e in quella poloidale, grazie alla topologia geometrica del tokamak. La rotazione del plasma ha un forte impatto sul confinamento e sulla stabilità del plasma, il che rende la sua comprensione una delle priorità della ricerca sulla fusione, dove le sue previsioni in regimi rilevanti per un reattore sono tuttora richieste. Ci sono molte discrepanze tra le previsioni teoriche e i risultati sperimentali sulla rotazione, che hanno stimolato una ricerca attiva in questo campo. In questo contesto, questo lavoro ha prodotto risultati sperimentali aventi un'accuratezza senza precedenti in TCV, dove la rotazione del plasma e i parametri delle impurità sono misurati tramite la diagnostica di spettroscopia di ricombinazione per scambio di carica (CXRS). Il CXRS utilizza il segnale attivo di scambio di carica (CX) generato da un iniettore di fasci neutri diagnostico (DNBI) avente bassa potenza, il quale applica sul plasma un momento torcente trascurabile, permettendo misure localizzate della rotazione "intrinseca". Anche la temperatura e la densità delle impurità del plasma, Carbonio o Boro, sono misurate dal CXRS, che quindi fornisce un set completo di profili cinetici delle impurità.

Durante questo lavoro, la diagnosica CXRS è stata migliorata con l'aggiunta di un nuovo sistema avente una alta risoluzione sia spaziale (< 3 mm) che temporale ($\geq$ 2 ms). Il nuovo sistema, chiamato CXRS-EDGE, ha lo scopo di studiare i profili al bordo del plasma. L'aumento dell'accuratezza del nuovo sistema rispetto ai vecchi sistemi è stato ottenuto tramite uno spettrometro a lenti ad alto throughput, appositamete progettato, e tramite ottiche aventi un'apertura numerica combaciante. Il risultato è una diagnostica con un'incertezza inferiore a 1 km/s sulla rotazione poloidale, che risulta necessaria per la caratterizzazione dei flussi poloidali.

La nuova diagnostica è stata usata sia nello studio sull'impatto che ha sulla rotazione l'instabilità magnetoidrodinamica (MHD) chiamata sawtooth (ST) in plasmi limitati e a basso confinamento (L-mode) che sui cambiamenti dei parametri delle impurità che avvengono al bordo del plasma quando viene raggiunto l'alto confinamento (H-mode) in scariche nella configurazione diverted. Il nuovo spettrometro è anche stato utilizzato per la caratterizzazione dell'emissione spettrale delle linee molecolari e di Balmer (in H e D) nel resonant antenna ion device (RAID) e per una diagnostica pilota per la misura dell'emissione D_α di ioni veloci (FIDA) a TCV.

L'evoluzione della rotazione e dei profili cinetici durante un ST "canonico" sono stati studiati con una risoluzione temporale di 2 ms per ST aventi un periodo da 8 a 36 ms, ottenuti fissando il periodo dei ST con la modulazione del riscaldamento a onde cicotroniche elettroniche (ECRH). Il profilo di rotazione cambia repentinamente al crash del ST, con una dinamica più complicata che un semplice appiattimento come ci si aspetta da un semplice aumento del trasporto. Il profilo passa da piccato contro-corrente a bucato in direzione della corrente nella zona centrale del plasma, segnalando la presenza di un momento torcente in direzione della corrente al momento del crash, con una intensità crescente con il periodo del ST. Questo spiega lo scaling $1/I_p$ osservato a TCV in plasmi a L-mode, dove il valor massimo della rotazione è limitato dalla dinamica del ST. Questo effetto deve essere incluso in modelli teorici realistici e può essere utilizzato per controllare la rotazione, usando il raggio ed il periodo del ST come degli attuatori. Il crash, inoltre, è caratterizzato dall'espulsione delle impurità dal centro del plasma, che risulta in profili bucati dopo il crash. Questo effetto può essere usato per evitare l'accumulo di impurità nel reattore e per la rimozione delle ceneri (elio), questo processo risulta più efficace per ST con periodo corto.

Le prime misure accurate dei cambiamenti nel flusso delle impurità attraverso la transizione all'H-mode senza ELM sono state eseguite in questo lavoro. Una depressione stretta ($\simeq 5.5$ mm) e profonda ($|u_\theta| \geq 20$ km/s) nella rotazione poloidale si sviluppa all'ultima superficie di flusso chiusa (LCFS) durante la transizione, oltre che un "pedestal" largo < 15 mm nella densità unito ad un uniforme aumento della temperatura delle impurità di circa 100 eV, sprovvisto quest'ultimo di un pedestal. Dai profili cinetici il campo elettrico radiale E_r è stato calcolato, dimostrando anche a TCV la formazione del caratteristico "pozzo" osservato in altre macchine durante l'H-mode. La larghezza del pozzo di E_r rispetta lo scaling inter-macchina. L'evoluzione delle componenti di E_r suggerisce una relazione di causalità della rotazione poloidale nell'innesco della transizione, anche se la risoluzione temporale è insufficiente per dimostrare tale relazione. Stime del flusso degli ioni principali suggeriscono che il maggior termine contribuente al campo elettrico radiale sia il gradiente della pressione degli ioni principali. Questo è consistente con il ragionevole accordo trovato nel paragone tra la rotazione misurata e quella predetta dalla teoria neoclassica.

Le osservazioni riportate in questo lavoro costituiscono dei forti vincoli per i modelli teorici, dimostrano la forte influenza che i rapidi eventi MHD hanno sul trasporto e impongono

condizioni più stringenti al comportamento delle impurità al bordo del plasma.

Contents

List of Figures

List of Tables

1 Introduction

1.1 Nuclear fusion and Tokamaks

The World energy consumption is for many decades in constant growth, with hydrocarbons accounting for the lion's share ≥ 65%. The indiscriminate use of fossil fuels is bound to end relatively soon, either due to reserve depletion or to the realization of its negative effects on world climate. The conventional renewable energy sources, wind-solar-hydro-geothermal power, although in constant growth, are not sufficient to completely supplant fossil fuels. Nuclear fission of uranium is a mature technique, that has been used from the late 1950's and provides ≃ 12% of the world's electricity demand. However this energy source has many drawbacks: it produces long lived radioactive waste (like plutonium-239) that has to be secured for thousands of years, the supply of fissile material is limited, and it is intrinsically unsafe due to the nature of the reaction (chain reaction). This last point is known to raise concerns in the population, that are not unfounded in the light of historical events like Chernobyl in 1986 and more recently Fukushima in 2011. For these reasons fission power is unlikely to ever be acceptable as a complete replacement for fossil fuel.

Nuclear fusion is considered the most promising energy source to replace, in the long term, fossil fuel and satisfy the world's energy needs. Fusion is a process where light nuclei fuse together to form heavier elements. For light elements, like hydrogen and its isotopes, the final mass of the products is smaller than the initial mass, i.e. $\Delta m < 0$, with the difference converted into energy following Einstein's well-known equation $E = m\,c^2$ [1]. Fusion presents many advantages in comparison with the legacy energy production methods, the fuel is accessible and abundant (at least Deuterium, that can be extracted from water), the reaction is intrinsically safe and it produces relatively short-lived (≃ 100 year) waste (activated materials) and Helium ash. For several decades, scientists have been working on the development of self-sustaining nuclear fusion as an economically viable energy source, but many challenging issues remain to be resolved before the realization of a working device. Some of these problems can be seen from the analysis of the Earth's closest working self-sustained fusion reactor, the Sun. In order for the fusion reaction to occur, the nuclei must overcome their Coulomb

electric repulsion. For thermonuclear fusion, this is achieved when the reactants have high enough kinetic energy, or in other terms, for high enough temperature ($\simeq 1.5$ keV in the Sun core). At these temperatures matter is in the plasma state, conceivable as a "gas" of free electrons and positively charged ions susceptible to electric and magnetic fields. Plasma cannot be confined with conventional materials, as any contact with a solid surface would result in damage to the device and plasma contamination/cooling. The problem of plasma confinement in the Sun is solved by gravity, which is not a viable solution on Earth. Scientists eventually considered two ideas to solve the confinement problem, using the particle inertia in an imploding pellet (inertial confinement) or using electro-magnetic fields to constrain particle movement (magnetic confinement). The latter option has been the most successful, and although several concepts of magnetic confinement devices are being tested, the tokamak design (the concept on which the majority of this thesis is based) has, to date, provided to demonstrate the best performance.

The electron density n_e and temperature T_e of tokamak plasmas are around $n_e \simeq 10^{20}$ m^{-3} and $T_e \simeq 10$ keV. In this range the thermal energy dominates over the Coulomb energy [2]

$$E_{Coul} = \frac{e^2}{4\pi\epsilon_0} n_e^{1/3} \tag{1.1}$$

The perturbing effect of a charge in a plasma is shielded by the displacement of other charges, it is therefore relevant on spatial scales below the Debye length λ_D [2]:

$$\lambda_D \simeq \sqrt{\frac{\epsilon_0 \, k_b \, T_e[K]}{n_e \, e^2}} \tag{1.2}$$

On larger scales quasi-neutrality, expressed by the relation

$$\frac{n_e - Z_i n_i}{n_e} \ll 1 \tag{1.3}$$

is attained typically within 10^{-6}. The number of electrons in a sphere of radius λ_D is termed Debye number $N_D = 4/3\pi n_e \lambda_D^3$, in a plasma $N_D \gg 1$. The typical time response of electrons to perturbations is given by the plasma frequency ω_p [3]:

$$\omega_p = \sqrt{\frac{n_e \, e^2}{m_e \epsilon_0}} \tag{1.4}$$

Electromagnetic waves with lower frequency cannot propagate and are reflected, while waves with higher frequency can enter the plasma and propagate. The plasma state is defined by the

conditions [2]:

$$\lambda_D \ll L \tag{1.5}$$

$$N_D \ll 1 \tag{1.6}$$

$$\omega_p \tau_n > 1 \tag{1.7}$$

where L is the plasma size and τ_n the electron-neutral collision time.

The rest of this chapter is devoted to the explanation of basic concepts in fusion research and tokamak devices necessary in the understanding of this thesis.

1.1.1 Thermonuclear fusion concept

Fusion reactions occur when nuclei get close enough, $\simeq 10^{-15}$ m, for the nuclear force to dominate and overcome Coulomb repulsion. In a thermonuclear fusion reactor the thermal energy of the energetic charged particles is exploited to reach this condition and engender the reaction. The cross section of the fusion process depends on the reactants and on their relative energy, it increases with energy up to a peak value, then it rolls over due to the decreasing interaction time. Research on thermonuclear fusion presently focusses on the most accessible Deuterium-Tritium (D-T) reaction [3]

$$_1^2D + {}_1^3T \rightarrow {}_2^4He \ (3.5 \text{ MeV}) + {}_0^1n \ (14.1 \text{ MeV}) \tag{1.8}$$
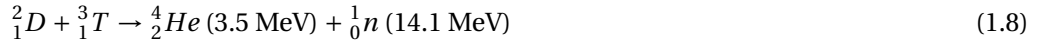
as it has the highest cross-section with its peak located at a lower temperature [3] than for the other hydrogen isotopic reactions. The reaction rate is maximised, assuming Maxwellian distributions, at $T \simeq 70$ keV, which is not attainable in present devices. However we shall see that optimization of a fusion device only requires lower, and thus more accessible, temperatures. Notice that in the core of the Sun the temperature is more than one order of magnitude lower than this, with a correspondingly lower reaction rate that is too low for practical terrestrial application.

The temperature is only one of the plasma parameters that needs to be satisfied in order to reach ignition, that is a self-sustained reaction where plasma is maintained by its self-generated fusion power. By balancing the power losses with the α-heating, i.e. the heating due to the thermalisation of the high energy α particles generated by the fusion reactions, the Lawson criterion [4], a.k.a. "triple product", expresses that ignition is reached when the product of plasma density n, energy confinement time τ_E and temperature T, surpass a value determined by the reaction rate $<\sigma v>$ and the energy per reaction E_f:

$$n \tau_E T \geq \frac{12 \, k_b}{E_f} \frac{T^2}{<\sigma v>} \tag{1.9}$$

The confinement time in steady state is defined as the ratio of the plasma energy W to the injected power P_{heat}, i.e. $\tau_E = \frac{W}{P_{heat}}$ [3]. Considering that any device has an upper operation limit for the pressure $p = n\,T$, the access to ignition is optimised when the quantity $\frac{<\sigma v>}{T^2}$ is maximised. For the D-T reaction this reads:

$$n\,\tau_E\,T \geq 3 \cdot 10^{21} \text{ keV s } /\text{m}^3 \tag{1.10}$$

and the optimal temperature is $T \simeq 14$ keV [5], considerably lower than the temperature that maximises the reaction rate. Magnetic fusion's goal is to satisfy the Lawson criterion by confining a tenuous plasma ($n \simeq 10^{20}$ m^{-3}) at high temperature ($T \simeq 10$ keV) with a sufficient energy confinement time ($\tau_E \simeq 1$ s). These three quantities are closely intertwined: injecting gas to increase the density would cool the plasma, raising the temperature often results in confinement degradation. A welcome exception is the transition to high confinement mode (H-mode) [6] in tokamaks, where above an injected power threshold the confinement improves by a factor of two with respect to the low confinement mode (L-mode) $\tau_{E-H} \simeq 2\,\tau_{E-L}$ attained at a lower power. H-mode operation is, however, often characterised by quasi-periodic disruptive instabilities occurring at the plasma edge, termed edge localised modes (ELM), which pose a major threat to the device integrity, due to their high energy transfer rate.

A reactor does not strictly need to reach ignition to operate, it must just produce more energy than the energy required to maintain a stable burning plasma with enough margin to compensate the complete system losses (power supply efficiencies, required auxiliary systems, etc.). The ratio Q of produced fusion power P_{fus} to the power needed for steady operation P_{heat} is called fusion energy gain factor:

$$Q = \frac{P_{fus}}{P_{heat}} \tag{1.11}$$

and is the main figure of merit for a reactor, where the condition $Q = 1$ is called breakeven. Present devices are not able to reach this condition, the highest values being achieved by the JET [7] tokamak with $Q_{Jet} = 0.65$ [8, 9]. The challenge of next-generation devices is to reach and surpass breakeven, which shall be attained by improving confinement. It is well established that confinement scales favourably with machine size [3, 5] and with magnetic field [3], therefore design for future devices concentrates on bigger and more costly devices, such as the international thermonuclear experimental reactor (ITER) [10, 11] currently under construction at Cadarache in France. Operation in H-mode is envisioned but requires strategies for ELM handling (mitigation or suppression).

1.1.2   Magnetic confinement and Tokamaks

The plasmas used in fusion research are mainly composed of light elements, that are fully ionised at the typical working temperatures $\simeq 10$ keV. In magnetic confinement devices the charged particles of the plasma are confined by externally applied magnetic fields. It is
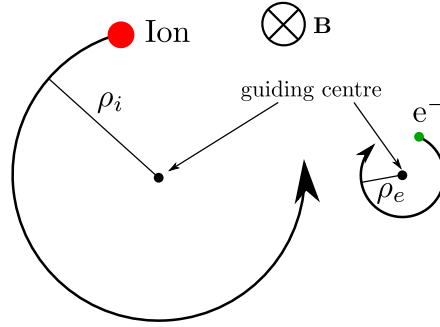
Figure 1.1: Gyration motion of an ion and an electron in a uniform and stationary magnetic field **B** (pointing inside the page). Ions and electrons gyrates in opposite directions around their guiding centre and are confined in the perpendicular direction on a distance ρ_i and ρ_e, known as Larmor radius.

instructive to first describe the trajectory of a charged particle in a uniform and stationary magnetic field **B** [T] to understand the working mechanism of magnetic confinement. The Lorentz force bends the trajectory of the particle, of mass m [kg] and charge q [C], into an helix, with axis parallel to **B** and radial (perpendicular to **B**) extent ρ [m], called the Larmor radius [2, 3, 12], equal to:

$$\rho = \frac{\gamma \, m \, v_\perp}{q \, B} \tag{1.12}$$

where $v_\perp$ is the velocity **v** [m/s] of the particle in the direction perpendicular to the magnetic field **B**, i.e. $v_\perp = \frac{\mathbf{v} \times \mathbf{B}}{|B|}$, and $\gamma = \sqrt{1/(1 - v^2/c^2)}$ is the relativistic Lorentz factor. The (angular) frequency of gyration of the particle around **B**, is the cyclotron frequency Ω_c [rad/s] [2, 3], given by

$$\Omega_c = \frac{q \, B}{\gamma \, m} \tag{1.13}$$

with the elementary relation $\rho = \frac{v_\perp}{\Omega_c}$. In this simplified picture (see figure 1.1) the magnetic field completely restrains the particle motion in the perpendicular direction, allowing the flow only along the parallel direction to **B**. However in a realistic situation Coulomb collisions and drift motions due to **B** non uniformity and perpendicular electric fields, induce a perpendicular particle transport, degrading confinement.

The tokamak concept

Several configurations, differing in the magnetic field geometry, have been proposed for a fusion device, among which the tokamak produced the best performances. The word tokamak is a transliteration of the Russian acronym "TOKAMAK", meaning "toroidal chamber with magnetic coils", which is a crude description of the device, that is sketched in figure 1.2. A torus is a surface of revolution generated by a circle and it can be parametrised by the toroidal
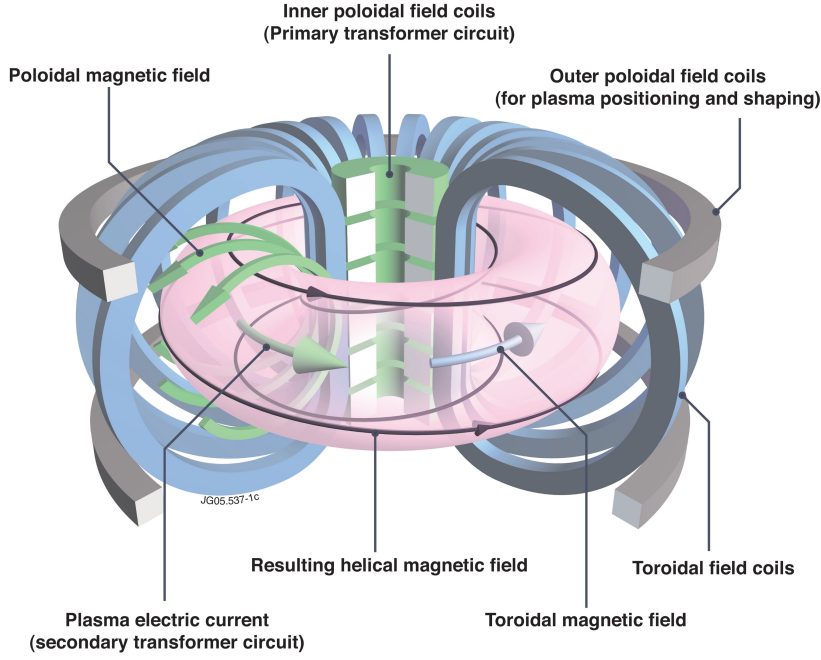
Figure 1.2: Sketch of a tokamak device, with the coils generating the toroidal field, the coils for inducing plasma current (that induces a poloidal magnetic field) and the poloidal coils for shaping. The combination of toroidal and poloidal magnetic fields results in a helical magnetic field. Source: EUROfusion website [13].

ϕ and poloidal θ angles with the equation:

$$x(\theta, \phi) \quad = \quad (R + r\cos\theta)\cos\phi \tag{1.14}$$

$$y(\theta, \phi) \quad = \quad (R + r\cos\theta)\sin\phi \tag{1.15}$$

$$z(\theta, \phi) \quad = \quad r\sin\theta \tag{1.16}$$

where r is the radius of the circle and R the distance of the circle centre from the axis of revolution. The toroidal, poloidal and radial directions are defined by $\mathbf{e}_\phi$, $\mathbf{e}_\theta$ and $\mathbf{e}_r$ respectively. In effect in a tokamak plasma is contained in a vacuum vessel of toroidal shape, and the external coils generate a strong toroidal magnetic field B_ϕ, that in most fusion relevant devices attains a few Tesla. A toroidal field solves the problem of losses at the magnetic field edges, as the field lines close upon themselves without touching a physical surface. In this geometry however the magnetic field have an unavoidable $1/R$ dependence resulting in a vertical drift and particle drifts arising from the field non uniformity leading to instabilities [3]. Due to this field dependence, the zone inside the vessel closer to the torus axis is called high field side (HFS) and the one closer to the outer wall is named low field side (LFS). A purely toroidal field is hence not sufficient for confining a plasma. The specific geometry of the confining magnetic fields has resulted in several additional terms to improve confinement and a set of
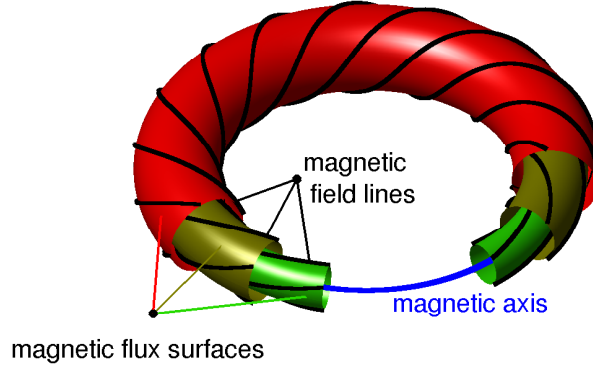
Figure 1.3: Nested flux surfaces formed by the helical magnetic field in a tokamak configuration.

relatively universal plasma coordinates that are now described.

In a tokamak a toroidal current I_p is induced in the plasma usually by the coils in the central column (see figure 1.2), that work as a primary circuit of a transformer, the plasma ring being the secondary circuit. Plasma current in a tokamak has two fundamental tasks, to heat the plasma by the power dissipated through plasma resistivity (Ohmic heating) and to generate a poloidal field B_θ, that compensate the particle drift due to B_ϕ gradient, stabilising the configuration [3, 5]. An inductive current cannot be sustained indefinitely, since the ramping magnetic field is limited by hardware restrictions, and so the inductive operation is intrinsically pulsed. Alternative non-inductive current drives, based on beams, EM waves and pressure gradients, are under investigation to overcome this limit allowing continuous operation.

An additional vertical (parallel to the torus axis of revolution) magnetic field B_ν is also required, the Lorentz force acting on the plasma due to I_p prevent the outward plasma expansion due to the 'hoop force' [5] and the 'tire tube force' [5].

The magnetic configuration resulting from the sum of the free magnetic field components is essentially helical, since the vertical component is much lower than the others, with the generic relations $B_\nu \ll B_\theta \ll B_\phi$. This configuration can be viewed as an infinite set of nested toroidal magnetic surfaces centered on the magnetic axis 1.3. By definition of magnetic surface the magnetic field does not cross any magnetic surface, instead each magnetic line lays on a specific surface, the magnetic flux enclosed in each magnetic surface is hence constant (hence the name flux surface) and can be used to label the surface. Since the flux varies monotonically from one closed surface to the next, either the poloidal flux ψ_{pol} or the toroidal flux Φ, can be used as radial variable. A more common expression for the radial coordinate is the normalised poloidal flux ρ_ψ, defined as:

$$\rho_\psi = \sqrt{\frac{\psi - \psi_0}{\psi_{LCFS} - \psi_0}} \tag{1.17}$$

where $\psi = \psi_{pol}/2\pi$ is the stream function at the considered surface, ψ_0 and ψ_{LCFS} the stream function at the magnetic axis and at the last closed flux surface (LCFS) respectively, the latter being the outermost flux surface on which the plasma is confined. A detailed analysis of flux coordinate systems and magnetic configurations can be found in [14]. A compact representation of the magnetic field is given by [14]

$$\mathbf{B} = \nabla\phi \times \nabla\psi + R B_\phi \nabla\phi \qquad (1.18)$$

recalling the relation $\nabla\phi = 1/R\,\mathbf{e}_\phi$.

By balancing the magnetic and pressure forces acting on the plasma, it can be shown that the pressure is constant on magnetic surfaces [15]. It is usually however assumed that equilibrium quantities such as density and temperature (and often the electric potential ϕ_{el}) are constant [16] along the magnetic field, since heat and particle transport timescales are much shorter along the field than across it. This can be used to reduce the description of the 3D plasma to a simplified 1D model, with equilibrium quantities functions of only the radial variable ρ_ψ. Hereafter we use simply ρ for the radial variable ρ_ψ.

The amount of "twist" of the field lines is characteristic for each flux surface and it is quantified by the safety factor q, that is defined as [17]:

$$q = \frac{d\Phi}{d\psi} \qquad (1.19)$$

with Φ the toroidal flux. It represents the number of toroidal turns needed to complete a poloidal turn. Flux surfaces with a rational $q = m/n$ are termed rational surfaces, the magnetic field lines of those surfaces close on themselves after m toroidal and n poloidal turns. The periodicity of these surfaces encourages the development of magneto-hydrodynamic (MHD) instabilities [15], that develop on fast timescales ($\simeq$ ms) and can lead to performance degradation and plasma disruption. The name safety factor mirrors this important feature, for example when $q \leq 2$ on the LCFS plasma is MHD unstable [3, 18] and quickly disrupts, while inside the $q = 1$ surface an MHD instability known as sawtooth [19] is observed. In standard scenarios with the plasma current preferentially circulating in the hotter plasma center, q rises monotonically from the plasma centre to the edge, while current research includes advanced scenarios with central negative shear (i.e. radial derivative of q). A more common expression for the safety factor is found applying the large aspect ratio approximation in pseudo-toroidal geometry (circular cross-section tokamak) to the definition 1.19, leading to [20]:

$$q = \frac{r B_\phi}{R B_\theta} \qquad (1.20)$$

where the minor radius r is the distance of the (circular) flux surface from the magnetic axis, and the major radius R is the distance of the considered point from the torus axis. The inverse
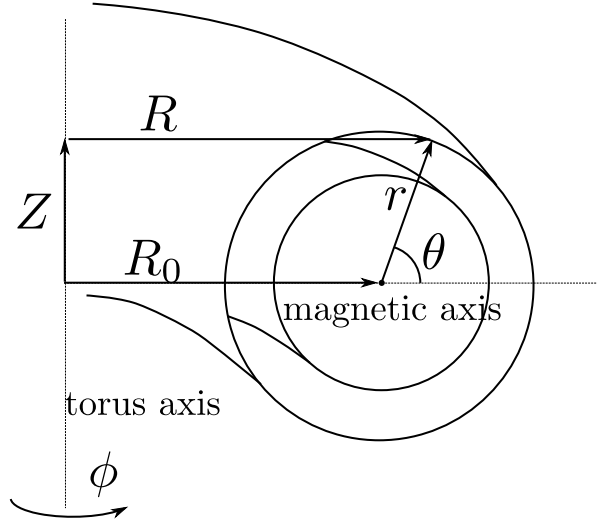
Figure 1.4: Cross section of a tokamak with definition of cylindrical (R, ϕ, Z) and pseudo-toroidal (r, θ, ϕ) coordinate.

aspect ratio ϵ is defined by

$$\epsilon = \frac{a}{R} \tag{1.21}$$

where a is the minor radius at the plasma boundary. The pseudo-toroidal coordinate (r, θ, ϕ) and the cylindrical coordinate (R, ϕ, Z) are shown in figure 1.4. For non-circular plasma shapes the radial coordinate r can be defined by the equation

$$\frac{\partial r}{\partial \psi} = \frac{1}{2\pi R B_\theta} \tag{1.22}$$

The plasma shape, i.e. the geometrical shape of the magnetic surfaces on a poloidal cross section, has great influence on stability and transport. Shape is often described by the moments in sinusoidal expansion of the poloidal cross section, the first two moments are elongation κ and triangularity δ and are usually sufficient for the flux surface description. It has been seen that triangularity, a parameter that describe a deformation of the plasma cross section into a D shape (see figure 1.5), can improve energy confinement by a factor of 2 [21]. Elongation is also an important parameter for plasma stability [3], it describes how elliptical is the plasma and is defined as the ratio of the plasma vertical to the horizontal semi-axis (see figure 1.5). Plasma shape can strongly affect plasma turbulence and also plays a fundamental role in developing intrinsic rotation in tokamaks [22].

The plasma must, in some way, interact with its enclosing vacuum vessel. In a tokamak the plasma boundary is defined by the the last closed flux surface (LCFS), also called separatrix, that separates the confined region (plasma core and edge regions) from the scrape off layer [18] (SOL). In the SOL the magnetic field lines intersect the wall (usually within a few meters at
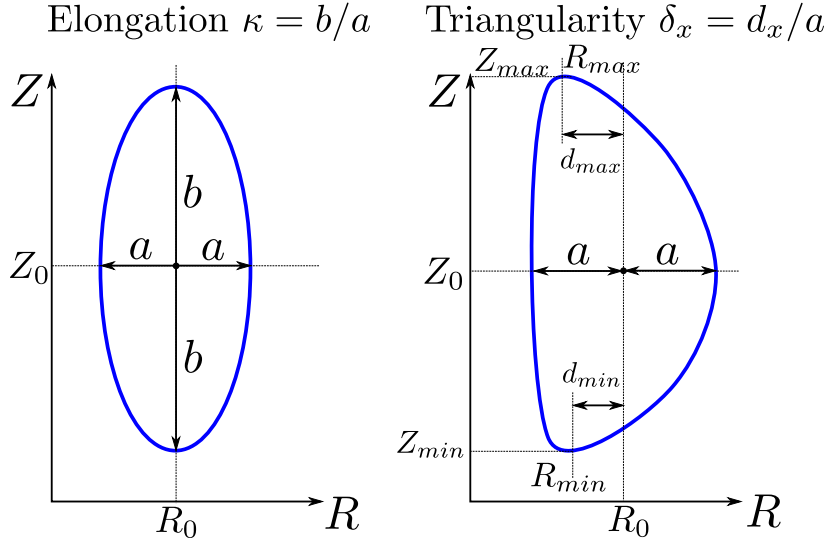
Figure 1.5: Definitions of elongation κ and triangularity δ.

most), the plasma exiting the LCFS is therefore rapidly ($\leq$ ms) convected (lost) on the wall. Depending on the topology of the LCFS two configurations are defined (see figure 1.6): limited and diverted. In the limited configuration the LCFS is in direct contact with a solid target called a limiter. This is historically the first configuration used in tokamaks and has the disadvantage that impurities released by the limiter are easily transported into the core, causing plasma contamination. This sets a restrictive limit on plasma edge temperature and density depending on the limiter materials. It can be shown that contamination, particularly for higher Z materials, can seriously prejudice our plans for a viable fusion-based reactor. The diverted configuration was introduced to avoid the direct contact of confined plasma with solid materials. This separation is realised by inducing a null point (or X-point) of the poloidal magnetic field component inside the vessel often using external shaping-control coils. The field lines that pass outside the X-point and intersect the divertor plates at the strike points are called separatrix legs, and constitute the main directed exhaust route for the plasma. The distance between the X-point and the striking point is the connection length L_c, that can be approximated by [18]:

$$L_c \simeq \pi R q \tag{1.23}$$

The SOL plasma cools down and can be strongly attenuated across its flow towards the strike point in the separatrix legs, due to radiation, charge exchange (CX) and volumetric recombination, reducing the power loads on the divertor plates. Sputtering in this configuration is reduced and the impurities are released far away, and no longer directly re-directed back to the confined plasma, reducing plasma contamination.
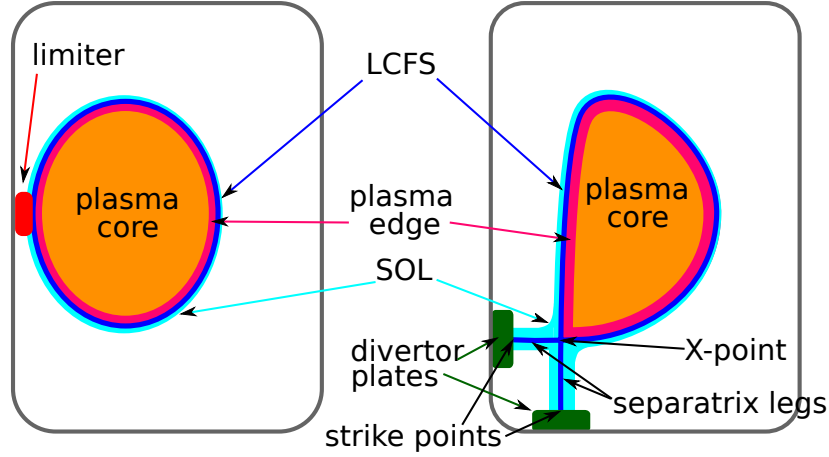
Figure 1.6: Sketch of a limited and diverted configuration. The confined plasma (core-edge) are separated from the SOL by the LCFS (also called separatrix).

1.1.3 Confinement and particles drifts

In section 1.1.2 we observed that particles in an uniform magnetic field are radially (direction perpendicular to **B**) confined by the gyro-motion caused by the Lorentz force. Their averaged trajectory can be described by the motion of the guiding centre that is a straight line parallel to **B**. If a force **F** with a non-null perpendicular to **B** component is applied, a drift of the guiding centre in the perpendicular direction of both **F** and **B** occurs. The general expression for such drift is [2, 23]:

$$\mathbf{v}_d = \frac{\mathbf{F} \times \mathbf{B}}{q B^2} \tag{1.24}$$

In a tokamak there are three fundamental particles drifts:

1. the $\mathbf{E} \times \mathbf{B}$ drift $\mathbf{v}_{\mathbf{E} \times \mathbf{B}}$ 1.25,

2. the curvature drift $\mathbf{v}_c$ 1.26,

3. and the grad-B drift $\mathbf{v}_{\nabla B}$ 1.27.

The $\mathbf{E} \times \mathbf{B}$ drift is due to the Coulomb force $\mathbf{F} = q E$ and is independent of the particle charge:

$$\mathbf{v}_{\mathbf{E} \times \mathbf{B}} = \frac{\mathbf{E} \times \mathbf{B}}{B^2} \tag{1.25}$$

It engenders uni-directional plasma motion, since it's in the same direction for both positive and negative charges, and it's one of the fundamental sources of rotation.

If the magnetic lines are bent, with a curvature radius $\mathbf{R_c}$, the centrifugal force acting on the particle results in a curvature drift:

$$\mathbf{v}_c = \frac{m\,v_\parallel^2}{qR_c^2}\frac{\mathbf{R_c}\times\mathbf{B}}{B^2}.\tag{1.26}$$

The grad-B drift is caused by the change in the Larmor radius due to the non uniformity of B and can be expressed as:

$$\mathbf{v}_{\nabla B} = \frac{\frac{1}{2}\,m\,v_\perp^2}{qB}\frac{\mathbf{B}\times\nabla B}{B^2}.\tag{1.27}$$

In a tokamak the toroidal field has a $1/R$ spatial dependence and the grad-B drift is unavoidable.

The curvature and the grad-B drifts acting in the toroidal magnetic field combine together to cause charge separation, since they are opposite for ions and electrons. The electric field induced by the charge separation causes a radial $\mathbf{E}\times\mathbf{B}$ drift of the whole plasma, resulting in disruption. The poloidal field, generated by the plasma current in a tokamak, compensates this drift, stabilising the configuration.

1.2 The TCV Tokamak

This work was carried out at the Swiss Plasma Center (SPC), on the *Tokamak à configuration Variable* (TCV). TCV is a medium size tokamak designed to study the influence of plasma shape on stability, confinement and transport. In order to maximise the shaping flexibility the vacuum vessel is highly elongated (height 1.5 m, width 0.5 m) and there is no dedicated divertor chamber, as can be observed in the TCV sketch of figure 1.7. The TCV first wall is almost completely covered by graphite tiles that serve either as limiter or as divertor targets. This gives almost complete freedom on plasma and X-point positioning, that in other devices is, at least partially, fixed by design. The Carbon released from the plasma erosion of the tiles constitutes the main impurity in TCV. Boron is another impurity found in TCV, that comes from boronisation [24], a procedure that reduces oxygen and other impurities release from the wall.

The main TCV mechanical specifications [24] and achieved plasma parameters are reported in table 1.1.

The toroidal Ohmic plasma current is induced by a transformer composed by 7 coils, (A) in figure 1.7. The toroidal magnetic field is generated by a set of 16 Ohmic coils (B) connected in series, and can reach a maximum value of 1.5 (normally 1.44) T on axis. A set of 16 poloidal field (PF) coils (D) is mounted on both sides outside of the TCV vessel (C), each coil has a dedicated power supply to maximise the plasma shaping flexibility. Figure 1.8 shows some

Parameter	Symbol	Value
Major radius	R_0	0.88 m
Minor radius	a	0.255 m
Aspect ratio	$1/\epsilon = R_0/a$	≤ 3.5
Vessel height	h	1.54 m
Vessel elongation	κ_{TCV}	3
Vessel base vacuum	p_{TCV}	$\leq 10^{-7}$ mbar
Vessel time constant	τ_{TCV}	6.7 ms
Toroidal field on axis	B_0	≤ 1.54 T
Loop voltage	V_{loop}	1-2 V
Plasma current	I_p	≤ 1 MA
Installed power	P_{TCV}	≤ 200 MW
Ohmic heating power	P_{OH}	≤ 1 MW
NBH heating	P_{NBH}	≤ 1 MW
ECRH X2 heating	P_{X2}	≤ 2.8 MW
ECRH X3 heating	P_{X3}	≤ 1.4 MW
Plasma species		D (He,H)
Main impurities		C,B
Plasma elongation	κ_a	0.9-2.8
Plasma triangularity	δ_a	-0.8 +0.9
Electron density	n_e	$\leq 2 \cdot 10^{20}$ m^{-3}
Electron temperature (OH)	T_e	≤ 2 keV
Electron temperature (ECRH)	T_e	≤ 15 keV
Ion temperature (OH-ECRH)	T_i	≤ 1 keV
Ion temperature (+ NBH)	T_i	≤ 3.7 keV
Electron cyclotron frequency	f_{ce}	41 Ghz
Plasma frequency	f_{pe}	30-120 Ghz
Electron Larmor radius	ρ_e	50-250 μm
Ion Larmor radius	ρ_i	2-7 mm

Table 1.1: Main TCV technical specs and plasma parameters.
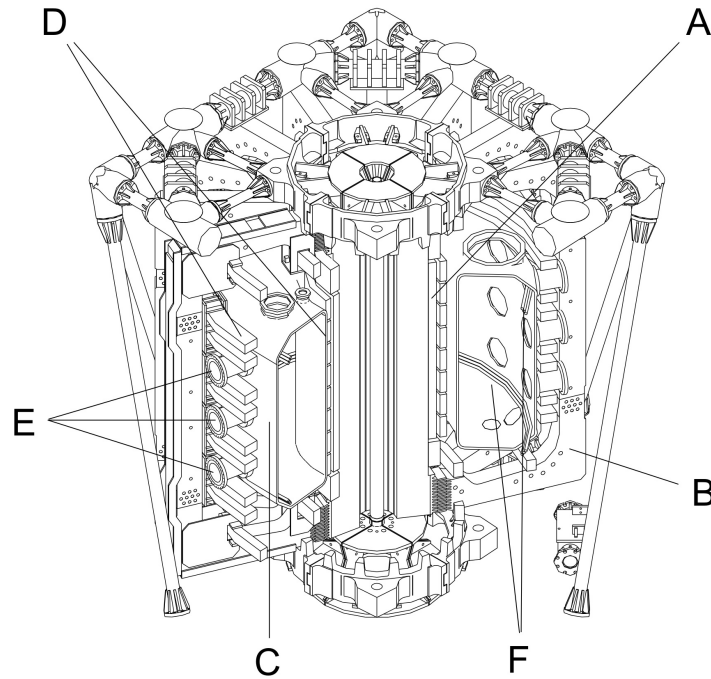
Figure 1.7: Sketch of TCV. (A) central solenoid for inducing ohmic current, (B) toroidal field coils, (C) vacuum vessel, (D) shaping coils (poloidal field coils), (E) flanges (access windows) and (F) in vessel vertical (poloidal) field coils.

examples of the most extreme plasma shapes achieved in TCV.

Vertical plasma stability is particularly challenging for highly elongated plasmas $\kappa > 2$; in TCV a feedback stabilisation is enhanced exploiting a set of two vertical field coils located inside the vacuum vessel (F), able to react on the plasma within 0.1 ms. These coils, in conjunction with a high conductivity (stabilising) vacuum vessel and the PF coils, enabled TCV to reach a record plasma elongation of $\kappa = 2.8$ [25].

1.2.1 TCV heating systems

In TCV the initial plasma heating is induced by the Ohmic current that is able to heat the plasma up to a temperature of $T_e \leq 1$ keV [26]. Two auxiliary heating systems are available in order to reach fusion-relevant temperatures: the electron cyclotron resonant heating (ECRH, or just ECH) and the neutral beam injection heating (NBI or NBH). The former system directly heats the electrons, the latter heats preferentially the ions.

TCV ECRH systems

The ECRH system exploit the resonant interaction between microwave beams and the gyro-motion of the electrons in the confining magnetic field. The interaction is resonant when
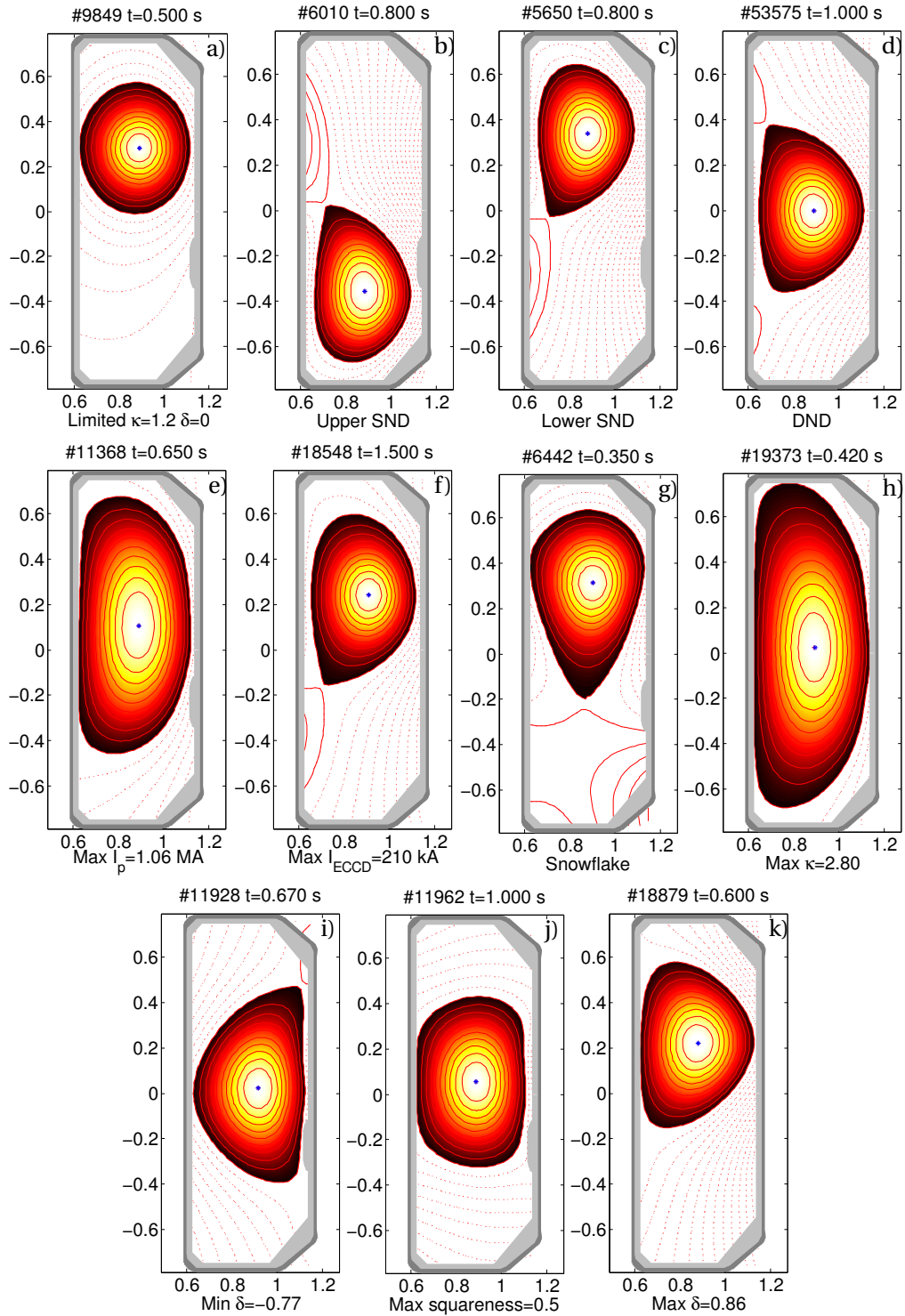
Figure 1.8: Magnetic reconstruction (LIUQE) of some selected TCV discharges showing TCV plasma shape capabilities.
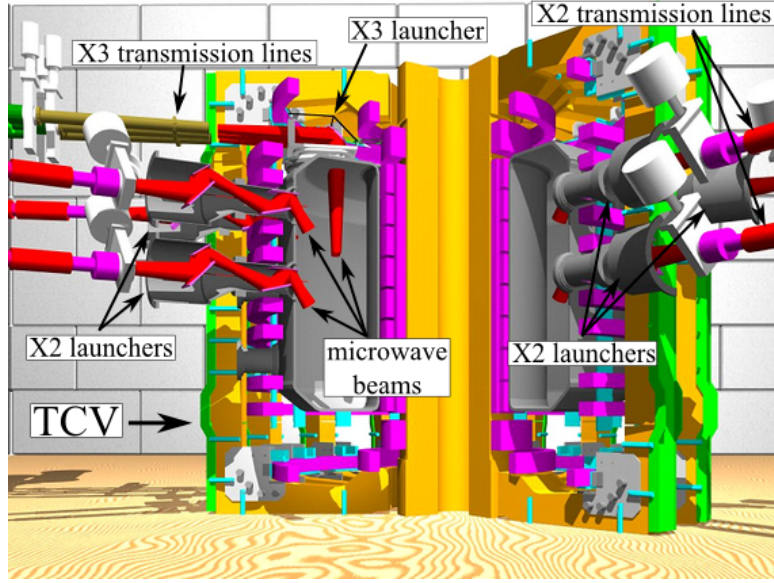
Figure 1.9: Sketch of the TCV ECRH launchers for the X2 and X3 systems.

the electromagnetic (EM) wave frequency is an integer multiple of the electron cyclotron frequency Ω_c. We showed above that Ω_c is proportional to $|\mathbf{B}|$ and that in a tokamak $B \propto 1/R$, it follows that the ECRH deposition heating is highly localised (≤ 1 cm) on an approximatively vertical resonant layer (fixed R), that can be adjusted varying B_ϕ. The power coupling is optimised for EM wave polarization in the extraordinary mode (X-mode), where the EM electric field is orthogonal to the tokamak magnetic field. The EM wave is also able to drive current if injected with a toroidal direction component, this effect is explained in [27] and it is known as electron cyclotron current drive (ECCD). The TCV ECRH system presently consists of up to six gyrotrons tuned to the second harmonic at 82.7 GHz termed X2, and three X3 gyrotrons tuned to 118 GHz. Each gyrotron can provide a nominal power of 465 kW for the X2 and 480 kW for the X3, for a total of 4.23 MW available ECH power. EM waves can propagate in a plasma only if their frequency is above the cut-off frequency, that is, itself, proportional to the square root of the electron density. The corresponding cut-off densities are $n_{e,max,X2} = 4.25 \cdot 10^{19}$ m^{-3} for X2 and $n_{e,max,X3} = 11.5 \cdot 10^{19}$ m^{-3} for X3. The EC X2 waves are injected in TCV through steerable launchers from lateral ports (see figure 1.9), allowing control on the poloidal and toroidal power (and ECCD) deposition. The ECCD-X2 system was extensively used for this work in the experiments devoted to the study of momentum transport across the sawtooth cycle. The final mirror of each system can be displaced during the plasma discharge allowing a modification of the absorption position as the discharge evolves.

TCV NBI heating system

The commissioning of the first NBI heating system in January 2016 TCV expanded the working parameter space to regimes where $T_i/T_e > 1$ [28], filling the gap between predominantly
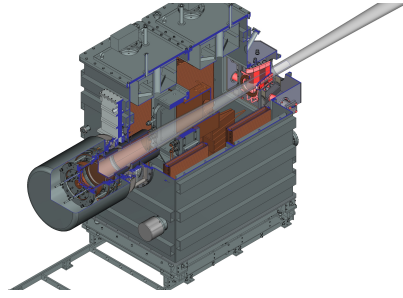
Figure 1.10: NBI CAD drawing.

Parameter	Value
Power injected in TCV	0.09 - 1 MW
Beam energy	10-25 keV
Max NB pulse duration	2 s
Full energy power fraction	73%
Beam main species	D - H
100% power modulation	≤ 200 Hz

Table 1.2: NBH specifications.

electron heated experiments and fusion reactor conditions. It also opened access to the study of fast ion physics, that can now benefit of the peculiar TCV plasma shape flexibility. To this end, a FIDA survey diagnostic was implemented in TCV, details of the implementation and results are presented in appendix A. The upgrade required to install the neutral heating beam took ≃ 19 months, that occurred during this thesis project, causing delay in the CXRS EDGE diagnostic commissioning and exploitation (the implications are further discussed later in this thesis). Figure 1.10 shows a CAD drawing of the NBH, whose main operational parameters are listed in table 1.2.

The beam power can be smoothly changed from 0.09 to 1 MW (albeit with a simultaneous change in ion energy from ≃ 15 keV to ≃ 25 keV), and can be modulated at up to 200 Hz. The beam energy depends on the requested power ranging from 10 to 25 keV, with a full energy fraction (in power) of 73%. An injection geometry tangent to the plasma axis at the machine mid-plane was chosen to maximise heating efficiency for the widest range of plasma parameters whilst satisfying machine access limitations.

Following initial tests, the total energy delivered by the NBH into TCV was limited to 0.5 MJ in 2016 and 2017 due to excessive beam divergence that caused overheating and damage to the beam duct. A modification of the beam duct and an improvement of the ion optics are under study to solve this problem to unlock the NBI's full potential.

The intensive testing of the NBI provided evidence that, on balance, it facilitates H-mode access, it changes sawtooth and ELM frequencies, and provides a significant plasma current drive. A new TCV record ion temperature of 3.7 keV was achieved early in the first medium size tokamak (MST1) campaign, a campaign involving multiple machine of European Fusion Programme organised by the EUROfusion Consortium [13].

The NBI provides TCV with an active source of torque allowing study of momentum transport other than the one related to intrinsic rotation. With the use of NBI torque, toroidal velocities up to 200 km/s in the beam direction ($-\mathbf{e}_\phi$) have been recorded, while the intrinsic rotation in TCV is limited to ≤ 60 km/s.

17

1.2.2 TCV diagnostics

TCV is equipped with an extensive set of diagnostics that measure most of the relevant experimental plasma parameters. The strong TCV versatility in plasma shaping has a heavy repercussion on diagnostics design, the measurement spatial coverage and dynamic range have to cover a large range of plasma densities and temperatures on a shot-to-shot basis. A brief description of the main diagnostics particularly relevant for this work can be found in the following paragraphs.

Magnetics

The magnetic equilibrium of TCV is reconstructed by the Grad-Shafranov solver LIUQE [29–32] exploiting the measurements of the Mirnov coils installed inside the TCV vacuum vessel, between the vessel and the graphite tiles, to avoid the finite magnetic diffusion time of the conducting vessel. These probes are also used in the MHD analysis to detect instabilities and modes. Four sets of poloidal probes arrays, of 38 probes each, measure the component of the poloidal field tangential to the vacuum vessel at fixed toroidal positions (equispaced by 90°). Three pairs of toroidal arrays are positioned at different vertical positions: TOP $Z = +35$ cm, MIDDLE $Z = 0$ and BOTTOM $Z = -35$. Each pair consists of a set of equispaced probes, 8 at the HFS and 16 at the LFS, with an additional probe in the LFS set (total of 17 probes) with the breaking of symmetry permitting the detection of modes with toroidal numbers up to $n = 16$. Three (TOP, MIDDLE and BOTTOM) sets of saddle loop, 8 probes each, complete the MHD acquisition system.

The maximum acquisition frequency is 1 MHz, although for standard operation an acquisition frequency of 250 kHz is used, which is satisfactory to measure MHD activity in most TCV plasmas and more than sufficient for plasma shape reconstruction.

The poloidal Mirnov coil array of TCV are treated as a discrete approximation of a Rogowski coil and are used to estimate the plasma current I_p [33].

Electron diagnostics

There are two main diagnostics in TCV dedicated to the measurements of the main electron parameters, which are density n_e and temperature T_e. These diagnostics are the Thomson scattering system (TS) and a far infrared interferometer (FIR).

Thomson scattering
The Thomson scattering diagnostic [34] provides local measurements of both electron density n_e and temperature T_e. It exploits the elastic scattering of EM waves from electrons called Thomson scattering. The electron density is proportional to the intensity of the scattered light, whilst the temperature can be calculated by a spectral analysis of the scattered signal, whose wavelength differs from the incident light due to Doppler broadening (this is somewhat

complicated by a relativistic term in the cross section that depends on the electron energy distribution but the principle remains as described). The incident light is provided by three Nd-YAG lasers. Their wavelength is 1064 nm, with a 20 Hz repetition rate and a maximum energy of 0.85 J each. The optical path of the lasers within the TCV vessel almost overlap, so they can operate either with a simultaneous trigger, to achieve a higher signal/noise ratio (S/N) required for low density plasmas, or with independent triggering to increase the time resolution of the system. The latter configuration can be exploited in the study of fast events, it allows the acquisition of 3 profiles with a short temporal inter-space of $\simeq 2$ ms, which is the sensor system sampling time, with a 20 Hz repetition rate imposed by the lasers' performance.

The laser beams traverse the plasma at $R = 0.9$ m (mid radius of the TCV vessel, figure 1.11-(a)). Currently there are 47 observation positions covering the region Z = (-31, + 66) cm, with a spatial resolution that depends on the channel location, higher at the plasma edge [35] (top and bottom). A set of 35 chords with intermediate resolution (integration length 16mm) has recently been installed to increase the diagnostic coverage and additional upgrades are planned. The radial profiles are calculated by mapping the measurements to the vertical laser path and the magnetic equilibrium reconstructed by LIUQE. Profile symmetry can also be used as an additional constraint for the magnetic reconstruction, although this approximation is sometimes seen to fail in particular plasma conditions on Tokamaks.

The scattered light is analysed using filter polychromators (4-6 spectral channels) optimised for measurements of the electron temperature over a range from 10 eV to 20 keV. The system is absolutely calibrated using Raman scattering of a N_2 gas filled TCV vessel, but drifts in the alignment of the laser beams and in the detection optics affect the calibration consistency. The absolute, but line-integrated, FIR diagnostic is used as a reference to adjust the TS density profile.

The TS diagnostic is the most important electron diagnostic in TCV, it is essential in many post-shots analysis routines and in the interpretation of other diagnostics, including CXRS.

FIR

The FIR exploits a Mach-Zender interferometer to provide line integrated electron density measurements, along 14 vertical paths showed in figure 1.11-(b). The interferometer measures the phase difference, due to the refractive index of the plasma, of the laser beam (wavelength 184.3 μm) passing through the 14 line of sight (LOS) with a reference external path. The line integrated electron density is proportional to this shift. The standard acquisition rate is 20 kHz, with a typical accuracy of 1%. The system is fully automated and is part of the essential diagnostic set in TCV operation, as the measurement along the central chord ($R = 0.9$ m) is used for real time control of the plasma density. The density profile can be reconstructed by Abel tomographic inversion, either employing Minimum Fisher regularisation or using the Singular Value Decomposition technique and base functions selected from the TS profiles results [36].
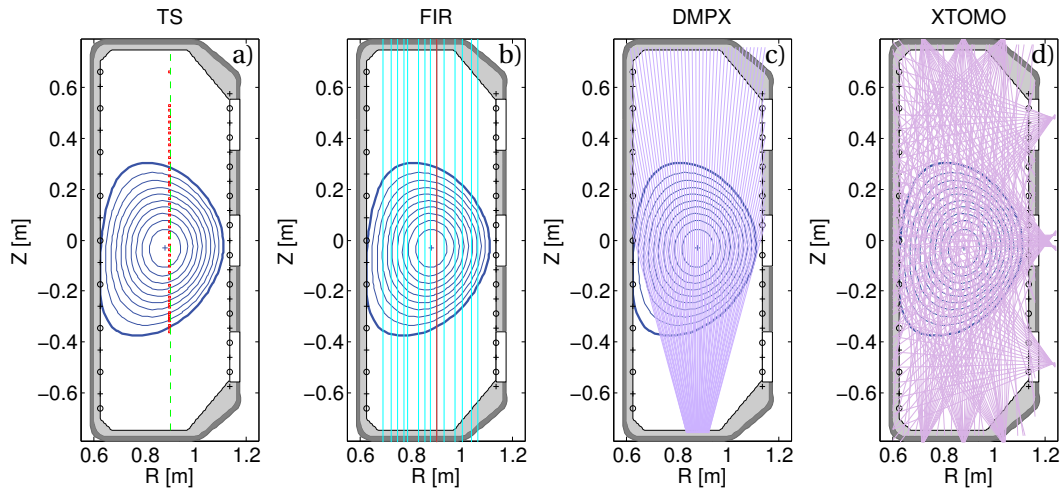
Figure 1.11: Graphical representation of the LOS for the diagnostics: a) Thomson scattering, b) FIR, c) DMPX and d) XTOMO.

Ion diagnostics

The main ion diagnostic in TCV are the charge exchange recombination spectroscopy (CXRS), that measures impurity parameters, and the compact neutral particle analyser (CNPA), for line integrated measurements of the plasma main specie.

CXRS

The CXRS diagnostics in TCV [37–39] provides local measurements (see figures 2.10 and 2.11) of plasma impurity density n_{imp}, temperature T_{imp} and rotation velocity v_{imp}. The system exploits the active charge exchange (CX) reaction between the impurity ion and an high energy neutral hydrogen atom of a diagnostic NBI (DNBI), which is detailed in section 2.2.1. The low power ($\leq$ 80 kW delivered into the vessel) of TCV DNBI allows for unperturbed rotation measurements, which are preferable for intrinsic rotation studies. The recombined impurities, excited after the CX reaction, emit line radiation that is analysed by spectrometers. The measured quantities are related to the first three moments of the impurity emission line. The main TCV intrinsic impurity is Carbon, that is released from the wall, and it is routinely measured through the CVI line at 529.06 nm.

The maintenance, development and upgrade of this diagnostic constituted the major work of this thesis. The CXRS diagnostic is thus described in detail in chapter 2.

CNPA

The compact neutral particle analyser (CNPA) [40] measures the high energy (0.64-50 keV H, 0.56-33.6 keV D, 0.98-18.1 keV He) neutrals (either the couple H-D or D-He can be measured simultaneously) escaping the plasma. These neutrals are produced by CX reactions of the main ions species with the background neutral atoms that penetrate in the plasma confined region, therefore from their energy distribution information on the initial ion distribution

can be inferred. Active measurements employing LOS intersecting a NBI are feasible for this diagnostic, although in TCV mostly passive measurements are performed. The CNPA has a single LOS situated on the midplane, that can be set either perpendicular or tangent to the magnetic axis, to study either the perpendicular or parallel ion velocity distribution. The CNPA provides complementary measurements to CXRS, in particular of the high energy tail of the distribution, to which the CXRS diagnostic is much less sensitive. With the help of the Monte Carlo code DOUBLE-TCV [41] it is possible to estimate the neutral density profile in TCV, which is fundamental for the passive CX that constitute the principal background in active CXRS measurements.

Plasma EM emission diagnostics

The passive EM emission of fusion plasmas encompass a wide range of phenomena and energies, and TCV is equipped with a variety of diagnostics to characterise these emissions. The principal EM emission are [34]:

- line radiation, due to electronic excitation, recombination or CX;

- continuum radiation, due to recombination and bremsstrahlung.

The EM diagnostics relevant for this work are:

1. Photodiodes for D_α line radiation (PD);

2. duplex multiwire proportional X-ray counter (DMPX);

3. Tomographic soft X-ray diagnostic (XTOMO).

PD
Eighteen photodiodes are installed on TCV [42], equipped with a set of spectroscopically chosen interference filters to acquire different specific spectral lines, at a typical acquisition frequency of 125 kHz. Ten photodiodes have a D_α filter and are used for plasma survey and in the identification of fast phenomena, such as the L-H transition.

DMPX
The duplex multiwire proportional X-ray counter [43] is a soft X-ray (SXR) detector composed of 2 Krypton-CH4 wire-chambers, that have a total of 64 LOS in a TCV poloidal section (see figure 1.11-(c)). The diagnostic is sensitive to X-rays in the energy range 1-30 keV, the lower limit of 1 keV is imposed by a fixed beryllium filter, that can be increased to 15 keV by inserting additional filters. It is particularly suitable in the study of fast events, like the sawtooth MHD instability, due to a 200 kHz sampling rate and high spatial resolution ($\simeq$ 8 mm at the midplane).

XTOMO

The XTOMO [44] is a 10 camera tomographic system working in the 1-15 keV X-ray range. The camera are placed in a poloidal cross section of TCV, 3 on top, 4 on the LFS and 2 on the bottom. Each camera houses 20 silicon photodiodes, for a total of 200 LOS that cover the whole TCV poloidal cross section (figure 1.11-(d)), allowing a full 2D tomographic reconstruction. This implies that XTOMO is capable of resolving the poloidal structure of the SXR emissivity, enabling the study of modes and instabilities. The maximum sampling rate of 80 kHz and the space resolution of 3-4 cm are the limiting factors for the reconstruction.

1.3 Thesis objectives and outline

1.3.1 Motivations

With the construction of ITER and the design of DEMO, fusion physics research is concentrating on improving our understanding of fundamental performance criteria such as the transport of particles and energy in the reactor plasma.

The radial transport of particles and heat in a tokamak is a complex and not fully understood process [45], that sets the performance limits of a fusion device.

Explanations of the measured level using collisional transport, either with a simplified model (classical transport) or considering the full magnetic geometry and particle drift (neoclassical transport), often underestimate the experimental transport by 1-2 orders of magnitude [46]. This observed enhanced transport, referred to as 'anomalous' transport, is considered to be the result of small scale turbulence, driven by temperature and density gradients.

Much of the theoretical work requires detailed knowledge of many plasma parameters that are not experimentally possible to measure. One of the plasma parameters that can be measured is bulk plasma flow, most often seen as a plasma rotation about some axis (often poloidal and/or toroidal). Rotation has, in some situations, been shown beneficial in stabilising and thus reducing turbulence, in particular is commonly accepted that the $\mathbf{E} \times \mathbf{B}$ velocity shear can suppress turbulence by decorrelating the turbulence eddies and vortex thinning [47]. Rotation has a stabilising effect also on a variety of MHD modes, such as the resistive wall modes (RWM) [48], neoclassical tearing modes (NTM) [49] and sawtooth, and it helps preventing locked modes at rational q surfaces.

Bulk plasma rotation is thought to play a role in the transition to the H-mode [6]. The reduction of turbulence caused by the poloidal sheared flow [50] may be a trigger for the transition, but definitive experimental evidence supporting this hypothesis is still lacking.

Since a Diagnostic Neutral Beam was installed on TCV, previous work focussed on the characterisation and interpretation of toroidal rotation, in particular on the dependence of intrinsic rotation on plasma parameters [38] and in the role of sheared rotation in the formation of

transport barriers [39]. During this period, understanding intrinsic rotation became a strong research avenue with the joint goals of developing a consistent model of a fusion reactor [11, 51], and in predicting the intrinsic rotation in a fusion device, where the torque driven by NBI is expected to be negligible [52] with respect to the intrinsic drive. In other fusion experiments plasma rotation is often dominated by external sources (NBI) and studies on intrinsic rotation are possible only in dedicated experiments by employing a power 'blip' technique [53, 54]. In this framework TCV's measurements are directly pertinent to fusion reactor research.

From TCV's earlier experiments, the light throughput of the spectroscopic system, together with a reliable calibration were paramount in obtaining physics results. The main objective of this thesis was to improve the accuracy and the spatial and temporal resolution of poloidal velocity measurements on TCV and to extend them across the LCFS. This could then resolve the detailed structure of the poloidal rotation inside and across the LCFS where, particularly for H-mode configurations, strong activity was expected.

A preliminary overview of TCV's CXRS diagnostic indicated that the commercial spectrometers, employed at the start of this thesis, would not provide the throughput, nor spatial resolution, necessary to track changes in this region. It was decided to construct an "in house" visible spectrometer, employing commercial lenses, with a much higher étendue and, where possible, change the plasma viewing optics to enhance the spatial resolution. During this thesis, three such lens-based spectrometers were constructed and employed and further devices constructed to replace the remaining legacy spectrometers.

To complete this overview, TCV went through a major shutdown from 2013 to 2015, where the vacuum chamber was open to air. This was then followed by nearly another year of TCV operation in the European first medium size tokamak (MST1) framework [55] with major crises involving poor performance of the newly installed 1 MW neutral heating beam. These events compressed the available time for TCV experimentation, and thus data analysis, considerably more than for a conventional Ph.D. thesis at the SPC.
This time was, however, gainfully employed in building and testing the new spectroscopic system and collection optics on a high efficiency negative ion plasma source to be used for high power, high neutral energy ($\simeq 1 MeV$), NBH on ITER and beyond (chapter 3). This resulted in the first spectroscopic characterisation of the helicon source in the linear resonant antenna ion device (RAID) at the SPC [56]. Analysis of the passive spectroscopic data collected in 2015-2016 on RAID was completed using the collisional-radiative (CR) code YACORA [57], through a collaboration with IPP Garching. The CR model required a measurement of the complete Fulcher α Q diagonal spectrum and the first three Balmer lines, with the determination of the absolute line intensity for both H_2 and D_2. The work done resulted in an article published by the journal Nuclear Fusion [58].

The intensive use of the newly installed NBI in the MST1 campaign provided yet another task for the new spectrometer involving testing and commissioning of a new diagnostic able to detect the fast ion population generated by the NBI (max injection energy $\simeq 25$ keV).

Characterising and understanding the physics of fast ions and their confinement dynamics is a major objective towards the development of a working fusion reactor. The lens spectrometer was therefore used for the first TCV fast ion D-alpha (FIDA) diagnostic, using the toroidal LOS of the CXRS LFS system (SYS1). This diagnostic measures the active D_α emission from CX of the DNBI neutrals with the fast ions in the plasma following high energy neutral beam injection. The FIDA survey diagnostic, explained in appendix A, contributed to the final TCV FIDA design.

The physics aims of this thesis on TCV were to study the behaviour of momentum transport in the plasma edge.
One of the main questions was to ascertain whether poloidal rotation in TCV is similar to other devices and whether it is well described by neoclassical theory. The reduced uncertainty in the poloidal velocity measurements of the new spectroscopic system, called EDGE CXRS (or simply SYS4 in order to distinguish it from the three CXRS systems already installed on TCV) was achieved using an high throughput spectrometer and by optimising, for poloidal measurements, the geometry of the diagnostic LOS, using a new periscopic view. This system required a review of the CXRS software suite to encompass situations with large signal intensity variations and complex triggering.

The role of MHD activity in determining the plasma rotation has already been the subject of Ph.D. work at the SPC [38, 39]. In this thesis, the sawtooth (ST) instability [19], a periodic relaxation of the plasma core that causes flattening of the electron density and temperature profiles, was again studied, where strong ST-period control was used to optimise the CXRS diagnostic's performance, permitting time resolved measurements of the plasma rotation and plasma electric field across a ST period. The strong role of just one of the possible known MHD modes in a Tokamak could then be quantified in terms of momentum conservation to probe whether such modes can act as a direct plasma torque. In this context the experiments on TCV provided evidence of a co-current kick in the core intrinsic toroidal rotation at the ST crash, with a resulting hollow profile, followed by steady relaxation to a peaked monotonic profile. This effect must be explained by a comprehensive ST theory.

Another reactor relevant topic is the H-mode operation, appealing for the confinement properties. The H-mode threshold is reduced by strong rotation [6], which is also considered to be a trigger for the transition; hence a characterisation of impurity parameters at the edge, where the H-mode transport barrier develops, has been performed to improve the understanding of the transition. In particular the changes in the poloidal flow and in the radial electric field across the transition suggested a strong importance of poloidal rotation for triggering the transition, although only time resolved measurement of the transition itself, which is unattainable in TCV yet, might definitively confirm the hypothesis.

This work was almost all performed with only the lower power diagnostic beam that is used to probe the ion kinetic profiles without perturbing the experiment directly. Although plasma momentum transport was the main goal of this thesis, the behaviour of impurity transport,

through absolute diagnostic calibration, is also available and of strong interest to the Fusion community [59]. In this thesis the transport of intrinsic Carbon impurity measured for the rotation experiments is also described showing that a simple diffusive model is not physically sustainable. In particular,there are evidence of impurities expulsion from the core at the crash, consistent with predictions in [60], that cannot be reduced to simple turbulence transport. Measurements with other impurities (N_2 and He) are described where it is shown that the DNBI is not appropriate for this research. An extension, by using the high power heating beam (installed in 2016 on TCV), is discussed.

1.3.2 Outline

This chapter introduced the reader to general concept related to nuclear fusion and to the tokamak device used in this work. The remainder of this thesis is structured as follow:

- Chapter 2 describes in details the CXRS diagnostic in TCV. The measurements principles are exposed and the status of the diagnostic is described, with emphasis on the design and characterisation of the EDGE system. Finally the analysis procedure of the experimental spectra is described.

- Chapter 3 presents the methodology and the results of the spectroscopic characterisation of helicon plasmas in RAID. With the delay in TCV operations, this was also used as a test bed for the EDGE system spectrometer and required considerable effort and time.

- Chapter 4 introduces some fundamental concepts of plasma rotation and momentum transport that are used in the following chapters.

- Chapter 5 illustrates the evolution of rotation and momentum transport across a sawtooth event in L-mode limited discharges. The measurement method is described in details and the results of a scan in ST period are interpreted.

- Chapter 6 describes the changes in rotation and impurity profiles that characterise the L-H transition, together with a characterisation of the electric radial field 'well'.

- Chapter 7 summarises the work described in this thesis and provides an outlook on future CXRS studies on TCV.

2 CXRS diagnostic in TCV

The study and understanding of momentum transport and rotation in tokamaks requires high accuracy and precision in the measured profiles. The charge exchange recombination spectroscopy (CXRS) represents the most widespread diagnostic employed for the localised measurement of impurity ion kinetic profiles. Local measurements are achieved exploiting active CX emission at the intersection of the CXRS spectrometer LOS with an NBI, that supplies high velocity donors for the reaction. Worldwide, it is customary to utilise a high power ($\geq$ 1 MW) NBI, primarily installed for auxiliary plasma heating, for CXRS measurements. Although this provides a strong active signal, it perturbs the measured parameters by injecting momentum and heat into the plasma, particularly the ions themselves. In TCV, an elegant solution was adopted to avoid these perturbations, where a diagnostic neutral beam (DNBI) is employed for CXRS measurements, which injects into the plasma $\simeq$ 50 keV H atoms in a near-radial direction, for a total power delivered in TCV $\leq$ 80 kW (with a considerable power fraction deposited upon the electrons). This configuration allows measurements of kinetic ion parameters including plasma intrinsic rotation, i.e. the rotation profile that spontaneously develops in momentum source-free tokamaks.

In the first part of this chapter, the principles and theoretical background of CXRS diagnostics are explained, with particular focus on the atomic physics effects that, if not taken into account, can influence and/or introduce systemic deviations in the measurements. A brief theoretical evaluation of uncertainty in these measurements is also introduced, that was then implemented into the CXRS analysis functions.

In the second part of this chapter, after a brief discussion on the current status of the legacy CXRS systems, a newly developed EDGE system is described, in both the hardware implementation and in the measured performance. Following an explanation of the alignment and calibration procedures, the specifics of analysis routines are discussed.

The chapter concludes with the results of the first attempts of Helium and Nitrogen CXRS measurements on TCV.

2.1 Measurement principle

The charge exchange reaction consists in a transfer of a bound electron from a donor neutral atom (typically for CXRS a H^0 or D^0 of an NBI) to a plasma ion, hereby represented by A^{+Z}. The reaction may be written as:

$$A^{+Z} + D^0(n_d, l_d) \rightarrow A^{+(Z-1)}(n, l) + D^+ \tag{2.1}$$

The electron after the reaction has a finite probability of occupying an excited state in the target ion of principal quantum number n and orbital quantum number l, with a maximum probability at $n_{max} \simeq Z^{3/4}$ [61] and $l \geq n_{max}$ for high energy (≥ 1 keV) donors. For fully stripped Carbon C^{6+}, the typical impurity measured in TCV, $n_{max} = 4$. The donor excitation level is also of fundamental importance, as the CX cross section magnitude and energy dependence are drastically dependent on n_d, as shown in figure 2.1.
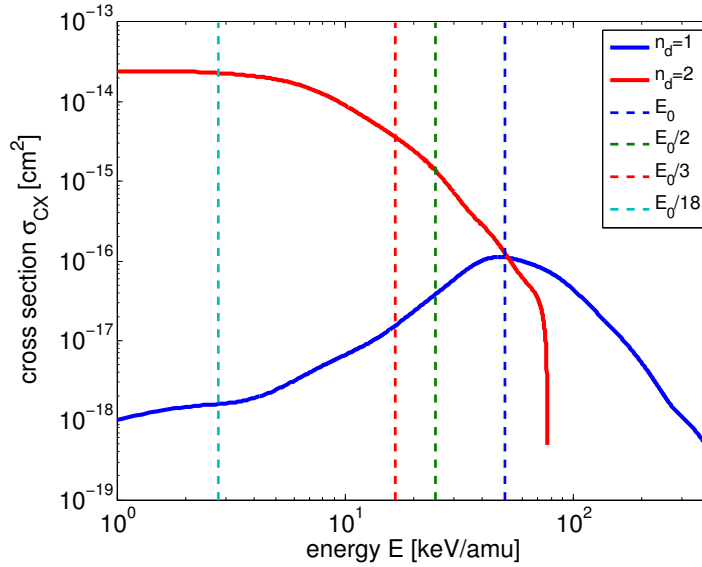
Figure 2.1: Cross section for the CX reaction populating the upper level of the CVI($n = 8 \rightarrow 7$) transition for donors at ground $n_d = 1$ and first excited $n_d = 2$ levels. Source ADAS database [62]. The vertical dashed lines represent the Hydrogen DNBI energy components with $E_0 = 50$ keV. Fractional energy components are explained in section 2.2.1.

The radiative de-excitation timescales (few ns) are much faster than ionisation timescales ($\simeq$ ms) for the usual tokamak plasma parameters, so the excited electron de-excites to the ground level $n = 1$ through a cascade of radiative transitions, in particular $(n, l) \rightarrow (n - 1, l - 1)$ for high l, before re-ionising. The emission lines of the cascade ranges from X-rays to the visible light, the latter is of particular interest for CXRS diagnostics due to the ready availability of high quantum efficiency sensors, optics and high resolution and dispersion imaging spectrometers. From the spectral analysis of a single emission line, the density, velocity and temperature can be calculated, which are related respectively to the zeroth, first and second moments of the

line spectral distribution (see below).

The Carbon transition chosen in TCV for CXRS is the CVI($n = 8 \rightarrow 7$) line, that is in the green region of the visible spectra at the wavelength $\lambda = 529.06$ nm. Carbon concentrations of few % are common after conditioning of the C-tiled TCV wall, whereas just after a boronisation procedure the C density drops significantly, due to the Boron coating on the graphite tiles preventing Carbon release. The wall conditioning typically lasts a few weeks (several tens of full power TCV discharges) and in this period a Boron emission line is observed instead. The selected emission line for Boron is in the blue visible range, from the transition BV($n = 7 \rightarrow 6$) centered at $\lambda = 494.467$ nm.

2.1.1 Main plasma ion and impurity profile comparison

The CXRS diagnostic measures impurities density n_α, temperature T_α and velocity v_α profiles, hence it is of great interest to identify how these quantities relate to the main ion corresponding parameters (n_i, T_i and v_i). From a comparison of the ion-electron equipartition time, in the range of $\tau_{e-i} \simeq 10 - 100$ ms for typical TCV plasmas, and ion-ion equipartition time, $\tau_{i-i} \simeq 0.1 - 1$ ms, it is estimated that the impurity and the main ions are, to a good approximation, in thermal equilibrium: $T_i \simeq T_\alpha$, which is confirmed by comparison with CNPA measurements in [40].

The connections between the impurity, main ion and electron density is embedded in the definition of the plasma effective charge Z_{eff}, which is:

$$Z_{eff} = \frac{\sum_l Z_l^2 n_l}{\sum_l Z_l n_l} \tag{2.2}$$

where l labels the ions in the plasma (both impurities and main ions). By including plasma charge neutrality $\sum_l Z_l n_l = n_e$ the relation between all the species densities is found. Equation 2.2 is usually relaxed in TCV by considering only the dominant impurity C^{6+}; with this approximation Z_{eff} profile is estimated using just the CXRS and TS data.

The relation between impurity and main ion rotation is more complicated, since neoclassical theory [63] allows for considerable differences in species' velocities, especially for poloidal rotation and in the presence of strong pressure gradients. This is caused by the diamagnetic contributions for each species and inter species friction forces. In previous works on TCV [38, 64], impurity toroidal velocity was studied and features unexplained by neoclassical theory, like rotation reversal, were found. Poloidal rotation, on the other hand, resulted more controversial, experiments on other devices resulted in cases of adequate agreement [65–69] and in cases of complete discrepancy [70–73] between the measured rotation and the neoclassical theory. The debate is still ongoing and improvements in both the experimental and theoretical knowledge are necessary in obtaining a conclusion.

2.1.2 Line shape

The spectral profile of the emission line used in CXRS measurements is considered in this section. A full understanding on the physical processes and atomic physics involved in the emission is paramount to correctly interpreting the measurements.

Considering a thermalised plasma impurity, Carbon in the following, the velocity distribution function follows the Maxwell-Boltzmann distribution function:

$$f_C(\mathbf{v}_C) = \frac{n_C}{\left(2\pi\sigma_C^2\right)^{\frac{3}{2}}} e^{-(\mathbf{u}_C - \mathbf{v}_C)^2/(2\sigma_C^2)} \tag{2.3}$$

with n_C [m^{-3}] the Carbon density, $\mathbf{u}_C$ [m/s] the rotation (bulk) velocity, and σ_C the standard deviation of the Gaussian, that is related to the Carbon temperature T_C [eV] by the equation

$$\sigma_C^2 = \frac{e\, T_C}{m_C} \tag{2.4}$$

where m_C [kg] is the Carbon mass and e [C] the elementary charge.

The spectral emissivity ϵ_λ [ph/s/m^3/sr/Å] of the active CXRS signal viewed by a LOS in direction $\mathbf{e}_{LOS}$ can be described, to first approximation, by a Gaussian function:

$$\epsilon_\lambda(\lambda, \epsilon_I, \lambda_1, \sigma_\lambda) = \frac{\epsilon_I}{\left(2\pi\sigma_\lambda^2\right)^{\frac{1}{2}}} e^{-\frac{(\lambda - \lambda_1)^2}{2\sigma_\lambda^2}} \tag{2.5}$$

where ϵ_I, λ_1 and σ_λ are the first three moments of ϵ_λ, termed respectively line emissivity, line central wavelength and line spectral width. A detailed derivation of this formula, with the assumption it implies, is found in appendix B. The moments of the spectral emissivity are related to the moments of the Carbon distribution function by the following equations

$$\epsilon_I = \sum_b \sum_k \frac{1}{4\pi} n_C\, n_{d,k,b}\, q_k^{eff}(E_b, n_e, T_e) \tag{2.6}$$

$$\lambda_1 = \lambda_0 \left(1 + \frac{\mathbf{u}_c \cdot \mathbf{e}_{LOS}}{c}\right) \tag{2.7}$$

$$\sigma_\lambda = \sqrt{\frac{e\, T_C}{m_C}} \frac{\lambda_0}{c} \tag{2.8}$$

where q_k^{eff} [ph m^3/s] is the effective emission coefficient for the transition $(n \to n')$ characterised by the rest wavelength λ_0.

The effective emission coefficient is calculated through the collisional radiative (CR) code ADAS [62], and depends on the donor energy E_b and plasma parameters.

The density $n_{d,k,b}$ of donors at the excited level k and energy E_b must be calculated or mea-

sured independently in order to extract n_C from radiance measurements, which is the LOS integrated emissivity of the active CXRS signal. In TCV, the DNBI neutral density is calculated across the plasma cross section for each energy component through a beam attenuation code [37, 40]. The population ratios R_{k1} of k level to ground level atoms are estimated from the local plasma parameters through a look-up table (see appendix C) generated from ADAS calculations. The procedure for absolute calibration of the CXRS system, which is necessary in the conversion counts-to-photons for radiance evaluation, is explained in section 2.2.3. An absolutely calibrated diagnostic directly measures the radiance L_{LOS} [ph/s/m^2/sr]

$$L_{LOS} = \int_{LOS} \epsilon_I(s)ds = \sum_b \sum_k \frac{1}{4\pi} \int_{LOS} n_C(s)\, n_{d,k,b}(s)\, q_k^{eff}(s)ds \tag{2.9}$$

which shows the necessity of a careful choice in the LOS geometry if localised measurements are desired, since the integral of the emissivity on the position s [m] along the LOS degrades the spatial resolution.

In TCV, with a quasi-perpendicular CXRS LOS to the small diameter DNBI ($\leq$ 10 cm, see figures 2.10 and 2.11), n_C and q_k^{eff} are considered constant across the intersection CXRS LOS-DNBI, equation 2.9 can be directly inverted, leading to an equation for the local density:

$$n_C\,[m^{-3}] = \frac{4\pi\, L_{LOS}}{\sum_b \sum_k q_k^{eff} \int_{LOS} n_{d,k,b}(s)ds} \tag{2.10}$$

The integral $\int_{LOS} n_{d,k,b}(s)ds$ is calculated from the beam attenuation code using the geometry of the CXRS-LOS and DNBI.

The rotation velocity projected on the LOS direction u_{LOS} is found by inverting equation 2.7:

$$u_{LOS}\,[m/s] = \mathbf{u}_c \cdot \mathbf{e}_{LOS} = \frac{\lambda_1 - \lambda_0}{\lambda_0}\, c \tag{2.11}$$

From equation 2.11 a velocity resolution of 1 km/s requires a diagnostic wavelength resolution $\delta\lambda_{diag} \leq 0.018$ Å.

The Carbon temperature is then calculated from the measured line spectral width using the relation:

$$T_C\,[eV] = \frac{m_C\, c^2}{e}\, \frac{\sigma_\lambda^2}{\lambda_0^2} \tag{2.12}$$

which assumes only the Doppler line broadening. In section 2.1.2 the dominant broadening mechanisms are described and included in the analysis when relevant.

The spectral analysis is complicated by passive emission due to CX reactions of the Carbon with the neutral gas surrounding the plasma, that diffuses in the confined region, and direct excitation of CV species. In TCV, using the lower density diagnostic neutral beam, the intensity

of the passive component dominates, with typical ratios active/passive in the range $25 - 5\%$, necessitating the adoption of a passive intensity subtraction technique (see 2.2.4).

Atomic physics corrections to the line shape

The description of CX line emission in the previous section is a simplified model of the actual emission as it neglects atomic physics effects that can modify the spectral emissivity distribution, inducing additional line shifts and broadening, that would be interpreted as apparent contributions to the measured velocity and temperature. These effects are:

1. Multiplet structure of the emitted line,

2. Stark splitting

3. Zeeman splitting

4. Energy dependence of the cross section.

Multiplet structure

The description of the transition $CVI(n = 8 \rightarrow 7)$ as a single atomic transition is inadequate. In the (n, l, s) wavefunction view, the spin-orbit interaction removes the degeneracy in the orbital quantum number l and l' of the Carbon energy levels $n = 8$ and $n' = 7$, resulting in 37 multiplet transitions $(nl \rightarrow n'l')$ 'allowed' by the dipole selection rules.

The emission from each transition depends on the branching ratio and on the population of the (n, l) sub-levels, which is influenced by the surrounding plasma parameters through
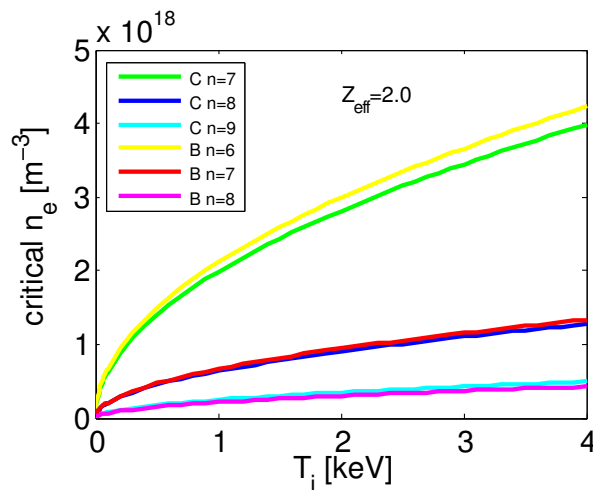
Figure 2.2: Critical density for l-mixing of Carbon and Boron excited levels. The transitions of interest for CXRS are $CVI(n = 8)$ and $BV(n = 7)$, both have critical densities $< 10^{18}$ m^{-3}.

collisions. To calculate the population structure a full CR mode is needed if no assumptions on the sub-levels can be made. This calculation is highly simplified if the levels are populated accordingly to their statistical weight (l-mixing). In [61] an expression for the critical density for l-mixing is found, with the results for Carbon and Boron shown in figure 2.2. The l-mixing assumption is applicable for both $CVI(n = 8)$ and $BV(n = 7)$ for densities above a critical density ($n_e \simeq 5 \cdot 10^{17}$ m^{-3}), that is well exceeded in the typical TCV parameter space ($n_e \simeq 10^{18} - 10^{20}$ m^{-3}). For this reason initial estimations were be performed with the l-mixing assumption.

The CR code ADAS [62] calculates the emissivity for each line of the 37 transitions forming the multiplet as function of plasma parameters by estimating the sub-level populations, considering initial distributions due to CX reactions (l-resolved cross-sections), redistribution within an n-shell and radiative cascade. An example of the multiplet structure of the transition $CVI(n = 8 \rightarrow 7)$ is shown in figure 2.3. The spectral emissivity of each transition in the multiplet is taken to be Gaussian, as expressed in 2.5. The change in the relative emissivity within the multiplet with plasma parameters cause a shift in the reference wavelength $\lambda_{0,mult}$ and in the broadening $\sigma_{\lambda,mult}$ of the total spectral emissivity.
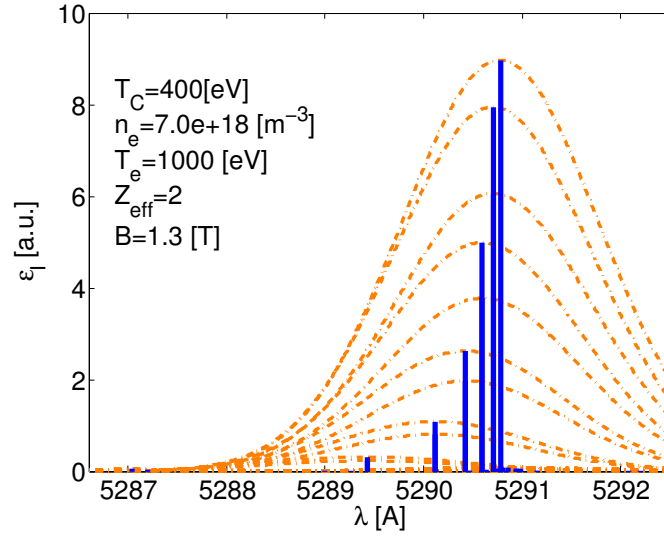
Figure 2.3: Multiplet-resolved structure emission of $CVI(n = 8 \rightarrow 7)$. The vertical blue lines show the wavelength for each transition of the multiplet while in orange is the spectral emissivity.

These effects are corrected in the TCV data analysis. A shift up to 0.05 Å with respect to the l-mixing estimations, corresponding to a velocity $\simeq 3$ km/s, is found in the typical range of TCV parameters. The multiplet effect on temperature is also not negligible, with maximum broadening of $\simeq 1$ Å, corresponding to $\simeq 60$ eV. The multiplet structure broadening must be also considered when in synergy with other broadening mechanisms, like the Zeeman effect.

Stark splitting

The Stark effect due to local electric fields is another mechanism that influences the atomic energy levels and population. An equation that estimates the critical n for l-mixing as function of T_i and B, for both linear and quadratic Stark effects, is reported in [61] and was used to generate figure 2.4-(a). The Stark effect therefore can further relax the condition for collisional l-mixing of figure 2.2. The change in the apparent temperature, also estimated in [61], are shown in figure 2.4-(b). The correction is within 1% for TCV relevant temperatures and is neglected in TCV's CXRS standard analysis.
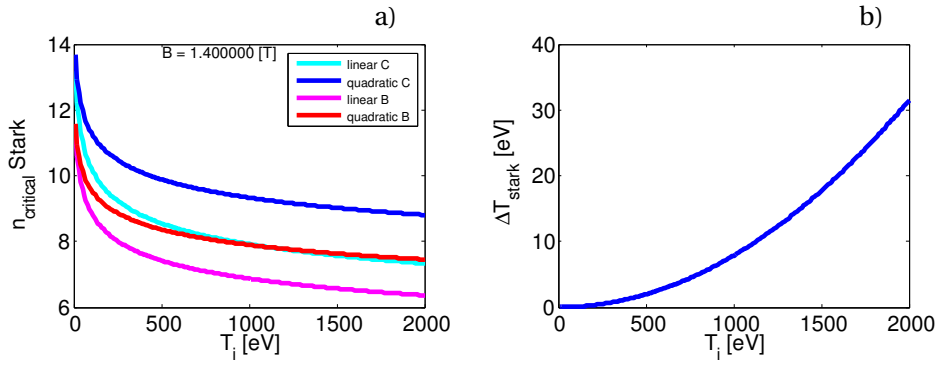
Figure 2.4: (a) critical n above which l-mixing is reached, as function of T_i, due to either linear or quadratic Stark effect, for both Carbon and Boron hydrogenic ions. (b) correction on Carbon temperature due to the Stark effect.

Zeeman splitting

The Zeeman effect is yet another mechanism that modifies the atomic energy levels. It is caused by the interaction of the external magnetic field with the electron angular and spin momentum. The net effect is to divide the transitions in three components depending on their polarisation: σ^-, π and σ^+. The energy levels of the π component are unperturbed (i.e. $\lambda_\pi = \lambda_{0,mult}$), while the changes in the energy levels of the components σ^- and σ^+ lead to a shift in the transition wavelength linear in B and given by

$$\Delta\lambda_{\sigma^\pm} = \lambda_{\sigma^\pm} - \lambda_\pi = K_Z \lambda_\pi^2 B \tag{2.13}$$

with the constant $K_Z = 4.67 \cdot 10^{-9}$ [1/(Å T)] found in [74], which agrees with results of [75].

The Zeeman effect is not isotropic, the radiant intensity of the three polarized components strongly depends on the angle θ_Z of emission with respect to the magnetic field direction. The pattern is described by the following equation

$$\frac{I_\pi}{I_\sigma^\pm} = \frac{2\sin^2(\theta_Z)}{1+\cos^2(\theta_Z)} \tag{2.14}$$

found in [75] and it is shown in figure 2.5-(a).
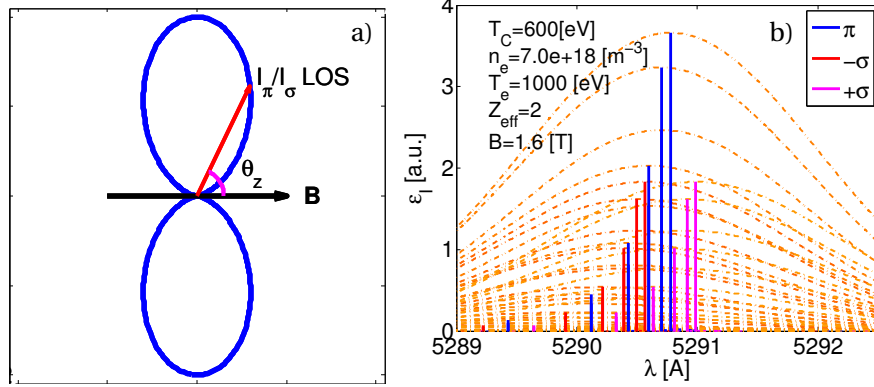
Figure 2.5: (a) pattern of the radiant intensity ratio $\frac{I_\pi}{I_\sigma^\pm}$ as function of the angle θ_Z of emission with **B** direction. (b) spectral emissivity (orange) of the components σ^-(red), π(blue) and σ^+(magenta) for selected plasma parameters at $\theta_Z = \pi/2$.
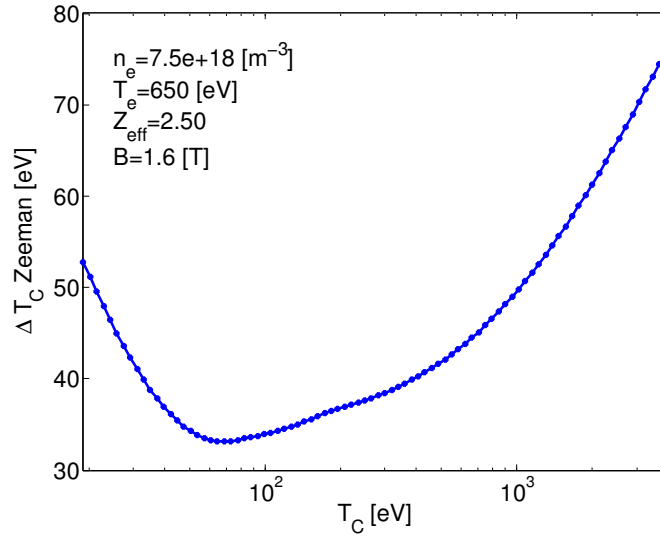
Figure 2.6: Difference between apparent temperature and true temperature due to the Zeeman effect. The correction is not negligible at low temperature and high magnetic field.

The modification in the total spectral emissivity are calculated from equations 2.13 and 2.14 and used to generate a correction look-up table, as function of plasma parameters and LOS geometry.

An example of the correction introduced considering the Zeeman effect is shown in figure 2.6. The Zeeman effect is not negligible at low temperatures (≤ 100 eV) and the correction increases with the magnetic field strength. E.g. the Doppler broadening at $T_C = 50$ eV is $\sigma_{Doppler} = 0.83$ Å, the shift in the emission wavelength of each σ component is $\Delta\lambda_{\sigma^\pm} = 0.35$ Å for an effective broadening $\Delta\sigma_{Zeeman} \simeq 0.7$ Å, which is comparable with the Doppler broadening.

Energy dependence of cross section

The equation for the spectral emissivity 2.5 represents an approximation of the emissivity even for a single transition. The assumptions and its analytical derivation are described in appendix B. Here the assumption $\sigma_{CX}(|\mathbf{u}_d - \mathbf{v}|) \simeq \sigma_{CX}(|\mathbf{u}_d - \mathbf{u}_C|)$ is removed and its effects are tested.
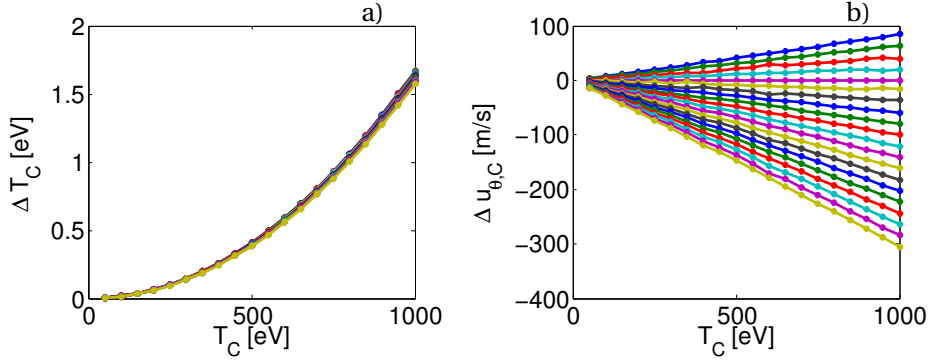
Figure 2.7: Errors in (a) the temperature and (b) rotation induced by neglecting cross section effects for all the EDGE system LOS, colour-coded. The corrections are negligible and are therefore neglected in the analysis.

This effect, that modifies both the central wavelength and the emission width, is treated in [61], for which an analytical approach can be used [76]. The profile shape deviates from a Gaussian when considering the detailed dependence of the CX cross-section on the particles' relative velocity. For example, ions moving towards the DNBI have a different probability of undergoing a CX reaction than those moving away, modifying the observed line emissivity accordingly.

This effect increases with T_c, as a more extended range of the cross section is sampled increasing the impurity temperature. If the diagnostic LOSs have a non vanishing component along the beam, this effect cause a change in the central wavelength that is not associated with ion flow, but to the derivative of the CX cross section. In TCV CXRS systems, this effect is minimised by adopting LOSs quasi-perpendicular to the DNBI.

The effects on perceived temperature, that are associated to the second derivative of the CX cross section, can not be countered by an astute LOS geometry and were estimated by numerical integration of equation B.9, as explained in appendix B.

The error induced by neglecting the cross section effect for the EDGE system LOS is shown in figure 2.7 and found to be negligible for all TCV plasma parameter ranges examined in this thesis.

Gyro-motion and finite lifetime

An additional effect is produced by the energy dependence of the cross section when con-

sidering the detailed particle motion in the poloidal plane. It was explained above that an apparent shift in the central wavelength, associated with an apparent velocity, is produced in the direction of the beam. This apparent shift is projected in the poloidal plane as an effect of the ion gyro-motion and the finite lifetime of the excited state [77].
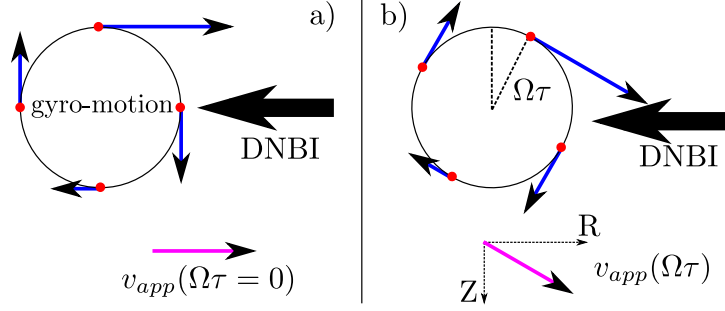
Figure 2.8: Graphical representation of the $\Omega_c\tau$ effect. The apparent velocity due to the energy dependence of CX cross section (a) is projected in the poloidal plane due to the curved trajectory of the ion gyro-motion (b).

The mechanism is explained in figure 2.8: the neutral atom-ion relative velocity depends on the ion gyro-motion phase (blue arrows) and for instantaneous emission ($\tau = 0$, figure 2.8-(a))the effect would be of an apparent velocity (violet arrow) in the DNBI direction. The finite lifetime of the excited state τ_C however causes the emission to be turned by an angle $\Omega_c\tau_C$ in the poloidal plane, producing an apparent velocity with a non vanishing vertical component (figure 2.8-(b)).

This effect scales with the magnetic field B (through Ω_c), with the temperature T_C and with rotation (both through σ_{CX}). An analytical approach to estimate the corrections due to the $\Omega\tau$ effect is reported in [78] and was used in testing the EDGE CXRS system behaviour. The results
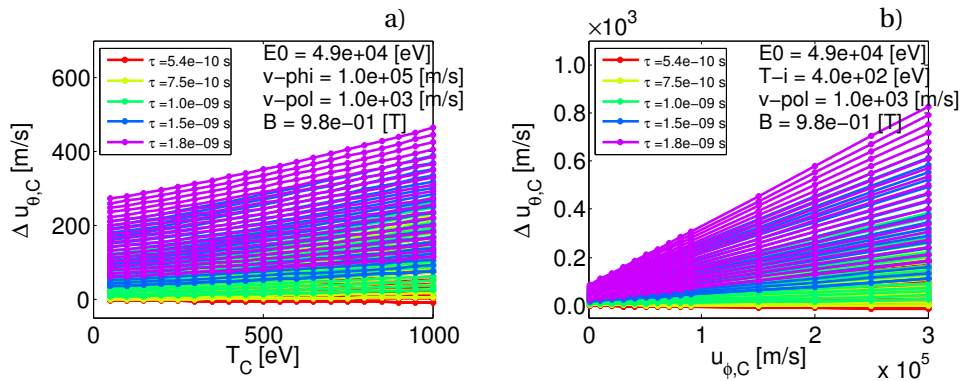
Figure 2.9: Apparent poloidal velocity Δv_i for CXRS EDGE LOS due to the ion gyro-motion and finite lifetime ($\Omega\tau$) effect as function of (a) ion temperature and (b) toroidal rotation, for a set of transition lifetimes. The correction are negligible for TCV relevant plasma parameters.

are shown in figure 2.9 for a set of CVI lifetimes, limited by the values reported in [77]. The apparent velocity correction is limited to $v_{app} < 1$ km/s for TCV relevant plasma parameters and is therefore neglected in the analysis. It should be noted that for states with a long enough lifetime [79] this helpful result is no longer valid.

2.1.3 Theoretical uncertainty

The aim of this section is to develop a consistent procedure to estimate uncertainties in CXRS measurements.

There are two main sources of uncertainty in spectral measurements: the first one due to photons statistics and intrinsic in the measurement, the other due to the additional noise induced by the measurement instruments, and determined by the implemented technology.

This section focuses on the first source of uncertainty assuming the photons follow classical statistics, i.e. a Poisson distribution. The total uncertainty is then calculated as the root mean square of all the contributions. Instrumental noise is treated in section 2.2.2.

Line position

Consider a set of measurements (index k) of a source of fixed spectral radiance $L_s(\lambda)$, each collecting a total of N photons. The centroid (line position) $\mu_{k,s}$ for each measurement in the set is:

$$\mu_{k,s} = \frac{1}{N} \sum_{i=1}^{N} \lambda_i \tag{2.15}$$

where λ_i is the wavelength for the i-photon of the measurement. If the width of the spectral radiance is σ_s, the uncertainty in the line position σ_μ is:

$$\sigma_\mu = \frac{\sigma_s}{\sqrt{N}} \tag{2.16}$$

which states that the uncertainty in the line position decreases with the square root of the collected number of photons. The width considered in equation 2.16 is the experimentally measured spectral width, including the effects of the instrumental function (instrumental broadening).

A case of interest for spectral measurements is when the measured spectral radiance is constituted of two components, an active component (subscript A), that represents the signal of interest for the measurement, and a background (or passive, subscript B) component, that acts as an additional source of uncertainty.

The total number of photons is then the sum of the two components $N = N_A + N_B$. Each component has a spectral shape characterised by a centroid, μ_A and μ_B respectively, and a

spectral width σ_A and σ_B. The uncertainty σ_{μ_A} in the centroid of the active component is then

$$\sigma_{\mu_A} = \sqrt{\frac{\sigma_A^2}{N_A} + \frac{\left(\mu_A - \mu_B\right)^2 N_B}{N_A N} + \frac{\sigma_B^2 N_B}{N_A^2}} \tag{2.17}$$

The statistical analysis supporting equation 2.17 is found in [80].

The first term of the right hand side (RHS) of equation 2.17 is the uncertainty due to photon statistics of the active signal. Interesting enough, if the active and passive components have similar spectral width ($\sigma_A \simeq \sigma_B$), and the passive emission is higher ($N_B \gg N_A$), typical of TCV CXRS measurements, the uncertainty is dominated by the passive component, represented by the third RHS term. The second term on the RHS is relevant only when $N_A \simeq N_B$ and for $\mu_A \neq \mu_B$.

Considering a fixed spectral source, equation 2.17 states that the uncertainty still decreases with the square root of the collected photons N, since an increase in the total counts implies a proportional increase in both N_A and N_B. This highlights the importance of optimising the transmission efficiency in optical measurements to obtain a higher N [81].

Line width

The uncertainty of the line width is more complicated to treat, since general statistical theorems are not directly applicable without approximations. A detailed analysis of the problem is found in [80].

The best estimate of the spectral width σ_A of the active component, used in the equations of the previous section, for each set of measurements, is:

$$\sigma_{k,A} = \sqrt{\frac{\sum_{i=1}^{N_A} \left(\lambda_i - \mu_k\right)^2}{N_A - 1}} \tag{2.18}$$

The uncertainty σ_{σ_A} in the line width of the active component is

$$\sigma_{\sigma_A} \simeq \frac{1}{2\sigma_A} \sqrt{\frac{2\sigma_A^4}{N_A} + \frac{2\sigma_B^4 N_B}{N_A^2}} \tag{2.19}$$

which is roughly proportional to the spectral width of the dominant signal divided by the square root of the counts.

Equations 2.17 and 2.19 show that an increase of the transmission efficiency of an optical diagnostic by a factor of 10 results in an increased precision in both line position and width by a factor of $\simeq 3$.

The CXRS analysis was upgraded to use the best estimates for the line position 2.15 and width 2.18, for both the measured active and passive components, to calculate the statistical uncertainties from 2.17 and 2.19. These uncertainties, previously neglected, determine the maximum precision reachable by each version of the CXRS diagnostic.

2.2 CXRS diagnostic systems

This section is devoted to the description of the TCV CXRS diagnostic, which consists of four separated systems dedicated to the measurements of impurity parameters at different positions and/or geometries. The four systems are termed:

1. LFS (SYS1): toroidal velocity measurements in the LFS;

2. HFS (SYS2): toroidal velocity measurements in the HFS;

3. VER (SYS3): poloidal velocity measurements in the LFS;

4. EDGE (SYS4): poloidal velocity measurements at the edge of the LFS.

Although different in design, all the four systems are composed by the following components:

1. an input optical system, that collects the light emitted by the CX reaction and focuses it on the optical fibres, determining the geometry of the LOS;

2. an optical fibre bundle that carries the photons from the collection optics to the spectrometer;

3. a spectrometer that disperses the collected light allowing its spectral analysis;

4. a charge coupled device (CCD) detector, i.e. CCD camera, that convert the photons composing the spectra into digital counts.

The computational steps that follow the data acquisition and lead to the desired impurity parameters are explained in section 2.2.4.

2.2.1 Legacy systems

The first version of the diagnostic was commissioned in 2004 [37], featuring only the low field side (LFS) system. The CXRS diagnostic in TCV was upgraded and optimised several times over the following years, and the major upgrades are described in [38] and [39], with the development of the high field side (HFS) and VER ('vertical') systems.

In the present manuscript the LFS, HFS and VER systems are labelled legacy systems, although their optimisation and upgrade continued during my work. The differences with the description in [39] consist in:

- The replacement of the HFS spectrometer: the Acton AM-506 spectrometer, that suffered from a strong comma aberration was replaced by a SPEX750Mi model, which is a copy of the LFS spectrometer.

- The replacement of the VER spectrometer with a copy of the EDGE lens spectrometer, to improve the system transmission efficiency and the image quality.

- A new input optical system, with improved imaging properties, for the LFS and HFS systems, composed of high transmission (≥ 99% in the visible range) coated lenses.

- An upgrade of the wavelength calibration function, that includes non-linear dispersion to improve the wavelength determination of the emission line and that enables spectral calibration at any spectrometer setup.

- An improvement in the robustness of the minimisation spectral fitting algorithm used in CXRS analysis.

- Improvements in the uncertainty estimation, with the addition of the minimal uncertainty due to photon statistics 2.1.3 and a residual verification following the convergence of the fitting algorithm.

In this section a brief description of the legacy systems is given. For the interested reader a more complete description is presented in [39].

Each of the legacy systems features 40 LOS, arranged in pair of 20 fibres per slit (hence 2 slits per system) at the spectrometer entrance. The spectra of the 2 slits overlap on the CCD sensor, as no narrowband filter is used. A total of 120 fused silica optical fibres are employed by the three legacy systems to transmit the light to the spectrometers. The core diameter is 636 μm, while the total diameter, including the cladding of each fibre , is 1000 μm, resulting in a fibre separation of $\simeq$ 400 μm when arranged vertically on a slit. The fibres numerical aperture is $NA = 0.12$, which doesn't limit the étendue of the systems, which is limited by the spectrometers.

The LOS geometry of the legacy systems is shown in figure 2.10 together with the DNBI orientation. The spatial resolution is ±1.5 cm for the toroidal systems (SYS1 and SYS2) and ±0.7 cm for SYS3.

The time resolution is limited by the photon statistics and the requirement of accurate background subtraction (section 2.2.4), with a typical range of 30-60 ms. An integration time of 2 ms is available for all the systems, and was used in the setup for ST related experiments, although this required modification of the data analysis.

The toroidal systems are equipped with the same Czerny-Turner spectrometer model, the SPEX750Mi, with 0.75 m focal length and f-number f/7.5. The image at the spectrometer output is demagnified of a factor 0.58 by an optical reducer to fit simultaneously all the 20 fibres onto the CCD detector. The VER spectrometer is an f/2, 200 mm focal length lens
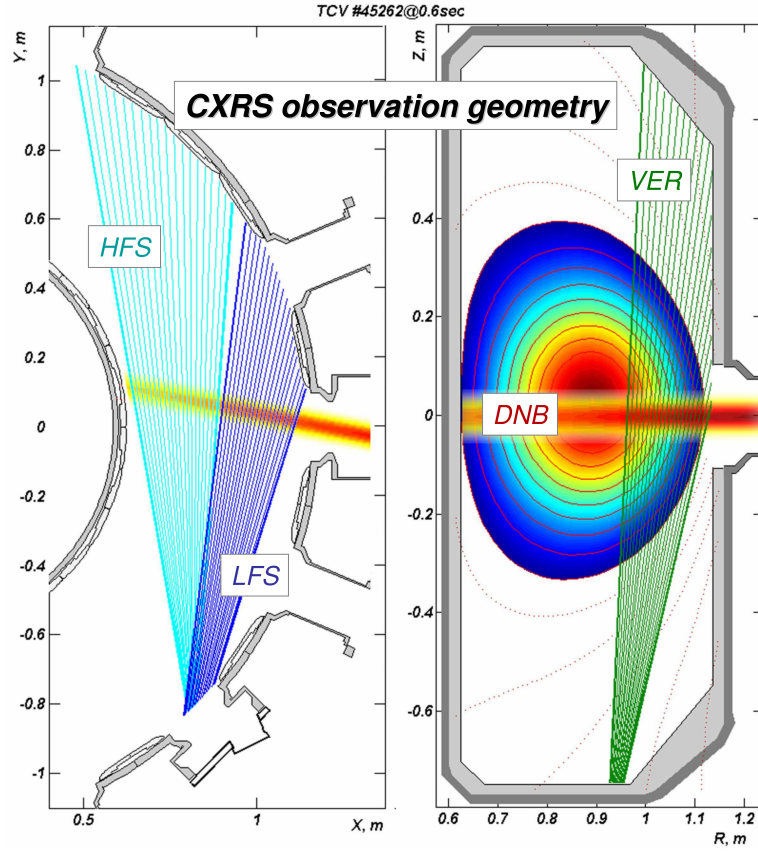
Figure 2.10: Toroidal (left) and poloidal (right) cross sections of TCV showing the LOS geometry of the legacy CXRS systems: LFS, HFS and VER. The intersections of the LOS with the DNBI provide a localised measurement.

spectrometer. The optical reducer for this system is placed at the spectrometer input to avoid an increase of the reciprocal dispersion. All systems are equipped with 2400 l/mm holographic grating, for an effective reciprocal dispersion of $\simeq 8$ Å/mm in SYS1 and SYS2 and 18 Å/mm for VER. The corresponding spectral range is 66 Å and 148 Å respectively.

The detector for both toroidal systems is the Andor camera iXon X3 EM+ DU897D-CSO-BV [82], that features a readout frequency of 10 MHz, the VER system employs the iXon Ultra EM+ DU897U-CSO-BV model, the same as the EDGE system, that attains 17 MHz. A detailed description of the CCD camera working principles and performance are given in section 2.2.2.

The estimated uncertainties for the toroidal systems in the core region of ohmic L-mode discharges are usually in the range $\sigma_{T_C} = 10 - 50$ eV and $\sigma_{u_\phi} = 3 - 10$ km/s, with absolute measured values up to $T_C \simeq 800$ eV and $u_\phi \simeq 60$ km/s. The uncertainties for the VER system are in the range $\sigma_{T_C} = 5 - 15$ eV and $\sigma_{u_\theta} = 1 - 4$ km/s, with absolute values up to $T_C \simeq 500$ eV and $u_\theta \simeq 5$ km/s. With the introduction of a heating NBI on TCV, these limits were increased up to $T_C \leq 3$ keV in the core and $u_\phi \leq 200$ km/s. The relative uncertainties generally increases due

Parameter	Value
Power injected in TCV	$\leq$ 80 kW
Beam energy	20-50 keV
Injection angle (from perpendicular)	11.25°
Max integrated pulse duration	400 ms
Energy [1 1/2 1/3 1/18] fraction (current)	58.4 : 9.5 : 29.1 : 3%
Energy [1 1/2 1/3 1/18] fraction (density)	43.3 : 10 : 37.3 : 9.4%
Beam main species	H (D)
100% power modulation	$\leq$ 200 Hz (typical 20 Hz)
Beam divergence	0.5°
Beam waist FWHM	78 mm

Table 2.1: DNBI parameters from [83]

to augmented passive emission variability during NBH operation, with relative uncertainty in the temperature $\leq$ 15% and in toroidal velocity $\leq$ 20%.

DNBI

The diagnostic neutral beam injector in TCV provides the neutral donors for the CX reactions while minimising the perturbations to the plasma for these measurements.

A detailed description of the injector is beyond the scope of this thesis, but is detailed in [40, 83], so here only the features concerning the CXRS diagnostic are reported and summarised in table 2.1.

The DNBI injects in TCV Hydrogen atoms (Deuterium operation is possible) at full energy $\leq$ 50 keV/amu. The beam energy was chosen to optimise the CX CVI emissivity, since the CX cross section reaches the maximum value in that region ($\simeq$ 48 keV/amu, see figure 2.1, although recent ADAS data locate the peak at $\simeq$ 52 keV/amu), whilst ensuring a good beam penetration at high plasma density ($n_e \simeq 10^{20}$ m^{-3}). An upgrade of the DNBI power supply unit (PSU) is envisioned to allow operation at $\leq$ 55 keV.

The injection geometry is horizontal at the vessel midplane, i.e. $Z = 0$, quasi-perpendicular to the toroidal direction. The beam cross section is Gaussian with a FWHM of $\simeq$ 7.8 cm at the waist, which is at half LFS TCV radius. A small divergence of 0.5° allows a pencil-beam description of the DNBI. The injection angle of 11.25° to the normal to $\mathbf{e}_\phi$ (in the counter-clockwise direction as seen from above) prevents trapping of the (re-ionised) injected particles, whilst minimising the injected toroidal momentum. An estimate of the torque from the direct collisional momentum transfer and from the $\mathbf{J} \times \mathbf{B}$ term due to the trapped particles [84], was performed in [38] and revealed a maximum DNBI induced toroidal rotation $\leq$ 1 km/s, which is smaller than the diagnostic sensitivity and hence ignored. The estimated effect on poloidal rotation [84] is lower and is also neglected in this work.

The DNBI total injected power in TCV is limited to 80 kW, but only a fraction is absorbed by the plasma. The absorbed power is estimated by the attenuation code [40] varying from 20% at low density ($n_e = 1 \cdot 10^{19}$ m^{-3}) to 80% at high density ($n_e = 6 \cdot 10^{19}$ m^{-3}). Moreover, most of this power is transfer to the electrons, with often only $\simeq$ 10% absorbed by the ions, resulting in a direct power transfer of only $\simeq$ 2 kW to the ions. This is 1-2 orders of magnitude less than the electron-ion equipartition power, showing that the DNBI should, indeed, not perturb the impurity kinetic parameters. It also does not perturb plasma density, since it provides a limited amount of fuelling. The total amount of neutral atoms injected in a 12 ms DNBI pulse, estimated from the equivalent current, are $N_{DNBI} \simeq 2 \cdot 10^{17}$ [atoms], which is an order of magnitude lower than the fuelling from the NBH $N_{NBH} \simeq 2 \cdot 10^{18}$ [atoms]. The fuelling from the DNBI is negligible compared to the gas injected by the gas valve, which has typical flows of 10-30 [mbar l/s], corresponding to $N_{gas} \simeq 2 - 8 \cdot 10^{19}$ [atoms] in 12 ms.

The DNBI operates in a pulsed regime, with typical pulse duration of $\Delta T_{DNBI} = 10 - 30$ ms and a duty cycle of 33% (ON-OFF ratio = 1/2). The pulses are synchronised with CXRS acquisition, allowing the acquisition of passive spectra during the beam OFF phase and the total emission (passive + active) during the ON phase. The DNBI rise time of $\leq$ 3 ms impedes the use of pulsed operation in the study of fast phenomena, but can be ignored for the typical CXRS exposure times (10-30 ms). Again, these limitations are, to a great degree, imposed by the DNBI PSU unit that will soon be upgraded.

The DNBI injected atoms have an energy spectra composed of four main components: E_0, $E_0/2$, $E_0/3$ and $E_0/18$, due to the acceleration of H^+, H_2^+, H_3^+ and H_2O^+ respectively. The beam energy optimisation is considered for the full energy component E_0 and ground level donors ($n_d = 1$ in figure 2.1), which constitute $\simeq$ 65% of the beam density. The measured energy fractions (in particle density) are [43.3% 10% 37.3% 9.4%] respectively. The contribution to CX emissivity of the lower energy components is negligible for ground level donors, due to both a decrease in CX cross section and in the donor density, but can be substantial for the excited donors, since the CX cross section increases at those energies (see figure 2.1). Appendix C explains how the excited $n_d = 2$ beam population was estimated, that for typical TCV plasma parameters ($T_i = 500$ eV, $n_e = 10^{19}$ m^{-3}) is $R_{21} \simeq 0.5\%$. An evaluation of the emissivity reveals that the contributing fractions due to $n_d = 1$ donors is [76.2% 4.36% 7.6% 0.07%] and for $n_d = 2$ [0.49% 0.68% 5.7% 4.3%]. The dominant contribution in the measured spectrum therefore remains due to the full energy component.

Plume effect

As stated above, the ionisation timescale for the CX recombined impurities is of $\simeq$ms, while the radiative de-excitation is on the ns scale. The recombined ion can be excited by electronic collision before being ionised, causing emission of line radiation at the same wavelength of the CX signal. If it crosses the CXRS LOS while radiating, it contributes to the measured signal, causing a deterioration of the measurement localisation. This effect is termed the 'plume' and it is of particular concern for toroidal viewing lines. Low Z ions (i.e. He) are particularly affected by this effect, as the electronic excitation is more efficient for low excited levels [79].

This effect was evaluated for CVI 529.1 nm and found negligible [37], due to the small electron excitation cross section for the transition upper level $n = 8$. As mentioned above, this helpful property can not be employed for He measurements.

Halo

The CX reaction of the DNBI donors with the main plasma ions generates a halo of plasma thermal neutrals ($T_{halo} \simeq T_i$) originating from the beam. This halo acts as an additional source of donors for CX reactions with the impurity, generating an additional, DNBI modulated, contribution to the active CX signal that interferes with the target density measurement. If the extent of the halo is relevant, with respect to the beam size, it will affect the spatial resolution of CXRS measurements. Since the halo effect is proportional to the injected neutral density, the relative intensity of the NBI active signal and halo signal is independent of the beam power, and hence potentially relevant for the low power TCV DNBI. The halo produced by the TCV DNBI was estimated in [40], and the effects on the measured density are estimated to be ≤ 10% (often far less) and are neglected in the analysis.

2.2.2   CXRS EDGE system

The CXRS EDGE system (or SYS4) is design to resolve small scale (< 3 mm) spatial features of the poloidal rotation in the TCV plasma edge and across the LCFS. A high spatial resolution profile must be supported by a high precision in the measurement to be meaningful. The optimisation of the whole system for transmission efficiency gave an increase in photon statistics, resulting in an increased precision as explained in section 2.1.3

In the following all the subsystems of the EDGE diagnostic are detailed. This system was one of the major instrumental contributions of this thesis work. It combined all the optical and spectroscopic upgrades during this thesis with a much improved poloidal view of the TCV plasma edge providing unprecedented spatial resolution and sensitivity across the plasma LCFS.

Periscope and input optics

A periscope is installed on the lower lateral port in sector 14, approximatively 40 cm below the DNBI duct, as shown in figure 2.11-(c). It consist of a movable cylindrical aluminium pipe of external diameter 44.5 mm, that houses the input optic lens system, a vacuum tight window and a mirror. The pipe displacement is horizontal, with a 1.55°tilt angle from the TCV radial direction, to ensure centering the periscope aperture with the DNBI when the periscope is fully inserted. The periscope is retracted automatically after every discharge to prevent damage during the glow discharge cleaning between TCV discharges. An automatic check for predicted periscope-safe operation was implemented. It considers the target shot parameters and inhibits operation if the plasma shape and position are considered too risky. The construction was hugely complicated by passing the periscope though the duct of one
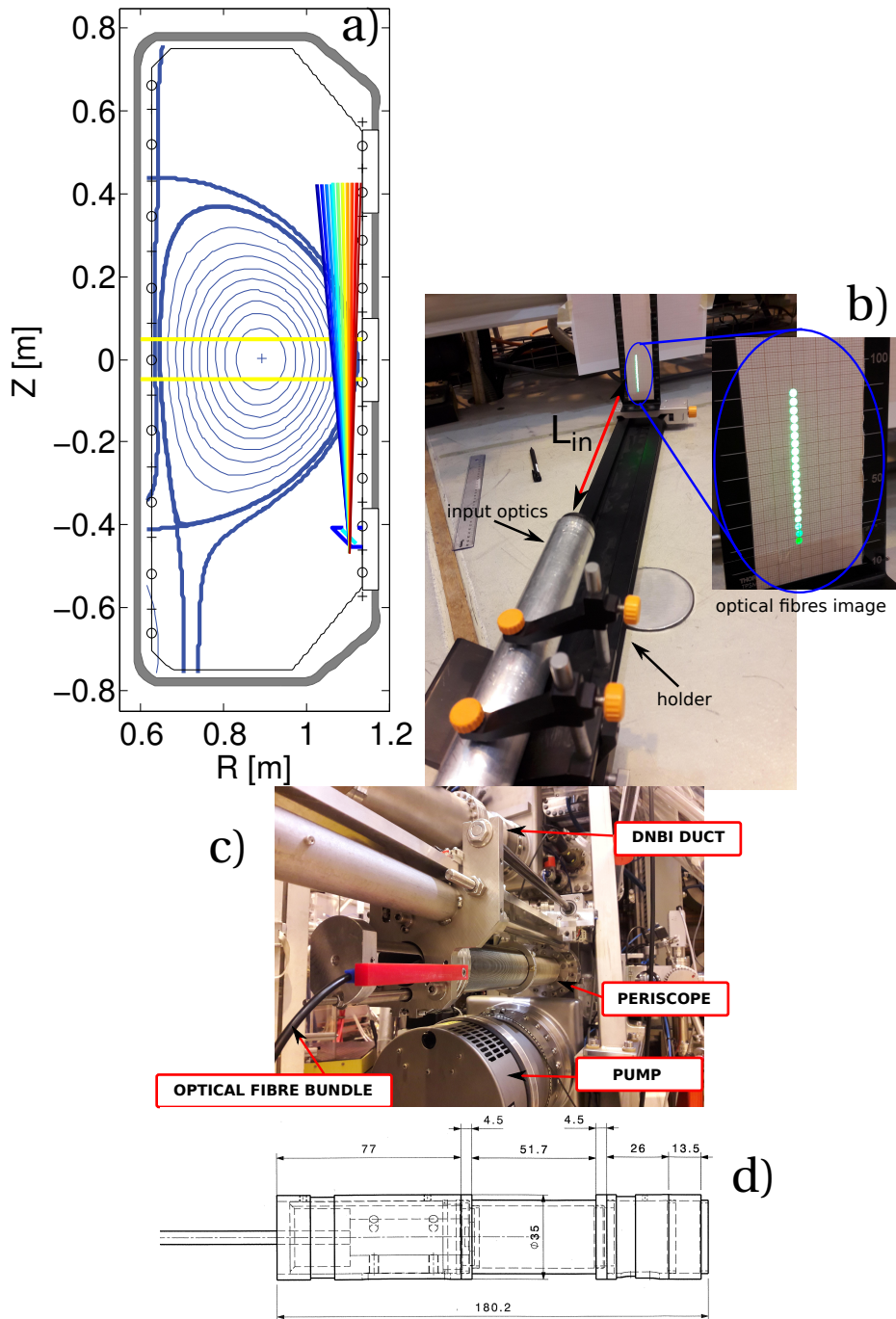
Figure 2.11: (a) TCV poloidal cross section showing the 20 EDGE LOS. (b) alignment of the EDGE input optics for a focal plane at L_{in} = 483 mm. (c) picture of the EDGE periscope installed on TCV on sector 14, below the DNBI. (d) input optics schematics.

of TCV's main vacuum pump assemblies. This took a large amount of work from the design, construction and vacuum teams for which this author is extremely thankful.

The elliptic (52x40) mirror has a Beral coating [85], with a transmission $\simeq$ 90% in the range 400-700 nm. It is tilted 44.1°with the horizontal direction and reflects the light entering the periscope elliptic aperture towards the vacuum window.

The circular window of diameter 37 mm and 4 mm thick has a transmission $\simeq$ 92 % in the range 250-1000 nm.

The input optics is a system of 2 lenses of 25.4 mm (1 inch) diameter, see figure 2.11-(d) that images the optical fibres at a distance $L_{in} = 483$ mm from the optical head with an acceptance f-number of 2, matching the fibre and spectrometer acceptance, with a magnification of 7.5. The lenses have an anti-reflection coating for a transmission in the visible range (450-750 nm) above 99%. The alignment of the system was performed outside the TCV vessel, the quality of the image of the optical fibres is demonstrated in figure 2.11-(b). The sampling spot of each fibre is $\leq$ 3 mm in diameter, for a total radial coverage of $\simeq$ 60 mm at the TCV outer midplane. The resulting LOS geometry is depicted in figure 2.11-(a), in section 2.2.3 the experimental LOS verification procedure is explained.

The optical fibres bundle is composed of 20 CeramOptec fused silica Optran UV 365/400-T fibres of numerical aperture $NA_{of} = 0.22$. The fibres are 25 m long with an attenuation of 10 dB/km, resulting in a transmission $\leq$ 95% on the fibres length. In addition the extremities are not anti-reflection coated, the estimated loss of $\simeq$ 4% due to reflections at each ends results in a total optical fibres transmission of $\simeq$ 87%.

With the periscope view, a quasi-vertical observation geometry was obtained, with a tilt angle range of 0.15°-5°, in comparison the legacy VER system tilt range is 3°-14°(see figure 2.10). The resulting increased resolution in ρ provided a huge increase in the spatial resolution of the plasma edge profile. Eg: for a $Z = 0$ positioned discharge with $\kappa = 1.5$ and $\delta = 0.4$ the extent of the ρ positions sampled (CXRS LOS-DNBI overlapping region) with SYS3 is $\Delta\rho_3 = 0.12 - 0.08$ while for SYS4 is more than two times lower, $\Delta\rho_4 = 0.05 - 0.03$. This results in improved profiles for SYS4, as the smoothing effect due to measuring a range of flux surfaces $\Delta\rho$ with each LOS is minimised to the lower viable geometrical limit.

Lens spectrometer

The EDGE system employs a custom-made lens based spectrometer, whose design is shown in figure 2.12-(a). A detailed description of the spectrometer operating principle is given in appendix D, in this section only the relevant parameters for the CXRS diagnostic are debated, with a comparison with the legacy spectrometers shown in table 2.2

The input slit is a commercial Standa 10AOS10-1 adjustable model, with a clear aperture of 26 mm, large enough to contain the optical fibres head, and attached directly to the c-mount
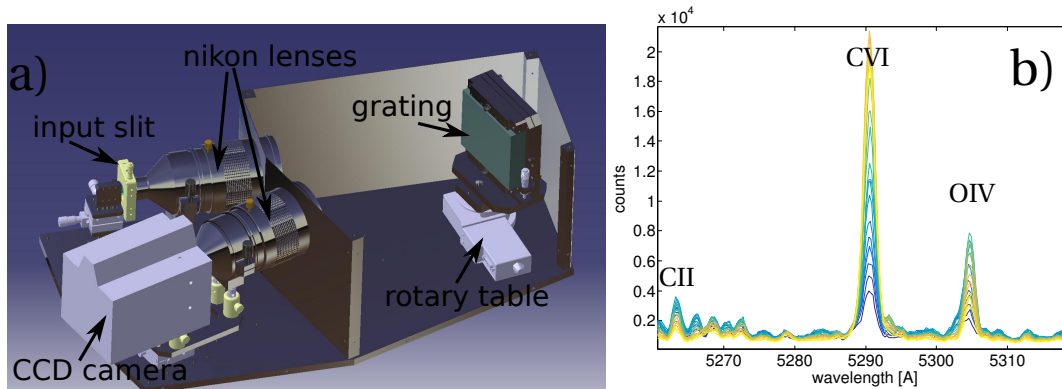
Figure 2.12: (a) CAD rendering of the EDGE spectrometer design, with its main components specified. (b) Zoom of a CVI spectrum in ohmic L mode (optimal conditions) for the 20 LOSs. The CVI line is the sum of the passive and active components.

joint of the collimating lens (ensuring a reliable mechanical alignment). The entrance slit is usually set to $\simeq 100$ μm width, but can range from 0 to 10000 μm. The optical fibres' head position is adjusted through a set of 3 orthogonal linear translation stages and it is placed in direct contact of the input slit to minimise the LOS cross talk and maximise the throughput.

Both the collimating and focusing lens, are commercial Nikon 200 mm focal length Nikkor-ED, with maximum f-number of 2. Their transmission was experimentally measured (see figure D.10) to be $\simeq 80\%$ between 450 and 650 nm (CVI and BV lines), with a sharp decrease below 450 nm. By using the same focal length for the collimating and focusing lenses a vertical magnification of 1 is obtained, which is required to fit the 20 optical fibres vertically aligned in the 8.19 mm sensor chip (see section 2.2.2). The angle between the two lenses optical axes is $2\phi = 20°$.

The spectrometer employs an Horiba [86] 2400 l/mm holographic grating of size 120X140 mm. The lenses clear aperture of 100 mm, smaller than the grating, ensures a minimisation of both vignetting and internal reflections. The combination of the Nikon lenses and the grating results in a reciprocal linear dispersion at 5290 Å of 0.288 Å/pix, corresponding to 18 Å/mm and a spectral range of 147 Å. The spectral bandpass for the typical slit width of 100 μm is 1.33 Å (4.6 pix).

The spectrometer central wavelength is selected through the scanning angle θ (see appendix D), which is controlled by the Newport rotary table RVS80CC [87]. The reproducibility of the image after a θ scan is better than 1/10 of pixel, corresponding to < 0.03 Å, which is of the order of the precision requested in CXRS measurements. Therefore a wavelength calibration is necessary after each θ modification, but is not worse than a legacy sine-bar arrangement.

Figure 2.12-(b) shows a raw spectrum acquired with the EDGE spectrometer in CVI setup during a DNBI ON phase of the shot 55447, in ideal conditions for CXRS Carbon measurements. Multiple emission lines are identifiable in this wavelength range, the CII @ 5257.2 Å and

Spectrometer	Acton	SPEX	Lens (EDGE)
f-number	5.6	7.5	2-22
focal length [mm]	660	750	200
grating [l/mm]	2400	2400	2400
entrance slit [μm]	200	200	100
optical fibre diameter [μm]	636	636	365
optical reducer	0.475	0.58	none
dispersion [Å/mm]	11.6	8.08	18
spectral range [Å]	95	66	148
étendue [10^{-8} m^2 sr]	3.2	1.8	7.3

Table 2.2: Comparison of legacy, Acton and SPEX750Mi, and the lens based spectrometer parameters.

OIV @ 5305.5 Å are highlighted. The relative brightness of the nearby lines depends upon plasma parameters that, for particular conditions, can appear to dominate the spectrum.

CCD camera

The charge coupled devices (CCD) camera is the sensor used in all TCV CXRS systems to convert the photons exiting the spectrometer in digital counts.

The sensor consist of a 2-D array of silicon MOS capacitors, termed pixels (pix), able to absorb the incoming photons, producing an electron-hole pair by photoelectric effect. Photons in the range $1.14 - 4$ eV produce a single electron-hole pair, resulting in a linear response of the sensor. Lower energy photons are not detected, as their energy is lower than the silicon band gap, while higher energy photons can produce multiple pairs, causing a non-linear response. The quantum efficiency of the photon-pair conversion (ratio of incoming photons over produced pairs) reaches values higher than 90% in the spectral range of interest for TCV CXRS, as shown in figure 2.13-a. This is achieved using a back side illuminated CCD and anti-reflection coating. The TCV CXRS cameras have a 512x512 pixels chip, each pixel of size 16x16 μm. The chip is positioned in the image plane of the spectrometer, the convention is to name horizontal direction the direction of the spectral dispersion. Each (couple of) fibre is therefore imaged on a different vertical position (direction perpendicular to the spectral direction).

The photo-electrons accumulate in each pixel's potential well during the acquisition time, i.e. integration time (IT). The pixels are composed of 3 conductive structures (gates) that can be placed at different potentials, controlled by clocking circuits. The shift of electrons in a vertical column of the chip is achieved by changing the gates potential sequentially (figure 2.13-b), the process has an efficiency close to 100%, quantified by the charge transfer efficiency (CTE). All rows are shifted simultaneously by one pixel in the vertical direction, the shift is completed in either [0.3 0.5 0.9 1.7 3.3] μs, depending on the selected vertical shift speed (VSS). The shift
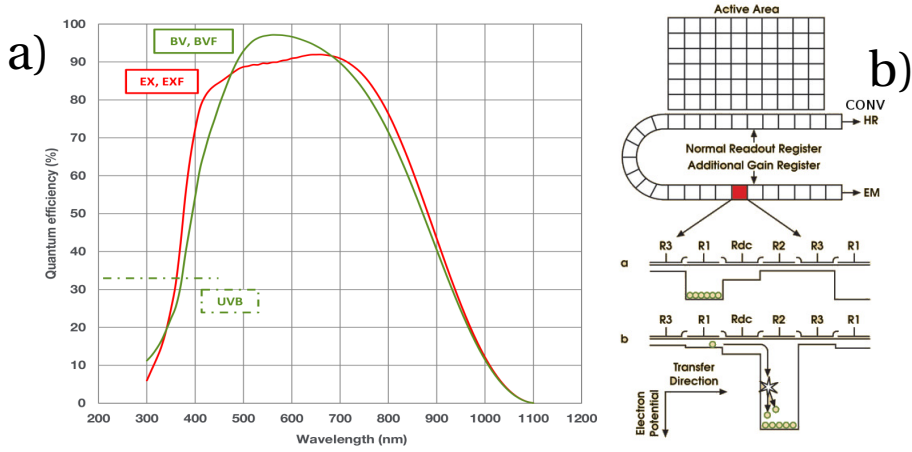
Figure 2.13: (a) quantum efficiency of the CCD camera chip used in the CXRS system (BV-BVF curve). (b) sketch of the CCD-EM working principle. The photo-electrons are collected in each pixel during the acquisition time and then shifted to the readout register. The shift is achieved by changing the capacitor's potential (b-a). In the EM-register the potential applied for the shift is higher than the one needed for charge transfer (b-b), resulting in the production of secondary electrons by impact ionisation. The signal is hence amplified before the readout, reducing the impact of the read-out amplification noise.

speed influences the frame transfer time (i.e. optical smearing) and CTE. The optimal VSS for these cameras is 0.5 μs.

The Andor cameras are frame transfer devices, the charges collected during the IT are shifted into a copy of the sensor chip that is unexposed, and it is then decoupled from the light sensitive region and used in the readout phase, while a new IT "starts after" this frame transfer (for a more detailed explanation of the acquisition cycle see appendix E).

The last row of the chip shifts into the readout register (figure 2.13-b), that transfer the charge to the analog-to-digital converter, where the charge of each pixel is converted in a digital number, i.e. counts or analog-to-digital unit (ADU). The converter of system 1 and 2 are 14 bit (max ADU= $2^{14} = 16383$), for system 3 and 4 are 16 bit (max ADU= $2^{16} = 65535$), but depending on the camera parameters, the saturation limit can be different (see figure 2.14 and table 2.3). The speed of this readout process (horizontal shift speed-HSS) heavily influences the readout noise and the camera performance, as shown in figure 2.14. The signal is amplified during the readout by an on-chip output amplifier, characterised by a gain G_{ro} [e^-/ADU], which represents the number of electrons to produce 1 ADU.

$$N_{ADU} = \frac{N_{e^- out}}{G_{ro}} \tag{2.20}$$

with $N_{e^- out}$ the number of electrons at the output of the readout register and N_{ADU} the resulting counts. A set of 3 readout gains G_{ro} are available, their values are shown in table 2.3 for both the camera models iXon X3 EM+ DU897D-CSO-BV (SYS1 and SYS2) and iXon Ultra

EM+ DU897U-CSO-BV (SYS3 and SYS4).
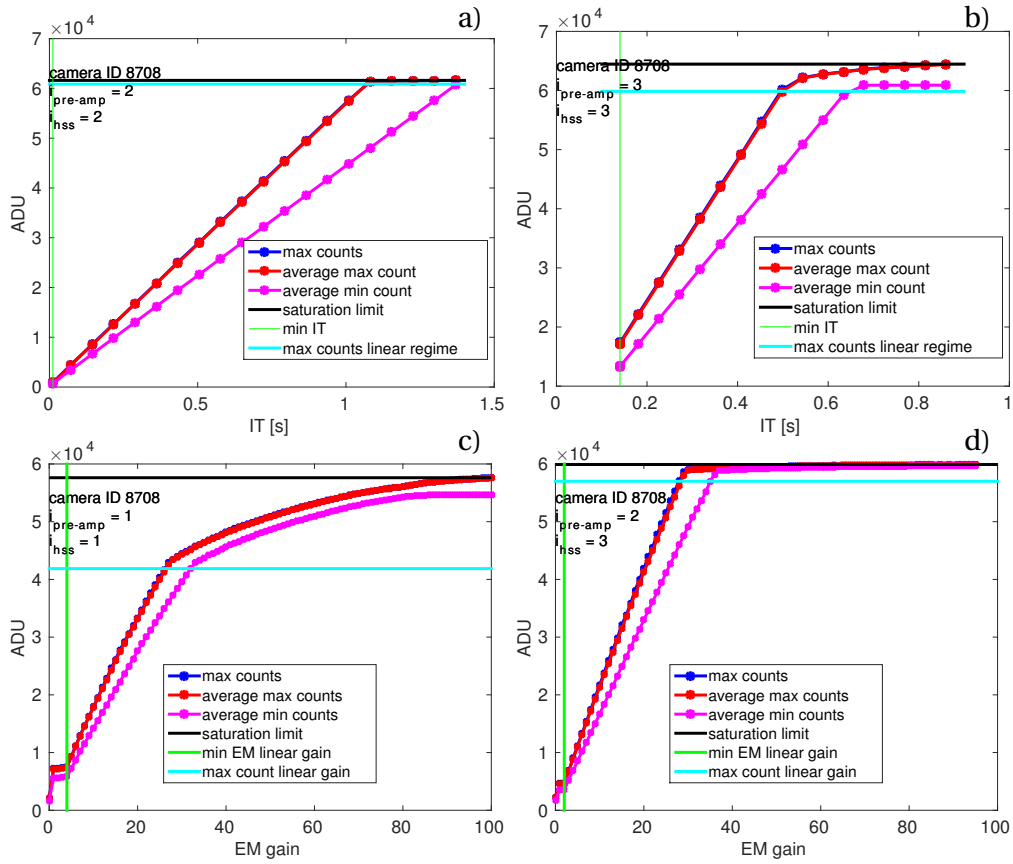
Figure 2.14: Camera linearity test. The conventional register (a) and (b) has a linear response for almost the whole dynamic range. The linearity of the EM register ((c) and (d)) is influenced by the readout setup.

The charge of multiple (vertical) pixels can be summed into the readout register before readout. This technique is called binning and have both the effects of reducing the readout time and increasing the S/N at the expense of reduced vertical resolution (which corresponds to integrating across the fibre height at the entrance slit). The standard CXRS acquisition is performed binning all the pixels receiving light from an optical fibre pair in the vertical direction, resulting in 20 regions of interest (ROI) or tracks. The tracks are defined before acquisition, the alignment is verified after each plasma discharge from the full-frame image acquired for wavelength calibration.

There are two readout registers available: a conventional register (CONV), where the readout is performed as explained above, and an electron multiplier (EM) register, where the photo-electrons are multiplied by an EMCCD process [88, 89] before readout. The multiplication of the photo-electrons is realised by the production of secondary electrons when the potential applied in the EM register for the charge shift is above the threshold for impact ionisation.

Figure 2.13-(b) shows this principle. The gain probability at each stage is $< 2\%$ and depends on the applied potential and temperature, a large number of multiplying elements assures a total gain in the range $G_{em} = 2 - 300$. The number of photo-electrons N_{pe} and the number of electrons at the output of the EM register are hence:

$$N_{e^- out} = N_{pe} G_{em} \qquad (2.21)$$

For the CONV register equation 2.21 is still valid with $G_{em} = 1$.

From equations 2.20 and 2.21 the counts are related to the photo-electrons by the equation:

$$N_{ADU} = \frac{N_{pe} G_{EM}}{G_{ro}} \qquad (2.22)$$

Tests on the camera indicate strong deviations from linearity for the lower output amplifier and the higher HSS (figure 2.14-(c)). A lookup table for the measured camera dynamic range, linear and saturation limits was determined, in order to validate experimental data. Knowledge of the saturation limit is fundamental in avoiding blooming, that consists of the spreading of the photo-electrons from one pixel to the neighbouring pixels when the pixel well capacity is exceeded, causing erroneous count even in the non saturated pixels. The phenomenon is emphasised in the vertical direction and can resemble optical smearing.

Optical smearing, due to light falling on pixels during the frame transfer, results in photo-electrons being erroneously attributed to a different pixel. It can be prevented by using physical shutters and it is mitigated in frame transfer camera. Still when the transfer time is a non-negligible fraction of IT it must be taken into account, especially for short IT ($\simeq 2$ ms). An algorithm for smearing correction was developed and successfully tested during this work(see appendix E), and it is now applied by default in the data analysis.

Noise sources
There are three main sources of noise in a CCD camera:

1. readout noise σ_{ro};

2. dark current noise σ_{dc};

3. shot noise σ_{sn}.

The readout noise $[e^-/\text{pix}]$ is due to spurious electrons generated by the readout electronics and in errors in the digital conversion. It is dependent on HSS configuration and chip temperature.

The dark current is a thermal noise due to electron-hole pairs generated by electrons collisions due to thermal energy. Cooling the chip to -85 C°assures a negligible contribution of the dark current $\ll 0.001$ $[e^-/s/\text{pix}]$, in particular considering IT $\ll 1$ s. At room temperature the dark

current can become the major contributor to the total counts, $N_{tot} \simeq N_{dc}$, therefore the dark current noise $\sigma_{dc} = \sqrt{N_{dc}}$ can dominate the noise for longer integration times.

The shot noise is due to photon statistics, as explained in section 2.1.3 it is Poissonian and it is proportional to the square root of the photo-electrons $\sigma_{sn} = \sqrt{N_{pe}}$.

There is an additional noise when the signal is amplified in the EM register, due to the stochasticity of the process. The noise factor F defines this increase as

$$F = \frac{\sigma_{e^- out}}{G_{em}\,\sigma_{pe}} \tag{2.23}$$

where $\sigma_{e^- out}$ [e^-/pix] is the electron noise at the output of the readout register and σ_{pe} [e^-/pix] is the electron noise at its input, which is:

$$\sigma_{pe} = \sqrt{\sigma_{dc}^2 + \sigma_{sn}^2} \tag{2.24}$$

For the EM register the noise factor is $F \simeq \sqrt{2}$ [90],while for CONV register $F = 1$.

The total noise σ_{tot} [e^-/pix] is then:

$$\sigma_{tot} = \sqrt{\sigma_{ro}^2 + \sigma_{e^- out}^2} = \sqrt{\sigma_{ro}^2 + F^2\, G_{em}^2\, \sigma_{pe}^2} = \sqrt{\sigma_{ro}^2 + F^2\, G_{em}^2 \left(\sigma_{dc}^2 + \sigma_{sn}^2\right)} \tag{2.25}$$

In a bias frame, which is a frame with null integration time and closed shutter, the histogram of the ADU is Gaussian. The mean is the offset, a value that is added in the readout to prevent negative conversion values. The width $\sigma_{ADU,dark}$ is related to σ_{ro} and G_{ro} by the equation:

$$\sigma_{ADU,dark} = \frac{\sigma_{ro}}{G_{ro}} \tag{2.26}$$

A procedure to measure σ_{ro} and G_{ro} is to take two sets of bias frame (B_1 and B_2) and two sets of exposed frame (F_1 and F_2). Then for each pixel to compute the average value of each set ($< B_1 >, < B_2 >, < F_1 >, < F_2 >$) and compute the standard deviation of the difference between B_1 and B_2, $\sigma_{B_1 - B_2}$ and between F_1 and F_2, $\sigma_{F_1 - F_2}$. The readout gain is:

$$G_{ro} = F^2\, G_{em} \frac{(< F_1 > + < F_2 >) - (< B_1 > + < B_2 >)}{\sigma_{F_1 - F_2}^2 - \sigma_{B_1 - B_2}^2} \tag{2.27}$$

and the readout noise:

$$\sigma_{ro} = \frac{G_{ro}\,\sigma_{B_1 - B_2}}{\sqrt{2}} \tag{2.28}$$

The measured readout gain were compared to the manufacturer specifications and found in agreement (see table 2.3).

		CONV readout register								
		3 MHz			1 MHz			0.08 MHz		
	SYS	PreAmp			PreAmp			PreAmp		
G_{ro}	1,2	10.7	4.2	1.88	10.7	4.2	1.88	9.95	3.91	1.71
[e$^-$ / ADU]	3,4	3.9	3.0	1.4	3.88	2.99	1.38	3.87	2.98	1.39
σ_{ro}	1,2	14.3	10.7	9.6	14.3	10.6	9.6	11.7	8.9	8.4
[e$^-$ / pix]	3,4	13.8	12	9.7	7.2	6.5	5.4	3.5	3.3	2.9
saturation	1,2	1.64	1.64	1.64	1.64	1.64	1.64	1.64	1.64	1.64
[10^4 ADU]	3,4	6.37	6.31	6.43	6.10	6.19	6.20	6.17	6.36	6.39

		EM readout register														
		17 MHz			10 MHz			5 MHz			3 MHz			1 MHz		
	SYS	PreAmp			PreAmp			PreAmp			PreAmp			PreAmp		
G_{ro}	1,2				60.7	26.4	12.0	57.0	23.0	10.5	57.2	22.8	10.4	57.3	22.7	10.4
	3,4	15.1	9.1	4.9	15.4	7.9	4.7	17.0	8.2	4.3				16.9	8.2	4.2
σ_{ro}	1,2				90.4	61.5	50.6	82.5	51.0	41.6	63.0	37.1	30.6	49.7	26.7	21.2
	3,4	199	130	80	171	94	64	70	46	36				25.5	17.6	15
sat.	1,2				1.61	1.64	1.64	1.64	1.64	1.64	1.57	1.64	1.64	1.59	1.63	1.64
	3,4	5.83	5.06	4.91	5.63	5.86	5.45	5.89	5.99	5.97				6.20	6.29	6.16

Table 2.3: CXRS cameras specifications: gain G_{ro} [e$^-$ / ADU], σ_{ro} [e$^-$ / pix] and saturation limit [10^4 ADU] for the three output amplifier (PreAmp) settings for each HSS configuration and for both CONV and EM readout registers.

The signal to noise ratio S/N_{tot} is expressed by

$$S/N_{tot} = \frac{N_{pe}}{\sqrt{\frac{\sigma_{ro}^2}{G_{em}^2} + F^2 \left(\sigma_{dc}^2 + \sigma_{sn}^2\right)}} \tag{2.29}$$

which shows that the EM register is beneficial when the readout noise would otherwise have been the dominant noise source. By increasing the EM gain the σ_{ro} term becomes negligible at the expense of an increase in the shot noise of a factor $F \simeq \sqrt{2}$. The EM setup is particularly useful when short integration times are needed ($\simeq 2$ ms) since the readout noise, that increases with the readout speed ($\simeq 200$ [e$^-$/pix] for Andor cameras at maximum HSS speed), can be moderated by EM gain. For slow integration times ($IT > 5$ ms) and high intensity light applications the CONV register is more advisable, since the dominant term is the shot noise (with $F = 1$), with a negligible readout noise $\sigma_{ro} < 15$ [e$^-$/pix] (for all HSS speed).

Performance

The throughput optimisation of all the subsystems of the EDGE CXRS diagnostics resulted in an increased transmission efficiency of about one order of magnitude with respect to the legacy systems (section 2.2.3, which considers the lens-spectrometer upgraded SYS3).

Figure 2.15 shows an example of profiles of Carbon (a) poloidal velocity, (b) temperature and (c) density for both the VER and the EDGE systems in the time window [1. 1.16] s of shot
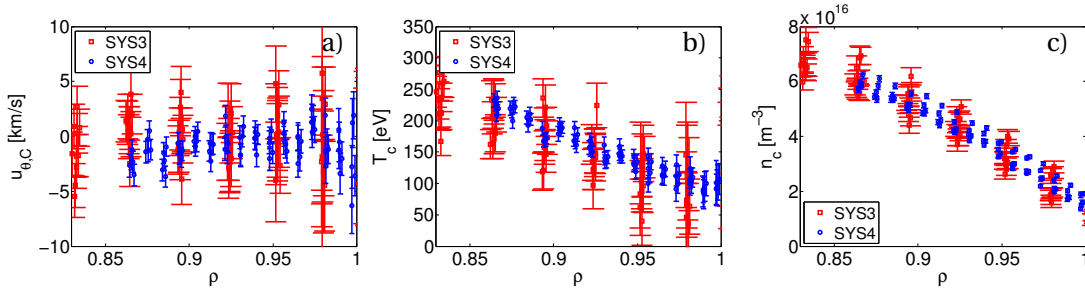
Figure 2.15: Profiles comparison of (a) poloidal velocity, (b) temperature and (c) density for VER (red squares) and EDGE (blue circles) systems, for shot 55597 in the time window [1. 1.16] s. The higher precision of the EDGE system, inferred from the smaller calculated errorbars, is confirmed by the data scattering in time.

55597, which is in a stationary regime. The error bar (standard deviation) are calculated from the photon statistics and the estimated fitting uncertainties as explained in sections 2.1.3 and 2.2.4. The scattering of data points in time for each LOS is consistent with the estimated uncertainties for both systems.

The typical parameters range of the EDGE system are $n_C \leq 5 \cdot 10^{17}$ m^{-3}, less than 5% of the local electron density, with uncertainties $\sigma_n \simeq 10^{16}$ m^{-3}, $T_C \leq 400$ eV with uncertainties $\sigma_T < 10$ eV and $v_\theta \leq 10$ km/s with uncertainties $\sigma_v \leq 1.5$ km/s. These improvements in the poloidal CXRS measurements represent a fundamental step forwards in the study of impurity transport in TCV, by providing accurate edge conditions that were previously unavailable.

2.2.3 Alignment and calibrations

In this section the alignment and calibration procedures for the CXRS systems are explained. A proper spatial alignment is essential to localise the measurement and obtain accurate profiles. The absolute calibration is necessary for density calculation and it is also useful, over time, in detecting transmission problems, such as displacement or degradation of optical elements. Finally the wavelength calibration, which is fundamental for velocity and temperature calculation, is presented.

LOS alignment

The viewing chord alignment is performed by inserting a target, covered with a millimetre paper, inside the vacuum vessel along the DNBI path, a precision of $\simeq 5$ mm in the absolute positioning is achievable ($\simeq 1$ mm in the radial direction). This procedure can be performed only with direct access inside TCV, and was made during the opening for the upgrade in 2014. The optical fibres are back-illuminated with a lamp (white light), the positions of the images are adjusted and then, when considered adequately aligned to the DNBI, recorded in a digital picture (figure 2.16). There are marks on the optimal positions to facilitate the alignment, as
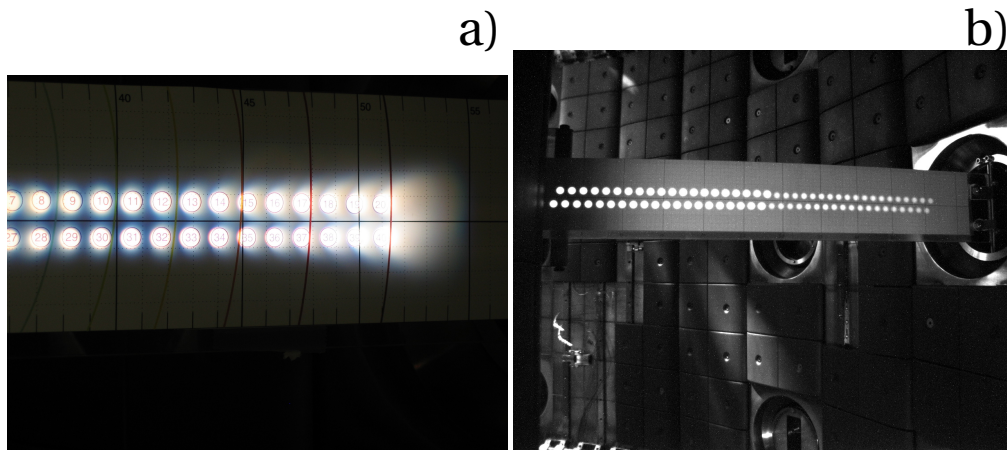
Figure 2.16: Picture of (a) 2012 alignment (HFS system) and (b) 2014 alignment (both HFS and LFS LOS). The new input optical system strongly reduced the aberrations for the outboard LOS of the toroidal systems.

shown in figure 2.16-(a). Then the target is moved to a different position and another picture recorded.

After removing the target another picture is taken, the 40 optical fibres images spot positions on the tiles for each system is used both to further constrain the LOS geometry and as reference for future alignment checks without requiring TCV entry.

The digital pictures are then analysed through a in-lab made software and the diagnostic chord description (DCD) obtained. The estimated final uncertainty in the absolute position is < 5 mm (often much less), which is smaller than the sampling size of the legacy systems.

The improvement of the imaging quality and aberration reduction of the newly designed input optics (2014 alignment, figure 2.16-(b)) for the toroidal systems is clear from the comparison with the 2012 alignment of figure 2.16-(a).

The alignment of the EDGE system was performed outside the vessel (figure 2.11) and the DCD were evaluated employing only the images of the fibres on the tiles, shown in figure 2.17-(a). A green laser for the back-illumination was employed to obtain a sufficient contrast. The origin of the DCD position was assumed to be consistent with the design, since no direct measurements from outside the vessel were possible during this thesis.

An alternative check for the alignment is to consider the experimental temperature profiles. Ion temperature is a flux function [69], so measurements corresponding to the same ρ must agree and the profiles from different systems must overlap. Figure 2.17-(b) shows the temperature profile of all the CXRS systems for shot 55447, the overlap of all the systems corroborates the correctness of the DCD description. In the future, a direct in-vessel alignment will be performed.
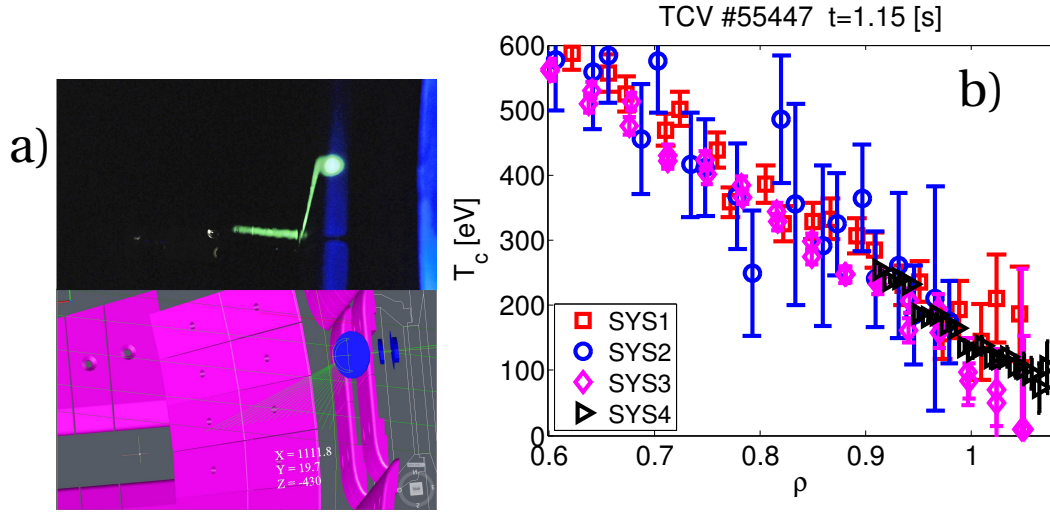
Figure 2.17: (a) picture used for EDGE DCD identification and corresponding 3D model. (b) T_C profile of shot 55447 showing the agreement of all CXRS systems, corroborating the DCD description of all systems.

Absolute and relative calibration

The aim of the absolute calibration is to work out the relationship between the photon counting rate on the ccd sensor R_s [ph$_s$ /s], of a certain wavelength range $\Delta\lambda_0$ centered at λ_0, to the radiance in the emission zone L_{emi} measured in [ph$_{emi}$ /s /m^2 /sr], that is the LOS integrated emissivity of the source ϵ_{emi} [ph$_{emi}$ /s /m^3 /sr]. Here ph$_s$ and ph$_{emi}$ are respectively the number of photons detected by the sensor (ccd camera) and emitted by the source in the measured zone in the considered wavelength range, so that the emissivity ϵ_{emi} is the spectral emissivity $\epsilon_{emi,\lambda}$ [ph$_{emi}$ /s /m^3 /sr/Å] integrated over the appropriate wavelength range $\Delta\lambda_0$:

$$\epsilon_{emi}(x,y,z) = \int_{\lambda_0 - \Delta\lambda_0/2}^{\lambda_0 + \Delta\lambda_0/2} \epsilon_{emi,\lambda}(x,y,z,\lambda)\,d\lambda \tag{2.30}$$

$$L_{emi}(x,y) = \int_{los} \epsilon_{emi}(x,y,z)\,dz \tag{2.31}$$

where z is the variable in the LOS direction.

R_s and L_{emi} satisfy the relation:

$$R_s = L_{emi}\,G_{in}\,T \tag{2.32}$$

where G_{in} is the étendue of the input optics of the acquisition system and T is the total transmission of the system. T is a function of λ_0 and of the spectrometer parameters (scanning angle θ, f-number, etc...).

The transmission T of the system can be measured using a source with known radiance L_{cal} and the experimental photon counting rate $R_{s,cal}$:

$$T = \frac{R_{s,cal}}{L_{cal}\, G_{in}} \tag{2.33}$$

in this notation it has the 'dimension' [ph_s / ph_{emi}]. The radiance L_{cal} is calculated for each pixel of the sensor from the known spectral radiance of the calibration source $L_{cal,\lambda}$ by integrating on the wavelength range covered by the pixel $\Delta\lambda_p$:

$$L_{cal}(pix) = \int_{\lambda_p - \Delta\lambda_p/2}^{\lambda_p + \Delta\lambda_p/2} L_{cal,\lambda}(\lambda)\, d\lambda \tag{2.34}$$

A more rigorous method to perform the integral in wavelength would be to include the normalized instrumental function g_{if} in the calculation, as a weight to take into account the spreading of photons of a fixed wavelength to the neighbours pixels, with the formula

$$L_{cal}(pix) = \int_{-\infty}^{+\infty} L_{cal,\lambda}(\lambda) \int_{-\infty}^{+\infty} \Pi(\widetilde{\lambda}, \lambda_p, \Delta\lambda_p)\, g_{if}(\lambda - \widetilde{\lambda})\, d\widetilde{\lambda}\, d\lambda \tag{2.35}$$

where the integral in $\widetilde{\lambda}$ is the convolution of the instrumental function g_{if} with the normalized rectangular function $\Pi(\widetilde{\lambda}, \lambda_p, \Delta\lambda_p)$ centered at λ_p and $\Delta\lambda_p$ wide. Since the spectrum is continuous and near to linear when the $\Delta\lambda_p$ region is small and the instrumental function FWHM is usually only a few pixels, including this effect gives a negligible correction to the previous method, with the disadvantage of a greatly increased complexity.

The calibration source used is a commercial Ulbricht sphere Labsphere, model US-060-SF, which is considered as an ideal Lambertian source (constant radiance independent on the viewing angle and on the sampled area). The Labsphere was placed inside the TCV vacuum vessel on a movable support, able to translate in the image plane of the CXRS systems input optics. A set of $\simeq 20$ acquisitions per systems (only the legacy systems were available at that time) were performed, ensuring that each of the optical fibres was completely filled at least in one of the acquisitions.

A brief description of étendue , a.k.a. throughput, is here presented, to elucidate its basic properties. An infinitesimal element of étendue dG [m^2 sr] for a light beam passing through an infinitesimal surface dS at an angle θ_s with the normal of the surface $\hat{n}$ and confined in a solid angle $d\Omega_s$, as depicted in figure 2.18, is defined as:

$$dG = n^2\, dS\, \cos\theta_s\, d\Omega_s \tag{2.36}$$

where n is the refractive index of the medium where the light propagates.
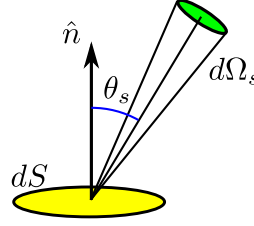
Figure 2.18: Sketch with quantities defining the infinitesimal étendue dG of a light beam crossing a surface dS at an angle θ_s with the normal of the surface $\hat{n}$ and confined in a solid angle $d\Omega_s$.

The radiance of such surface is then, neglecting transmission losses,

$$L_{e,\Omega} = n^2 \frac{\partial \Phi_e}{\partial G} = \frac{\partial^2 \Phi_e}{\partial S \cos \theta_s \partial \Omega_s} \tag{2.37}$$

where Φ_e is the radiant flux [W] or [ph_{emi}/s]. For Lambertian sources $L_{e,\Omega}$ is independent of θ_s. The quantity $L_{e,\Omega}/n^2$ is an invariant (again for no losses), so if the input and the output of an optical system are in the same medium $L_{e,\Omega}$ itself is conserved at the ends of the system.

Taking into account the transmission losses, from equations 2.32 and 2.33 we can obtain the radiance emitted by a source L_{emi} from the measured photon rate R_s with the following equation:

$$L_{emi} = \frac{R_s}{G_{in}T} = \frac{R_s}{R_{s,cal}} L_{cal} = k_{ABS} R_s \tag{2.38}$$

that shows that the knowledge of the input étendue G_{in} of the whole acquisition system is not critical in the determination of L_{emi} as long as the absolute calibration $R_{s,cal}$ is performed in the same conditions as the experiment, i.e. same geometry and optical elements. This forces an in-vessel calibration source approach. The ratio $\frac{L_{cal}}{R_{s,cal}}$ is the coefficient of absolute calibration k_{ABS} and its inverse (related to the system transmission) is shown in figure 2.19 for the last absolute calibration (2014 data set). The absolute calibration for the EDGE system was performed in 2016 outside the vessel, since no access inside the vessel was possible, by considering the transmission of the flange and the periscope mirror provided by the manufacturer. The total transmission of the EDGE system is strongly dependent on the position of the ROI with respect to the optical axis. The highest transmission (see figure 2.19) is for ROIs close to the optical axis, while transmission of the most distant ROIs is lower by a factor $\simeq 0.65$. This is a consequence of the Nikon lenses vignetting, which gets stronger for off axis beams, effectively increasing the working f-number with the distance from the axis (see also appendix D). This effect is reduced in SYS3 due to the non-matching f-number of the spectrometer's input optics.

It remains useful to analyse the properties of the input optics in improving the system performances and calculating the optical transmission. The étendue of an optical fibre of numerical
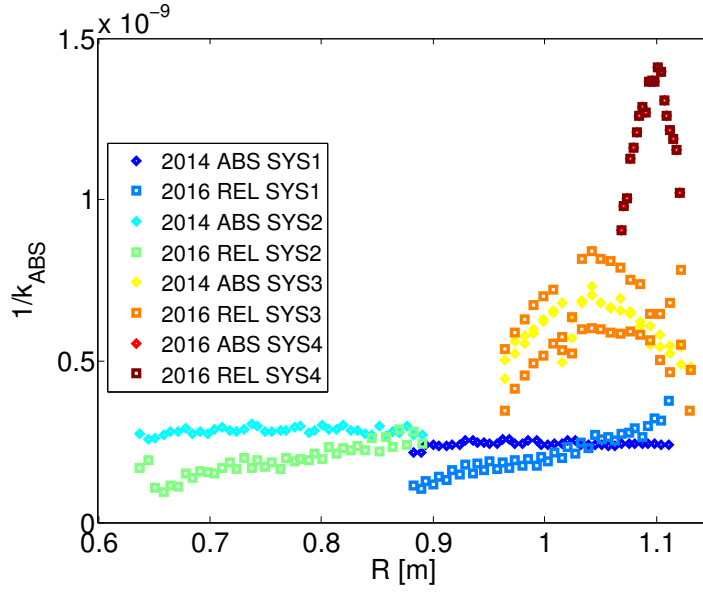
Figure 2.19: Inverse of the absolute calibration coefficients, $1/k_{ABS}$, for all CXRS systems for the CVI line. The coefficients for each LOS are shown as function of the intersection position with the DNBI for clarity. The 2014 coefficients are obtained from the in-vessel absolute calibration. The 2016 coefficients are obtained from the D_β BES, which is a relative calibration, rescaled to the absolute calibration. The difference in the ABS-REL slopes for the toroidal systems might be related to beam-LOS misalignments, mirror degradation or invalidity of the assumption of constant emissivity.

aperture NA_{of} and core radius r_{of} is:

$$G_{of} = (\pi\, NA_{of}^2)(\pi r_{of}^2) \tag{2.39}$$

this value should be used as the system input étendue G_{in}, assuming no vignetting in the input optics.

Relative calibration

The absolute calibration procedure is lengthy and can be performed only during a prolonged TCV vacuum vessel opening, which, as a result, only occurs every 3-4 years. A novel relative calibration procedure was tested during this thesis to verify the reference calibration coefficients and possibly correct them.

The procedure is based on beam emission spectroscopy (BES), that consists in acquiring the H_β wavelength-shifted lines produced by the interaction of the fast H DNBI atoms with a low pressure D_2 gas filling TCV. The H_β line emitted by the four DNBI energy components is shown in figure 2.20-(a) for the first track of the HFS system (double slit configuration), together with the rest D_β line from the background gas.

The beam attenuation, calculated with impact cross section with D_2 [91],is below 7% at a

pressure of $5 \cdot 10^{-4}$ mbar, and since the emission cross section of H and H^+ projectiles are comparable (data found for H_α line in [92]) and the beam divergence is negligible, the total beam line emissivity ϵ_{H_β} is taken to be constant across the device. The radiance L_{H_β} observed for each LOS is then the product of the line emissivity and the DNBI-LOS intersection length L_{int}, and the transmission coefficients k_{ABS-H_β} are calculated from 2.38. The total photon rate calculated from the sum of all the H_β components for each LOS and each system is shown in figure 2.20-(b).
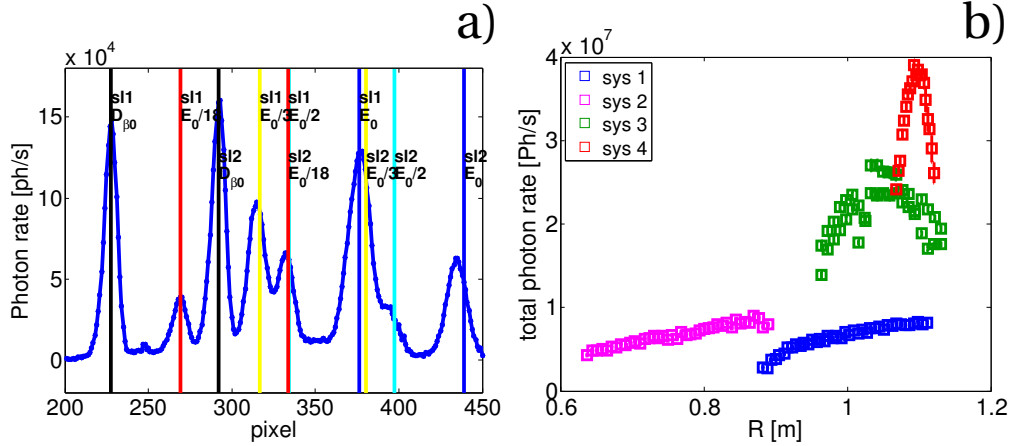
Figure 2.20: (a) Spectra of DNBI H_β emission for SYS2 ROI number 1, shot 55176. All four DNBI energy components and the D_β line from the background gas are highlighted for both slits. (b) BES total H_β photon rate for all the CXRS systems and for each LOS, shot 55176, represented as function of the DNBI-LOS intersection position. The EDGE system photon rate is one order of magnitude higher than LFS and HFS, and peaks at almost twice the value of SYS3, which also employs the new optical spectrometer but with a not optimised optical transmission line.

Since the transmission T is wavelength and system dependent, the procedure is used only to cross calibrate LOS within the same system and the k_{ABS} coefficients at different wavelengths are estimated by renormalising the k_{ABS-H_β} coefficients to the averaged value of the absolute calibration and then rescaled to match the profiles between all the systems. The resulting k_{ABS} coefficients for CVI are shown in figure 2.19. The difference in the slope of the absolute and relative calibrations for the toroidal systems might be related to a possible beam-LOS misalignment, change in relative ROI transmission at the different wavelength, mirror degradation or invalidity of the assumption of constant emissivity (due to both beam divergence and H depletion). Explaining this "discrepancy" should be one main goal of the next absolute in vessel calibration.

Wavelength calibration and instrumental function

The interpretation of the measured spectrum requires an extremely precise wavelength calibration of each system. For rotation measurements, this is particularly challenging, as an error in the wavelength assignment of only $\Delta\lambda_{1-km/h} = 0.018$ Å, corresponding to a fraction of

a pixel (0.06 pix), engenders an erroneous velocity estimation of $\simeq 1$ km/s. A change in the barometric pressure of only 2%, typical in weather fronts, causes a wavelength shift of the same order [65], invalidating the calibration reference values. Mechanical drifts and temperature excursions also influence the spectrometer dispersion properties in time [38]. For these reasons periodic wavelength calibrations are necessary, for which the CXRS legacy systems are equipped with a remotely controlled pneumatic system that position a calibration lamp in the LOS optical path, filling the fibres' light acceptance cone. This solution allows for an automatic wavelength calibration after each TCV discharge, ensuring a continuous diagnostic wavelength calibration. The EDGE system wavelength calibration instead is performed manually and, requiring human access to the TCV zone, it is performed more sparsely. An upgrade for automatic wavelength calibration after each shot, requiring the installation of a window on the pump duct, is envisioned.
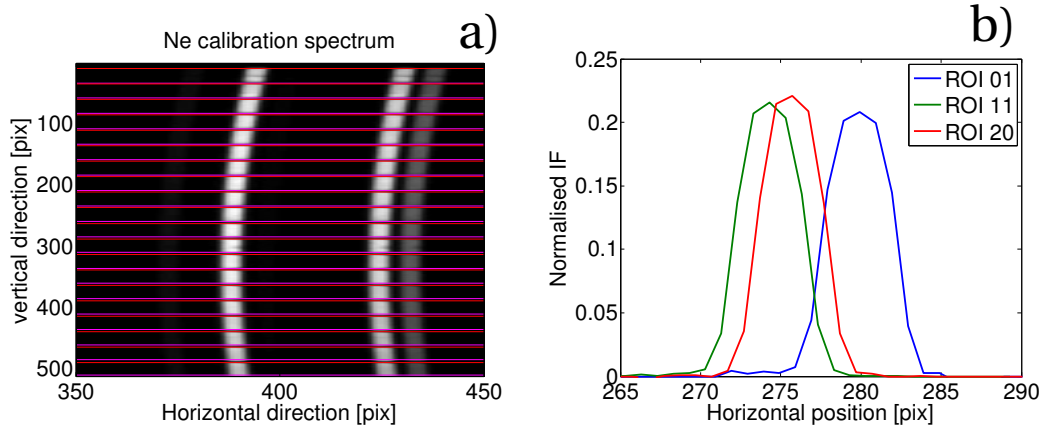
Figure 2.21: (a) zoom of a full frame Ne spectrum for SYS4 wavelength calibration, horizontal lines delimit the tracks definition. The slit image curvature and channels imperfections are visible. (b) corresponding measured normalised instrumental functions for a subset of channels. The drift in the average position is due to the slit curvature.

The calibration procedure employs a full frame image of the spectrum of a Pen-Ray Neon lamp, averaged over multiple acquisitions, for a total integration time ≥ 10 s. An example of such image is shown in figure 2.21-(a), where a sub-section of the frame shows the three brightest lines (NeI 5330.78 Å, NeI 5341.09 Å and NeI 5343.28 Å) in the wavelength range for the CVI setup. The full frame image is also used to verify the track alignment, which are represented in the figure by horizontal lines. The curvature of the straight entrance slit image visible in figure 2.21-(a) is a consequence of the dependence of the dispersion on the vertical tilt angle for non axial rays. It is approximatively parabolic [93], as described in equation D.18, and influences the wavelength-pixel relation and the spectrometer instrumental function (figure 2.21-(b)), since spectra at different heights belonging to a ROI are summed in the binning operation. For very strong slit curvature this can result in asymmetric instrumental function (IF). Other factors influence the IF, such as imperfections of the entrance slit and of the optical fibres, misalignments, the presence of dust, etc. Accounting for all these effects by describing the IF

with an analytic function, which following common practice is performed with combinations of Lorentz and Gaussian functions, may not be possible and can engender ambiguity in the calibration. The solution adopted for TCV CXRS is to use directly the experimental IF in the calibration fitting procedure, which removes the ambiguity in the wavelength definition, since the same IF, that perfectly fits the reference line (zero variance), is then employed in the fitting of the active CXRS signal. The uncertainty in the absolute wavelength position for a measured line is then determined by the uncertainty in the reference Ne line position, which is $< 10^{-3}$ Å (in the case of perfect convergence of the fitting algorithm).
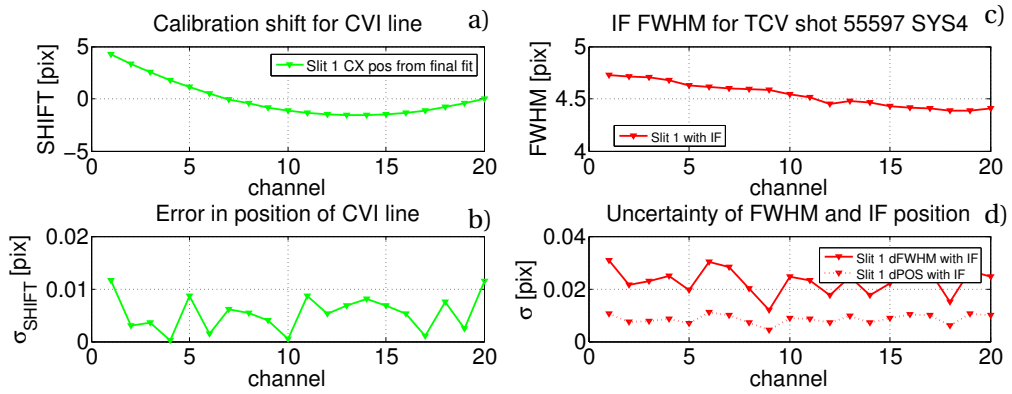
Figure 2.22: Parameters resulting from the wavelength calibration (SYS4 shot 55597): (a) relative pixel shift of CVI reference position among ROI, (b) uncertainty of the CVI reference line position (c) IF FWHM and (d) IF FWHM and position uncertainties.

The grating equation D.4 express the non-linear relation between the light wavelength and its position on the CCD. In the legacy systems calibration the relation was linearised and a linear regression fit of the measured spectrum was employed to assign a wavelength at each horizontal pixel for each ROI. The non-linearity of the EDGE spectrometer dispersion, that increases for shorter focal lengths, required an upgrade of the calibration functions, that now employs the full model described in equation D.4. This resulted in improvements to the calibration convergence and in the diagnostic precision, as shown by the uncertainty in line position and width of figure 2.22. The uncertainties are estimated from the Hessian of the minimisation matrix, the same procedure used in the CXRS active spectrum fit. The typical uncertainty achieved in the reference line position of ≤ 0.01 pix, corresponding to $\delta\lambda \leq 0.003$ Å, generates a negligible uncertainty in the velocity $\delta v \leq 0.2$ km/s.

Figure 2.23 shows the experimental Ne spectrum used in the wavelength calibration plotted as function of wavelength. The alignment of all the Ne emitted lines for all the tracks suggests convergence of the calibration, which is not achievable employing the simpler linear model.
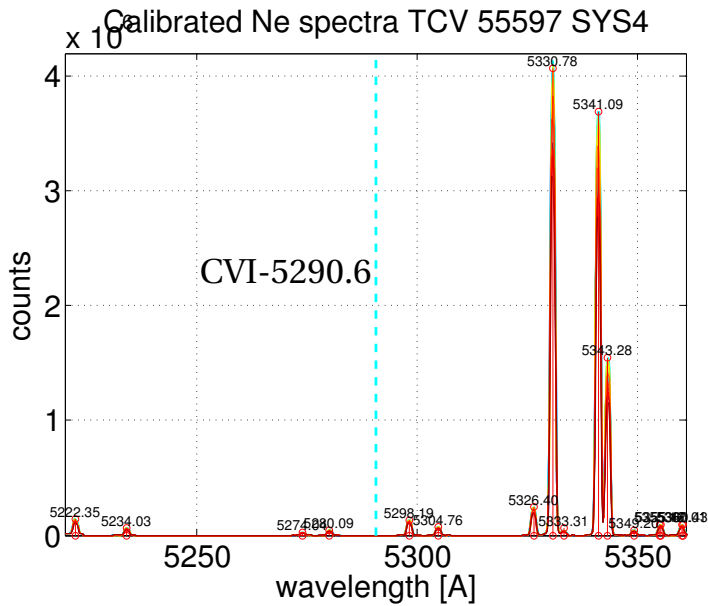
Figure 2.23: Experimental calibration Ne spectrum as function of wavelength (from the wavelength calibration function). The correct convergence of the calibration results in the alignment of the Ne lines of all the tracks. The reference CVI wavelength is shown by the cyan dashed vertical line.

2.2.4 CXRS analysis routines

In this section, the computational steps that are applied to the raw data (CCD counts) to obtain the final temperature, velocity and density profiles are presented in detail. The procedure consists of:

1. CCD offset subtraction and counts-photon conversion.

2. estimation of passive (P) contribution to the spectrum during the DNBI pulse.

3. calculation of the active (A) CX spectrum, by subtracting P from the total spectrum (P+A).

4. fit of A with a Gaussian function convolved with the IF.

5. calculation of the impurity parameters for each LOS from the fit output values and the DNBI attenuation code.

6. mapping of the LOS-DNBI intersection positions (R, Z) with the LIUQE magnetic reconstruction to obtain profiles in the radial variable ρ.

The first point was explained in sections 2.2.2 and 2.2.3, with any offset (bias and stray light) evaluated from the initial frames recorded by the camera before the onset of the discharge.

Passive spectra subtraction

The passive spectrum represents the larger contribution to the total spectrum in TCV CXRS measurements, typically ≥ 75%. An accurate recognition and processing of this contribution is mandatory for a correct interpretation of the experimental data. The main physical processes
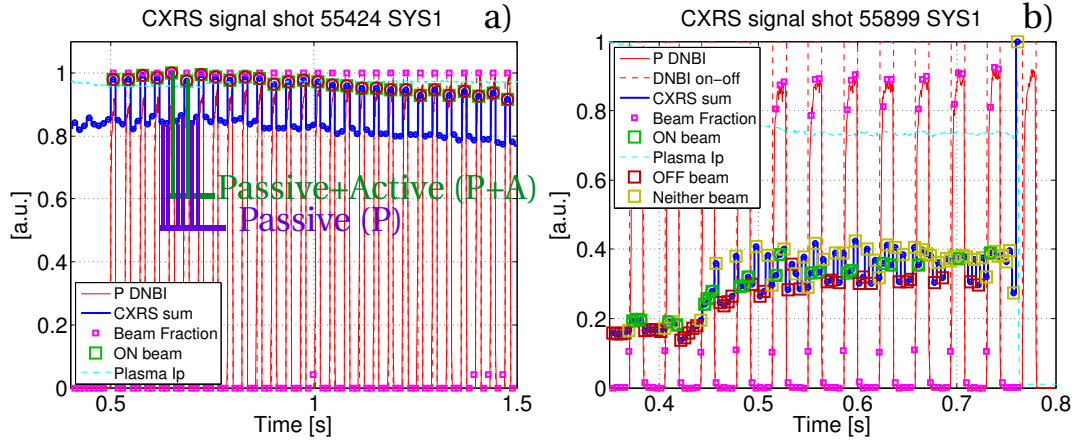
Figure 2.24: CXRS overall signal that illustrates the increased in photon rate in phase with the DNBI pulse due to active CX, for (a) L-mode shot #55424-Δt_{IT} = 12 ms and (b) H-mode shot #55899-Δt_{IT} = 4 ms. The passive signal (P) in shot 55424 is stationary, allowing a good passive signal subtraction from the total signal (P+A). In shot 55899 the signal is perturbed by ELMs, the perturbed frames (labelled Neither beam) are excluded from the analysis, reducing the diagnostic effective IT.

that cause passive emission are, in order of importance:

1. CX of neutrals diffusing from the plasma edge with impurity ion.

2. Free electron recombination.

3. Electronic excitation.

The contribution of electronic excitation in the visible range was evaluated in previous works [37] and found negligible. The free electron recombination and CX are competing processes, the smaller cross section of the first is compensated by a higher concentration of electrons than neutral donors needed in the second. Their emission profile differ, as the contribution of recombination is relevant across the whole plasma cross section, while the CX reactions are limited in a shell where the overlap of impurities and donors are relevant. In TCV the main CX passive contribution is due to reactions with excited donors [37].

The passive spectra evaluation is realised exploiting full modulation of the DNBI. The purely passive spectra measured during the DNBI-OFF phase are interpolated by means of a cubic spline on the DNBI-ON phase to estimate the corresponding passive spectra P. This requires the CXRS acquisition to be synchronised with the DNBI pulse within a fraction of a ms. The active

component of the spectrum is then calculated by subtracting the estimated passive spectrum P from the total (P+A) measured spectrum. Figure 2.25 shows the P and A components, together
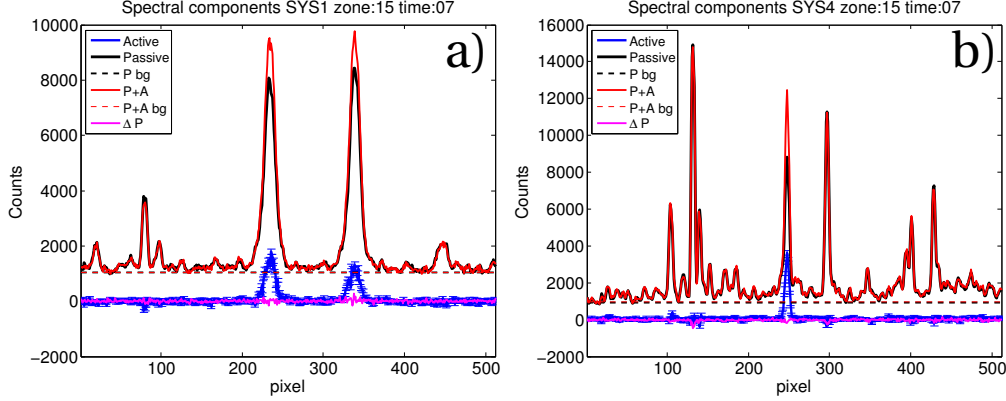
Figure 2.25: Components of the spectra measured in shot #55424 for a selected ROI of (a) SYS1 and (b) SYS4 (Δt_{IT} = 12 ms for both). The estimated passive component (P) is the dominant component, ΔP is the estimated noise due to the passive signal time variation.

with the total spectrum, for the L-mode shot #55424.

A DNBI duty cycle of 33%, meaning that the basic beam pulse sequence is OFF-ON-OFF, is usually employed. During this thesis, the DNBI PSU limited the total beam injected power for a TCV discharge, so this approach allowed coverage of the entire $\simeq$ 2 s TCV discharge duration. The presence of multiple passive acquisition for each active phase is essential to correctly evaluate the passive variation in time and validate the procedure. A duty cycle of 50%, for increased diagnostic time resolution, is available; it is nevertheless advisable to use this setup only in repeated experiments, where the constancy of the passive spectrum has been previously verified.

The subtraction procedure relies on a slow variation of the passive signal $\tau_P \ll IT$, such that shown in figure 2.24-(a). In presence of fast MHD events such as sawtooth crashes and ELMs this assumption is invalid and the standard procedure fails. During this thesis a different approach was successfully tested to allow measurements in these extreme conditions. A fast IT $\leq$ 5 ms allows multiple acquisition during each DNBI phase. The frames recorded during ELMs and other perturbing events, identified by an algorithm exploiting the PM D_α data, are then excluded. Figure 2.24-(b) shows the result of this process, the remaining frames are then used in the analysis. If the frequency of the perturbing events is higher than the limit imposed by the minimum IT, which is $\simeq$ 200 Hz, the procedure is not applicable and an unambiguous interpretation of the spectra is not possible with TCV's DNBI.

Active spectra fit

The assessment of the spectral features (section 2.1.2) of the active signal, needed for the ion parameters estimation, is complicated by the modification of the spectral shape induced by the

spectrometer instrumental function. The measured spectrum provided by the spectrometer is a convolution of the actual spectrum with the spectrometer IF. The wavelength calibration (section 2.2.3) provides the experimental IF from measurements of a cold Ne spectral line. A direct deconvolution of the spectrum is however not performed, as the deconvolution is an ill posed mathematical problem, whose solution is strongly dependent on the noise in the input spectrum. A more robust and elegant solution to this problem consists in fitting the experimental spectrum with a convolution of the IF and a Gaussian function. The fitting procedure is a χ^2 minimisation implemented with the gradient expansion algorithm described in Bevington [94] developed by Marquardt [95]. The minimisation is implemented for an arbitrary number of entrance slits and it is performed simultaneously over the active spectra of all the slits. Figure 2.26 shows the fit result for a double slit (SYS1) and single slit (SYS4) configurations. The time frame, shot number and selected ROI are the same as in figure 2.25.
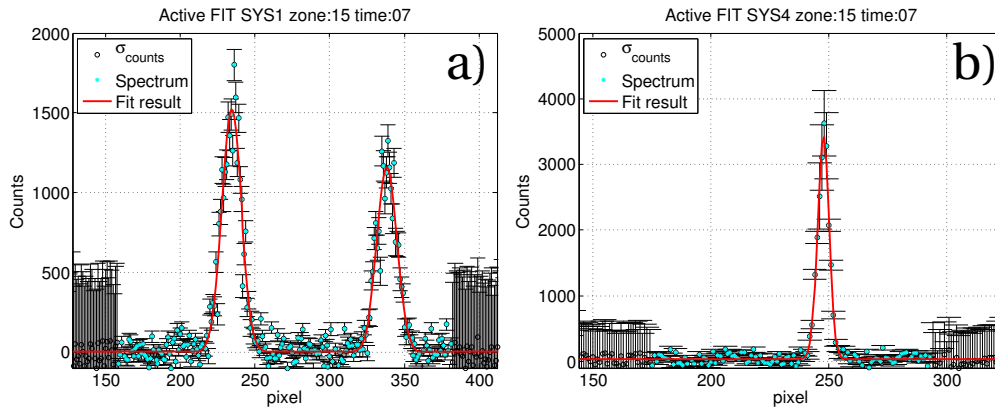
Figure 2.26: Graphical representation of the result of the fitting procedure for the selected ROI of (a) SYS1 and (b) SYS4 (Δt_{IT} = 12 ms for both).

The Marquardt algorithm provides an estimate of the uncertainty in the fitted parameters by evaluating the Hessian matrix. These uncertainties are considered in the impurity parameter uncertainty evaluation.

An additional check of the convergence quality consists on the evaluation of the residuals in the active line spectral region for each slit. If the sum of the absolute values of the residuals normalised to the line intensity exceed a threshold value $\ll 1$, the spectrum is considered inadequate and the automatic fit results are rejected. This is often the case when the passive subtraction procedure fails but the algorithm still converges to reasonable values, but human intervention is required to estimate the data validity for these situations.

Profile evaluation

The impurity parameters (n_C, T_C and v_C) are then calculated for each LOS. The direct application of equations in 2.1.2 can be used for an approximated evaluation of the physical

parameters, but a more comprehensive analysis, that accounts for the relevant atomic physics effects of section 2.1.2, is implemented.

The corrections found to be relevant in section 2.1.2 are due to the multiplet structure of the emission line and the Zeeman splitting, the former influencing both the line rest position and the width, the latter only the line width. The density calculation is therefore unaffected by these effects, that are pertinent to the velocity and temperature.

The inclusion of these effects in the analysis is performed through a correction look-up table, that was generated in the following plasma parameter ranges, which include the whole TCV operational space, for both the CVI and BV lines: $T_e(10 - 3 \cdot 10^4)$ eV, $T_i(10 - 1.5 \cdot 10^4)$ eV, $n_e(10^{16} - 5 \cdot 10^{21})$ m^{-3}, $Z_{eff}(1-5)$, $B(0.9-1.6)$ T, $\theta_Z(0, \pi/2)$ [rad]. The multiplet structure, i.e. relative intensity of the (n, l) transitions, is calculated by the ADAS 306 function on a 5D plasma parameter grid encompassing the reported plasma values (emission independent from θ_Z). For each transition the Zeeman pattern, i.e. the lines position and relative emissivity in dependence of B and θ_Z, is calculated through equations 2.13 and 2.14. Each of the emitting lines is then modelled as a Gaussian of width given by the ion temperature (equation 2.8), with the calculated position and relative emissivity. A synthetic spectrum, sum of all the transition lines, is then generated. The contribution of both active CX from ground and first excited level donor is considered. The synthetic spectrum is then fitted with a Gaussian function, with the same procedure adopted for the evaluation of the experimental spectrum, and the corresponding fit values are used in the construction of the look-up table. The procedure of fitting with a Gaussian function ensures to account for each of the multiplet transitions with the same weight in both experimental and synthetic spectra, rather than comparing just the moments of the two distribution, since the fitting is a non-linear procedure. A direct comparison of the generated reference fitting values with the experimental fit results gives the required plasma parameters.

The last step is to remap the local measurements on the reconstructed magnetic equilibrium to obtain profiles in the variable ρ. The position of the LOS-DNBI intersections is basically fixed by the diagnostic setup in the (R, Z) parameters, with a possible small displacement (< 2 mm) in case of strong beam attenuation, which is calculated for each shot. The LIUQE magnetic equilibrium reconstruction is then employed to map the (R, Z) positions in the ρ space for each time. An uncertainty $\leq 1\%$ of the plasma radius is estimated on the final ρ positions.

Figure 2.27 shows the resulting profiles (in ρ space) of the CXRS analysis for shot 55424 and the LFS (SYS1) and EDGE (SYS4) systems, for a selected time of the discharge ($t = 1.082$ s).

Uncertainty and error evaluation

The root mean square (RMS) of the uncertainties from the fitting procedure (section 2.2.4) and the photon statistics (section 2.1.3) is computed and constitutes the total uncertainty in the
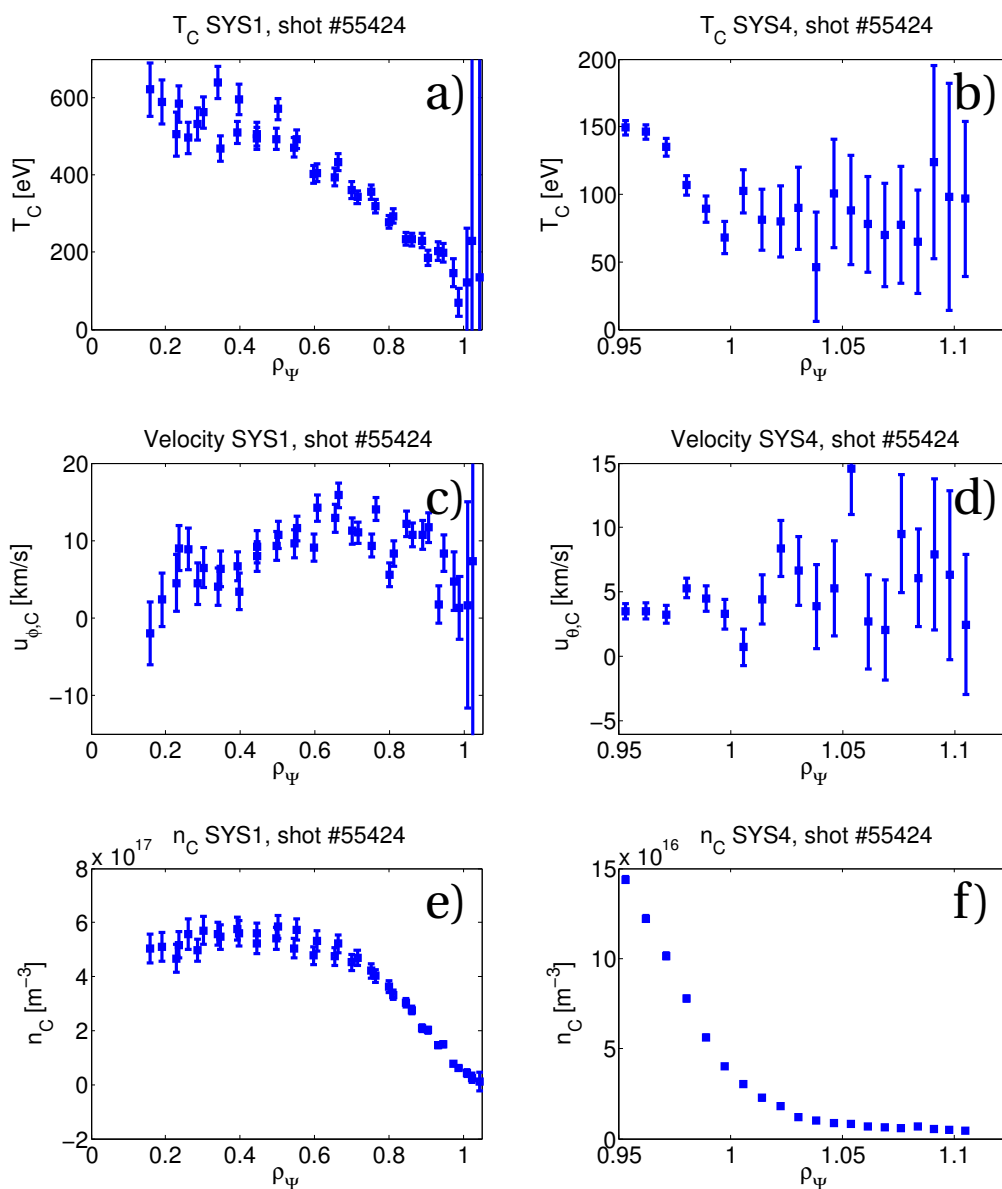
Figure 2.27: Profiles of (a-b) temperature, (c-d) rotation and (e-f) density resulting from the analysis of SYS1 and SYS4 for a selected time in shot #55424 ($\Delta t_{IT} = 12$ ms for both systems).

spectral shape parameters. These uncertainties are propagated with a standard error propagation technique in order to evaluate the impurity parameters uncertainties. The errorbars of figure 2.27 represent one standard deviation in the parameter uncertainties.

There are multiple possible sources of uncertainties in CXRS measurements, particularly for rotation, which have been considered and minimised during this work:

- **Passive subtraction.** When the plasma parameters evolve rapidly the passive spectrum subtraction procedure may fail. The presence of spurious lines in the active spectrum reveals the error and the evaluation of the fit residuals is used to discriminate the failed frames. The automatic analysis is therefore able to exclude heavily polluted spectra, but estimated contaminations of the A spectrum from P of ≤ 30% are not detectable and can affect rotation, temperature and density estimations.

- **Reference line position.** An error in the rest wavelength produces a systematic difference in the absolute rotation value. Although this effect is not easily detected, modelling the emission with the use of the CR code ADAS will minimise this source of error.

- **Wavelength calibration.** An inadequate wavelength calibration engenders a systematic error in the velocity and in principle in the temperature. Since each ROI is evaluated independently, different mismatch in different channels can result in different relative errors and change the profile shape, not only the absolute value. By evaluating the position of known lines from a different source (Hg is available on TCV) both these errors can be detected. Tests for several spectrometer configurations confirmed the convergence of the wavelength calibration to the correct value.

- **DCD.** Misalignments and errors in the LOS description cause mismatch in profiles. Comparison of different CXRS systems and with known features (e.g. H-mode pedestal) is the main procedure to assess errors in the alignment.

- **Absolute calibration.** The coefficients for the counts-photon conversion suffers from variable uncertainties in the range $10 - 30\%$ due both to the various camera setups and uncertainties in the calibrated source. Damage and misalignments due to interaction with plasma, such as mirror erosion, or to mechanical shocks, can modify the transmission efficiency and invalidate the calibration, resulting in incorrect density measurements. The periodic repeat of a standard shot is mandatory to detect such events.

- **CX q_{eff}.** CX cross sections from both experiments and theoretical calculations are used as input in ADAS for calculating q_{eff}. Errors in the cross section would induce systematic mismatch in the estimated density. An absolute uncertainty of ≤ 20% is usually assumed.

- **Atomic physics.** The effects due to the multiplet structure of the emission line and the Zeeman energy level splitting is accounted for in the analysis. Other effects such as Stark

splitting, energy dependence of CX cross section and finite lifetime-gyromotion, were evaluated, found negligible and omitted from the analysis.

- **DNBI attenuation.** An incorrect evaluation of the DNBI attenuation directly affect the density evaluation, modifying the profile shape. A solution is the experimental evaluation of the DNBI density by means of BES. In TCV a strong difference in the LFS and HFS density profiles can be used to detect problems in the attenuation calculations.

- **DNBI halo and plume.** Both halo and plume have the effect of increasing the active emission, causing density overestimation. Their effect was evaluated in previous works [37] and found negligible.

- **LIUQE reconstruction.** Errors in the magnetic reconstruction results in profile shape modification, that can be detected by inter-system comparison. Uncertainty ≤ 5 mm in the reconstruction is usually accepted.

Test measurements of HeII and NVII

The implementation of wavelength calibration routines working in all the accessible regions of the spectra opened the opportunity to study different impurities other than Carbon and Boron, used for the majority of the physics interpretation described later in this thesis.
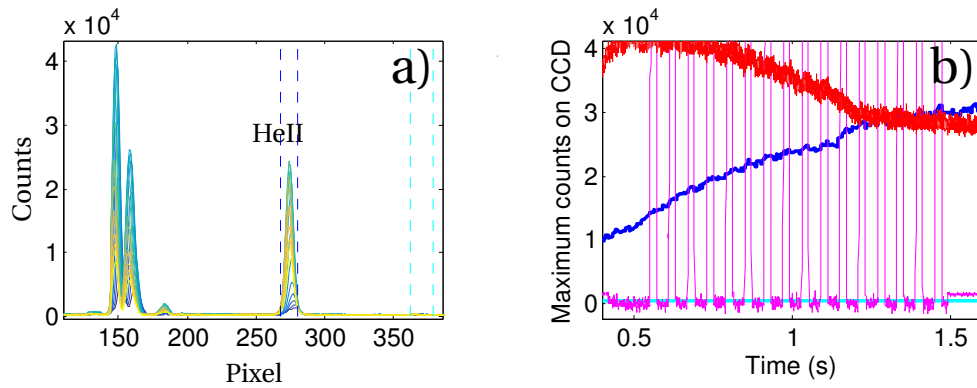
Figure 2.28: Test of HeII CXRS measurements on TCV, (a) HeII spectrum for EDGE LOS, (b) time trace of the maximum counts of HeII line (blue), reference CCD background level (cyan) and D_α line (red) from PD, for shot #56052 ($\Delta t_{IT} = 2$ ms). Although the HeII line radiance is intense (a), the time trace (b) do not show correlation with the DNBI pulses (in magenta), but correlates with the D_α emission perturbations, suggesting that the signal is passive.

A first attempt was performed for the HeII($n = 4 \rightarrow 3$) line @ 4685 Å. HeII CXRS is of interest for the next generation devices like ITER, where the concentration and transport of the Helium ash produced by the fusion reaction must be experimentally determined and characterised. To this purpose, study on HeII spectrum are undertaken in several fusion devices: ASDEX [79, 96],
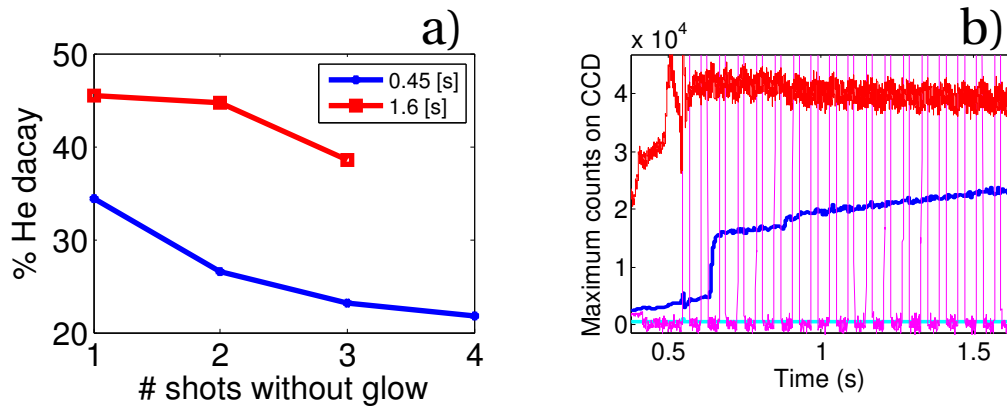
Figure 2.29: (a) He concentration decay for shots without conditioning He glow, estimated from passive emission. (b) time trace of the maximum counts of HeII line (blue) for shot #56062 (Δt_{IT} = 5 ms), having a He puff at 0.6 s. The injected He increases the HeII passive emission without beneficial effects for the active component.

TEXTOR [97, 98], PDX [61] with the goal of improving the understanding and interpretation of the HeII spectrum, which is more complex than the CVI and BV lines, due to a strong plume contribution [79]. Helium is routinely used in TCV between experiments (Helium glow) to clean and conditioning the tiles, hence significant He concentrations and recycling are expected and often observed.

First measurements on TCV revealed an unforeseen problem; the active CX component could not be extracted from the measurements with the passive subtraction technique. This was due to the strong passive emission, whose fluctuations dominate the time evolution of the emissivity, concealing the active component, which is estimated to constitute < 5% of the passive. To prevent camera saturation the EDGE spectrometer f-number was increased to 2.8 and IT≤ 5 ms were used. Figure 2.28-(a) shows the spectrum measured by SYS4 in HeII setup, the HeII line is well resolved and isolated from other lines. Nevertheless the time trace of the maximum value of the HeII radiance, figure 2.28-(b), reveals that a clear active component is not detected.

The reference shot 56052 was repeated multiple times (56054-56057) without inter-shot cleaning glow to verify the influence of He concentration on the A/P ratio. The passive emission indeed decreased as a function of the shot number, as shown in figure 2.29-(a). At the beginning of the shot (blue line) the He concentration after 4 shots without glow decreases to ≃ 20% of the reference value, while towards the end of the shot these values diverges less ≃ 40%, due to the He released during the discharge. The decrease in He concentration had no influence on the A/P HeII ratio, but allowed testing He puffing without saturating the sensors. The results remained discouraging: the effect of the He puff (figure 2.29-(b)) was to increase the passive signal, without any increase of the active component.

In conclusion, the test on HeII revealed that the active component of the spectrum is too

weak to produce meaningful results. Decreasing the DNBI energy from $\simeq$ 50 keV/amu to $\simeq$ 40 keV/amu, where the HeII effective emissivity coefficient peaks [62] would not be beneficial, since the degradation of the beam focussing properties and hence density, would annul the increased efficiency of the CX process. A solution is envisioned by employing LOS viewing the NBH, that is expected to produce a stronger active component by a factor of $\simeq$ 13 [99], but requires hardware modifications.

Another impurity of interest for the fusion community is Nitrogen, used in study on plasma radiation cooling [97]. Measurements of the NVII($n = 9 \rightarrow 8$) line @ 5669.37 Å were performed in ASDEX [93] and TEXTOR [97], the availability of the CX cross section for the transition (ADAS [62]) allows density calculations and study of the impurity diffusion. The measurements of this spectral line in TCV is particularly challenging, due to strong passive NII lines polluting the spectrum, see figure 2.30.
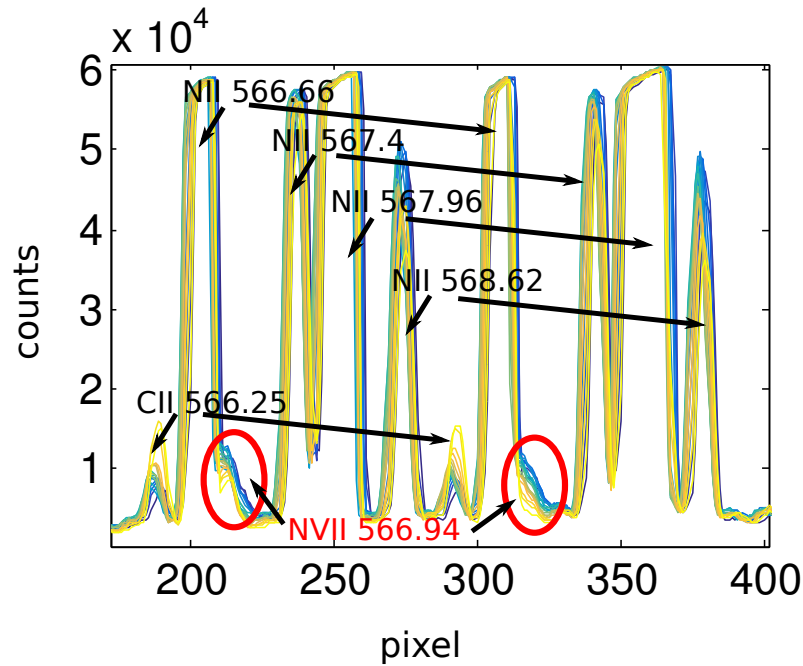
Figure 2.30: Raw spectra for a NVII setup of SYS3 in the DNBI ON phase (shot #53647, $\Delta t_{IT} = 3$ ms). The NVII($n = 9 \rightarrow 8$ @ 5669.37 Å) line for both slits is encircled. The spectra is clearly dominated by the passive NII lines, that saturates the sensor. The observed NVII line is overlapping with the passive NII line @ 566.66 nm, complicating the measurement.

An additional problem in the radiation cooling experiments is the strong temporal variation of the passive spectrum that invalidate the passing subtraction technique, making an adequate recognition of the active spectrum problematic. Figure 2.31 show the time plot of the average counts of NVII and two selected passive NII lines (5666.6 Å and 5679.6 Å) for shots 53647 and
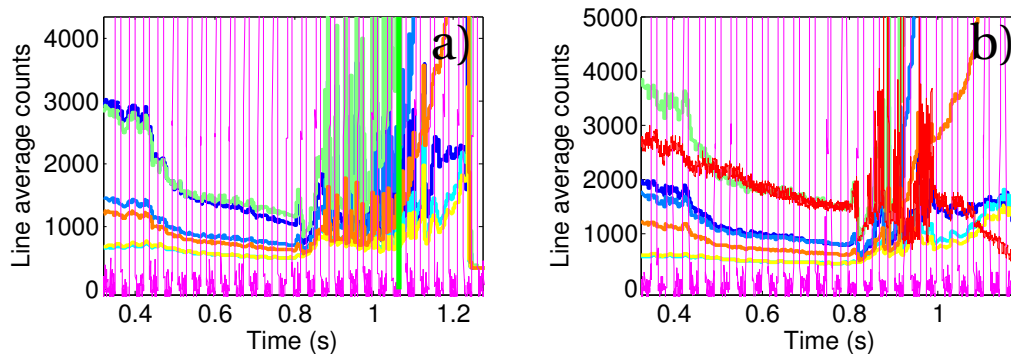
Figure 2.31: Time trace of NVII (cyan and yellow) and few selected NII lines for shot (a) #53647 and (b) #53648 ($\Delta t_{IT} = 3$ ms for both). The transition to H-mode is at 0.8 s, the passive spectrum variation in time invalidate the passing subtraction technique. The A/P ratio is below the threshold for a meaningful analysis for the duration of both shots.

53648. The transition to H-mode is at 0.8 s for both discharges, while the Nitrogen injection is at 0.95 s and 0.9 s respectively. After the gas injection the passive spectrum increases as expected, without improvements in the A/P ratio, which is below 5% for the duration of both shots, preventing a successful analysis. The use of LOS viewing the NBH is a viable option for CXRS NVII measurements in TCV.

In conclusion CXRS measurements in TCV of both He and N are particularly challenging due to the predominance of the passive component of the spectrum, and proximity of polluting line for NVII. To date, these tests were inconclusive, due to the weak active emission from the 80 kW DNBI. Measurements with LOS intersecting the NBH are envisioned for future with an expected increase in the active CX component about an order of magnitude. These cases are described to highlight the limits of using a diagnostic neutral beam in a plasma with a strong passive emission. The benefits of a purely diagnostic beam setup can be quickly eroded in these situations. Fortunately, all the spectroscopic and analysis improvements described above can be applied to CX observations of TCV's new heating beam to gain insight into these more challenging situations.

2.3 Conclusions

In this section the CXRS diagnostics on TCV were described in detail for the current configuration, with particular focus on the newly developed EDGE system, that constitutes the main diagnostic development of my work. The CXRS measurement principle was explained, with the appropriate corrections from atomic physics necessary to interpret the measured spectra. Improvements in the diagnostics' uncertainty estimations were described and implemented, with consideration of both photon statistics and accuracy of the active spectra fit, together

with the instrumental noise.

The legacy systems, from before this thesis, and their upgrades were briefly described and their performance elucidated. The low power DNBI used by the CXRS diagnostic was described and its effects on plasma were evaluated. The peculiarity of TCV CXRS relies in the ability of the DNBI of not perturbing the plasma, allowing for intrinsic rotation measurements. The drawback in employing a low power beam is the relatively low level of active signal and the corresponding low ratio A/P that forced the development of a passive spectra subtraction technique (DNBI modulation) and that can prevent the study of more challenging impurities (HeII and NVII).

The EDGE hardware, optimised for high throughput, was described and the transmission properties compared with the legacy systems. The optimisation of the LOS for poloidal measurements and high spatial resolution produced an increase in the measurement localisation in ρ with respect to the legacy VER system. A full non-linear grating equation in the wavelength calibration function was developed to increase the calibration accuracy, that combined to the diagnostic improved photon statistics resulted in an accuracy on the line position better than 0.02 Å, corresponding to an uncertainty in the velocity ≤ 1 km/s. The accuracy on both the temperature and density regularly attain levels $< 10\%$ and $< 15\%$ respectively. All these measurements, employed a DNBI that was shown to not directly perturb the measurement. Here the active signal can only be discerned by careful subtraction of the, often dominant, background light emission. This is to be positively compared to more usual measurements that piggy back a high power heating beam that provides spectral intensities that often dominate the background emission but strongly affect the plasma itself. Measurements from such systems have to rely on extrapolating the measured values back to a hypothetical negligible beam and just "hope" that the plasma behaviour in terms of transport and/or turbulence were not changed.

The improvements of the CXRS profile accuracy at the plasma edge, which constitute the boundary condition for all the plasma parameters, achieved by the EDGE system set the scene for a comprehensive transport studies in TCV and answer to the pressing request by the theory of more accurate experimental measurements. The application of the EDGE system to studies of impurity parameter evolution across ST and at the L-H transition resulted in unprecedented characterisation of the poloidal velocity well developing just inside the LCFS.

In conclusion, a large increase in the spectrometer throughput and improved collection optics can now be used to make measurements that were previously only accessible using perturbing methods.

3 Spectroscopic characterisation of H2 and D2 helicon plasmas

A spectroscopic characterisation of helicon plasmas in the resonant antenna ion device (RAID) was the first scientific application of the spectrometer designed for the EDGE system. This work was initially launched as a test bed for the EDGE optical spectrometer, to verify the correctness of the acquisition functions and of the wavelength and intensity calibrations by benchmarking the instrument with another spectrometer, a Princeton instruments' IsoPlane-320 [100]. After the validation of the spectrometer performance the project scope was augmented to encompass a complete characterisation of the source, for both the scientific and technological importance of the development of the RAID source and the unavailability of TCV during the closure for NBH upgrade. This chapter, following the reasoning reported in [58], explains the motivations, the procedure and the results of the project, with a brief introduction on the context of negative ion helicon source development, a description of the RAID, of the experimental procedure and of the data analysis. This work resulted in a journal paper publication [58] on which this chapter's contents are based. The chapter ends with the estimated species densities and outlook for future works.

3.1 Introduction

The heating scheme for future fusion reactor, as DEMO, relies on multiple actuators, among which NBI systems play a major role [101]. In order to reach the core region, the neutrals must have high energy, ~ 800 keV or higher. At the same time, to effectively heat the plasma, high (up to 50 MW) powers are necessary. Most NBIs are presently based on positive ion sources that have been developed to attain high reliability and easy maintenance. After acceleration to the desired energy, the positive atoms are neutralised by charge exchange reactions with a neutral gas. However the neutralisation efficiency of positive ions decreases drastically above 100 keV/amu [102] prohibiting their use for high particle energy NB. Conversely, the gas neutralisation (in reality ionisation) efficiency of negative ions remains essentially constant above 100 keV/amu, with typical values of 60 %, and also other more efficient methods that can exceed 80% can be implemented, such as photodetachment [103]. Present negative ion sources supply negative ion densities one order of magnitude lower than those of positive

sources, which has led to a strong research and development on alternative negative ion sources. The requirements on such sources are stringent. Eg: in DEMO the target extraction current density is 200 A/m^2, the pressure 0.2 Pa, the pulse duration up to 2 h, the extraction area 0.1 m^2 with a beam uniformity $\pm$ 10 % and a co-extracted electron fraction < 1. The last requirement is particularly challenging due to the higher mobility of electrons compared to negative ions. The generation of negative hydrogen or deuterium (represented throughout this chapter by the character H when referring to both) ions is based on two processes [102]:

1. surface production, where negative ions are the result of the interaction of a neutral atom H or an ion H^+ with a low work function surface:

$$
\begin{aligned}
H + e_{surf} &\rightarrow H^- \\
H^+ + 2 e_{surf} &\rightarrow H^-
\end{aligned}
$$
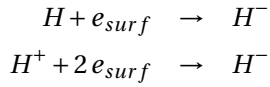
2. volumetric production, where the negative ions are produced by dissociative attachment (DA) of electrons to molecules that are in an excited ro-vibrational level v:

$$
H_2(v) + e \rightarrow H^- + H.
$$
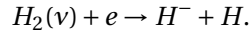
Most present-day efforts in the development on new negative ion sources focus on surface production, using caesium for its low surface work function. Eg: filament arc sources [104] and radio frequency (RF) sources [105]. Recently, it was proposed to use a helicon plasma source from consideration of its high ionisation efficiency [106], (particularly at low pressures) and its volumetric ion production. The cross section for DA production is strongly dependent on the molecular vibrational level v. It increases by four order of magnitude from $v = 0$ to $v = 4$ [102]. A high vibrationally-excited molecular population requires relatively high electronic energies $\geq$ 10 eV, as the radiative decay of excited electronic states, known as E-V singlet excitation [102], is an effective source of vibrationally excited molecules. This mechanism is responsible for the peak in DA cross section at $\simeq$ 14 eV [107, 108]. T_e must, however, be kept below 2 eV to reduce H^- detachment from electronic collisions, which is a very effective process due to the low binding energy (0.75 eV) of the extra captured electron [109]. To fully understand the negative ion production mechanism, a complete characterisation of the electron energy distribution function (EEDF) may therefore be required, especially for helicon sources, which have revealed, under certain conditions, the presence of non-Maxwellian features [110, 111], although for the purpose of this project a Maxwellian EEDF was assumed. The negative ion volumetric production in helicon plasmas is efficient with a high temperature electron population, confined by the magnetic field in the plasma-producing region, and a low temperature population diffused over a larger area, which provides the electrons for DA whilst reducing collisional losses. The main disadvantage of the volumetric production compared to surface production for negative ion beam application is the higher co-extracted electron fraction. It is also not proven yet whether volumetric processes could produce the same quantity of negative ions as in surface conversion at low pressure.

Figure 3.1: CAD drawing of (a) RAID and the helicon resonant antenna ((b) and (c)). The device has a circular cross section of 0.4 m diameter and a length of 1.8 m. The input optics for OES measurements are mounted on a port ~ 68 cm from the resonant antenna.

This chapter is focussed on the characterisation of the helicon resonant birdcage network antenna recently developed at SPC, for application as negative ion source in the source NBI test Cybele [103]. The experimental setup is described in section 3.2, with emphasis on the spectroscopic configuration for this application. Section 3.3 explains the steps used to compute the emissivities from the measured spectra, which consists of the same procedure as CXRS for radiance measurements and an ad hoc tomographic inversion (3.3.2). Emissivities are interpreted in section 3.4 to estimate the density of ions and neutral atoms. Emphasis is given on the dissociation degree, the ionisation degree and on the negative ion density. The results are discussed in section 3.5 and, finally, the conclusions and outlook are illustrated in section 3.6.

3.2 RAID experimental setup and spectroscopic system

The reported optical emission spectroscopy (OES) measurements are performed in the resonant antenna ion device (RAID) shown in figure 3.1, where the antenna and the input optics for OES are highlighted. The vacuum chamber is cylindrical, with a length of 1.8 m and a 0.4 m diameter. RAID is equipped with 6 magnetic field coils, able to generate an axial magnetic
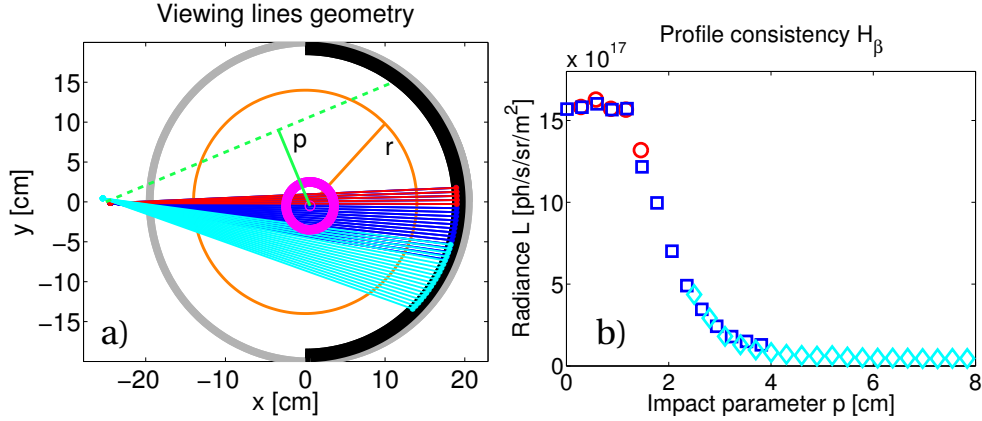
Figure 3.2: (a) LOS for the two sets of measurements, red and blue lines corresponds to the core measurements, above and below the plasma column centre respectively. In cyan the LOS for the edge set. The plasma column is schematically represented by a violet circle. The dashed green line simulates a LOS for the definition of the impact parameter p. The orange circle is used to define the radius r from the device axis. (b) Profile consistency check, same colours as figure (a), the cylindrical symmetry and the connection of the core and edge set are verified.

field up to 800 G. A coil current $I_{coil} = 150$ A provides an axial B field in the vacuum chamber axis of 150 G, which meets the specifications of the Cybele source [103]. The current of the first coil next to the antenna is reversed, $I_{coil1} = -30$ A, that increases the B gradient to give better antenna performance [106, 112]. The pressure is controlled by the gas inflow through a Bronkhorst mass flow controller at constant pumping speed and monitored by a Balzers pressure gauge. The pressure of 0.3 Pa, also required for operation in Cybele, is attained with a 7.5 ml$_n$/min flow. This relatively low gas pressure is one of the ITER NBI's source requirements, whose purpose is to minimise the negative ion losses due to collisions with molecules in the accelerator. Pressure variations are limited to < 20% during the measurements. The antenna (see figure 3.1-(b) and (c)) is designed to efficiently couple with the plasma helicon wave field, for modes $m = \pm 1$ [113]. It has 9 straight copper rods 15 cm long, an internal diameter of 13 cm, and a single RF power injection. It contains 16 high current, high Q, non-magnetic capacitors, each with a capacitance of 3.96 nF. The antenna, able to deliver up to 10 kW at the standard ISM frequency of 13.56 MHz, is installed at one end of RAID, outside the main coil region, as shown in figure 3.1-(a). The plasma generated by the antenna forms a column of approximately constant radius that ends on a target at the other end of the device.

The spectroscopic setup consists of a field lens coupling through an optical fibre bundle to a high throughput spectrometer and a detector. The input optics is a Navitar f/1.4 35mm lens and the image focal plane is optimised to image the RAID axis at 25 cm from the lens. The input lens is mounted on a port ~ 68 cm from the antenna to sample the plasma column far from the source. The fibre bundle is composed of 19 fibres of numerical aperture 0.22, with a fused silica core of diameter 365 μm, 2.5 meters long. The diameter of their adjacent images
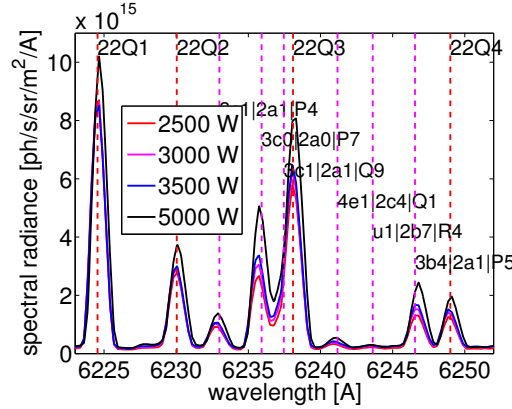
Figure 3.3: H_2 spectrum of Fulcher-α 22QN lines for different RF powers.

on the focal plane is 2.9 mm, resulting in a 55.1 mm wide sampling region. The geometry of the Lines Of Sight (LOS) is shown in figure 3.2-(a), together with the sketch of RAID's cross section. A violet inner ring schematically represents the plasma column position. In the figure are also defined the impact parameter p for a LOS, i.e. the distance of the LOS from the centre of the plasma column, and the radius r for a generic point, that is the distance of the point from the device axis. In RAID, the centre of the plasma column coincides with the mechanical axis. A core observation set that views the plasma column and an edge set that focuses on the outer region are available. Core LOSs view the plasma column both above and below its centre and are represented by red and blue lines respectively. Their goal is to ascertain the cylindrical symmetry of the plasma column emission. The edge measurements set observes impact parameter ranges up to 8 cm and partially overlaps with the core set, so that the consistency across the set merge region can be assessed as shown in figure 3.2-(b), where the $n_{LOS} = 38$ LOS are displayed. The LOS geometry was verified by back illuminating each fibre with a He/Ne laser and measuring the projected spot position on a reference anti-reflection graphite ring installed inside the vacuum vessel, represented by a black semicircle in figure 3.2-(a).

Collected light is analysed by the EDGE lens spectrometer described in section 2.2.2. The spectrometer spectral coverage in the red region of the visible spectrum is ∼ 14 nm and is too small to cover all the lines of interest within a single exposure. A set of 8 scanning angles, that include a partial overlap in the Fulcher-α range between 600 and 650nm, was used. This method is viable only if the emission of all lines is stable in time for the whole scan, an assumption that was verified by repeating the full angular scan at least twice for each antenna power. A constant emissivity (within 5 %) is observed within a few seconds for each input power value. The spectrometer input slit width was set to 80 μm for a spectral bandpass of 0.9 Å at 615 nm. This is sufficient to resolve most of the Fulcher-α molecular lines. The Andor camera (section 2.2.2) integration time and EM gain are adjusted at each scanning angle and power to maximise the counts and signal-to-noise ratio whilst avoiding saturation. The allowed integration time is in the range $3.5 \cdot 10^{-4}$-0.2 s where EM gains between 8 and 60 were employed. A complete spectrum is the result of an average of 15-30 of such acquisitions, with
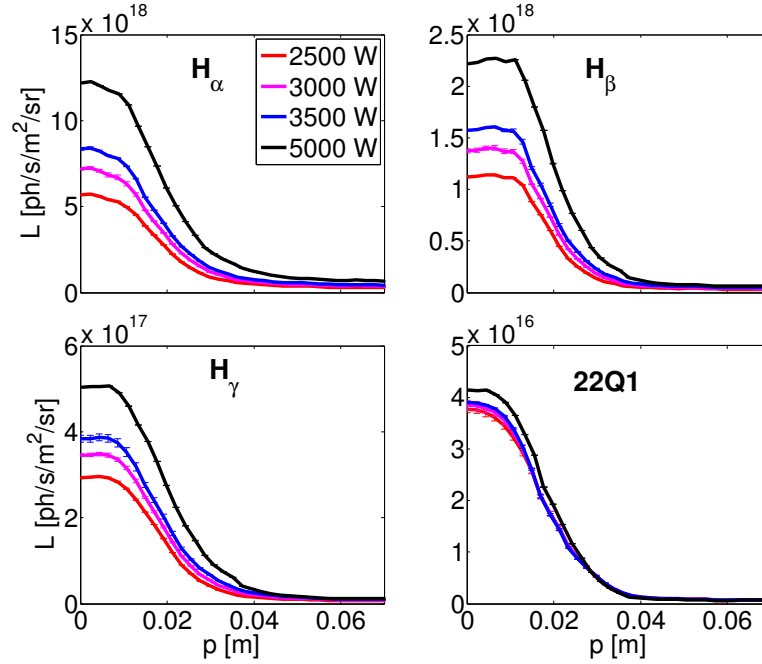
Figure 3.4: Radiance profiles $L(p)$ of Balmer and 22Q1 lines for H_2. Different colours indicate different RF powers.

the experimental uncertainty estimated from the inter-spectra standard deviation. Figure 3.3 shows a spectrum of the H_2 Fulcher-α 22QN lines for different RF powers, obtained with the procedure described above.

3.3 Absolute radiance measurements and emissivity profiles

The procedure to calculate absolute line emissivity is described in this section. It consists of two steps: a radiance calculation from the measured spectra and the tomographic inversion of these radiance profiles. The experiments were performed at a constant pressure of 0.3 Pa, in both hydrogen and deuterium. A scan in the antenna input power was performed for both isotopes, but with a different power range. The minimum possible power was determined by plasma stability: 2.5 kW for H_2 and 2 kW for D_2. The maximum power for these experiments was limited by thermal loads on the device. A measurement at 5 kW was performed in H_2, and resulted in damage to the target. The scan in D_2 was therefore limited to 3.5 kW.

3.3.1 Radiance calculation

The absolute radiance is computed from the acquired spectra. The light from each optical fibre is imaged by the spectrometer into a region of interest (ROI) on the CCD. 19 ROIs of approximately 20 vertical pixels are defined. The remaining section of the CCD that is not

Figure 3.5: Radiance profiles $L(p)$ of Balmer and 22Q1 lines for D_2. Different colours indicate different RF powers.

illuminated was used for CCD-shift smear correction. The photon rate R_{exp} [ph/s] of each emitted line for each ROI is evaluated using the same multi-Gaussian fitting procedure developed for CXRS, that in this case is applied to the full spectrum. The photon rate of lines that are partially overlapped was still computed with satisfactory accuracy. The radiance L_{exp} [ph/s/sr/m^2] of a line is calculated with the same procedure as CXRS (see section 2.2.3), here equation 2.38 is rewritten for clarity

$$L_{exp} = \frac{R_{exp}}{R_{cal}} L_{cal} \tag{3.1}$$

where R_{cal} and L_{cal} are the calibration source (Labsphere) photon rate and radiance respectively. An example of a H_2 molecular spectrum in the range of the 22QN (N from 1 to 4) lines is shown in figure 3.3, where the molecular lines are identified from reference wavelengths in Dieke [114]. The same procedure is implemented for D_2 using the reference lines in Lavrov's Atlas [115]. Figures 3.4 and 3.5 show the resulting radiance profiles for the first three Balmer lines and the molecular 22Q1 line, for H_2 and D_2 respectively. Each line has a characteristic radiance profile shape that is independent of the input RF power, which only determines the absolute radiance value. There is a noticeable isotope effect too on both profile shape, broader in deuterium, and radiance level, higher in deuterium for the atomic lines. The 22Q1 D_2 line radiance is much lower than the 22Q1 H_2. This is partially due to the different nuclear spin of the isotopes, that interchange the statistical weight for even-odd rotational molecular levels [116]. Nevertheless, the total D_2 Fulcher-α Q-branch emission is lower than for H_2.

The radiance of Balmer lines increases linearly with the RF power, while there is no clear dependence for the molecular line radiance.

3.3.2 Tomographic inversion

A tomographic inversion is then applied to extract the emissivity profiles from the radiance. The inversion of the line integrated data, in this case the radiances L_j with $j = 1, 2 \cdots n_{LOS}$, is a well known ill-posed mathematical problem, as the system of integral equations for the emissivity ϵ

$$L_j = \int_{LOS_j} \epsilon \, dl \tag{3.2}$$

is under-determined. To make it treatable further conditions must be applied [117]. This is increasingly problematic with a limited number of LOS, as is the case for the measurements reported here. In comparison, in medical tomography, $\sim 10^5$ LOS are routinely used. An important improvement for accurate Abel tomographic inversion is having multiple observation positions, not possible on RAID due to diagnostic access limitations at the time of the experiment. This requirement can be relieved in cases where the object has symmetry properties and, as mentioned above, the RAID plasma column has cylindrical symmetry. The chosen approach was to subdivide the cross section into n_r radially-concentric pixels of constant emissivity ϵ_i, $i = 1, 2, \cdots n_r$ and recast the integral problem as a system of algebraic equations in matrix formalism:

$$\epsilon_i = T_{ij} L_j \tag{3.3}$$

where the element T_{ij} of the transfer matrix T is the intersection length of the LOS j with the pixel i. The transfer matrix size is $n_r \times n_{LOS}$. A unique solution of system 3.3 can be found by choosing $n_r < n_{LOS}$ and imposing a further regularisation on the solution, achieved by minimising the functional

$$\widetilde{h} = \frac{1}{2} \chi^2 + \alpha \mathcal{R}. \tag{3.4}$$

The positive parameter α acts as a weighting factor between the regularising functional $\mathcal{R}$ and a least-squared optimized fitting. A desirable property for the regularisation is to perform a strong smoothing when the emissivity is low yet allow larger variations when the emissivity is high, to better distinguish features in the luminous core region. The Fisher information,

$$I_f = \int \frac{\left(\frac{d\epsilon(l)}{dl} \right)^2}{\epsilon} \, dl \tag{3.5}$$

has this property [118], and was chosen as regularising functional. The implemented algorithm, called minimum Fisher regularisation method [119], solves the system of normal
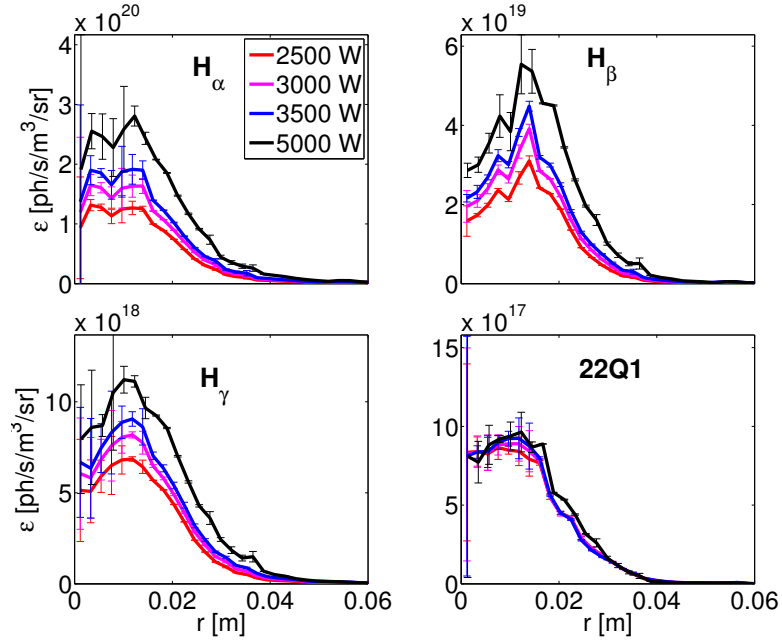
Figure 3.6: Emissivity profiles $\epsilon(r)$ of Balmer and 22Q1 lines for H_2. Different colours indicate different RF powers.

equations, equivalent to minimising the functional of equation 3.4,

$$\left(T^T * T + \alpha \widetilde{H}\right) * \epsilon = T^T L \tag{3.6}$$

where the $\widetilde{H}$ matrix contains the Fisher information. The parameter α is optimally chosen by the algorithm. Appropriate convergence of the algorithm is verified by reconstructing the input radiance profiles from the output emissivities and comparing with the initial data. A value $n_r \leq n_{LOS}$ is selected to preserve as many of the smaller features as possible in the inverted profile. Particular care must be taken in choosing the boundary conditions. Measurements were limited to impact parameter $p_{max} \sim 8$ cm, where the radiance has yet to vanish; a straightforward inversion thus yields a non-physical spike in the emissivity profile at this position. The correction of this feature required an extrapolation of the radiance profile, before the inversion, to the unknown zero radiance point p_0. Several extrapolation methods were tested, linear, quadratic and exponential, to choose p_0. The resulting emissivities are thus robust against variations of the extrapolating methods and p_0 position, with an uncertainty within 25% at p_{max}, decreasing to less then 10% at 6 cm, for impact parameters of p_0 in the range 16-20 cm. From these assessment results, a linear extrapolation with p_0 at 20 cm was chosen for all the inversions as the lowest order, and thus more stable, approach. An uncertainty estimate of the Abel-inverted profiles was performed using a Monte Carlo approach [69]. For each radiance profile a set of 400 virtual profiles was generated, varying the radiance value at each position according to a normal distribution centered at the original profile value, with a standard deviation given by the computed uncertainty. Each one of these
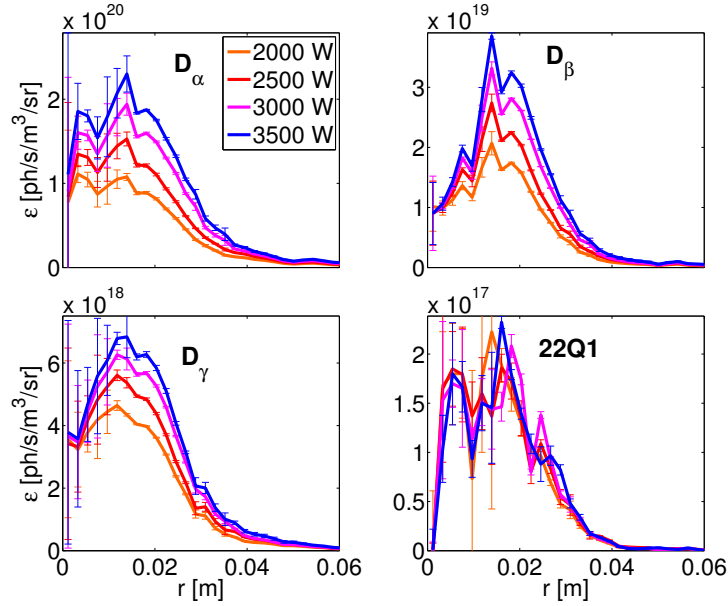
Figure 3.7: Emissivity profiles $\epsilon(r)$ of Balmer and 22Q1 lines for D_2. Different colours indicate different RF powers.

virtual profiles was then inverted using the methods described above, with the emissivity uncertainty taken as the standard deviation of the virtual emissivity profiles. The average value of the virtual profiles was verified to converge to the inversion of the original profile.

Figures 3.6 and 3.7 show the computed emissivity profiles and their uncertainties for the Balmer lines and the molecular 22Q1 line, for H_2 and D_2 respectively. Emissivity profiles are generally hollow and their shape is preserved for different input powers. The most hollow profile is for the Balmer β line (for both H_2 and D_2), that is a consequence of the already hollow radiance profile. The Balmer α line is only slightly hollow, and, considering the estimated uncertainties, remains compatible with a flat profile. The molecular line profiles are also slightly hollow, with a similar behaviour as the H_α line. The estimated uncertainties from the Monte Carlo assessment provide a high confidence in the inverted profiles in the 1.5-6 cm radial range, where their values are typically ≤ 15 %.

3.4 Analysis with YACORA code and power scan results

Now that the experimental emissivity profiles are measured and their uncertainties estimated, we seek to deduce the ion population profiles in the RAID plasma. The radial profiles of the first 3 Balmer lines and the sum of the diagonal Fulcher-α lines are interpreted using the collisional-radiative (CR) code YACORA [57]. The code solves the CR rate equations for the population density n_s of the hydrogen atom, resolving the lower 40 energy states ($s = 1, 2 \cdots$ 40). The reactions included in the model are: excitation and de-excitation by e^- collisions,
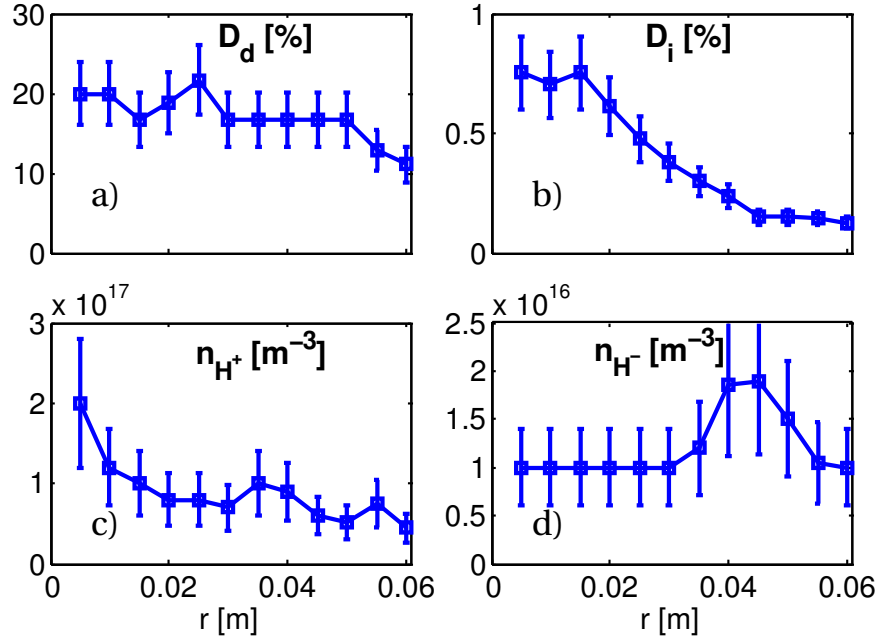
Figure 3.8: Profiles of (a) dissociation degree D_d, (b) ionisation degree D_i, (c) H^+ density and (d) H^- density estimated by YACORA for input power 3 kW in hydrogen.

spontaneous emission, ionisation, (radiative, dielectronic and three-body) recombination of H^+, dissociative excitation of H_2, dissociative recombination of H_2^+ and H_3^+ and mutual neutralisation of H^- with H^+, H_2^+ and H_3^+. When available, cross sections are preferred to rate coefficients, which gives YACORA the ability to perform calculations with non-Maxwellian EEDF. The analysis was performed assuming a Maxwellian EEDF. YACORA is able to include effects due to opacity, but these are neglected in the current analysis since they are expected to be negligible at the low plasma density of these experiments [120]. The densities of the 6 species H, H^-, H_2, H^+, H_2^+ and H_3^+ are varied independently, together with the electron density n_e and temperature T_e, for each code run that is then compared with the measured emissivity, with a trial and error procedure. When the deviation from the experimental value is lower than 10% a match is determined. The use of H_2^+ and H^- is mandatory to reach convergence. This implies that other, simpler, OES analysis methods, that neglect some of the species considered by YACORA, could lead to erroneous estimations if the excluded channels are important [121]. In these plasmas, the mutual neutralisation channel of H^+ is fundamental in the analysis while the H^+ recombination channel is essentially irrelevant. Uncertainties of 20% are assigned to the electron density and temperature accordingly to results from code validation in similar low pressure plasmas [57]. The uncertainty on the density ratio of atoms to molecules is given by the uncertainty of the corresponding emissivities, as the ratio of the rate coefficients is insensitive to T_e and n_e. For this reason an upper limit for uncertainty of 20% is chosen. The uncertainty for the other species (H^-, H^+, H_2^+ and H_3^+) depends strongly on the contribution of the corresponding process to the Balmer line radiation. In this case an
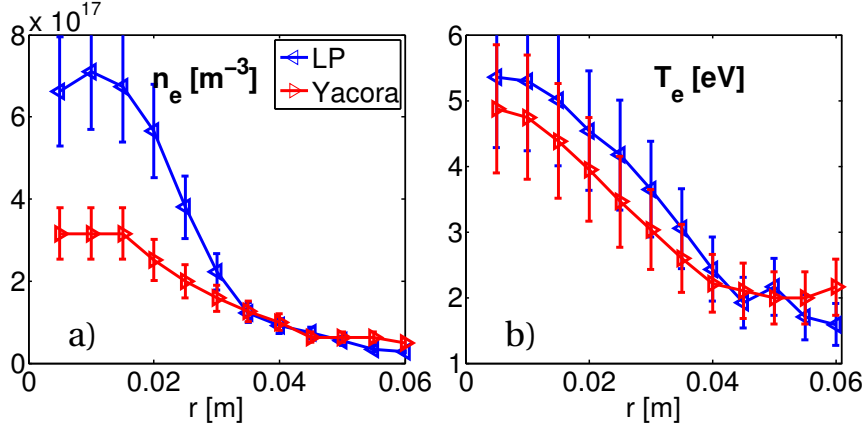
Figure 3.9: Comparison of experimental (a) n_e and (b) T_e profiles (LP) with YACORA convergence values for input power 3 kW in hydrogen.

estimated upper limit to the uncertainty of 40% is applied. The procedure is time consuming and is performed manually; so only a reduced set of three radial positions (at 1.5, 3 and 4 cm) was considered for the analysis. These positions were chosen from the results of the 3 kW RF power in hydrogen, which was the only case for which the full profile was completed, as detailed below.

Figure 3.8 shows the dissociation degree, the ionisation degree and the H^+ and H^- density profiles estimated by YACORA for this latter case. The dissociation degree D_d is defined as

$$D_d = \frac{f}{f + 2} \tag{3.7}$$

with f the ratio of atomic to molecular density and is approximately constant for radii smaller than 5 cm, with values larger than 15%. The ionisation degree D_i, defined as

$$D_i = \frac{n_e}{n_H + n_{H_2}}, \tag{3.8}$$

is peaked in the core region, r ≤ 1.5 cm, where it almost reaches 1%. It decreases linearly with radius by one order of magnitude at 4.5 cm, remaining constant at larger radii. The H^+ density is strongly peaked on axis, for r < 1 cm, while the negative ion density has a peak in the edge region, between 4 and 5 cm. The radial position 1.5 cm is representative of the core region, the 3 cm point is a transition region for both n_{H^+} and n_{H^-} and the final position at 4 cm is where the negative ion density peaks. The n_e and T_e profiles determined via YACORA are compared in Fig. 3.9 with experimental profiles, measured with an RF-compensated Langmuir probe (LP), by integrating the EEDF. A voltage sweep of [-60, +35] V was used in order to characterize the I-V curve. The T_e profile is in agreement but there remains a discrepancy of about a factor 2 in the n_e profile in the core region that is still under investigation. Nevertheless the hollow electron density profile measured by the LP probe is in agreement with the hollow emissivity
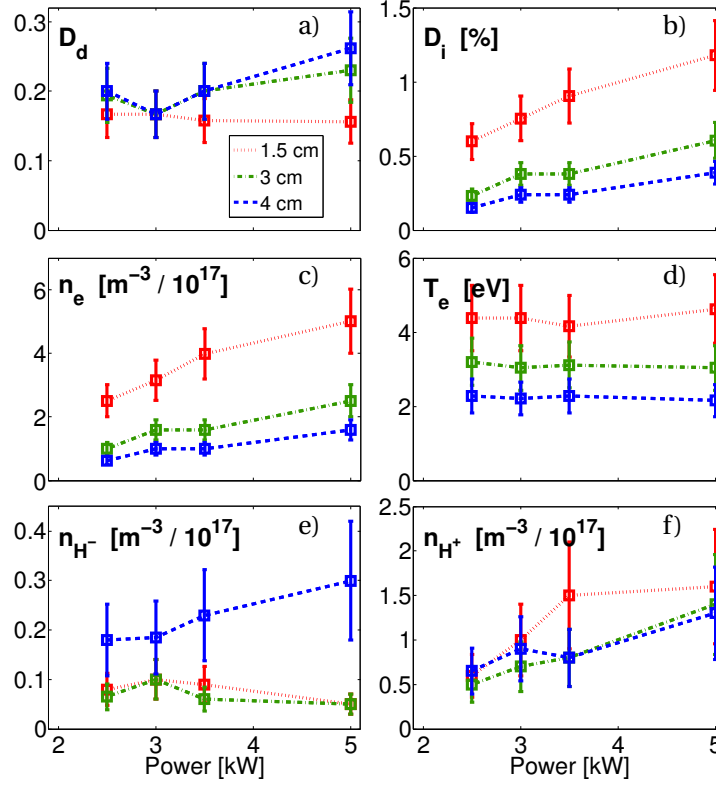
Figure 3.10: Results of YACORA analysis for power scans in hydrogen H_2 at radial positions 1.5,3,and 4 cm, as function of input power. (a) dissociation degree D_d, (b) ionisation degree D_i, (c) n_e, (d) T_e, (e) n_{H^-} and (f) n_{H^+}.

profiles. The gas translational and vibrational temperatures are estimated from Boltzmann plots of the Fulcher lines [122] and are respectively $T_{tran} = 900 \pm 200$ K and $T_{vib} \geq 6000 \pm 1000$ K for the first 5 vibrational levels in the ground state. These values are found not to depend upon input power and remain constant at all radii.

Figures 3.10 and 3.11 show the results of the analysis for hydrogen and deuterium respectively, at the three radial position considered, as a function of the input power, clearly displaying the isotope effect. For the same conditions, the dissociation degree and the ion densities are larger for deuterium than for hydrogen, while electron temperatures are lower. Trends with power are generally similar for both isotopes. Both n_e and T_e are decreasing functions of the radius, as already seen in figure 3.9, but while n_e increases linearly with input power, T_e is almost insensitive at all positions. Being able to increase the plasma density without increasing the temperature is a typical feature of helicon sources, and it is highly desirable for a negative ion source for NB, as it would permit an easy tuning of the negative ion production rate. The dissociation degree slightly increases with power and with the radius, reaching 35% and 25% at 4 cm for deuterium and hydrogen, respectively. The weak dependence of the dissociation degree on position could be explained by the H mean free path, which is estimated to be
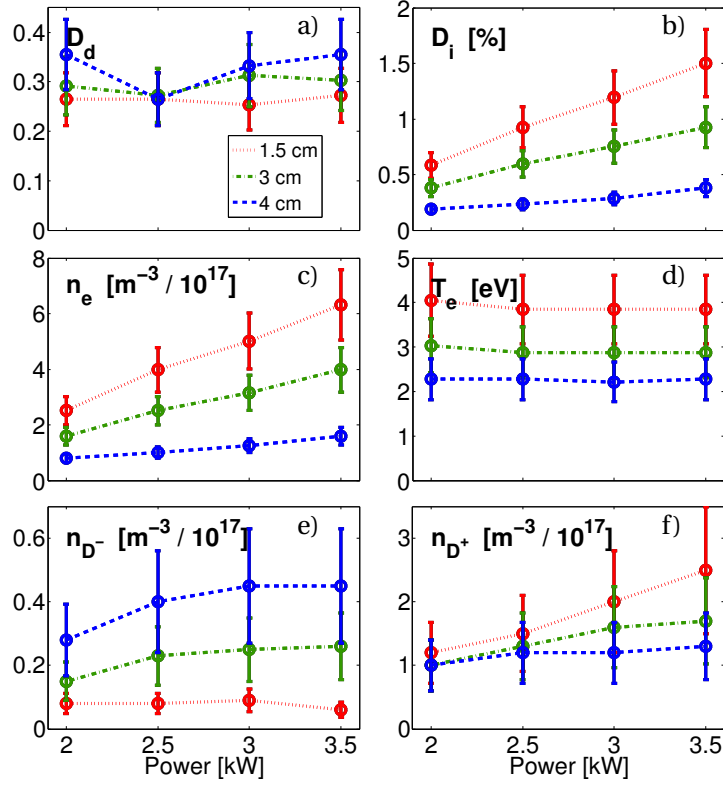
Figure 3.11: Results of YACORA analysis for power scans in deuterium D_2 at radial positions 1.5,3,and 4 cm, as function of input power. (a) dissociation degree D_d, (b) ionisation degree D_i, (c) n_e, (d) T_e, (e) n_{D^-} and (f) n_{D^+}.

of a few centimetres. The neutral hydrogen atoms are generated by dissociation in the core region, where T_e and n_e are high, and diffuse to larger radii. The flat neutral density profile is related to a relatively large mean free path compared to the observation volume. The positive ions H^+ exhibit the same behaviour as n_e, but with lower values, H_2^+ and H_3^+ (not shown) ensuring quasi-neutrality. The negative ion density is relatively low and insensitive to the input power inside the plasma column, radius < 3 cm, where the relatively high T_e reduces stable H^- formation and lifetime. At the edge of the plasma column, for $r \geq 4$ cm, the negative ion density attains high values of strong interest for a negative source development. The trend at 4 cm is different between the two isotopes (see figures 3.10-(e) and 3.11-(e)). For hydrogen, the negative ion density increases linearly with power, reaching $3 \cdot 10^{16}$ m^{-3} at 5 kW, while for deuterium it saturates to $4.5 \cdot 10^{16}$ m^{-3} at 3 kW, with a similar trend, but lower values, at 3 cm.

3.5 Discussion

The results shown above are extremely encouraging for the application of the helicon antenna as negative ion source for high energy NBI that will be tested in the Cybele configuration, which

exploits an extremely elongated extraction geometry. The dissociation degree D_d reaches relevant values for surface production at all the powers of the scan. The ionisation degree D_i, which directly determines the ability to extract negative ions from a source, is a limiting factor at these input powers. However the application of this plasma source for surface production is still feasible (in both H_2 and D_2) if the D_i linear increase is maintained at higher powers.

The scan in power was interrupted at 5 kW following damage assessment on the machine during hydrogen operation. Furthermore, the antenna matching box was not compatible with higher powers. A new matching box and improvements on the chamber cooling system were designed and are now in commissioning phase, to extend the antenna exploitation to its full potential.

A first analysis of the possible application of this antenna as a volumetric source is presented. Direct extraction and acceleration of the negative ions surrounding the plasma column should be feasible, without the positive ion flux which is essential for surface production. The limiting factor in this case is the maximum attainable negative ion density and the ratio n_{H^-}/n_e, which is directly related to the co-extracted electron fraction. The negative ion density has contrasting trends for the two isotopes tested. In deuterium, it appears close to saturation while for hydrogen it retains a linear dependence so that extrapolation at higher powers remains unclear. The ratio of negative ions to electron density is likely to decrease with power, from the deduced values of about 0.3, whereas the required ratio should be higher than one. It is possible that this behaviour can be corrected by modifying the magnetic configuration and an extensive study will be necessary to assess this possibility.

3.6 Conclusions and outlook

OES measurements were performed in RAID to characterise the performance of both the spectrometer designed for CXRS EDGE measurements and a newly developed resonant network helicon antenna. The spectrometer complied with the expected performance in terms of a high throughput and dispersion, a stable wavelength configuration and reliable radiance estimation. Since this work was performed during TCV's long vacuum opening, this was taken as a highly successful commissioning of the new EDGE spectrometer.

Absolute emissivity profiles for the first three Balmer lines and the molecular diagonal Fulcher-α lines were computed by Abel-inverting multi-channel radiance profile measurements. The emissivities were interpreted using the collisional radiative code YACORA, which provided an estimated density for the 6 species H, H^-, H_2, H^+, H_2^+ and H_3^+. The population trends with input power were initially studied at three different radial positions. The results obtained are promising for application of the antenna as a negative ion source if maintained and should extraction and acceleration in a beam source behave as expected on the beam test stand. The plasma is effectively confined in a column all along the length of RAID. On the device axis, a high plasma density $n_e \geq 6 \cdot 10^{17}$ m^{-3} is attained at low input power, with a relatively high electron temperature $\simeq 5$ eV. At the edge of the plasma column, $r \geq 4$ cm, where the electron

density and temperature decrease to $\simeq 1 \cdot 10^{17}$ m^{-3} and $\simeq 2$ eV respectively, high dissociation degree ≥ 35 % and high negative ion density $\simeq 4.5 \cdot 10^{16}$ are obtained. It should be noted that these negative ion densities already reach values close to those near the extraction region of caesium negative sources [105]. Extrapolation of these results to a nominal antenna power of 10 kW remains complicated by the large gap between the upper power in deuterium and the observed isotope dependencies. To reduce the extrapolation uncertainties, source performance at 10 kW will be verified with a new set of measurements after the commissioning of the chamber cooling system and installation of the new matching box are completed. Increasing the diagnostic array around this new source will allow us to harden these conclusions. In addition to refining the spectroscopic and Langmuir measurements, a photodetachment diagnostic is under development that can independently measure the negative ion density. A helicon antenna based system may provide the negative ion injectors, considered necessary for fusion reactor development, with a welcome alternative source.

For the main purpose of this thesis, the high throughput spectrometer was already tested and analysed in detail before its implementation for TCV poloidal measurements. Furthermore, in view of the large increase in light throughput, two new EDGE-type spectrometers were commissioned to replace the legacy 0.75 m toroidal TCV spectrometers. Following the success of this work, a further spectrometer is planned for permanent installation for RAID-like research.

4 Rotation: theoretical background

This chapter presents an overview of the theoretical description of plasma rotation, with particular focus on the processes that will allow a better understanding and interpretation of the experimental measurements. It should be stressed that, not only is rotation and rotation shear strongly related to changes in Tokamak plasma transport and susceptible to magnetic field geometry errors, but that it can be directly measured: a luxury compared to many other plasma parameters that are known to strongly affect performance.

4.1 Momentum balance equation and rotation

A plasma is statistically described by the distribution function $f_\alpha(\mathbf{x}, \mathbf{v}, t)$ of each species α it contains (main ions $\alpha = i$, electrons $\alpha = e$, impurities $\alpha = C, B, \cdots$). The evolution of the distribution function is determined by the Fokker-Planck [123], a.k.a. Boltzmann equation [23, 124]:

$$\frac{\partial f_\alpha}{\partial t} + \mathbf{v} \cdot \nabla f_\alpha + \frac{q_\alpha}{m_\alpha} (\mathbf{E} + \mathbf{v} \times \mathbf{B}) \cdot \nabla_v f_\alpha = \mathscr{C}_\alpha (f_\alpha) \tag{4.1}$$

where the right hand side is the collisional operator $\mathscr{C}_\alpha (f_\alpha) = \sum_\beta \mathscr{C}_{\alpha\beta} (f_\alpha)$, which describes the change in time of f_α due to collisions (mostly Coulomb in a plasma) both between the same species $\beta = \alpha$ and different species $\beta \neq \alpha$, that can be described as a combination of friction forces, viscosity and electrical resistivity. In a plasma, small deflection collisions dominate [17], which allows a description of the collisions by the Fokker-Planck operator [17], which is basically a diffusion operator in velocity space, resulting in a simpler description than the more general and complex Boltzmann collisional operator.

The charge q_α of an impurity is often represented by the charge state Z_α and the elementary charge e, i.e. $q_\alpha = Z_\alpha e$. The solution of Maxwell's equations [125] and the Boltzmann equation 4.1, describes the plasma evolution. This problem is however too complex for either an analytical or a numerical general solution. A significant reduction in the complexity is provided by considering a multi-fluid plasma description, and then calculating only the first

few moments of the Boltzmann equation. The first and second moments gives the mass 4.2 and momentum 4.3 conservation equations respectively:

$$\frac{\partial n_\alpha}{\partial t} + \nabla \cdot (n_\alpha \mathbf{u}_\alpha) \quad = \quad S_n \tag{4.2}$$

$$n_\alpha m_\alpha \left(\frac{\partial \mathbf{u}_\alpha}{\partial t} + \mathbf{u}_\alpha \cdot \nabla \mathbf{u}_\alpha \right) \quad = \quad n_\alpha q_\alpha (\mathbf{E} + \mathbf{u}_\alpha \times \mathbf{B}) - \nabla p_\alpha - \nabla \cdot \boldsymbol{\pi}_\alpha + \mathbf{R}_\alpha + \mathbf{S}_\alpha \tag{4.3}$$

with S_n the particle source and $\mathbf{S}_\alpha$ the momentum source due to external torques and the definitions [2, 17, 23]:

$$\text{particle density: } n_\alpha \quad = \quad \int f_\alpha \, d^3 v \tag{4.4}$$

$$\text{fluid velocity : } \mathbf{u}_\alpha \quad = \quad \int \mathbf{v} f_\alpha \, d^3 v \tag{4.5}$$

$$\text{temperature : } T_\alpha \quad = \quad \frac{1}{n_\alpha} \int \frac{m_\alpha |\mathbf{v} - \mathbf{u}_\alpha|^2}{3} f_\alpha \, d^3 v \tag{4.6}$$

$$\text{isotropic pressure: } p_\alpha \quad = \quad \int \frac{m_\alpha |\mathbf{v} - \mathbf{u}_\alpha|^2}{3} f_\alpha \, d^3 v = n_\alpha T_\alpha \tag{4.7}$$

$$\text{pressure tensor : } \mathbf{P}_\alpha \quad = \quad \mathbf{1} p_\alpha + \boldsymbol{\pi}_\alpha = \int n_\alpha m_\alpha (\mathbf{v} - \mathbf{u}_\alpha)(\mathbf{v} - \mathbf{u}_\alpha) f_\alpha \, d^3 v \tag{4.8}$$

$$\text{friction force : } \mathbf{R}_\alpha \quad = \quad \int \mathbf{v} \, \mathscr{C}_\alpha (f_\alpha) \, d^3 v \simeq \sum_\beta \mathbf{R}_{\alpha\beta} = \sum_\beta -m_\alpha n_\alpha \nu_{\alpha\beta} (\mathbf{u}_\alpha - \mathbf{u}_\beta) \tag{4.9}$$

where the tensor $\boldsymbol{\pi}_\alpha$ is termed viscosity and the approximation $\mathbf{R}_\alpha \simeq \sum_\beta \mathbf{R}_{\alpha\beta}$ of the friction term is made by considering the momentum transfer due to collisions with different species, with $\nu_{\alpha\beta}$ the collision frequency.

In a steady-state plasma ($\frac{\partial \cdot}{\partial t} = 0$) with subsonic flow ($\mathbf{u}_\alpha \cdot \nabla \mathbf{u}_\alpha$ term negligible), isotropic pressure ($\boldsymbol{\pi}_\alpha = 0$), neglecting friction ($\mathbf{R}_\alpha = 0$) and external torques ($\mathbf{S}_\alpha = 0$), equation 4.3 reduces to the force balance equation [2, 23]:

$$\nabla p_\alpha = n_\alpha q_\alpha (\mathbf{E} + \mathbf{u}_\alpha \times \mathbf{B}) \tag{4.10}$$

which states that, to the lowest order, the pressure force balances the Lorentz force.

The expression for the perpendicular velocity $\mathbf{u}_{\alpha,\perp}$ (to the magnetic field $\mathbf{B}$) is found from the cross product of equation 4.10 with $\mathbf{B}$:

$$\mathbf{u}_{\alpha,\perp} = \frac{\mathbf{E} \times \mathbf{B}}{B^2} - \frac{1}{q_\alpha n_\alpha} \frac{\nabla p_\alpha \times \mathbf{B}}{B^2} \tag{4.11}$$

The first term is the $\mathbf{E} \times \mathbf{B}$ velocity (equation 1.25) with the second termed the diamagnetic

drift [2, 23],

$$\mathbf{u}_{\alpha,\nabla p} = -\frac{1}{q_\alpha n_\alpha} \frac{\nabla p_\alpha \times \mathbf{B}}{B^2} \tag{4.12}$$

since it is an effective mass flow (not a guiding centre drift), caused by unbalance in the diamagnetic current (due to B gradient) [23], which is proportional to ∇p_α. The lowest order solution (equation 4.11) of the momentum equation 4.3 projected in the radial direction states that the perpendicular flow drives are the electric field and the pressure gradient. The $\mathbf{E} \times \mathbf{B}$ drift is independent of particle parameters, hence it's the same for all species, while the diamagnetic drift is in opposite directions for electrons and ions, allowing differential species' rotation. The timescales on which the flow described by 4.11 is established is in the fast compressional Alfvenic range $\tau_A \simeq 1 - 100\mu s$, which represent the zero order of the gyroradius expansion [124]. On longer timescales the rotation evolves accordingly to the parallel force balance equation [124] on ion collisional timescales ($\tau_{ii} \simeq$ ms) and to the toroidal force balance on transport timescales ($\tau_{tr} \simeq 10 - 100$ ms in TCV), which determines the final rotation state.

4.2 Rotation decomposition

The rotation may be decomposed in the parallel and perpendicular directions:

$$\mathbf{u}_\alpha = u_{\alpha,\|}\, \mathbf{b} + \mathbf{u}_{\alpha,\perp} \tag{4.13}$$

where $\mathbf{b} = \mathbf{B}/|\mathbf{B}|$ is the unit vector in the magnetic field direction and $\mathbf{u}_{\alpha,\perp}$ is given by equation 4.11. When valid, as expected for tokamaks, the first order flows lie on a magnetic surface, as $\mathbf{u}_{\alpha,\perp}$ is perpendicular to the radial direction $\nabla\psi$ since both ∇p_α and $\mathbf{E} = -\nabla\phi_{el}$ are parallel to $\nabla\psi$.

Another common decomposition of the velocity is in the toroidal and poloidal directions:

$$\mathbf{u}_\alpha = u_{\alpha,\phi}\, \mathbf{e}_\phi + u_{\alpha,\theta}\, \mathbf{e}_\theta \tag{4.14}$$

where $\mathbf{e}_\phi = 1/R\, \nabla\phi$ is the unit vector in the toroidal direction, and $\mathbf{e}_\theta$ is the unit vector in the direction $\nabla\phi \times \nabla\psi$ that corresponds to the geometrical angle θ direction only for circular concentric flux surfaces. In case of a straight field coordinate system, where θ is not the geometrical angle, $u_{\alpha,\theta} = \mathbf{u}_\alpha \cdot \nabla\theta/|\nabla\theta|$.
The velocities $u_{\alpha,\phi}$ and $u_{\alpha,\theta}$ lie on a magnetic flux surface and define plasma rotation (alternatively $u_{\alpha,\|}$ and $\mathbf{u}_{\alpha,\perp}$ can be used).

The radial component $u_{\alpha,\rho} = \mathbf{u}_\alpha \cdot \nabla\psi/|\nabla\psi|$ is neglected in the first order flows, but represents the radial particle flux Γ_ρ

$$\Gamma_\rho = m_\alpha n_\alpha u_{\alpha,\rho} \tag{4.15}$$

It is important to note that, although $u_{\alpha,\parallel}$ and $u_{\alpha,\phi}$ are similar in magnitude due to the relation $B_\phi \gg B_\theta$, and often confused, their theoretical distinction is fundamental in the calculation of momentum transport that determines the rotation profiles [124]. In particular, the parallel dynamics sets the value of poloidal rotation on the ion collisional timescales, while the toroidal dynamics generates the radial fluxes that determines the rotation evolution on the transport timescales ($\tau_{tr} \simeq 10 - 100$ ms).

The rotational flow is usually assumed incompressible [17, 126], i.e. $\nabla \cdot (n_\alpha \mathbf{u}_\alpha) = 0$, the additional assumption of constant impurity density on a flux surface leads to the following general expressions [69] (dropping the subscript α for clarity):

$$\mathbf{u} = \hat{\omega}(\rho)\, R\, \mathbf{e}_\phi + \hat{u}(\rho)\, \mathbf{B} \tag{4.16}$$

$$u_\phi = \hat{\omega}(\rho)\, R + \hat{u}(\rho)\, B_\phi \tag{4.17}$$

$$u_\theta = \hat{u}(\rho)\, B_\theta \tag{4.18}$$

where the functions $\hat{\omega}$ and $\hat{u}$ are explicitly constant on a flux surface (depending on ρ alone). The term $\hat{\omega}$ describes a rigid toroidal rotation, that can be visualised as a spinning doughnut, so that the toroidal rotation u_ϕ is composed by a rigid rotation plus a correction related to the poloidal velocity and the toroidal magnetic field. When the poloidal velocity is negligible, e.g. in presence of strong external injection of toroidal momentum from NBIs, the rigid rotation description is expected to hold. This is however not the case for TCV intrinsic rotation, where the poloidal intrinsic rotation contribution is not, in general, negligible.

Equations 4.17 and 4.18 imply that neither the toroidal nor poloidal velocities are exact flux surface quantities, and neither are the angular velocities $\omega_\phi = u_\phi/R$ and $\omega_\theta = u_\theta/r$. The flux surface quantities $\hat{\omega}$ and $\hat{u}$ can be calculated either by measuring u_ϕ and u_θ at the same position or by measuring just u_ϕ at different positions on the same flux surface. The latter measurement provides an indirect measurement of the poloidal velocity that was tested in TCV [69] that found qualitative agreement with neoclassical prediction. The method relies on the inboard-outboard rotation measurement capabilities of TCV, by defining $u_{\phi,H}$ and $u_{\phi,L}$ the toroidal velocities measured at the HFS and LFS on the same flux surface, at radial positions R_H and R_L respectively, the functions $\hat{\omega}$ and $\hat{u}$ are given by:

$$\hat{\omega}(\rho) = \frac{u_{\phi,H}\, R_H - u_{\phi,L}\, R_L}{R_H^2 - R_L^2} \tag{4.19}$$

$$\hat{u}(\rho) = \frac{1}{F}\left(\frac{u_{\phi,H}}{R_H} - \frac{u_{\phi,L}}{R_L}\right)\left(\frac{1}{R_H^2} - \frac{1}{R_L^2}\right)^{-1} \tag{4.20}$$

where $F = RB_\phi$ is a constant on a flux surface; and hence applying equations 4.17 and 4.18 both the poloidal and toroidal rotation are calculated on a 2D poloidal cross section. The advantage of this method is that the uncertainty in the calculated poloidal velocity is reduced

from the uncertainty of the directly measured toroidal rotation by a factor $4q$, as given by the approximated relation for $u_{\theta,L}$, the poloidal velocity on the LFS [69]:

$$u_{\theta,L} \simeq \frac{1}{4q} \left(1 + \epsilon\right) \left(u_{\phi,H} - u_{\phi,L}\right) \tag{4.21}$$

while simultaneously avoiding the atomic physics contributions (see section 2.1.2) of a direct poloidal measurement. However uncertainties in the magnetic reconstruction, which introduces errors in the LFS-HFS mapping, limit the precision of the method. In TCV, the complete coverage of the cross section of the toroidal systems allows for a global evaluation of the poloidal rotation across the whole section, but the spatial resolution (≤ 1 cm) is insufficient to resolving sheared flows structures, particularly at the edge, where the EDGE system provides unmatched results.

4.3 Radial electric field

Although the origin of the radial electric field E_r are not theoretically fully understood, its presence at the edge of tokamaks, particularly in H-mode, AUG [93], C-Mod [127], DIII-D [128], JET [129], JFT-2M [130], NSTX [65] and MAST [131] is well documented. Several processes are considered as sources of the electric radial field [132]: plasma heating, that expands ion orbits more than electrons' causing charge imbalance, turbulent transport that may not be ambipolar [133], imperfections in the magnetic field surfaces that allows electrons to escape and first orbit losses in fast particles generated by NBIs. A comprehensive theoretical description able to predict its magnitude is still missing. The connection of the radial electric field with plasma flow is of fundamental importance in tokamaks physics. It is indeed the strong perpendicular rotation shear generated by E_r that is thought to cause the edge transport barrier (ETB) characterising the H-mode, by suppressing turbulence [50]. It is worth underlining that any electric field, including this radial field, simultaneously influence all plasma species and thus must be the self-consistent sum of the effects on all these species.

The force balance equation 4.10 evaluated in the radial direction $\nabla \psi$ allows the determination of the radial electric field from any of the plasma species:

$$E_r = \frac{1}{n_\alpha q_\alpha} \frac{\partial p_\alpha}{\partial r} - u_{\alpha,\theta} B_\phi + u_{\alpha,\phi} B_\theta \tag{4.22}$$

On TCV, the magnetic field components B_θ and B_ϕ are provided by the magnetic reconstruction code LIUQE, and the CXRS systems provide all the remaining quantities to calculate E_r from equation 4.22.

The representation of the first order flow 4.16 allows a reshape [69] of equation 4.22 into

$$E_r = \frac{1}{n_\alpha q_\alpha} \frac{\partial p_\alpha}{\partial r} + \hat{\omega} R B_\theta \tag{4.23}$$

allowing the determination of E_r in TCV even at positions not covered by the poloidal systems, thanks to the complete coverage of the cross section of toroidal systems and equation 4.19.

For improving confinement it is important not only the absolute value of the electric field but also the rate of change of E_r across the flux surfaces, quantified by the $\mathbf{E} \times \mathbf{B}$ shearing rate [134, 135], which is defined as:

$$\omega_{\mathbf{E} \times \mathbf{B}} = \frac{r}{q} \frac{d}{dr} \left[\frac{q}{r} \frac{E_r}{B} \right] \tag{4.24}$$

High values of shearing rate are often thought related to turbulence suppression and transition to H-mode [136].

4.4 Neoclassical rotation

Classical theory describes the plasma particle, momentum and energy flow (transport) in a cylindrical plasma in a homogeneous magnetic field. In tokamaks, the magnetic field has a significant curvature and it is not constant along the particle trajectory, being stronger closer to the torus axis ($B \propto 1/R$), introducing additional effects that are not considered in classical theory, such as the trapping of particles in a magnetic mirror, field curvature (equation 1.26) and ∇B (equation 1.27) drifts. Neoclassical theory [16, 63] was developed to include the effects of the magnetic field toroidal geometry, resulting generally in enhanced transport in all channels.

The trapped particles bounce both in the toroidal and poloidal directions describing a trajectory that projected in the poloidal cross section resemble a banana on the low field side, from which the name banana orbit. The bouncing frequency ω_b is

$$\omega_b = \frac{\epsilon^{1/2} v_T}{R q} \tag{4.25}$$

The interplay between bouncing (or transit for passing particles) and collisions (de-trapping effect) determines the actual particle trajectory, dividing the neoclassical description in three regimes:

1. Pfirsch-Schlüter, or high collisionality $v^* > \epsilon^{-3/2}$;

2. plateau regime $1 < v^* < \epsilon^{-3/2}$

3. banana regime, or low collisionality $v^* < 1$.

The collisionality v^* is the parameter defining the regime, and it is given by:

$$v^* = v \epsilon^{-3/2} \frac{R q}{v_T} \tag{4.26}$$

where $\nu = \nu_{\alpha\alpha}$ is the collision frequency for a species and ν_T its thermal velocity. For the Pfirsch-Schlüter regime a fluid description of the plasma is sufficient, while a kinetic description is required for passing particles in the plateau regime and for both passing and trapped particles in the banana regime. The regime heavily influences the transport properties, and although the main ions and electrons are roughly in the same regime, due to the effective mass cancellation in ν/ν_T, impurities are often more collisional.

Neoclassical theory predicts an, often considerably, smaller radial particle and energy transport than measured in tokamaks [16, 63], for example the electron heat flux is $\simeq 100$ higher than the neoclassical prediction and, under certain conditions, also the ion heat transport is underestimated by neoclassical theory [137]. This 'enhanced' transport is referred to as anomalous transport, and although still not fully explained, it is commonly believed originating from plasma micro-instabilities, commonly known as turbulence, that are not take into account in the standard neoclassical theory. However, in the edge region of H-mode discharges turbulent transport is strongly reduced and the ion heat and particle transport, particularly for impurities [138], approach neoclassical values, even though the electron heat transport remains higher than neoclassical predictions. Neoclassical theory predicts the flux-surface averaged particle, momentum and heat fluxes. In the following we will focus on the momentum flux.

The poloidal velocity expected from neoclassical theory has been calculated with the Hirshman-Sigmar moment approach [63] in the Pfirsch-Schlüter regime [139], neglecting friction with electrons and the orbit squeezing (reduction of ion banana width due to any gradient in E_r) [140], giving the results (expressed here for the main ions i and impurity C):

$$u_{i,\theta} = \frac{1}{2}\nu_{T_i}\rho_i \left(K_1 \frac{1}{L_{T_i}}\right) \frac{B\,B_\phi}{\langle B^2 \rangle} \tag{4.27}$$

$$u_{C,\theta} = \frac{1}{2}\nu_{T_i}\rho_i \left[\left(K_1 + \frac{3K_2}{2}\right) \frac{1}{L_{T_i}} - \frac{1}{L_{p_i}} + \frac{Z_i\,T_C}{Z_C\,T_i} \frac{1}{L_{p_C}}\right] \frac{B\,B_\phi}{\langle B^2 \rangle} \tag{4.28}$$

where the length scales are given by the logarithmic derivative, i.e. $L_{T_\alpha}^{-1} = d(\ln T_\alpha)/dr$ etc., the thermal velocity is defined as $\nu_{T,\alpha} = \sqrt{2T_\alpha/m_\alpha}$ (adding the appropriate conversion factor for T_α for the unit system used) and the Larmor radius (equation 1.12) is evaluated at the thermal velocity $\nu_{T,\alpha}$. The coefficients K_1 and K_2 are defined in [139] (in cgs-Gaussian units) and depend on the inverse aspect ratio ϵ and the main ion collisionality ν_i^*. These equations imply that the poloidal velocity of impurities can substantially deviate from the main ion poloidal rotation, particularly at the edge and in presence of large density gradients, due to the strong coupling of the parallel flows (friction forces) and the weak coupling of poloidal flows due to magnetic pumping [132, 141–143]. Since the impurity rotation 4.28 depends strongly on the main ion parameters and weakly on the impurity parameters, only through ∇p_C, similar poloidal velocities are expected for trace low-Z impurities, which are expected to be in the electron diamagnetic direction. The main ions' rotation is expected close to zero, the direction

can go either with the electron or ion diamagnetic velocity, depending on v_i^* through the sign of K_1. The poloidal rotation for both main ions and impurities is proportional to B_ϕ, hence it changes sign upon B_ϕ inversion, while it is invariant to B_θ, leading to insensitivity upon I_p reversal.

The magnetic pumping mechanism is very effective in damping the poloidal velocity to neo-classical values [132]. This damping is caused by the tokamak magnetic field non uniformity; a plasma volume element rotating in the poloidal direction experiences a time varying magnetic field, stronger on the HFS and weaker on the LFS. The magnetic pumping [132] converts the rotation energy into thermal energy through ion viscosity, heating the plasma and damping the rotation on timescales of the order of ion-ion collision, $\tau_{ii} \simeq 1$ ms in TCV.

The heating mechanism can be separated into collisional and collisionless processes. The collisional process dominates when the collision time is smaller than the period of the magnetic perturbation. The magnetic moment $\mu = m_\alpha u_\perp^2 / 2B$ is a constant of motion between collisions, which implies that moving towards the HFS, where B increases, the particle perpendicular kinetic energy $m_\alpha u_\perp^2 / 2$ increases. Due to energy conservation, the parallel velocity $u_\parallel$ decreases towards the HFS. When a collision occurs at the HFS, on average, the extra perpendicular kinetic energy is redistributed, heating the plasma and reducing μ. When the particle reaches the LFS, it has, on average, a lower kinetic energy, resulting in a net reduction of u_θ.

The collisionless process, when the collision time is larger than the magnetic perturbation period, is also termed transit-time magnetic pumping and involves the trapped particles. Since trapped particles do not complete a full poloidal turn, they do not contribute directly to the poloidal momentum, but their interplay with the periodic magnetic field produces an effect which is akin to Landau damping [132], reducing the poloidal flow across the whole plasma volume.

Analogous equations to 4.27 and 4.28 are found for the toroidal velocity with the assumption $E_\parallel = 0$, with a structure depending on the impurity-main ions density ratio. The toroidal velocity in the banana-plateau regime, with $n_C Z_C^2 \geq n_i Z_i^2$, can be estimated as [139]

$$u_{i,\phi} \quad = \quad \frac{E_r}{B_\theta} - \frac{1}{2} v_{T_i} \rho_{i,\theta} \left(\frac{K_{n_i}}{L_{n_i}} + \frac{K_{T_i}}{L_{T_i}} \right) \tag{4.29}$$

$$u_{C,\phi} \quad = \quad \frac{E_r}{B_\theta} \tag{4.30}$$

where the coefficients K_{n_i} and K_{T_i} are functions of ϵ and v_i^*, and the poloidal Larmor radius $\rho_{i,\theta}$ is calculated from equation 1.12 with the thermal velocity v_{T_i} and the poloidal magnetic field B_θ. In the case $n_C Z_C^2 < n_i Z_i^2$ the difference of impurity and ion toroidal velocity becomes:

$$\Delta u_\phi = u_{C,\phi} - u_{i,\phi} = \frac{3}{4} K_2 \frac{v_{T_i} \, \rho_{i,\theta}}{L_{T_i}}$$ (4.31)

which can become significant at low current ($\Delta u_\phi \propto B_\theta^{-1}$) and high T_i. The toroidal rotation changes sign with B_θ due to the explicit dependence of equations 4.29 and 4.30, while it is insensitive to the sign of B_ϕ. The radial electric field E_r of equations 4.29 and 4.30 is not predicted by the model, hence, to solve the system of equations, experimental rotation profiles are needed. Typically the toroidal impurity rotation is measured [144], allowing the estimation of the main ion flow, the impurity poloidal rotation and E_r.

4.5 Momentum transport

The objective of transport theory is to describe the space-time evolution of the density, temperature and rotation of all species by identifying their fluxes and sources. Focussing on the momentum, we can recast the momentum balance as a continuity equation of the form [17]

$$\frac{\partial m_\alpha n_\alpha \mathbf{u}_\alpha}{\partial t} + \nabla \cdot \mathbf{\Pi}_\alpha = n_\alpha q_\alpha \left(\mathbf{E} + \mathbf{u}_\alpha \times \mathbf{B} \right) + \mathbf{R}_\alpha + \mathbf{S}_\alpha$$ (4.32)

where the momentum flux $\mathbf{\Pi}_\alpha$ is formed by three terms: the isotropic pressure, the viscosity and the inertial terms.

$$\mathbf{\Pi}_\alpha = \mathbf{1} \, p_\alpha + \boldsymbol{\pi}_\alpha + m_\alpha n_\alpha \mathbf{u}_\alpha \mathbf{u}_\alpha$$ (4.33)

Equation 4.32 states that the rate of momentum change in a volume element is determined by two factors: the exchange of momentum through the volume surface due to the momentum flux and the sum of the forces (electro-magnetic forces, friction force and external forces) acting on the volume. In the neoclassical framework the momentum flux $\mathbf{\Pi}_\alpha$ is composed by terms that are proportional to the velocity (convective term) and its gradient (diffusive terms), and additional terms proportional to the gradients of the temperature and the density known as residual stress. It is termed "residual" simply because it neither fits with a convective nor diffusive term yet the plasma still reacts proving it was still out of equilibrium. The residual stress is thought responsible for the intrinsic rotation that develops in tokamaks, with experimental results often disagreeing with neoclassical predictions [145], that are unable to explain features such as the intrinsic rotation reversal observed in TCV [146], ASDEX [54] and C-Mod [147].

A more comprehensive treatment, that also includes effects due to turbulence, was performed in the framework of gyrokinetics [148]. The conservation of toroidal angular momentum takes the form:

$$\frac{\partial}{\partial t} \left\langle \sum_\alpha n_\alpha \, m_\alpha R u_\phi \right\rangle_\psi + \frac{1}{V'} \frac{\partial \left(V' \Pi \right)}{\partial \psi} = T_\phi$$ (4.34)

where $< \cdots >_\psi$ represent a flux surface average, $V' = \frac{\partial V}{\partial \psi}$ is the derivative of the volume $V(\psi)$ enclosed by the flux surface of stream function ψ, T_ϕ is the total torque applied by direct sources like NBH [149], and Π is the radial flux of toroidal angular momentum, that is, itself, composed of three terms:

$$\Pi = -\hat{\chi}_\phi \frac{\partial \omega_{\alpha,\phi}}{\partial \psi} + \hat{P}_\phi \omega_{\alpha,\phi} + \Pi_{intr} \tag{4.35}$$

The momentum diffusivity $\hat{\chi}_\phi$ has contributions from a neoclassical and a turbulence term. The momentum convection $\hat{P}_\phi$ has three components: two are ascribed to the particle transport from neoclassical effects and turbulence respectively and an additional term from the Coriolis pinch [150]. Contributions to the intrinsic momentum flux Π_{intr} arise from symmetry breaking in the second order expansion of the distribution function in the parameter $\rho^* = \rho_i/a$, which can result from: up-down plasma shape asymmetry [151–153], neoclassical flows [154], radial variation of the turbulence characteristics [155], particles turbulence acceleration and finite orbit widths.

The following heuristic equation for momentum transport [156], that mimics equation 4.34 in cylindrical coordinate, is adopted in interpreting experimental data [157]

$$\frac{\partial (n_\alpha m_\alpha u_{\alpha,\phi})}{\partial t} = \frac{1}{r} \frac{\partial}{\partial r} \left[r n_\alpha m_\alpha \Gamma_{\phi r} \right] + S_\phi \tag{4.36}$$

$$\Gamma_{\phi r} = -\chi_\phi \frac{\partial u_{\alpha,\phi}}{\partial r} + P_\phi u_{\alpha,\phi} + C_\phi v_{T,\alpha} \tag{4.37}$$

where the radial flux of toroidal momentum $\Gamma_{\phi r}$ has three terms: the product of the diffusive coefficient χ_ϕ [m^2/s] with the radial derivative of the toroidal velocity represent the diffusive term, the convective (or pinch) coefficient P_ϕ [m/s] is multiplied by the toroidal velocity $u_{\alpha,\phi}$ for the convective term and the residual term is parametrised by the coefficient C_ϕ [m/s] and the thermal velocity $v_{T,\alpha}$. The last term of equation 4.36 accounts for the local direct injected toroidal momentum [149] and the possible sinks, i.e. friction with neutrals [158], interaction with magnetic islands and field ripples [159], etc. The determination of the coefficients of equation 4.37 from experimental data allows a detailed comparison with theoretical predictions and a complete description of the profile evolution, but requires dedicated experiments of non-trivial interpretation [160–163] , so often a less complex description is used [157], assuming only diffusive momentum transport [164–166]. An effective momentum diffusion coefficient χ_ϕ^{eff} is then computed, for comparison with models, using the following equation:

$$\Gamma_{\phi r} = -\chi_\phi^{eff} \frac{\partial u_{\alpha,\phi}}{\partial r} \tag{4.38}$$

that can be solved from steady-state transport analysis after determining all the momentum sources. Typical measured χ_ϕ^{eff} in TCV are $\simeq 1$ [m^2/s], which exceed the prediction of neoclassical theory, given by $\chi_\phi^{eff,neo} = 0.14 \epsilon^2 \nu_{ii} \rho_i^2$ [167]. It was experimentally found in different

devices [168, 169] that the Prandtl number, which is the ratio of the momentum diffusion to the heat diffusion coefficient χ_i, is of the order of unity, suggesting that the main transport channel for both quantities is similar and of turbulent origin. Seen another way, the characteristic timescales and gradients of the ion temperature and rotation observations are often similar and highly correlated.

Momentum transport in the poloidal direction is based on an equation with a different structure than the equation in the toroidal direction 4.34. In the poloidal projection of the force balance equation 4.3 the effect of poloidal flow damping (magnetic pumping) must be included, as a non-negligible term of the viscous tensor [170]:

$$\langle (\nabla \cdot \boldsymbol{\pi})_\theta \rangle = \alpha \left(u_\theta - u_\theta^{neo} \right) \tag{4.39}$$

where u_θ^{neo} is the poloidal velocity predicted by neoclassical theory (equation 4.28) and α is a parameter that depends on plasma parameters, particularly on the collisionality regime [132]. The poloidal force balance equation, neglecting the inertia term and adding the friction with neutrals, becomes [170]

$$\alpha \left(u_\theta - u_\theta^{neo} \right) = - j_r B_\phi - \left(1 + q^2 \right) n_n m_n v_{CX} u_\theta \tag{4.40}$$

which does not include the radial derivative of the velocity, contrary to the toroidal momentum equation. This implies that the poloidal velocity is radially decoupled, allowing the development of strong and persistent radial gradients. This also implies that the effect of a poloidal torque on poloidal rotation is strongly localised at the position where it is applied. High spatial resolution diagnostics are therefore essential to resolve any narrow features that may even be expected to develop in the poloidal rotation.

4.6   Conclusions

This chapter summarises the most important results in theory of momentum transport and introduced concepts useful in the analysis of experimental data. The dynamics starts with the force balance equation, which implies that it is the equilibrium between rotation, pressure and radial electric field that determines the rotation profile on fast Alfven timescales. This can be used to determine the radial electric field from CXRS experimentally measured quantities as expressed by equation 4.22. The parallel force balance equation that determines the dynamics on ion collisional timescales ($\tau_{ii} \simeq$ ms), is particularly important in determining the poloidal rotation, as magnetic pumping acts on these timescales, that should damp the poloidal rotation to neoclassical values. On longer transport timescales ($\tau_{tr} \simeq 10 - 100$ ms), toroidal dynamics determines the radial fluxes and the final relaxed evolution.

Experimental evidence of anomalous transport led to the development of more sophisticated theoretical considerations than neoclassical, that include many varieties of turbulence effects [154]. The effects of large scale instabilities, like the ST MHD instability, that can result in

strong redistribution of particles, momentum and energy, are often neglected, complicating any comparison of experimental results with theoretical estimates, or predictions for reactor relevant machines.

In an experimental measurement, as provided in this work, a combination of all these factors will be required in any attempt to describe what is observed. Where possible, these theoretical considerations can be used to design experiments where one or another of the predicted terms might be expected to dominate.

5 Effects of sawteeth on rotation

5.1 Introduction

MHD activity has a strong influence on transport due to its ability to modify the magnetic field topology through magnetic reconnection, temporarily rupturing the nested flux surface configuration. Particles in the reconnection zones are not radially confined, as streaming along the field line effectively results in radial transport due a generally non null radial field component, leading to strong enhancement of transport coefficients. The flattening of electron temperature and density in magnetic islands forming on rational q surfaces during MHD activity (NTM, ST, etc.) is well documented [3]. Magnetic reconnection could, therefore, influence momentum transport, but since the rotation diagnostics' time resolution is insufficient to resolve this MHD phenomena, its effect are often accounted as simple diffusion, or completely neglected in transport models, as only time-averaged plasma parameter profiles are available.

In this chapter the effect of the MHD instability known as sawtooth (ST) [19] on the Carbon impurity profiles, particularly momentum, is addressed, with sufficient time resolution to resolve the effects of the ST from MHD-free transport. The ST is a macroscopic periodic instability first described by Von Goeler [171], which has an effect on a significant portion of the plasma core. Its effects are dominated by a periodic relaxation of the plasma core gradients, resulting in flattening of the electron density and temperature profiles. The ST cycle is divided in three phases, as shown in figure 5.1-a:

1. A ST ramp phase, where the plasma core pressure increases in time, with little MHD activity detected;

2. A precursor phase, when a helical magnetic perturbation grows, resulting in the typical oscillatory traces in n_e and T_e diagnostics (DMPX,ECE,XTOMO...);

3. A crash phase (or fast phase), in which the plasma core gradients collapse and magnetic reconnection occurs, flattening the T_e and n_e profiles, demonstrated by sudden decreases in the core emissivity.
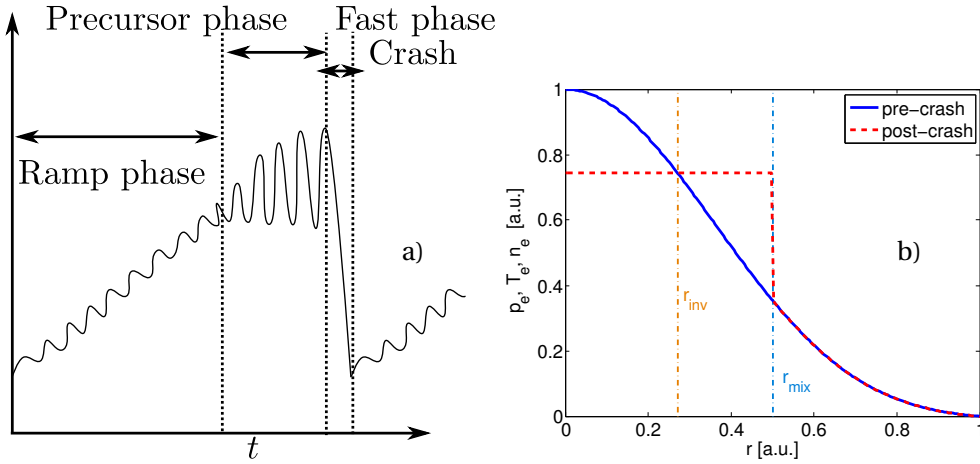
Figure 5.1: (a) typical core FIR and/or soft-X ray time trace during a ST period, defining the ramp phase, the precursor phase and the crash (fast phase). (b) sketch of a pre and post ST crash electron profile defining the inversion radius r_{inv} and the mixing radius r_{mix}.

The particles and energy expelled from the core region are redistributed in a region enclosed by the mixing radius r_{mix}, such that outside r_{mix} plasma is barely perturbed. Inside r_{mix} two regions are identified: the region expelling (on average) particles and energy and the region receiving these fluxes, separated at the inversion radius r_{inv}. Figure 5.1-b shows the positions of r_{mix} and r_{inv} deduced from a comparison of schematic electron profiles before (pre) and after (post) the ST crash. At TCV an algorithm exploiting the GTI package and the XTOMO signal is routinely used to experimentally determine r_{inv} [118] and is employed in the analysis of this chapter.

The period of a complete ST cycle τ_{ST} depends on plasma parameters and magnetic configuration [172], increasing with the machine size [19]: $\tau_{ST} \simeq 20$ ms in TEXTOR ($R_0 = 1.75$ m), $\tau_{ST} \simeq 100$ ms in JET ($R_0 \simeq 3$ m). In TCV the natural ST period in ohmic discharges is of few ms, which is comparable to the minimal CXRS integration time, making natural ST resolved measurements presently unattainable. The ST period can be considerably extended depositing ECRH and/or ECCD close to the $q = 1$ flux surface [173, 174]. This was exploited in TCV for ST pacing [173], i.e. extending the ST period to a predetermined value, and locking [175], i.e. to lock the ST period to the ECRH modulation period, effectively fixing the ST timing before the experiment. This last technique was exploited in the experiments reported in this chapter, making possible to perform multiple CXRS measurements across the whole ST cycle with the minimal achievable diagnostic IT $\Delta t_{IT} = 2$ ms. A large portion of the ST period is constituted by the ramp phase, the precursor phase being of the order of a tenth of the ST cycle with the crash phase on Alfvenic timescales ($\tau_A \leq 100\mu$s) [176]. In TCV due to the short ST period and strength, the precursor phase is often unresolved.

The ST instability is identified as an internal resistive $m/n = 1/1$ kink mode [177] driven by a plasma pressure gradient threshold. It occurs only when the safety factor q drops below
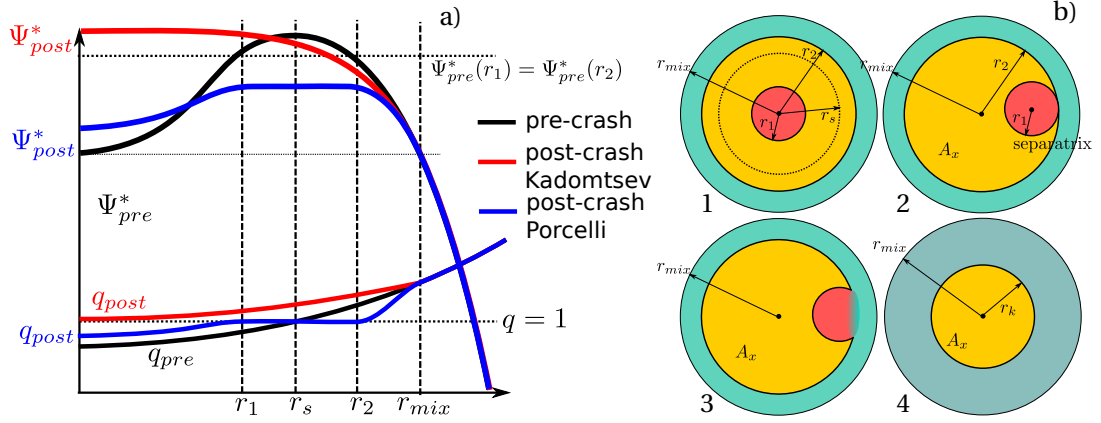
Figure 5.2: (a) pre and post crash profiles of Ψ^* and q for the Kadomtsev (red) and Porcelli (blue) models. The pre crash profiles (black) are identical for both models. (b) sketch of the magnetic surfaces reconnection in a ST crash. The kink displaces the core (1), when surfaces of identical helical flux touch (2) reconnection begins (3) resulting in the expulsion of the core plasma into the region $r_{inv} \leq r \leq r_{mix}$, preserving the area A_x.

one, i.e. when there is a resonant surface $q = 1$ located in the confined plasma region, which usually is the case when the current profile is sufficiently peaked.

The first attempt to explain the ST dynamics was performed by Kadomtsev [177], which developed a full ST reconnection model in a cylindrical geometry. The hypothesis of the model are two:

1. Magnetic surfaces with equal helical flux Ψ^* reconnect;

2. Toroidal flux Φ is conserved.

The helical flux Ψ^* is defined as

$$\Psi^*(r) = \int_0^r \left(B_\theta - \frac{r}{R} B_\phi \right) dr' \tag{5.1}$$

that in cylindrical approximation becomes

$$\Psi^*(r^2) = \int_0^{r^2} \left(\frac{1}{q} - 1 \right) dr'^2 \tag{5.2}$$

A sketch of the Ψ^* profile in the pre and post crash conditions, Ψ^*_{pre} and Ψ^*_{post} respectively, is shown in figure 5.2-a. The maximum of Ψ^*_{pre} is at the $q = 1$ surface, denoted by r_s. A generic radius inside (outside) r_s is denoted by r_1 (r_2), and clearly for each r_1 exists an r_2 satisfying $\Psi^*_{pre}(r_1) = \Psi^*_{pre}(r_2)$; that defines the surfaces that reconnects during the crash. The reconnection starts when the two surfaces touch, as result of a displacement due to the kink mode (see figure 5.2-b). The second condition of Kadomtsev's model implies the conservation

of the area A_x enclosed by the two reconnecting surfaces:

$$\pi(r_2^2 - r_1^2) = A_x = \pi r_k^2 \tag{5.3}$$

which defines r_k, the radius of the reconnected surface. The $m = 1$ magnetic island of the kink mode is assumed to grow until it fills the whole volume inside r_{mix} and the new magnetic axis is the O-point of the island, therefore the flux surface that reconnects with the magnetic axis defines the mixing radius:

$$\Psi^*_{pre}(0) = \Psi^*_{pre}(r_{mix}) \tag{5.4}$$

The resulting safety factor q_{post} profile after the full reconnection is monotonic, increasing from the axis $q_{0,post} = 1$, which is now stable to internal kink modes.

Although the Kadomtsev model describes many features of the ST instability, the predicted crash time $\tau_{kam} \simeq (\tau_\eta \tau_A)^{1/2}$, with $\tau_\eta = \mu_0 r_1^2/\eta$ the resistive time and $\tau_A = r_1(\mu_0 \rho)^{1/2}/B_\theta(1 - q_0)$ the Alfvenic time, exceeds the experimental measured crash time [176]. There is also experimental evidence of ST cycles featuring partial reconnection, with $q_{0,post} < 1$ [178]. In 1996, Porcelli proposed an incomplete relaxation model [179], in which the magnetic island is allowed to grow until it reaches a critical width w_{crit}, after which the core undergoes a Taylor relaxation process [180] while the island relaxes to a constant helical flux $\Psi^*_{post}(r_1 \leq r \leq r_2) = \Psi^*_{pre}(r_1)$ (see figure 5.2-a); here r_1 and r_2 satisfy $r_2 - r_1 = w_{crit}/2$ and r_2 acts as the effective mixing radius, which is smaller than the predicted r_{mix} from Kadomtsev's model (see figure 5.2-a). The predicted q_{post} profile is lower than unity in the relaxed core region $r < r_1$, and equal to unity in the relaxed island region $q_{post}(r_1 < r < r_2) = 1$.

Both models explain the measured effect of ST on electron density and temperature, which is well documented experimentally, but no predictions are made on impurity profile changes nor momentum transport, i.e. rotation. Recently numerical studies were carried out to quantify the effect of ST on impurity density, mostly to verify the effectiveness of ST in exhausting impurities from the core [60], but extensive studies on rotation are still missing. In the remainder of this chapter a phenomenological approach is adopted to quantify the effects of ST on Carbon, in order to significantly increase the constrains for a realistic ST model, verify the ability of ST to remove core impurities and study the momentum evolution across the ST cycle. It will be shown that the ST effect on Carbon rotation and density is strong and dominates the dynamics governing the core profiles.

5.2 Toroidal rotation in limited L-mode plasmas in presence of sawteeth

Previous studies in TCV [38, 39] showed that the averaged effect of ST activity on rotation is to bulge the velocity profile in the co-current direction. To separate the ST influence on profiles from turbulent transport a scan in plasma current was performed in [39], that is
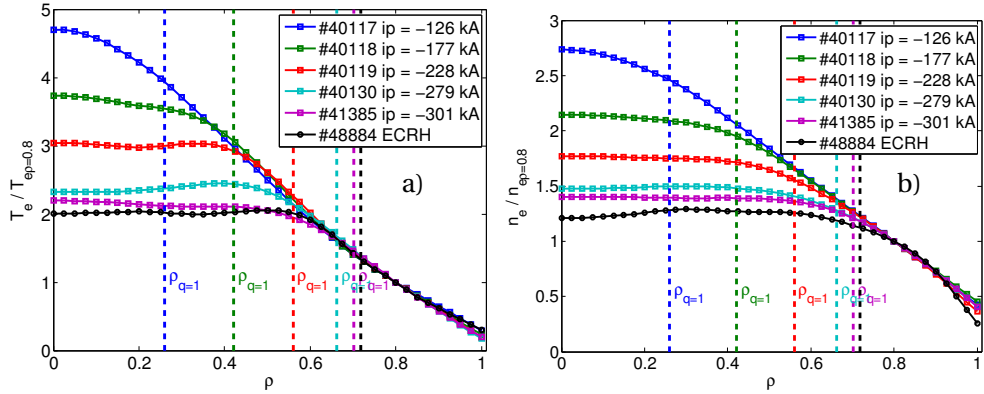
Figure 5.3: Normalised TS profiles dependence on plasma current for the TCV discharges: #40117/-126 kA, #40118/-177 kA, #40119/-228 kA, #40130/-279 kA. The position of the $q = 1$ flux surface is shown by vertical dashed lines. Profiles for the discharge #48884 with $I_p = -282$ and 450 kW of ECRH are shown in black for comparison. The electron temperature increases with I_p and flattens inside $\rho_{q=1}$. (a) the temperature normalised to $T_e(\rho = 0.8)$ is shown to emphasise the flattening effect. The effect of ECRH (black) is to further flatten the profile. (b) the electron density normalised to $n_e(\rho = 0.8)$ shows that the density is flat inside $\rho_{q=1}$. Adding ECRH has no significant effects on the density profile.

summarised in this section. A limited Ohmic scenario was developed featuring a stationary sawtoothing phase with $B_0 = -1.44$ T, $q_{edge} = 3.2 - 3.6$, $\delta_{edge} = 0.17 - 0.3$, $\kappa_{edge} = 1.4 - 1.5$ and line averaged density $n_{e,ave} = 2.2 - 2.7 \cdot 10^{19}$ m^{-3}, below the threshold for rotation reversal, i.e. in the counter-current intrinsic rotation regime. The scan consisted in the couplets shot/I_p [kA]: #40117/-126, #40118/-177, #40119/-228, #40130/-279 and #41385/-301. A discharge with $P_{ECRH} = 450$ kW of ECRH power, shot #48884 $I_p = -282$ kA, $B_0 = -1.191$ T, was also performed to rule out possible additional effects on averaged profiles introduced by auxiliary heating (see below). A lower than standard toroidal magnetic field was used to optimise the ECRH deposition close to the $q = 1$ surface, resulting in lower $n_{e,ave} = 1.1 \cdot 10^{19}$ m^{-3}.

Increasing the current results in increased T_e and n_e, but the transport mechanism appears unaltered. This is verified by considering the profiles normalised to their value at $\rho = 0.8$, that constitute the boundary condition for the core plasma. Figure 5.3 shows the normalised (a) T_e and (b) n_e profiles for the discharges of the scan. The position of the $q = 1$ surface $\rho_{q=1}$ calculated by LIUQE, shown by vertical dashed lines, is displaced outwards for increasing currents, resulting in an increased ST radius. The electron temperature and density profiles flattens inside $\rho_{q=1}$, a result expected from the ST crash. The normalised gradients remain remarkably similar in the region $\rho_{q=1} < \rho \leq 0.8$ for all the shots of the scan, supporting an invariance of the underlying transport mechanism. Adding ECRH power (#48884) does increase T_e, without substantially modifying the normalised, both T_e and n_e, electron profiles. This gives us confidence that employing ECRH does not modify the transport phenomena under study.
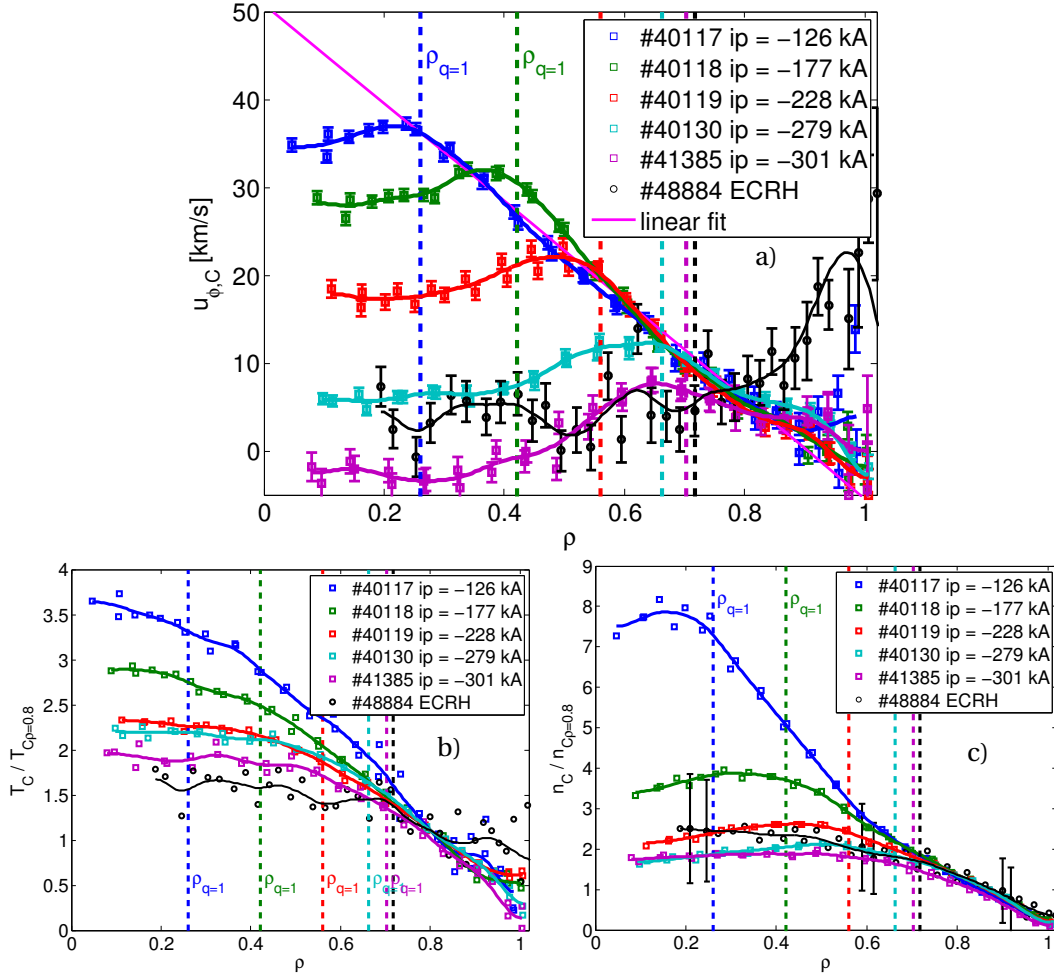
Figure 5.4: LFS CXRS profiles for a scan in plasma current, TCV discharges: #40117, #40118, #40119, #40130, #41385 and #48884 (ECRH). The position of the $q = 1$ flux surface is shown by vertical dashed lines. The (a) toroidal rotation profile for all the discharges is overlapping and has a linear dependence (magenta line) in ρ from the edge ($\rho = 0.85$) up to $\rho_{q=1}$. The rotation profile inside $\rho_{q=1}$ is hollow, bulged in the co-current direction ($u_{\phi,C} < 0$). Adding ECRH (discharge #48884) does not essentially perturbs core rotation, compared to similar current discharges #40130-#41385. The Carbon temperature increases with I_p and tends to flatten inside $\rho_{q=1}$, but to a lower degree than T_e. This results in a weak dependence on I_p of the T_C gradient between $\rho_{q=1}$ and $\rho = 0.8$, that suggests minor changes in the ions heat transport within the I_p scan. The (b) temperature normalised to $T_C(\rho = 0.8)$ is shown to emphasise the flattening effect. The effect of ECRH (black) is to further flatten the profile. The (c) Carbon density normalised to $n_C(\rho = 0.8)$ shows that the density in ohmic discharges is hollow inside $\rho_{q=1}$, the ECRH effect is to flatten the density profile.

Carbon profiles are shown in figure 5.4 for CXRS measurements with standard IT $\Delta t_{IT} = 20$ ms, with $\Delta t_{IT} \gg \tau_{ST} \simeq 2.5$ ms, which provides profiles averaged on several ST cycles. The core toroidal rotation (figure 5.4-a) is in the counter-current direction ($I_p < 0$), with a linear dependence on ρ, independent on I_p, in the region $\rho_{q=1} \leq \rho \leq 0.8$, represented by the magenta line. The current determines the position of $\rho_{q=1}$ (i.e. ST radius) and hence the rotation peak value, with little influence on the linear fit coefficient, that is set by transport which, as seen before for the electron profiles, is unaltered by I_p changes. This was concluded as responsible for the $1/I_p$ scaling reported in [64], and also implies that the residual stress, essential to generating toroidal intrinsic rotation, scales with I_p together with the momentum transport, resulting in constant rotation gradients. A flattening of the rotation profile in the region $\rho < \rho_{q=1}$, as observed for T_e and n_e, was expected if the mixing of core with edge plasma at the ST crash due to magnetic reconnection occurs. Figure 5.4-a show a more complicated dynamics, with an inversion of the rotation gradient just inside $\rho_{q=1}$ leading to a differential core rotation from the peak rotation of $\Delta u_\phi \simeq -6$ km/s, directed in the co-current direction. Applying ECRH close to the $q = 1$ flux surface, in discharge #48884, does not essentially perturb core rotation, compared to similar current discharges #40130-#41385, although it increases the measurement uncertainties by increasing background fluctuations. In [38] rotation measurements above the critical density for rotation reversal were reported. The rotation inside the ST mixing radius resulted bulged in the co-current direction also in that case, suggesting that the ST net effect is to generate a core torque in the co-current direction. The aim of ST cycle resolved CXRS measurements is to ascertain whether this torque results from modifications of the transport characteristics, i.e. a 'continuous' torque between crashes, or it is localised at the crash time and, thus, ascribable to magnetic reconnection.

The normalised Carbon temperature, figure 5.4-b, is less sensitive to ST activity than T_e. The profile slope inside $\rho_{q=1}$ changes, with less steep gradients, but profiles do not flatten completely. The gradient of the normalised temperature also has a weak dependence on I_p in the region $\rho_{q=1} < \rho < \rho = 0.8$, that suggests minor changes in the ions heat transport within the I_p scan. ECRH increases the T_C profile flatness inside $\rho_{q=1}$. In contrast, the Carbon density profile peaks in the proximity of $\rho_{q=1}$ resulting in hollow core density. This implies a stronger effect of ST on impurity rather than electron transport, for which only a simple flattening occurs (figure 5.3-b). The effect of ECRH on n_C is stronger compared to the other Carbon kinetic profiles ($u_{\phi,C}$ and T_C) resulting in a monotonically decreasing profile that is close to flat in the $\rho < \rho_{q=1}$ region. It will, however, be shown that Carbon ejection from the core region at the crash is substantial even with ECRH.

5.3 CXRS profiles evolution across the sawtooth period

To resolve the ST cycle with the CXRS diagnostic, which on TCV has a lower IT $\Delta t_{IT} = 2$ ms limit determined by both readout speed and photon statistics, (without reducing the spatial resolution by multiple fibres binning), one option available is to increase the ST period to $\tau_{ST} \geq 10$ ms. Multiple studies, in JET [181], MAST [182], ASDEX [183] and TEXTOR [184],

demonstrated ST stabilisation from fast ions [185] generated from NBI, with the fast rotation induced by the NBI torque masking at the same time the effect of ST on rotation, which excluded this option for our study. A solution for our goal was identified in the stabilising effect of ECRH and ECCD on ST, which has been extensively studied, mostly to control/reduce τ_{ST} (ST destabilisation) [186] in order to avoid NTM triggering [187–191] by power deposition inside the $q = 1$ surface. Conversely, by depositing ECRH power just outside the $q = 1$ surface a strong stabilisation of the ST is obtained [192]. Removing the ECRH power at a determined time after the crash, using a real time (RT) controller [38, 39], was used to control single ST periods [173] (ST pacing) becoming a valuable tool in ST related experiments. The only drawback of the procedure is that the actual ST crash time is not known, effectively preventing synchronisation with the CXRS system, that is programmed before the plasma discharge. Furthermore, with each ST period slightly different, dividing a ST cycle into regular sub-periods is not possible. A further improvement of the ST control technique termed ST locking solved this last issue.

5.3.1   Locking technique and target discharge

ST "locking" [175] uses ECRH power modulation with a period τ_{ECRH} smaller than the maximal ST period τ_{ST-max} reachable with continuous stabilisation (continuous, optimally located, ECRH power). During the ECRH "on" phase the ST is stabilised and the core pressure builds up. The crash following the ECRH switch off time often occurs within $\delta t_{off-cr} = 0.3$ ms. With this method is possible not only to choose τ_{ST}, as in ST pacing, but to also impose the ST timing, since the ST locks to the ECRH modulation timing that is selected before the experiment. This can then be used to synchronise CXRS timing (both the DNBI and camera timing) with beneficial consequences on the coherent averaging based analysis (see section 5.3.1). Determining τ_{ST-max} experimentally first requires a discharge where the ECRH deposition location is scanned across the $q = 1$ surface, by slowly ramping either I_p or B_0 whilst monitoring the soft X-ray emission. In discharge #54474, a scan in B_0 was used to identify the optimal conditions for the ST stabilisation, with $\tau_{ST-max} \simeq 38$ ms, allowing to successfully lock the ST period to values up to $\tau_{ST} = 36$ ms in discharge #54487 (see table 5.1).

The target limited L-mode discharge #54477, shown in figure 5.5, was developed following the scenarios in [38, 39]. The low density $n_{e,ave} = 1.1 \cdot 10^{19}$ m^{-3}, high current $I_p = -288$ kA, low magnetic field $B_0 = -1.191$ T target discharge was developed for long ST periods with a large ST mixing radius ($\rho_{mix} \simeq 0.9$), to maximise the effect of ST on rotation and Carbon density transport, whilst simultaneously limiting the safety factor to $q_{edge} = 3.2$, which is relevant for ITER. The resulting $q = 1$ surface is located at $\rho_{q=1} = 0.65$. Time traces of some important plasma parameters, together with the LIUQE magnetic reconstruction, are shown in figure 5.5 for shot #54477. The elongation $\kappa_{edge} = 1.5$ and triangularity $\delta_{edge} = 0.37$ were chosen for high plasma vertical stability, long ST periods [172] and to enhance the observation geometry of the EDGE system.
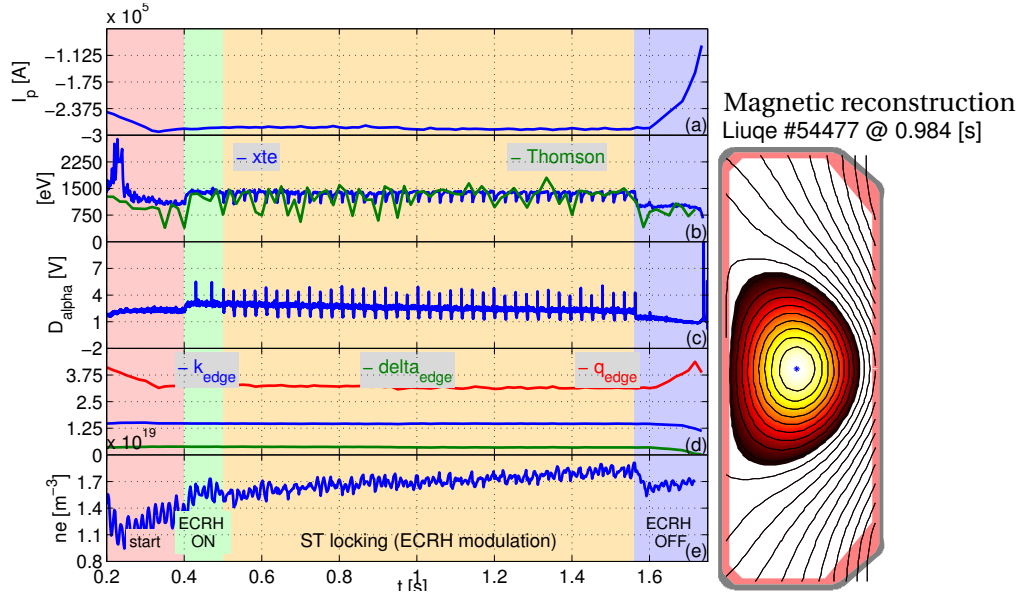
Figure 5.5: Time traces of plasma parameters of the target discharge, TCV #54477, used in the ST locking experiment: (a) plasma current, (b) electron temperature from XTE and TS, (c) D_α from PM, (d) elongation κ_{edge}, triangularity δ_{edge} and edge safety factor q_{edge}, (e) line integrated electron density from FIR. The discharge is composed of four phases: the ramp up phase ($t = 0$-0.4 s) in pink, constant ECRH ($t = 0.4$-0.5 s) in green, ECRH modulation and ST locking ($t = 0.5$-1.56 s) in yellow and ramp down in azure. The magnetic reconstruction at $t = 0.984$ s is shown on the right.

The ECRH deposition was verified with the ray-tracing TORAY-GA code [193], whose output is visualised in figure 5.6 for shot #54477. The deposition is in a layer $\Delta\rho \simeq 0.1$ at $\rho_{ECRH} = 0.66$, just outside $\rho_{q=1} = 0.65$ for both gyrotrons 4 and 6. Their maximal power is 480 kW and 560 kW respectively, for a total injected power $P_{ECRH} = 1040$ kW. The ECRH total power was lowered for some discharges (see table 5.1) to ascertain the ECRH influence on the measured plasma quantities. Both gyrotrons have a 12° toroidal launching angle, which produces a non-inductive total current $I_{CD} = -16.2$ kA, directed with the ohmic current. This ECCD, although small compared to the Ohmic current $I_p = -288$ kA, is highly localised and contributes significantly on the ST stabilisation, by replacing the missing bootstrap current in the ST island, improving the local q profile shear [186]. The ECRH deposition and ECCD profile proved to be stable and reliable over many discharges, allowing multiple parameter scans.

Table 5.1 shows the relevant parameters of some successful discharges of the mission. A scan in the ST period τ_{ST} from 20 ms to 36 ms was achieved at constant ECRH power, while for shorter periods (12 and 8 ms) lower power was required for ST locking. Shots #54480, #54481 and #54482 feature a scan in ECRH power, while #54478 and #54479 ascertain that there is no influence of the CXRS setting on the results (smearing effects, readout noise, etc.). The camera fastest configuration, 17 MHz (10 MHz for SYS1 and SYS2) HSS readout, EM register,
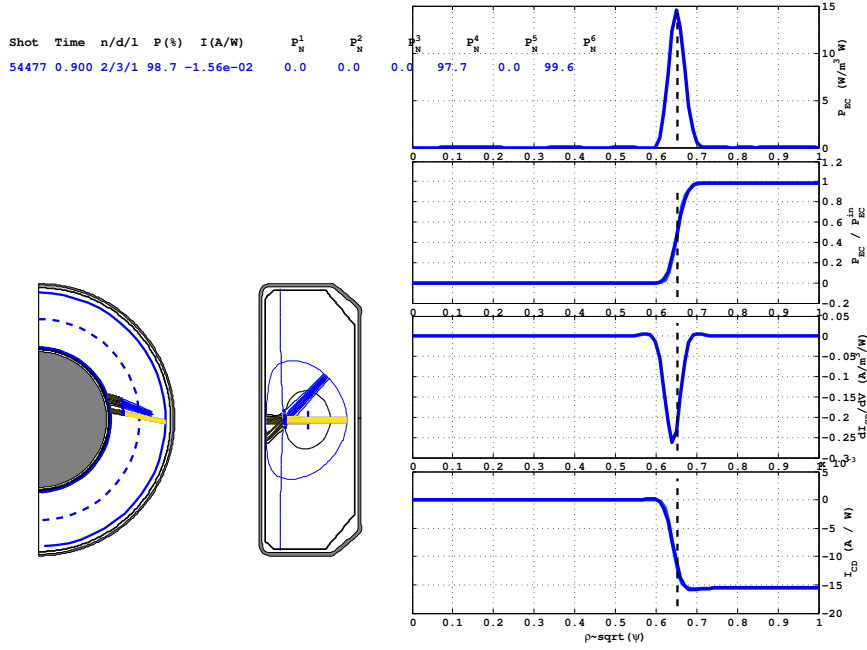
Figure 5.6: ECRH power deposition profile for TCV discharge #54477. The deposition is in a layer $\Delta\rho \simeq 0.1$ at $\rho_{ECRH} = 0.66$, just outside $\rho_{q=1}$. The 12°toroidal launching angle produces a non-inductive current $I_{CD} = -16.2$ kA, directed as the ohmic current, $I_p = -288$ kA.

was employed, with relatively high EM gain $G_{em} = 70$ to compensate for the readout noise of the EM register. Table 5.1 lists the applied ECRH on-off modulation times, which for technical reasons are different from the programmed times, with an extension of the off phase of 2 ms, corresponding to a minimum applied off phase of 3 ms. The experimentally determined τ_{ST} demonstrates the success of ST locking, that can be deduced also from the time traces of figure 5.7. The time delay δt_{cr} of the first CXRS frame after the crash is also shown. The CXRS frame time is defined by the centroid of the camera IT, so that the beginning of the frame acquisition is $\delta t_{cr} - \Delta t_{IT}/2$. For the low power discharges #54484 and #54486, this delay is reduced to $\simeq 1$ ms, meaning that the post-shot frame represent exactly the post-crash conditions, while for high power discharges there is a 1 ms additional delay. The exact CXRS frame phase in the ST cycle is paramount for data processing, as explained in the next section.

Coherent averaging

The reduction of the CXRS IT from the standard 12-20 ms to 2 ms implies a reduction of the active CXRS signal to an unacceptable level, excluding an application of the standard CXRS analysis to these experiments. An additional problem is that the computation of the active signal from the total signal requires an evaluation of the passive signal, which is expected to

shot	τ_{ST} [ms]	ECRH on-off [ms]	ECRH power [kW]	CXRS Δt_{IT} [ms]	CXRS δt_{cr} [ms]
54477	28	24-4	1040	2	2.26
54478	28	24-4	1040	4	3.24
54479	20	16-4	1040	4	2.98
54480	20	16-4	1040	2	1.96
54481	20	16-4	936 (90%)	2	2.01
54482	20	16-4	832 (80%)	2	2.13
54483	32	28-4	1040	2	1.99
54484	12	9-3	728 (70%)	2	1.06
54486	8	5-3	728 (70%)	2	1.04
54487	36	32-4	1040	2	1.94

Table 5.1: Parameters of the ST experiment discharges: ST period obtained with the locking technique τ_{ST}, applied ECRH ON-OFF time modulation and power, CXRS diagnostic integration time and time delay δt_{cr} of the centroid of the first CXRS camera frame time from the ST crash, averaged across all the ST of the discharge.

vary on smaller timescales than the DNBI minimum modulation, invalidating the assumption adopted by the standard CXRS analysis (section 2.2.4). To overcome these limitations the analysis procedure exploited the periodicity of the ST instability, by using a coherent averaging (CA) approach.

CXRS frames are grouped in sets depending on their phase within the ST cycle, i.e. on the time since the preceding ST crash. Frames in the DNBI ON and OFF phases are sorted into sets, which are used to compute an averaged total and passive signal for each ST phase. The averaged active signal is then computed, on which the standard CXRS analysis can be applied. It is paramount to sample each ST at exactly the same phase, i.e. CXRS frames within each ST cycle with always the same delay from the previous crash, for an optimal CA implementation and to obtain as many comparable observation cycles as possible. This was achieved by exploiting the ST locking technique, that allowed for a programmed synchronisation of the ST cycle (ECRH modulation) with the CXRS acquisition time. In previous approaches [38, 39], synchronisation was achieved by RT triggering the CXRS cameras using a ST crash detection observer, but this procedure restricted measurements to only the early ST phases and generated irregular ST periods that were not optimal for CA. The new procedure achieved impressive improvements in synchronisation and ST cycle coverage. The ST resolved measurements in those attempts were also restricted to the LFS system, giving an incomplete picture of the dynamics. To overcome the low photon statistics multiple LOS binning was performed, resulting in a spatial resolution unable to resolve the features reported here.

Figure 5.7-a shows the (normalised) time traces of two plasma diagnostics used in the ST phase recognition (D_α and DMPX), together with the pre-programmed ECRH modulation, the DNBI modulation and the CXRS signal level. The identified ST crash times, highlighted by
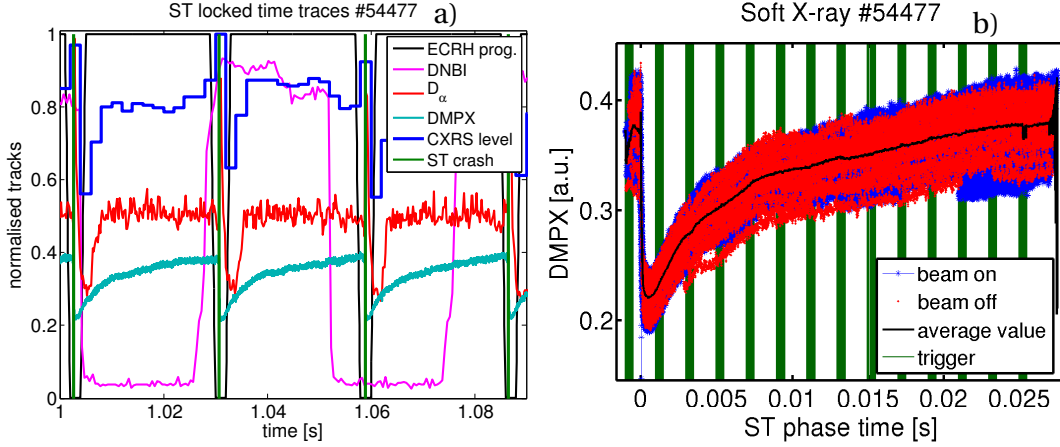
Figure 5.7: Time traces showing locked ST in shot #54477. (a) normalised time traces of the programmed ECRH and plasma diagnostics, showing the regularity of ST events obtained with the locking technique, the green vertical lines represent the crash times. The CXRS counts increase in the DNBI ON phase constitutes the active CXRS signal. (b) DMPX time trace rescaled on the CXRS triggering times, represented by the vertical green lines. The DMPX signal during the DNBI ON (OFF) phase is in blue (red), showing the similarity of ST cycles used in the active and passive CXRS frames for the coherent averaging.

vertical green lines, are locked to the ECRH modulation, with the condition

$$\tau_{ECRH} = n_s \Delta t_{IT} \tag{5.5}$$

ensuring synchronisation of the ST cycle with the CXRS acquisition. Here n_s is the (integer) number of CXRS frames (samples) per ST period. The synchronisation is verified in figure 5.7-b by plotting the DMPX signal as function of the ST cycle time together with the CXRS triggering times (vertical green lines). An entire ST cycle is sampled with $n_s = 14$ CXRS frames, and the time delay of each of the n_s frames from the ST crash ($t = 0$) is invariant for all the ST crashes. As an additional check, DMPX signals during different DNBI phases are plotted with different colours (ON-blue, OFF-red), to highlight possible biases. From figure 5.7-b we deduce that the ST used in the CA are indeed similar and that the deviations of each ST cycle from the averaged ST are expected to be negligible (which for these experiments means $\leq 20\%$).

The analysis therefore focussed on the properties of an averaged, or canonical, ST rather than each individual event. An example of the total (DNBI ON) and passive (DNBI OFF) canonical CXRS spectra, resulting from the coherent averaging applied to discharge #54477, is shown in figure 5.8-a for a core ROI (track #1) of SYS1 in the post-crash phase, together with the active signal computed by their difference. The near perfect subtraction of the background and nearby passive lines gives high confidence on the adequacy of the CA method. A comparison between the active CXRS spectra in the pre and post ST crash phases is shown in figure 5.8, again for track #1 of SYS1 in shot #54477. A wavelength shift of few pixels is noticeable, indicating, just by eye, clear changes in toroidal rotation velocity across the crash. In the next
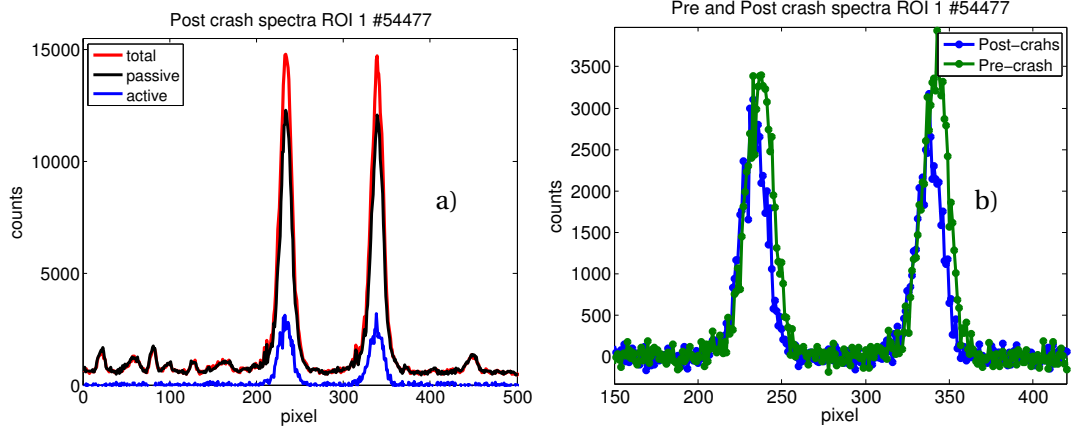
Figure 5.8: CXRS spectra resulting from the coherent averaging in discharge #54477 for a core ROI of SYS1. (a) total, passive and active spectra of the post-crash frame, (b) comparison of the active spectra of the pre and post crash CXRS frames. The effective integration time is $\Delta t_{IT} = 36$ ms, considering the sum of the 2 ms integration time for all the 18 coherent active measurements.

sections the outcome of the CXRS analysis will be described.

5.3.2 EDGE profiles: stable boundary conditions

This section treats the evolution of the Carbon impurity profiles ($u_{\theta,C}$, T_C and n_C) across a canonical ST, which resulted from the CA analysis of CXRS data of the EDGE system, and constitutes the EDGE-SOL boundary conditions for Carbon in the considered discharges. From our understanding of the ST dynamics, no relevant perturbations are expected in the EDGE profiles across the ST cycle, since the plasma portion observed by the EDGE system is well outside the mixing radius, that from TS n_e profiles is estimated as $\rho_{mix} \simeq 0.9$.
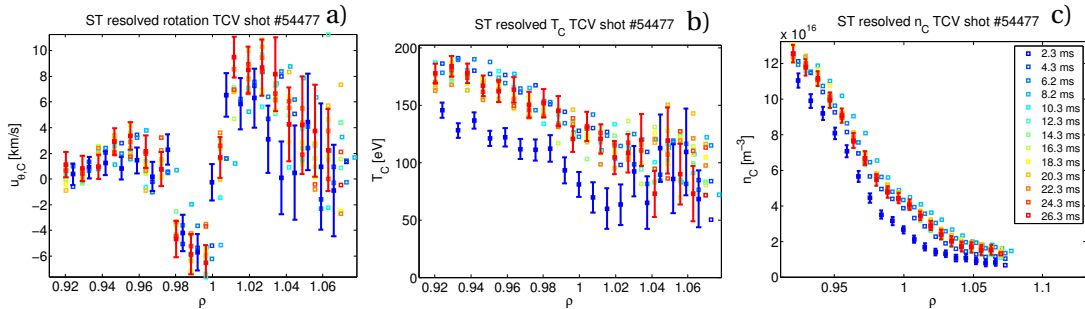
Figure 5.9: Raw profiles of EDGE systems: (a) $u_{\theta,C}$, (b) T_C and (c) n_C for shot #54477. Colours are used to distinguish the phase of the profile from the ST crash. Selected errorbars for few radial points and phases are shown for clarity. The poloidal rotation is almost insensitive to the crash, while the temperature and density in the post-crash phase are noticeably lower than in the pre-crash phase.

Figure 5.9 shows the raw profiles for shot #54477. The poloidal velocity profile features a 'well' (i.e. differential velocity Δu_θ) in the electron diamagnetic direction just inside the LCFS of amplitude $\Delta u_\theta \leq -12$ km/s, well resolved with the experimental uncertainty ($\simeq 1$ km/s), which is represented by errorbars, plotted only for the pre (red) and post (blue) crash profiles for clarity. Colours are used to distinguish the time delay (phase) of the profile from the ST crash. In shot #54477 there are $n_s = 14$ CXRS frames per ST cycle, but only 13 phases are shown in figure 5.9 since the frame containing the crash is excluded, being a mixed condition between the pre and post crash phases. In the discharges of this mission the maximum radial position for reliable EDGE measurements is identified as $\rho_{max-EDGE} = 1.025$, deduced by the increase in uncertainties for $\rho > \rho_{max-EDGE}$, the rise in T_C and flattening of the n_C profiles in the SOL (see appendix E).

There is a clear change in the Carbon temperature and density profile following the crash, shown in figure 5.10 for shot #54487, where a spline fit of the raw profiles is plotted. The
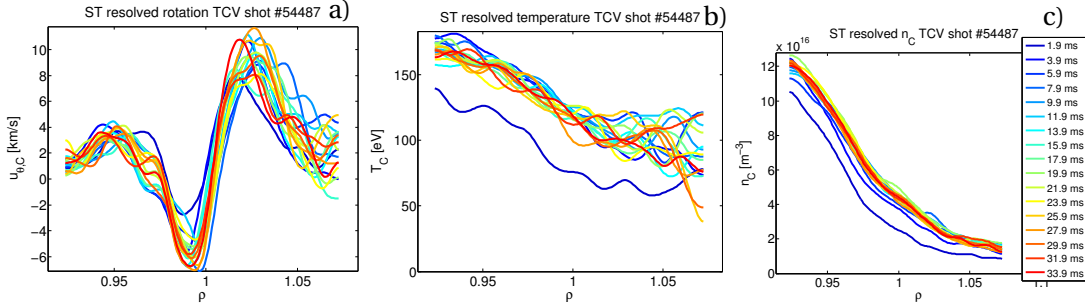
Figure 5.10: Profiles of EDGE systems: (a) $u_{\theta,C}$, (b) T_C and (c) n_C for shot #54487. The post-crash poloidal rotation is damped, but retains the same shape than the pre-crash profile. The temperature and density behaves as in #54477 (figure 5.9).

decrease in both the Carbon temperature and density profiles after the crash cannot be explained by inaccuracies in the magnetic reconstruction, since a translation of the ρ variable of $\delta\rho \simeq [0, 0.04, 0.02]$ for $u_{\theta,C}$, T_C and n_C profiles respectively are required to match the pre-crash conditions.

The decrease in the T_C and n_C profiles is common for all the discharges featuring an ECRH off time of 4 ms (see table 5.1). Discharges #54484 and #54486, featuring an ECRH off time of 3 ms and lower ECRH power (70% of the full power), are barely perturbed by the crash. This is in agreement with the energy confinement time computed from the diamagnetic loop, which is $\tau_{E-full} \leq 3.2$ ms for the full ECRH power and $\tau_{E-70} \simeq 3.8$ at 70% of the power. In shots #54484 and #54486 the ECRH off time is shorter than the energy confinement time, reducing considerably changes to these near edge plasma parameters. Figure 5.11 shows the profiles for shot #54484, the lower ECRH power resulting in lower relaxed temperatures and densities, although the profile shapes are nearly invariant that can be seen by comparing with figure 5.10.

A more complete understanding of the dynamics is possible comparing the time evolutions
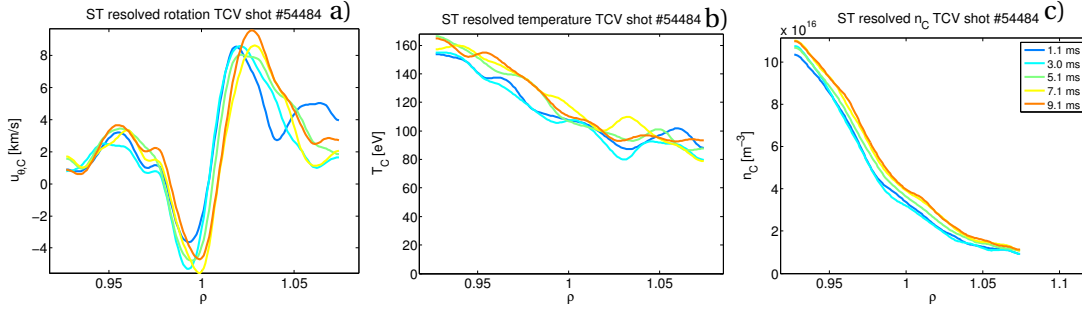
Figure 5.11: Profiles of EDGE systems: (a) $u_{\theta,C}$, (b) T_C and (c) n_C for shot #54484. The profiles perturbation due to the crash is within the experimental uncertainty. The reduced profiles perturbation is ascribed to the reduced $\Delta T_{ECRH-off}$.

of the measured quantities as function of the ST cycle phase for all the shots in the τ_{ST} scan. Figure 5.12-a shows the evolution of the differential velocity Δu_θ: the difference between the minimum rotation in the well and the maximum rotation in the region $0.95 \leq \rho \leq 0.99$. The
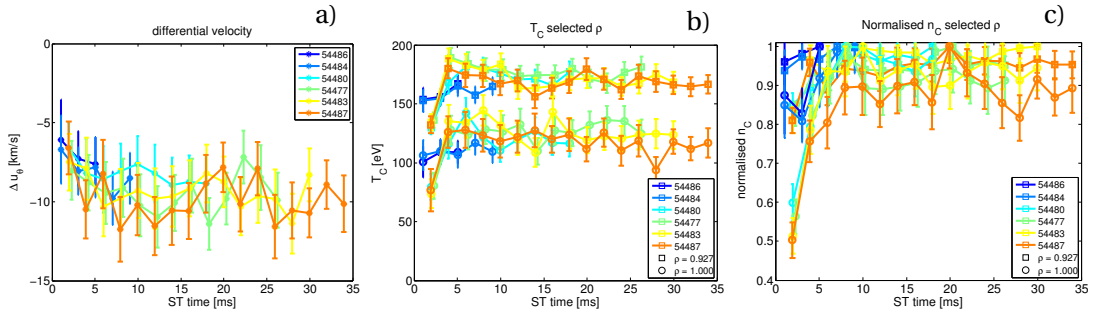
Figure 5.12: Time evolution of (a) differential poloidal velocity Δu_θ, (b) T_C and (c) normalised n_C for selected positions. The differential poloidal velocity evolution is consistent in all the shots, with a relaxation time $\tau_{rel-\Delta u_\theta} < 8$ ms. The temperature and density perturbations in the post-crash frame are considerably smaller in shots #54484 and #54486, due to the reduced $\Delta T_{ECRH-off}$. The relaxation times are $\tau_{rel-T} < 4$ ms and $\tau_{rel-n} < 8$ ms respectively.

evolution is remarkably similar for all the discharges, that encompasses shots with different ECRH parameters #54484 and #54486. The differential velocity relaxes to a saturated value $\Delta u_\theta \simeq -12$ km/s within $\tau_{rel-\Delta u_\theta} \leq 8$ ms, following the post-crash condition $\Delta u_\theta \leq -5$ km/s. The trend is followed even for shot #54486 that does not reach the relaxed rotation state in its shorter ST period $\tau_{ST} \leq \tau_{rel-\Delta u_\theta}$. This suggests a common mechanism for poloidal rotation evolution independent of the ECRH power level and τ_{ST}.

The perturbations on the temperature, figure 5.12-b, are relevant for the 4 ms ECRH off shots, where drops of $20 - 50\%$ are observed at positions $\rho = 0.927$ and $\rho = 1$ respectively. The temperature relaxation time is faster than for the velocity, and is estimated to be $\tau_{rel-T-edge} < 4$ ms. This allows us to decouple the poloidal rotation dynamics from the temperature evolution, that is more strongly influenced by the ECRH modulation and power.

The density perturbation, figure 5.12-c, resembles the temperature, with decreases of $20-50\%$ at the same positions as T_C. The time evolution resembles the velocity evolution, with a relaxation time $\tau_{rel-n-edge} < 8$ ms. This is expected as the rotation dynamics at the edge is coupled with the density gradient (see section 4.4).

We can conclude that the EDGE boundary conditions for Carbon are remarkably resilient, with saturated values and relaxation times independent of τ_{ST}. Perturbations of the profiles following the crash are observed, with drops in Δu_θ, T_C and n_C, but the profiles shapes are preserved and all relax within 8 ms. Relaxed profiles from different shots are similar, and only the low power shots are distinguishable by their lower relaxed temperature and density.

5.3.3 Toroidal profiles

This section focusses on the ST resolved profiles obtained from the toroidal CXRS systems, HFS and LFS. The two systems cover the complete cross section of TCV, allowing for an accurate measurement of the entire profile and to investigate possible asymmetries, particularly for the lower plasma densities where the beam attenuation is smaller.
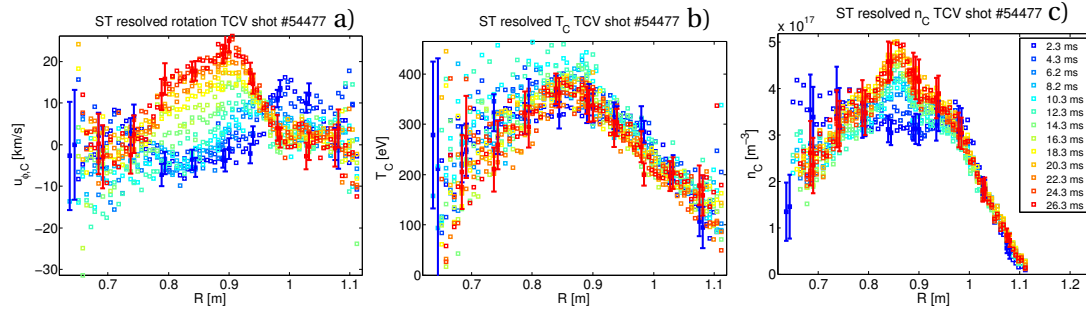
Figure 5.13: Raw profiles of toroidal systems: (a) $u_{\phi,C}$, (b) T_C and (c) n_C for shot #54477. Selected errorbars at few radial points and phases are shown for clarity. $u_{\phi,C} > 0$ is counter-current.

The raw profiles are shown in figure 5.13 for shot #54477, with errorbars representing the evaluated standard deviations. The perturbation in the profiles due to the crash is clearly resolved by the diagnostic, with an evident redistribution, particularly in the toroidal rotation and density channels.

Perhaps the easiest way of understanding the effect of ST on toroidal rotation is to consider the pre and post crash profiles as function of τ_{ST}, as shown in figure 5.14. The pre-crash rotation strongly depends on τ_{ST}. For $\tau_{ST} < 20$ ms, hollow profiles are observed, with an asymmetric counter-current velocity peak, $\simeq 6$ km/s higher at the LFS. The pre-crash profile evolves with τ_{ST} towards an asymmetric counter-current peaked profile, steeper on the LFS (also in the radial variable ρ). The peak is located on the LFS and migrates towards the magnetic axis as function of τ_{ST}; its value increases linearly with τ_{ST}, reaching a maximum value of $u_{\phi,C} \simeq 30$ km/s at $\tau_{ST} = 36$ ms. This is not believed to be a limiting value, as relaxed core rotation $\simeq 50$

km/s are expected for a ST-free scenario (see figure 5.4-a), but further extending the ST period at the time of the experiment was technically not possible, due to the τ_{ST-max} limit, and was not attempted.

In contrast, the post-crash profiles (figure 5.14-b) are remarkably similar for all the shots in the τ_{ST} scan. They are strongly hollow, with the core plasma rotating in the co-current direction and the edge rotation peaking in the counter-current direction, resulting in a rotation difference $\Delta u_{\phi} \simeq -20$ km/s. The only relationship between these profiles and τ_{ST} seems to be a 'rigid' translation of the profile towards more counter-current velocities with longer τ_{ST}. The co-current core acceleration occurring at the crash, assuming the main ions rotate at the same velocity as Carbon, cannot be explained by plasma mixing with an associated enhanced transport, as can be deduced from the pre-crash rotation in the case $\tau_{ST} = 36$ ms, which is positive (counter-current) across the entire TCV section. The negative (co-current) velocity in the post-crash frame requires some co-current torque applied to the core plasma across the crash. In contrast, the velocity peaking at the $q = 1$ surface appears strongly related to momentum conservation (see below). Following Kadomtsev's model, momentum is expelled outside ρ_{inv}, where a sudden change in the velocity gradient is indeed observed.

A comparison of the rotation evolution in the canonical ST cycle, for five selected positions, is shown in figure 5.15-b for all the τ_{ST} in the scan. Figure 5.15-a shows the evolution of the complete profile for shot #54477, for reference. The rotation evolves alike at each position for all the shots, depending only on the time elapsed since the crash, up to the rotation value change that is reset by the ST crash and thus determined by the ST period. This is also inferable comparing, for the same elapsed time, a profile of figure 5.15-a with a pre-crash profile (figure 5.14-a). The shape for profiles at the same elapsed time are identical, supporting the conclusion that the transport mechanism remains unchanged.
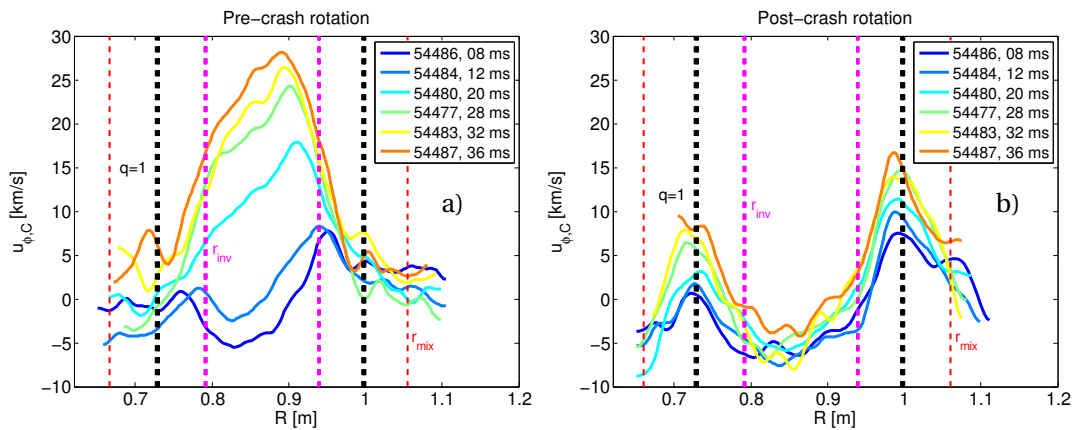
Figure 5.14: Pre and post crash toroidal rotation velocity profiles for multiple shots, colours distinguish the ST period τ_{ST} imposed with ECRH locking for each shot, displayed in the legend. $u_{\phi,C} > 0$ is counter-current.
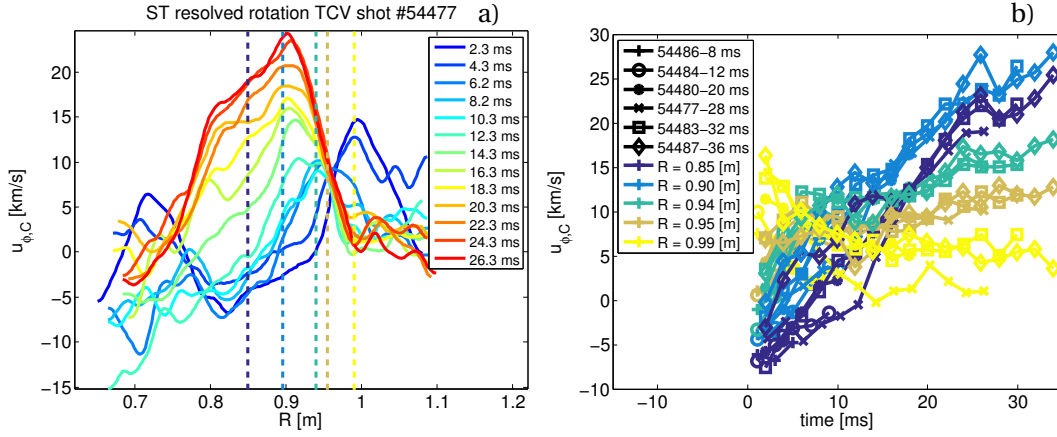
Figure 5.15: Toroidal rotation evolution across the ST cycle: (a) radial profiles for all the ST phases of shot 54477, (b) time traces at selected positions for multiple shots. The profile evolution of shot 54477 is remarkably similar to the pre-crash rotation for the scan in τ_{ST} of figure 5.14-a. $u_{\phi,C} > 0$ is counter-current.

The relaxation time for toroidal velocity is constrained to $\tau_{rel-u_\phi} > 36$ ms, as core rotation is still evolving for the maximum ST period of the scan (figure 5.15-b), although the edge rotation relaxes within 20 ms, e.g. to 5 km/s at $R = 0.99$ m.
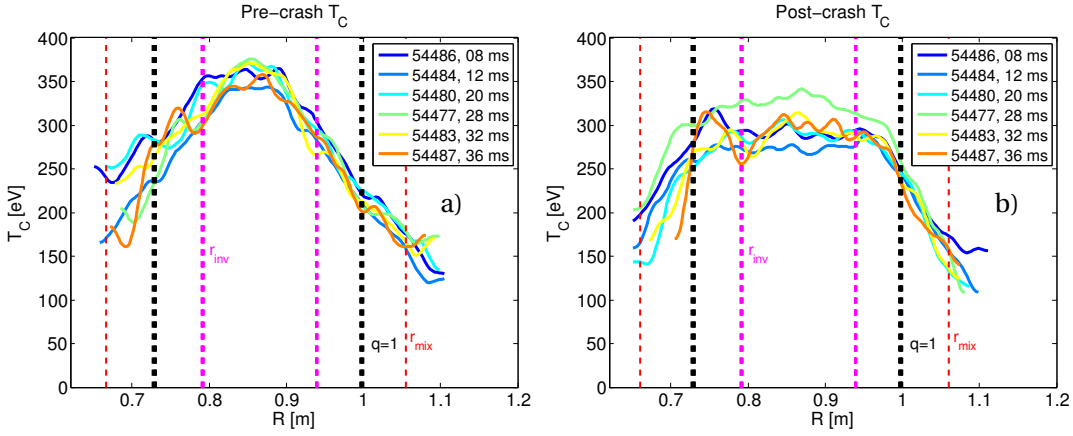
Figure 5.16: Pre and post crash Carbon temperature profiles. The temperature profiles are independent of the ST period. The pre-crash profiles are peaked at the axis. The post-crash profiles are flat in the core region up to the $q = 1$ flux surface.

The temperature profile agrees reasonably well with the model from Porcelli with $w_{crit} \simeq 0.25$ m. The peaked pre-crash profile (figure 5.16-a) is completely flattened by the crash up to $\rho_{q=1}$ (see figure 5.16-b). Kadomtsev's model predicts flattening in the region enclosed by $\rho_{mix} \simeq 0.9$, which is more extended than $\rho_{q=1} = 0.65$. This suggests a possible partial reconnection is occurring at the crash, reducing the extent of the flattening at the $q = 1$ surface. The collapse in the core ion temperature is only $\Delta T_C \simeq 50$ eV and it is rapidly recovered: $\tau_{rel-T-core} < 10$

ms, as shown in figure 5.18-a. The post-crash T_C profiles inside the $q = 1$ surface behave similarly to the electron temperature profiles, as shown in figure 5.19-a by the flatness of the post-crash profile of the ratio T_C/T_e.
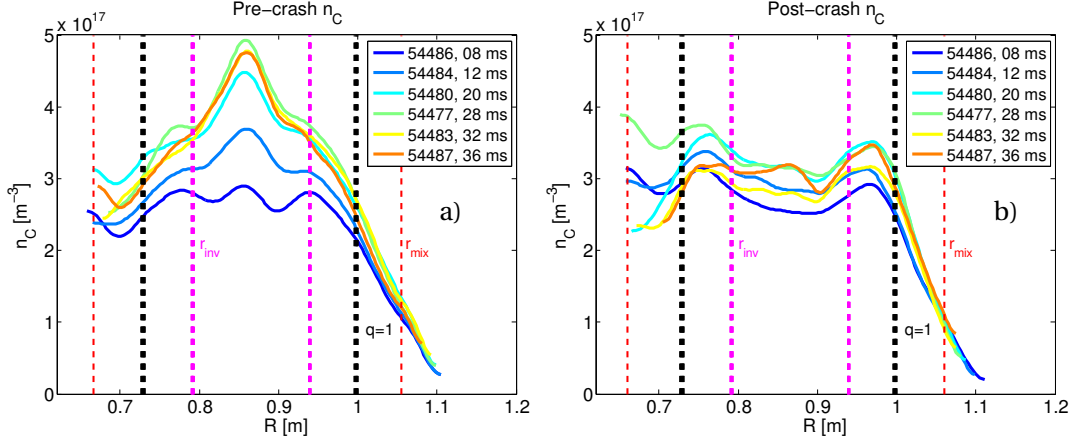
Figure 5.17: Pre and post crash Carbon density profiles. The pre-crash density profiles get more peaked on axis with the ST period, reaching a stationary profile within 25 ms. The post-crash profiles are flat in the core region up to the inversion radius r_{inv}, between r_{inv} and the $q = 1$ flux surface there is a bump in the density profile.

The effect of the crash on Carbon density is important for impurity exhaust applications. The pre-crash profiles, shown in figure 5.17-a, are strongly peaked on axis, for $\tau_{ST} > 10$ ms. The density attains a stationary profile within $\tau_{rel-n-core} < 25$ ms in the ST cycle, as shown by the time traces of figure 5.18-b and confirmed by the pre-crash profiles of ST longer than $\tau_{ST} > 25$ ms. The effect of the crash is stronger than on electron density, as shown in figure 5.19-b by the post-crash profile of the ratio n_C/n_e. The post-crash n_C profiles (figure 5.17-b) are hollow in the core region enclosed by ρ_{inv}. In the layer $\rho_{inv} < \rho < \rho_{q=1}$ a bump is observed, with
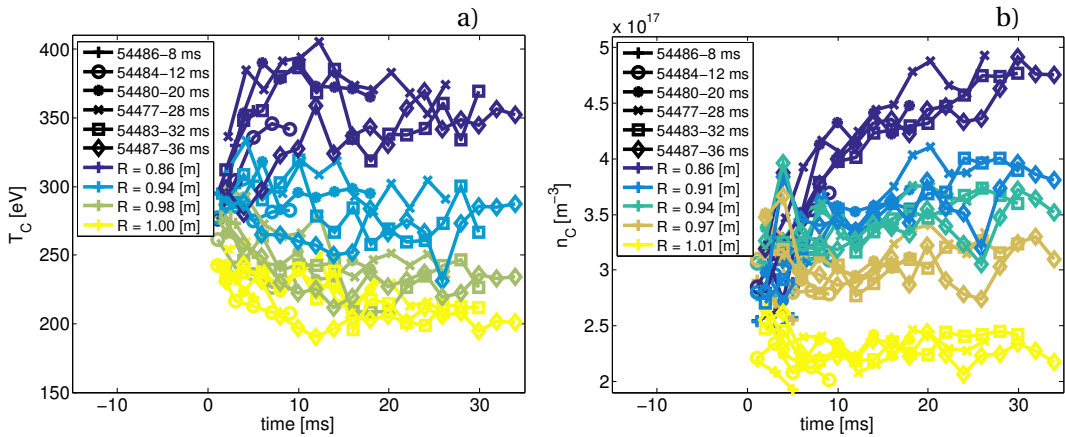
Figure 5.18: Time traces at selected positions of (a) T_C and (b) n_C across the ST cycle for all the discharges of the τ_{ST} scan.
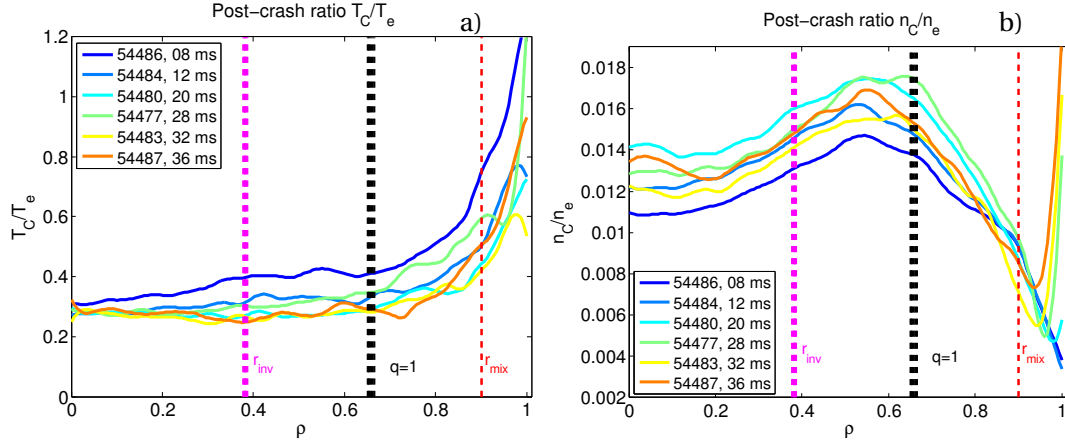
Figure 5.19: Post-crash profiles of the ratios (a) T_C/T_e and (b) n_C/n_e for all the discharges of the τ_{ST} scan.

densities 20% higher than in the core region. This high density ring feature rapidly dissipates by particle transport within < 5 ms, and it is consistent with prediction in [60], where the two fluid XTOR-2F code simulated the transport of an impurity ion species, modelled as a passive scalar. The overall post-crash profile is observed to be asymmetric, featuring higher density on the HFS. These observations suggest that ST with short $\tau_{ST} < 10$ ms and large ρ_{inv} are beneficial in reducing impurity core accumulation, again confirmed by comparison to the pre-crash profile of shot #54486, which presents the highest density profile for the canonical $\tau_{ST} = 8$ ms ST. This profile maximum reaches less than 60% of the relaxed peak density profile observed in longer ST shots.

5.3.4 Toroidal angular momentum and radial electric field

In absence of torques, the total toroidal angular momentum is conserved. This can be exploited to probe the presence of momentum sink or sources, particularly across the ST crash. The total plasma angular momentum L_{tot} [Js] is computed from the Carbon density and rotation through:

$$L_{tot} = \int_{Vol} (m_C\, n_C + m_D\, n_D)\, u_{\phi,C}\, R\, dVol \tag{5.6}$$

where $dVol$ is an element of the plasma volume Vol, routinely calculated by LIUQE. It is assumed here that rotation for main ions (Deuterium, of mass m_D and density n_D) and Carbon is the same across the ST period, although it is known that toroidal acceleration due to induced electric fields, as it is the case in reconnection events, is stronger for main ions than impurities [194]. The momentum carried by the electron is here neglected. The main ion density is estimated from the electron and Carbon density:

$$n_D = n_e - 6\, n_C \tag{5.7}$$

The flux surface averaged angular momentum density, i.e. the integrand of 5.6, is also a noteworthy quantity, that highlights the transport and redistribution of momentum in the radial direction. It is drawn in figure 5.20 for shots: #54484-short τ_{ST} = 12 ms, #54480-medium τ_{ST} = 20 ms and #54487-long τ_{ST} = 36 ms. The hollow profile of the angular momentum
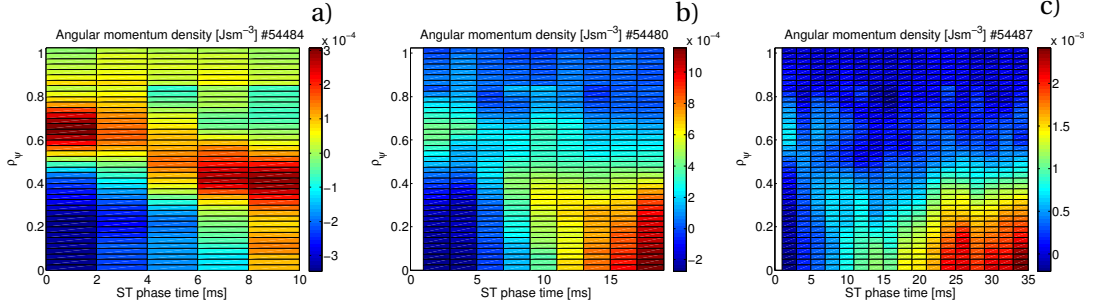
Figure 5.20: Flux surface averaged toroidal angular momentum density profiles as function of ST phase for discharges: (a) 54484, (b) 54480 and (c) 54487.

density in the post-crash phase ($t = 0$) is similar in shape for all the shots (the magnitude is however influenced by τ_{ST}), with a negative momentum change in the core and a positive change that peaks at $\rho_{q=1}$. The angular momentum density subsequent evolution clearly involves an inward pinch of the positive momentum peak, estimated at V_p = 7 [m/s]. Simultaneously, the core negative momentum is convected/diffused outwards, and with the positive momentum influx a completely positive (counter-current) momentum profile is obtained in < 8 ms. A bulged profile structure persists until the relaxation time $\tau_{mono} \geq 14$ ms, where a monotonic profile is reached. In shot 54484 τ_{ST} is shorter than τ_{mono} and the angular momentum profile can not attain a monotonic shape. At later times, the momentum peaking in the core follows the density build up, that saturates at $\tau_{rel-n-core} \leq 25$ ms, and the change in the velocity, that does not saturate within the τ_{TS} range of the scan.

Now that we have a clear picture of the radial evolution of the angular momentum, we can focus on the total angular momentum evolution. Figure 5.21 shows the evolution of L_{tot} across the ST cycle for a scan in (a) τ_{ST} and (b) P_{ECRH}. A trend in the total angular momentum is deduced from figure 5.21-a: both the pre and post-crash momentum increase with τ_{ST}. This is a consequence of the observed increase in the toroidal rotation with τ_{ST} both in the pre and post crash phases (figure 5.14).

The momentum evolution after the crash is complicated, but a general trend can be identified. An initial phase where the total momentum is further reduced is followed by a phase where L_{tot} increases, eventually surpassing the post-crash value. The duration of the two phases changes on a shot-to-shot basis and for short τ_{ST} is hard to distinguish. A possible explanation of the initial decrease in the angular momentum is ascribable to diffusion of the positive momentum bump located near $\rho_{q=1}$ following the crash. The outward diffusing momentum may then reach the plasma edge, where contact with the wall (limited configuration) and friction with neutrals act as a source/sink term, i.e. as a boundary condition $u_{\phi,C} \simeq 0$ [195]. Another explanation is provided by a differential acceleration of impurities and main ions
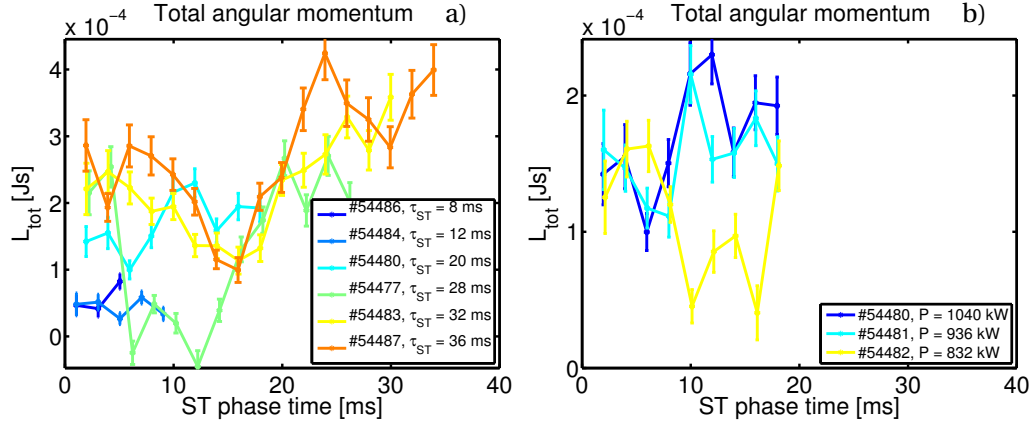
Figure 5.21: Total toroidal angular momentum as function of the ST phase in discharges where (a) the ST period and (b) the ECRH power is scanned.

at the crash. If acceleration at the crash, due to transient E_ϕ generated during reconnection is stronger for the main ions, as suggested in [194], the inter-species friction would tend to accelerate impurities in the co-current direction after the crash.

The total angular momentum just after the crash appears reduced, the braking effect being stronger for longer τ_{ST}, suggesting a co-current torque at the crash that scales with τ_{ST}. The estimated torque acting on the plasma (assuming $\tau_{crash} = 1.5 \cdot 10^{-4}$ s, as inferred from DMPX measurements) ranges from 0.24 Nm for #54486 to 0.75 Nm for #54487. For short τ_{ST} (shots #54486 and #54484), the momentum change at the crash is within uncertainties and hence compatible with total momentum conservation, which is not the case for longer τ_{ST}.

The influence of the ECRH power, shown in figure 5.21-b for #54480-100%, #54481-90% and #54482-80%, does not show a clear trend, although the pre-crash (and post-crash) L_{tot} appear consistent. This again suggests that the Carbon evolution has a weak dependence on ECRH power and is essentially set by intrinsic transport across the whole ST period.

The radial electric field was computed from the Carbon profiles, in the core (figure 5.22-a) by exploiting the combination SYS1-SYS2 and equation 4.23 and at the edge (figure 5.22-b) using SYS1-SYS4 and equation 4.22. The core E_r is negative, with peak values $\simeq -6$ kV/m. In the post-crash phase E_r is hollow, close to zero inside ρ_{inv} and peaking close to $\rho_{q=1}$. The evolutions resemble the rotation evolution, with the peak region moving towards the magnetic axis with an amplitude that decreases with time. The E_r profile outside ρ_{inv} tends to relax to a value close to zero during the ST cycle.

At the very edge, the boundary condition are best evaluated from SYS4. E_r profiles of figure 5.22-b sets the condition $|E_r| < 2$ kV/m at $\rho = 0.95$. A strong shear inside the LCFS is observed, with an E_r negative peak of $\simeq -10$ kV/m and a positive E_r in the SOL. The dominating component of E_r in the EDGE is due to the $u_{\theta,C}$ term of equation 4.22.
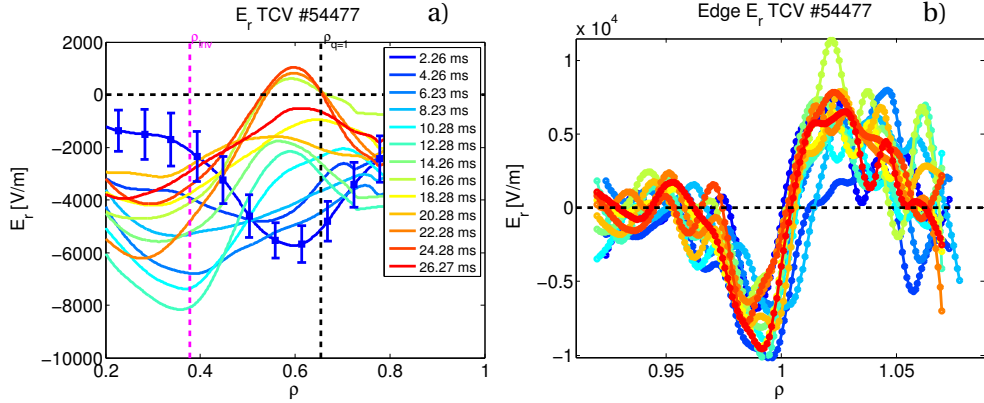
Figure 5.22: Radial electric field profile for each ST phase of TCV shot #54477 calculated from (a) SYS1-SYS2 and (b) SYS4-SYS1.

5.4 Synthetic averaged profiles

Carbon profiles averaged over the ST period are obtained from the τ_{ST} scan discharges performing the standard CXRS analysis on the sum of the active spectra. These profiles are compared in figure 5.23 with ST-unresolved measurements performed on discharge #41385, which has a plasma current $I_p = -301$ kA comparable with the current of the ST-resolved discharges. This reference discharge features natural ST of period $\tau_{ST} \simeq 3$ ms, as ECRH was not applied. The Carbon temperature and density shown for shot #41385 in figure 5.23-b and
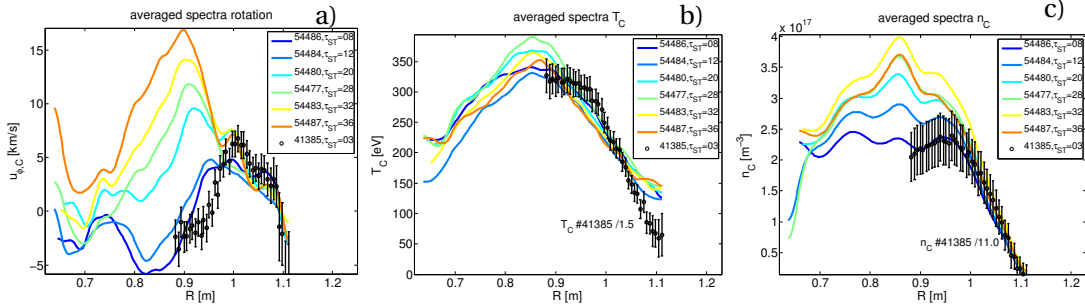
Figure 5.23: Profiles resulting from the CXRS analysis of the sum of the ST resolved spectra, corresponding to a ST averaged profile ($\Delta t_{CX} = \tau_{ST}$), for (a) $u_{\phi,C}$, (b) T_C and (c) n_C.

5.23-c are divided by a factor of 1.5 and 11 respectively, to facilitate the comparison.

The profiles shape for the reference discharge strengthen the deductions of the previous sections: the core rotation ($0.9 < R < 1$) has an average value which is lower (more co-current) than what observed in the discharges of the τ_{ST} scan, as expected due to the higher crash frequency, resulting in a higher average core co-current torque. This results also in an averaged rotation profile similar to the post-crash profile for short τ_{ST}, as shown in figure 5.24-a. The more the ST period is extended, figures 5.24-b and 5.24-c, the larger is the difference of the averaged profile from the post-crash profile. At the same time, the temperature profile is flatter
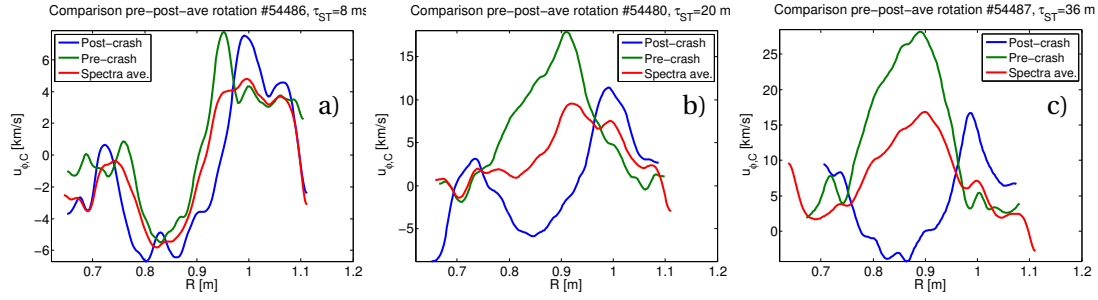
Figure 5.24: Comparison of pre-crash, post-crash and ST averaged profiles for shots: (a) 54486-$\tau_{ST} = 8$ ms, (b) 54480-$\tau_{ST} = 20$ ms and (c) 54487-$\tau_{ST} = 36$ ms. For short τ_{ST} the averaged profile i

and the flattening region is larger, a behaviour that is again in agreement with the finding of the scan and the increase in inversion radius due to the slightly higher current. The density also follows the τ_{ST} scan trend, with a hollow core profile that is deeper than the profiles of the scan, due to the higher frequency of the core Carbon ejection occurring at the crash.

The striking similarity of the short τ_{ST} $u_{\phi,C}$ profiles with the profile of discharge #41385, where no ECRH power is used, is additional evidence that employing ECRH power to stabilise the ST for these experiments does not directly influence Carbon momentum transport, which is dominated by the dynamics at the crash.

5.5 Conclusions

The effect of ST activity on rotation and Carbon transport was experimentally addressed from a scenario developed in early works that allowed multiple measurements of Carbon profiles time resolved across the ST cycle. The scenario employed a locking technique to obtain regular and long ST synchronised with the CXRS acquisition, acquiring at the fastest readout $\Delta t_{IT} = 2$ ms. The plasma parameters were chosen to increase the impact of ST, by positioning the $q = 1$ surface far from the machine centre at $\rho_{q=1} \simeq 0.65$. Profiles with unprecedented, at least for TCV and probably worldwide, spatial and time resolution were obtained from coherent averaging of the raw data, describing the evolution of a "canonical" ST. This so termed "canonical" ST is expected to be highly similar to each individual ST and therefore can be used to describe the parameters evolutions within the ST cycle.

The main features observed in the profiles evolution are here resumed. The toroidal rotation shows a discontinuity across the crash. The pre crash profile is peaked in the counter-current direction, with a magnitude that increases with τ_{ST}. After the crash, the core rotation is in the co-current direction, even for fully counter-current pre-crash profiles, revealing the presence of a co-current torque acting at the crash. The positive (counter-current) momentum expelled from the plasma core at the crash is redistributed on a ring of plasma centered at the $q = 1$ surface, rotating in the counter-current direction. The decrease of the total angular

momentum after the crash suggests an unidentified active torque acting in the co-current direction. The toroidal rotation after the crash evolves continuously towards a peaked counter-current profile, without reaching a saturation level for the τ_{ST} available in the experiments. This phenomena explains the $1/I_p$ scaling presented in [64] as a crash-fast transport & co-current torque effect, contradicting what assumed in theoretical models, e.g. in [196], where MHD phenomena are neglected. Furthermore this can be exploited to actively set the intrinsic rotation level, a feature extremely convenient and yet currently neglected, in a reactor relevant scenario, by using the ST period and inversion radius as actuators.

By using CXRS, time resolved information on the ion temperature and Carbon profiles are also available. The Carbon temperature is flattened by the crash up to the $q = 1$ surface and recovers an on axis peaked profile within $\tau_{rel-T-core} < 10$ ms.

Impurities are effectively expelled from the core by the ST crash. A high Carbon impurity density ring, 120% of the pre-crash core density, is formed at the crash between ρ_{mix} and $\rho_{q=1}$. The ring dissipates within 5 ms probably by the prevalent transport processes of particle transport and diffusion, but the core recovery time is significantly longer, with a peaked saturated profile attained in $\tau_{rel-n-core} < 25$ ms. This supports the possibility of impurity control through ST, with fast ST $\tau_{ST} < 10$ ms and large ρ_{inv} being beneficial in preventing impurity core accumulation.

The boundary conditions (EDGE profiles) were shown to be fairly stable, as expected from the magnetic recombination models. With short ST periods, where the ECRH power was lower, although the profiles could not completely recover, no effects on the ST dynamics was noticed. This permits to concentrate more on the core behaviour, as it has been shown on TCV that the edge boundary can strongly influence the core rotation.

The technique developed in this work is relevant for a substantial number of future studies on ST dynamics. Those studies should encompass the development of a scenario with smaller $\rho_{q=1}$ to ascertain the influence on momentum conservation of the boundary conditions. With a $\rho_{mix} \leq 0.7$ (actual value $\rho_{mix} \simeq 0.9$) the core dynamic would be decoupled from the edge, ensuring a better understanding of momentum conservation/transport following the crash. A scenario in diverted configuration should also be developed, where the influence of the boundary conditions on profiles evolution could be tested in a different magnetic topology. The commissioning of higher power gyrotrons, planned in TCV for the near future, can be exploited to access longer τ_{ST}, extending the ST period scan and possibly determine the ST-free velocity saturation level and relaxation time.

This represents, to this author's knowledge, the best rotation, ion temperature and impurity profile ST resolved measurements ever achieved. It provides the basis for a new analysis of the ST phenomena where the ion transport behaviour is available. Although ECRH was used in these measurements, it was concluded to not have had a direct effect on the reconnection ST-crash physics. With the new NBI heating beam, these measurements can be extended to the dynamics of fast ion ST stabilisation processes.

6 Rotation changes at the L-H transition

6.1 introduction

Plasmas confined in toroidal devices (tokamaks and stellarators) in diverted configuration exhibit a sudden improvement in confinement when an input power threshold, dependent on plasma parameters and geometry, is reached [197]. This enhanced confinement regime, discovered at ASDEX in the early 1980's [6], is termed high confinement mode, or H-mode, in contrast to the low confinement mode, or L-mode, below the transition threshold. The energy confinement time τ_E increases by about a factor of two: $\tau_{E-H} \simeq 2\,\tau_{E-L}$. After including other empirical and theoretical consideration, this is better quantified in the ITER confinement time scaling [198]. The improvement results from the development of a transport barrier at the plasma edge (ETB), where turbulence and fluctuations are suppressed (see figure 6.2), leading to the development of steep gradients in electron (and ions) density and temperature. In this region, termed pedestal, both n_e and T_e are well described by hyperbolic tangent functions [199]. The improvement in the edge boundary conditions directly increases plasma core performances due to stiffness of the core profiles [200] on top of this pedestal.

The physics of the ETB formation is not yet understood, but observations of strong perpendicular flows at the onset of the H-mode suggests that rotation is involved in the transition [201], as it is analytically proven that a sheared poloidal rotation quenches turbulence [50]. A self-consistent evolution of the poloidal flow, the kinetic profiles and the radial electric field inside the LCFS has not yet been satisfactorily explained. Toroidal rotation is also reported to increase at the transition, propagating inward from the plasma edge [147, 202] on timescales of the order of the observed energy confinement time, in a manner connected with a modification in the SOL flow [203]. A relatively narrow negative radial electric field well is seen to develop just inside the LCFS at the onset of H-mode, causing the sheared $\mathbf{E} \times \mathbf{B}$ flow that suppress the turbulence [204], while L-mode is characterised by a small, in both magnitude and shear, radial electric field. Although the E_r well is observed in every device reaching H-mode, its characteristics vary, with a well depth of -35-50 kV/m and $\simeq$ 1 cm wide in AUG [68], a deep (up to -300 kV/m) and narrow 4-6 mm well in C-Mod [127], a shallow (-15-25 kV/m) and wide $\simeq$ 1

cm well in DIII-D [205], a depth of -15-60 kV/m and very wide $\simeq$ 2 cm well in JET [129, 206] and a shallow -15 kV/m and wide $1-2$ cm well in MAST [131, 207]. The newly developed EDGE CXRS system allowed the first observation and characterisation of the E_r well developing in TCV H-mode discharges, that will be detailed below. A phenomenological description of the rotation and E_r changes at the transition can shed light on the physics involved and help develop an adequate explanation of the transition and of the sustaining of H-mode. It should be stressed that TCV has been able to achieve H-mode without auxiliary heating so the TCV observation can be contrasted with that observed on other machines where, particularly for NBI heating, the parallel plasma flow can be strongly perturbed by the heating scheme itself possibly changing the physics of the transition itself.

The power threshold for the L-H transition depends on plasma parameters and geometry [208]. It is lower for a diverted configuration rather than limited, particularly when the ion grad-B drift $\mathbf{v}_{\nabla B,i}$ is directed towards the X point, which is termed a "favourable" configuration (see section 1.1.2). Wall conditioning (He glow discharges and boronisation) can also engender a lower power threshold, while decreasing the gap between the confined plasma and the wall increases the threshold power, which also depends close to linearly on B_ϕ and on n_e, where the latter dependence is only valid for a plasma above a minimum density $n_{e,min}$. Experimental evidence suggests that the threshold is closely related to the edge ion heat flux [209], which influences the radial electric field well induced by the main ions. In general, although there are many experimental observations and empirical scaling for the H-mode transition, its base cause remains unclear although it has been seen on many devices. The ITER standard configuration will depend on H-mode like confinement so any improvement in our empirical or theoretical understanding remains of strong interest.

The steep gradients in the plasma parameters of the pedestal region often reach an MHD instability threshold, particularly for Peeling-Ballooning modes [210], resulting in bursts of fast duration, $\tau_{ELM} \leq 1$ ms, of particles and energy from the edge into the SOL, commonly termed edge localised modes (ELMs) [211, 212]. ELMs have a filamentary structure with elevated toroidal number ($n = 5-22$) [213, 214] and can have a significant influence on the plasma energy balance; the decrease in plasma stored energy and density due to a single ELM event can be $5-20\%$ [213], constituting an escape channel for particles that can be used to enable a quasi stationary operation when periodic ELMs occur. The energy release however can pose a severe threat to the divertor exhaust region, where, for example, heat fluxes exceeding 20 MJ/m^2 are predicted in ITER [215], clearly exceeding the acceptable material thermal load limit of 0.5 MJ/m^2 [216]. ELMs are easily detected, in most machines, as spikes in the D_α signal in the plasma edge and divertor regions (see figure 6.1 and 6.2), corresponding to the increase in the ionisation rate in the plasma edge following the momentarily breach of the ETB. The D_α line is not the only emission line perturbed by ELMs, the passive emission from plasma impurities are also affected by the sudden release of energy and particles, that perturbs and thus limits an accurate CXRS measurement on TCV (see section 2.2.4), where the passive emission often dominates the spectrum. For this reason, discharges featuring H-modes without ELMs, the so called ELM-free H-mode, are particularly attractive for impurity studies

in TCV. ELM-free H-modes exhibit higher confinement than ELMy H-modes [217], resulting in monotonic increase of electron density and in impurity accumulation (see figure 6.8), which, due to radiative losses, eventually leads to a H-L back transition or to a high density disruption. The radiated power causes a decrease in T_e and τ_E after an initial peaking (see figure 6.7) and can eventually exceed the power input resulting in discharge termination. ELM-free H-modes are therefore intrinsically transient with evolving plasma parameters, which constitutes a challenging regime for studies on the edge poloidal rotation and on the radial electric field.

Understanding the physics of the L-H transition and reaching a stable H-mode operation avoiding ELMs [218] are among the main current challenges for the fusion community, since an economically sustainable thermonuclear reactor would likely operate in H-mode, to benefit from the higher confinement, as foreseen for ITER standard scenario [219]. To this end an experimental characterisation of the edge plasma flow and the connected E_r evolution are of paramount importance; in this thesis accurate edge CXRS measurements were performed for the first time in TCV providing the first characterisation of the changes in Carbon impurity profiles at the H-mode transition. Noticeably the H-mode was obtained without employing auxiliary heating, providing truly intrinsic rotation measurements, relevant for a reactor scale physics, for which the effect of NBI on rotation is expected to be negligible. This could also allow in TCV a comprehensive study of the H-mode power threshold, not attempted for lack of time, by direct comparison of the power across the LCFS in Ohmic H-modes and in transitions triggered with auxiliary heating (NBH and ECRH), to test the present day theoretical and empirical transition models [208, 209, 220, 221].

6.2 Target discharge

ELM-free H-mode discharges are readily obtained in TCV ohmic discharges with input powers close to the threshold for the transition [222], in diverted geometry with the favourable $B \times \nabla B$ drift configuration. For a full coverage of the plasma cross section of the CXRS systems the plasma vertical position was centred at $Z = 0$, and the geometrical coefficients δ_{edge} and κ_{edge} optimised to centre the intersection of the LCFS with the DNBI on the central chord of SYS4, whilst simultaneously retaining a relatively large gap between the X point and the wall, to favour the transition and reduce any measurement contamination from plasma wall interactions. High values of δ_{edge} and κ_{edge} are also favourable for ELM-free operation. Plasma parameters and geometry of the target discharge are shown in figure 6.1 and listed in table 6.1.

I_p [kA]	-315	B_0 [T]	-1.36
δ_{edge}	0.5	κ_{edge}	1.5
q_{edge}	3.9	Z_{axis} [mm]	$\simeq 5$
n_{e0} [m^{-3}]	$\simeq 5 \cdot 10^{19}$	T_{e0} [eV]	$\simeq 1000$

Table 6.1: Parameters of the L-H transition experiment discharges.

The moderate density $n_{e0} \simeq 5 \cdot 10^{19}$ m^{-3} provided a reliable access to H-mode, high DNBI penetration and reasonable duration of the often resulting ELM-free phase (where the plasma density monotonically increases, sometimes reaching large fractions of the Greenwald limit [223] before disrupting). The current in the flat-top phase of the discharge is then reduced in the interval (0.95,1.2) s to encourage an H-L back transition (already occurred in the discharge shown in figure 6.1) that avoids a disruption and possibly engender another transition. The current was increased to -330 kA in two discharges, #55608 and #55610, to probe the plasma response.

A list of the mission successful shots is shown in table 6.2 with the time of the transitions to ELM-free H-mode and its duration. The parameters of CXRS acquisition are also reported.

Early runs used a fast acquisition IT, $\Delta t_{IT} = 3$ ms, represented here by shots #53920 and #54031 for the CVI and BV lines respectively. The initial goal was to identify the rotation changes with this high time resolution by employing an inter-shot passive spectral subtraction, that would then allow measurements within 3 ms of the transition. This method requires high repeatability in the discharge parameter evolution, that for a ohmic discharge, devoid
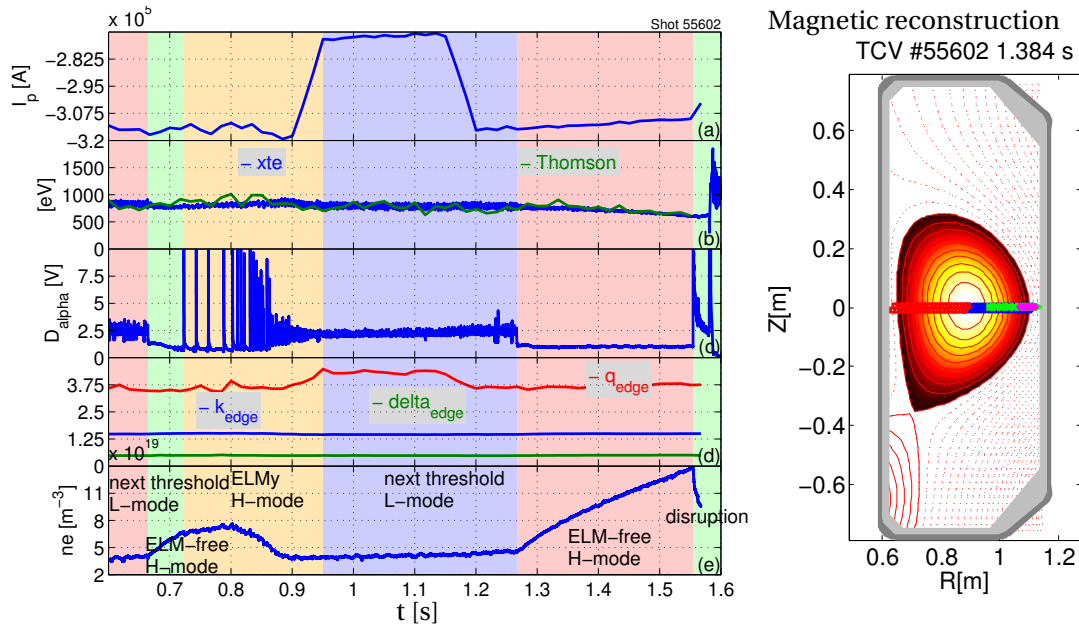
Figure 6.1: Time traces of plasma parameters of the target discharge, TCV #55602, used in the L-H transition experiments: (a) plasma current, (b) electron temperature from XTE and TS, (c) D_α from PM, (d) elongation κ_{edge}, triangularity δ_{edge} and edge safety factor q_{edge}, (e) line integrated electron density from FIR. The discharge is composed of six phases: an L-mode next to the threshold (t =0-0.66 s) in pink, an ELM-free H-mode phase (t =0.66-0.723 s) in green, an ELMy H-mode (t =0.723 -0.95 s) in yellow, another L-mode next to the threshold (t =0.95-1.266 s) in azure followed by an ELM-free H-mode phase (t =1.266-1.55 s) and a disruption at t = 1.55 s. The magnetic reconstruction at t = 1.384 s is shown on the right with the CXRS sampling positions, LFS in blue, HFS in red, VER in green and EDGE in magenta.

shot	time L-H transition (duration ELM-free) [s] ([ms])	CXRS Δt_{IT} [ms]	line
55545	0.536 (360)	12	CVI
55547	0.628 (290)	12	CVI
55597	1.240 (220)	12	CVI
55599	0.8 (60) - 1.232 (260)	12	CVI
55600	0.681 (250)	12	CVI
55602	0.664 (59) - 1.266 (270)	12	CVI
55605	0.76 (190)	12	CVI
55607	1.405 (260)	12	CVI
55608	0.640 (260)	12	CVI
55610	0.750 (150)	12	CVI
53920	0.58 (190) - 1.281 (240)	3	CVI
54031	0.774 (40)	3	BV
57580	0.530 (130)	12	BV
55748	0.568 (210) - 0.883 (110)	6	CVI
55751	0.703 (190) - 1.226 (250)	10	CVI

Table 6.2: Parameters of the L-H experiment discharges: time of the L-H transition and duration of the ELM-free regime, CXRS IT and observed line.

of direct actuators for the transition, was unattainable. ELM-free H-mode was regularly achieved, but the plasma parameters at the transition and the transition time differed for each shot, impeding a reliable passive subtraction. The standard CXRS analysis also displayed only modest reliability of the measurements close to the LCFS, i.e. the zone of interest, due to poor photon statistics and excessive smearing (see appendix E). This last effect is particularly important for H-mode plasmas, where the strong density gradient at the plasma edge results in a difference in LOS brightness that can exceed 2 orders of magnitude between the top of the pedestal and near-SOL chords. Measurements with longer IT and a DNBI duty cycle of 1:1 (ON:OFF) were also attempted in shots #55748 and #55751, with 6 and 10 ms IT respectively, showing improvements in the photon statistics and smearing, but again displaying a unsatisfactory passive subtraction. The standard CXRS acquisition, $\Delta t_{IT} = 12$ ms with a DNBI duty cycle of 1:2, provided the best trade-off between time resolution and spectra quality, and was hence employed for the bulk of the mission discharges.

Measurements of both CVI and BV lines were carried out, but the presence of a nearby strong passive line for BV, identified as a BII 494.0376 nm, strongly perturbed the BV spectrum of bottom pedestal LOS, preventing a reliable reconstruction of B^{+5} profiles. The mid-top pedestal LOS of Boron follow a similar behaviour as the Carbon profiles, with acceleration at the transition and the formation of a well (characterised in the following), although the estimated uncertainty are much higher than for CVI. For this reason only CVI profiles are here reported.

Figure 6.2-a shows the D_α PM signal together with (figure 6.2-b) a spectrogram of an MHD coil
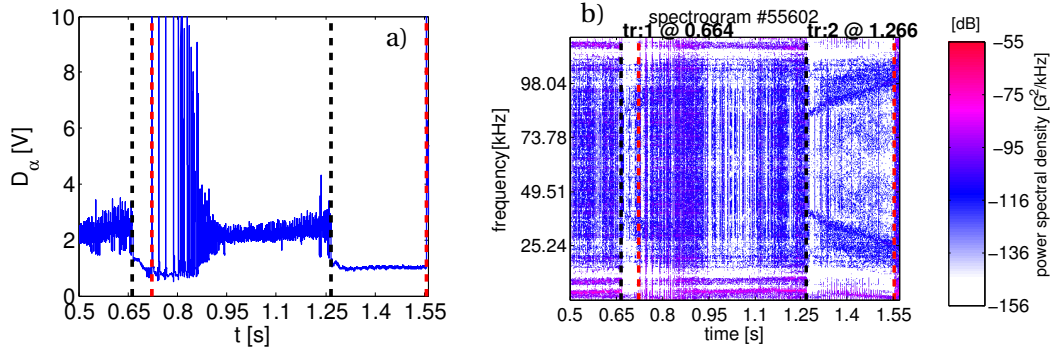
Figure 6.2: (a) D_α signal from PM showing the two ELM-free phases of the discharge, delimited by the vertical dashed black lines at the forward transition and vertical dashed red lines at the end of the ELM-free H-mode. (b) spectrogram of the MHD Mirnov coils signal showing the reduction in magnetic fluctuations during ELM-free H-mode.

signal for discharge #55602. The D_α intensity is used to identify the phases of the discharge, with the onset of the H-mode clearly marked by the sudden drop in the D_α level and fluctuations (RMS), which is a consequence of the improved particle confinement. A drop in the magnetic perturbations during the ELM-free phase is observed, with the disappearance of the 115 kHz and 11 kHz modes, the reduction of the 5.4 kHz mode amplitude and a reduction in the broadband signal level in general. In the first H-mode phase of the discharge, ELMs are detected (spikes in the D_α signal), in correspondence with an increase of the magnetic perturbations and reappearance of the 115 kHz and 11 kHz modes. Profiles during the ELMy H-mode phase are not considered in this work, as the spectra perturbation caused by ELMs introduces sources of error in the LCFS measurements that can not, at present, be compensated.

In the following section, the results of the CXRS standard analysis applied to the discharges listed in table 6.2 employing a $\Delta t_{IT} = 12$ ms IT will be discussed. Profiles for which the active acquisition IT was closer than one and a half Δt_{IT} to the transition are rejected, as the background subtraction is not sufficiently accurate. This leaves a minimum gap between the L-H transition and the closest CX profile of $\Delta T = 18$ ms. Although measurements reached positions in the far-SOL, up to $\rho = 1.08$, only profiles up to $\rho = 1.02$ are considered, as measurements for the outer LOS in the H-mode phase appeared dominated by smearing and reflections (see appendix E). It is worth pointing out that these measurements on TCV are particularly challenging in view of the low intensity of CX spectra with a diagnostic neutral beam and that the CX intensity does not dominate the overall spectral intensity that can thus be strongly perturbed by changes in the background emissivity. This is to be contrasted to measurements that employ a heating neutral beam where the background can often be considered as a relatively small perturbation to the total signal.

6.3 Edge profiles before and after the transition

From the comparison of the TS profiles before (pre) and after (post) the L-H transition, shown in figure 6.3 for discharge #55602, the onset of an edge particle and energy barrier can be deduced. The spatial resolution of the TS diagnostic (the 2016 version), $\delta L_{TS} \simeq 1$ cm, is not sufficient to resolve the pedestal structure, but is sufficient to assess its main features. The TS time resolution is $\delta t_{TS} \simeq 16.6$ ms; in this discharge profiles 1 ms after the transition are available.

The temperature profile develops a pedestal in less than 1 ms from the transition, figure 6.3-a. T_e at the LCFS is ≤ 100 eV in both L and H-mode, while at $\rho = 0.95$ the temperature jumps from $\simeq 120$ to ≥ 200 eV in less than 1 ms (assuming there is no evolution before the transition during the L-mode, which is supported by measurements from similar discharges). The time evolution of the pedestal-top temperature is shown in figure 6.7, where is compared with the Carbon temperature. It increases to 300 eV in the first 100 ms, and then shows a roll over that may be ascribed to an increase of impurity radiated power, reaching ≤ 200 eV at 300 ms. The temperature pedestal is hence fully formed 1 ms following the transition.

The density pedestal development is slower, where the density 1 ms after the transition (yellow profiles in figure 6.3-b) at $\rho = 0.95$ is only $\simeq 15\%$ higher than in L-mode (the T_e increase is $\geq 66\%$), and does not reach a saturation value, but increases linearly in time, as shown in figure 6.8.

The resulting pressure pedestal, $p_e = n_e \, T_e$, shown in figure 6.9, reaches a saturation value of $p_e \leq 3000$ Pa within 100 ms, then remaining more or less constant, where any increases in density are compensated by decreases in temperature.
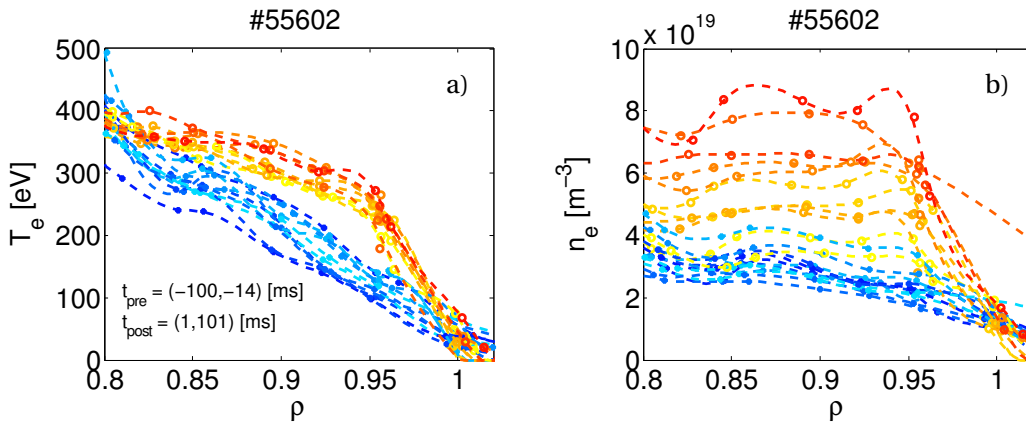
Figure 6.3: Edge profile of (a) T_e and (b) n_e across the transition for shot #55602 showing the formation of a pedestal. Experimental points are represented by circles. Cold colours (blue-cyan) represent the pre-transition profiles, warm colours (yellow-red) the post transition, with cyan and yellow for profiles closer to the transition.
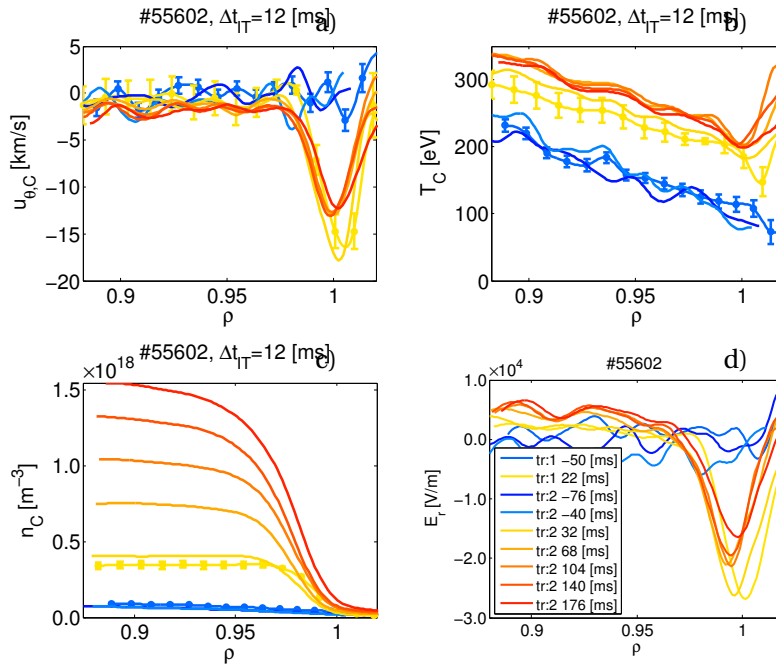
Figure 6.4: EDGE Carbon profiles across the L-H transition for shot #55602: (a) poloidal velocity, (b) temperature, (c) density and (d) radial electric field.
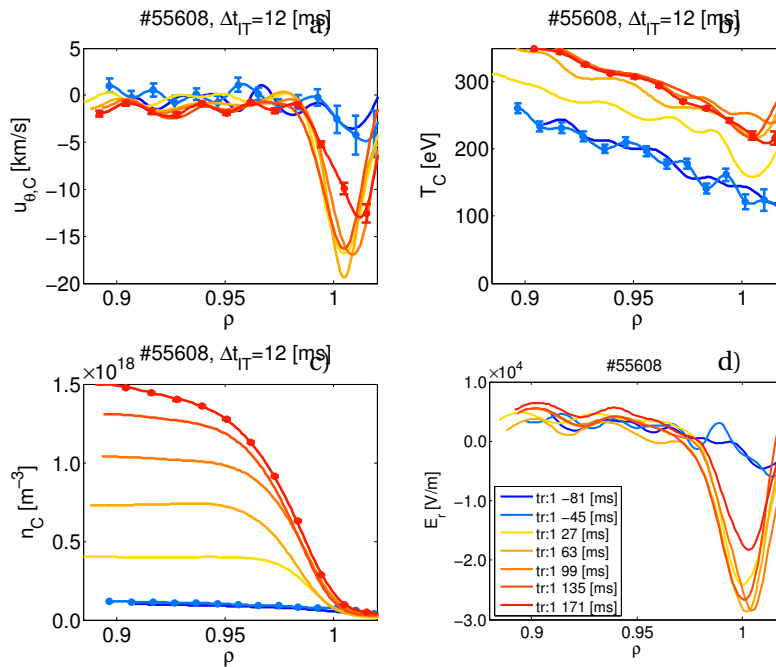
Figure 6.5: EDGE Carbon profiles across the L-H transition for shot #55608: (a) poloidal velocity, (b) temperature, (c) density and (d) radial electric field.

Figures 6.4 and 6.5 show the measured profiles of CVI poloidal velocity, temperature, density and the calculated radial electric field for discharges #55602 and #55608. Profiles during L-mode, just before the transition, are plotted in cold colours (blue-cyan), profiles after the onset of H-mode are in warm colours (orange-red). In the legend of figures 6.4 and 6.5, "tr:1" and "tr:2" refer respectively to the first and second L-H transition of the discharge. There are clear changes in the Carbon profiles after the transition to H-mode:

- formation of a negative well with a poloidal rotation up to -20 km/s;

- T_C profile increases of $\Delta T_C \simeq 100$ eV, preserving a constant gradient inside the LCFS;

- formation of a density pedestal inside the LCFS of width 13 ± 2 mm, and top density increasing linearly with time (see figure 6.8), eventually stopped by ELMs, back-transition to L-mode or plasma disruption;

- formation of a negative electric field well of depth ≤ -30 kV/m.

In L-mode, the poloidal rotation inside the LCFS is approximately zero. The increase of poloidal rotation at the transition is not temporally resolved, as it is faster than the CXRS integration time; the first measurement after the transition presents already a fully developed rotation well in all discharges. The parameters of the poloidal velocity well are determined by fitting the velocity profiles with a Gaussian function (with typical adjusted coefficient of determination $\overline{R}^2 > 0.99$). Their averaged values are listed in table 6.3. The acceleration is in the electron diamagnetic velocity direction, consistently with what observed in [127]. The rotation well parameters time evolution are depicted in figure 6.6. The velocity well depth reduces in time
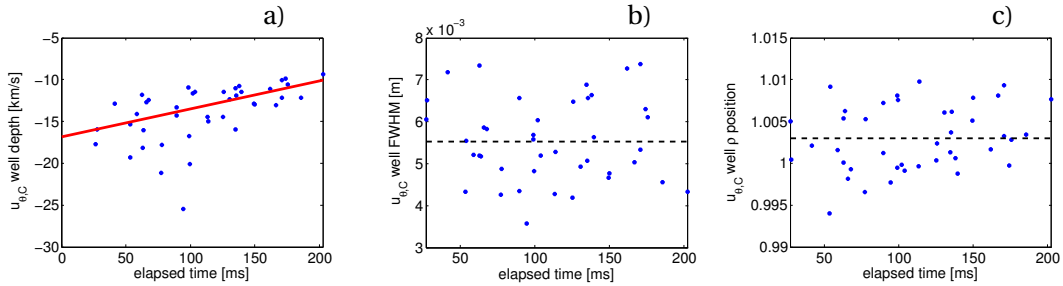
Figure 6.6: Poloidal velocity well parameters evolution in time for all the discharges: (a) depth, (b) FWHM and (c) position. The well depth reduces in time while the width and position are preserved.

from the transition, from $u_{\theta,C} \simeq -16$ km/s to -10 km/s in 200 ms (figure 6.6-a), while the position and the width are roughly constant, with average values $R_{well} = 1.098$ and $FWHM = 5.5$ mm. The corresponding position in the radial variable ρ is $\rho_{well} = 1.003$, i.e. just outside the LCFS, highlighting the importance of accurate near-SOL measurements.

depth	-14 ± 3 km/s	position R	1.098 ± 0.002 m
FWHM	5.5 ± 1 mm	position ρ	1.003 ± 0.004

Table 6.3: Parameters of the poloidal velocity well developed in H-mode.

The Carbon temperature profiles in H-mode reach a stationary state that, inside the LCFS, looks like the L-mode profile displaced to $\Delta T_C \simeq 100$ eV higher values. In the near-SOL, $1 < \rho \leq 1.02$, an unexpected feature is observed, the temperature strongly increases with ρ. This effect is probably ascribed to a reflection of active signal originated in the inner plasma (see appendix E) and is reported here for completeness. It prevents a clear identification of a pedestal in the Carbon temperature, but a possible detrimental effect on the electric field calculation is mitigated by the low values of the SOL Carbon density. The timescale of the increase in temperature is slower than the CXRS temporal resolution, with the new steady state at higher temperature attained after $\simeq 60$ ms. During the transient period, the profile shape remains unchanged, with just lower values than the final stationary state. This 'rigid translation' of the T_C profile is seen across the whole plasma cross section by the other CXRS systems. The time evolution of T_C at the top of the pedestal, taken at $\rho = 0.95$ as for the electron temperature, is shown in figure 6.7, where the $\simeq 60$ ms transient is visible. The stationary value of the temperature should be contrasted with the electron temperature, that starts to decline after 100 ms.
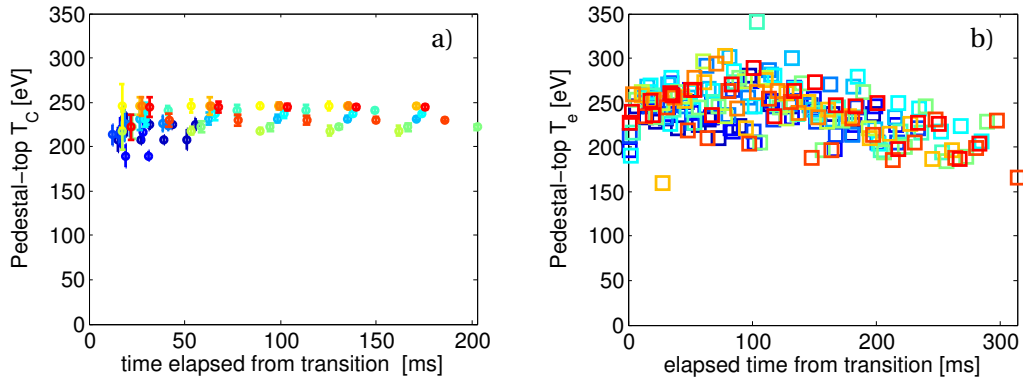
Figure 6.7: Pedestal-top (a) C^{+6} and (b) electron temperature as function of time from the H-mode transition for all the considered shots. The electron temperature rolls over 100 ms after the transition to H-mode, while Carbon temperature remains constant at $T_C \simeq 230$ eV.

The density profile in L-mode monotonically increases towards the plasma core, without strong gradients at the LCFS. After the transition to H-mode, a pedestal forms inside $\rho = 1$. The density at the top of the pedestal increases linearly with time, as shown in figure 6.8, with coefficient $7.83 \cdot 10^{18}$ m^{-3}t^{-1}, until the end of the ELM-free phase.
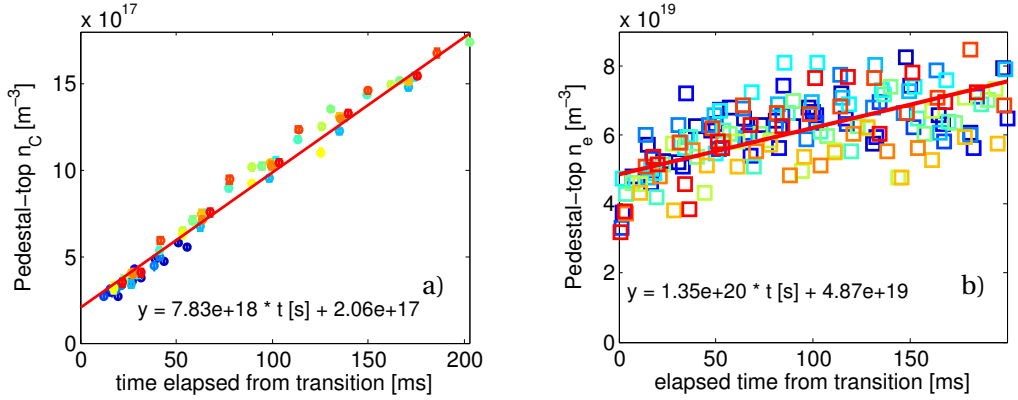
Figure 6.8: Pedestal-top (a) C^{+6} and (b) electron density as function of time from the ELM-free H-mode transition for all the considered shots. The red line is a linear fit, that satisfactorily represent the data.
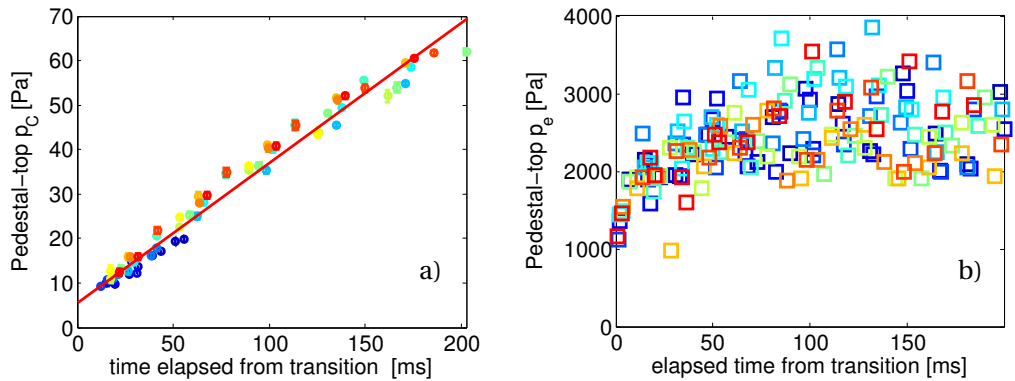
Figure 6.9: Pedestal-top (a) C^{+6} and (b) electron pressure as function of time from the H-mode transition for all the considered shots. The Carbon density increases linearly in time, while the electron pressure saturates within 100 ms.

From the pedestal-top density and temperature, the pedestal-top Carbon pressure is computed, and shown in figure 6.9. It increases linearly in time, due to the density evolution, contrary to the electronic pressure, that saturates within 100 ms.

The kinetic Carbon profiles across the transition for all the CVI discharges in table 6.2 are shown in figure 6.10 for completeness.

The radial electric field, that is approximately zero in L-mode inside the LCFS and is positive in the far-SOL (for $\rho > 1.02$, measurements are probably not sufficiently reliable), develops a well
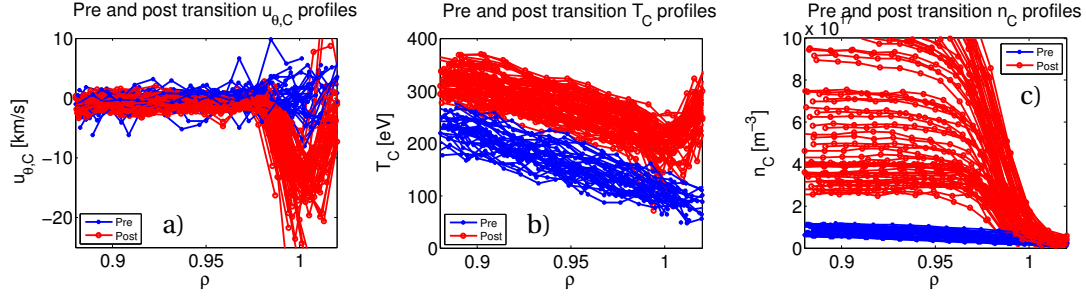
Figure 6.10: SYS4 CVI profiles across the L-H transition (blue for L-mode, red for H-mode) for all the discharges of the experiment: (a) edge poloidal velocity, (b) T_C and (c) n_C.

just inside the LCFS, but otherwise remains unchanged at other locations. A more detailed analysis of E_r is given in the next section.

The toroidal velocity, shown in figure 6.11-a for shot #55605, increases in the co-current direction (negative direction) after the transition to H-mode. The L-mode profiles exhibit a gradient in the edge region, with a flat velocity core profile $u_{\phi,C} \simeq -25$ km/s and a velocity at the LCFS of $u_{\phi,C} \simeq -10$ km/s. The co-current increase is stronger in the edge region, as can be seen in figure 6.11-b where the time evolution of $u_{\phi,C}$ at selected R positions is shown, resulting in a flat profile across the TCV cross section around $\simeq 200$ ms after the transition with a rotation of $u_{\phi,C} \leq -30$ km/s.

The profiles of Carbon density (figure 6.11-c) and temperature (figure 6.11-e) are also shown for the two confinement modes of shot #55605.

The increase in time of the carbon density in H-mode, shown in figure 6.11-d, agrees with the measurements of the EDGE system.

Similarly the Carbon temperature, figure 6.11-f, saturates in H-mode to a value $\simeq 100$ eV higher than during L-mode, as previously reported for the EDGE system.
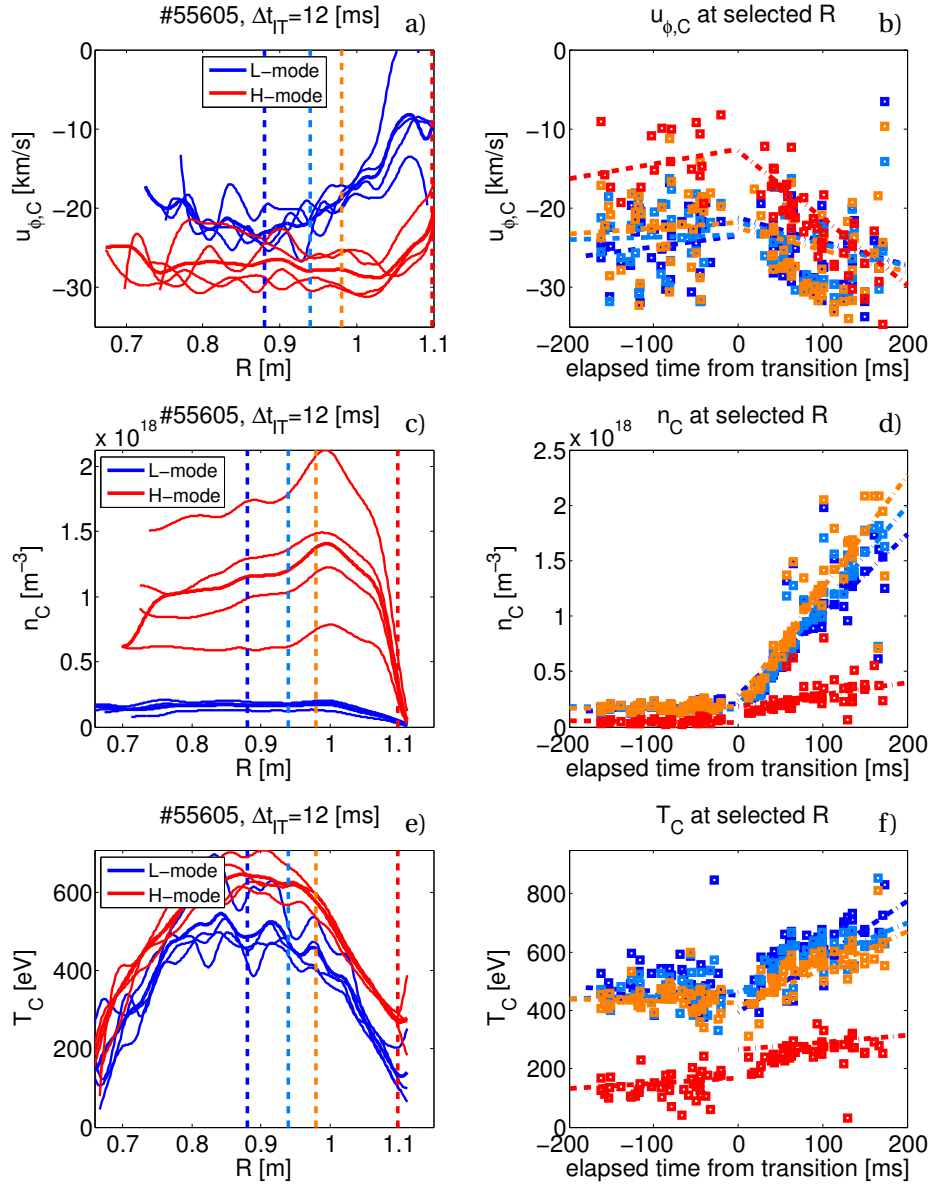
Figure 6.11: Profiles from CXRS systems 1 and 2 across the L-H transition for discharge #55605 for: (a) $u_{\phi,C}$, (c) n_C and (e) T_C. Time evolution at selected positions across the transition for all the shots in the database is shown for (b) $u_{\phi,C}$, (d) n_C and (f) T_C. The dashed lines are linear fit during either the L-mode and H-mode phases. In (b), $u_{\phi,C}$ increases in the co-current direction after the transition, resulting in flat profiles after $\simeq 200$ ms.

6.3.1 Electric field contributions

Figure 6.12 shows the radial electric field profile (blue line) calculated through equation 4.22 for shot #55608. The three terms forming the electric field are also shown, namely the diamagnetic term $\frac{\nabla p_\alpha}{q_\alpha n_\alpha}$ in black, the poloidal velocity term $-u_\theta B_\phi$ in red and the toroidal velocity term $+u_\phi B_\theta$ in magenta.
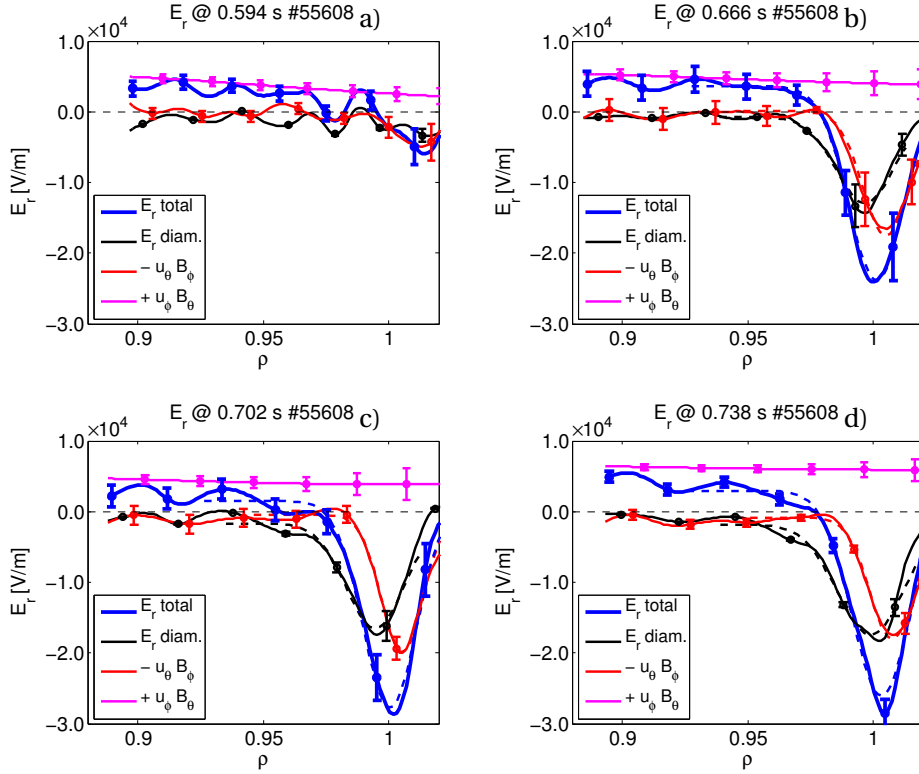
Figure 6.12: E_r profiles and its components (a) 45 ms before (L-mode), (b) 27 ms, (c) 63 ms and (d) 99 ms after the transition for shot #55602. The dashed lines after the transition represent the fit to a Gaussian function. The $-u_\theta B_\phi$ components is dominant after the transition and decays in time, while the diamagnetic component is stationary.

The toroidal velocity term is positive in both L and H-mode, although it reaches higher values in H-mode following the increase in $u_{\phi,C}$. The profile here reported results from an interpolation of SYS1 (toroidal) measurements on the SYS4 (periscope poloidal) positions. The original data is composed by only ≤ 4 LOS in this region, due to the lower spatial resolution of the

depth	-25 ± 4 kV/m	position R	1.097 ± 0.002 m
FWHM	7.3 ± 1 mm	position ρ	0.997 ± 0.004

Table 6.4: Parameters of the radial electric field well developed in H-mode.

toroidal diagnostic, that may be the reason of the approximately flat profile. On the other hand, similar measurements on other devices [68, 127, 131, 205] showed little or no influence of the toroidal rotation on the radial electric field well, providing some justification for the use of interpolation methods in this region.

The poloidal velocity and the diamagnetic terms are negative inside the LCFS and effectively counter the positive toroidal term in L-mode, resulting in a total field near zero in the confined region. In H-mode, the contribution of the toroidal term is higher and the resulting field is positive in the core region. In the far-SOL (not shown) the electric field is positive due to the contribution of both the toroidal and poloidal velocity terms, in both L and H-mode.
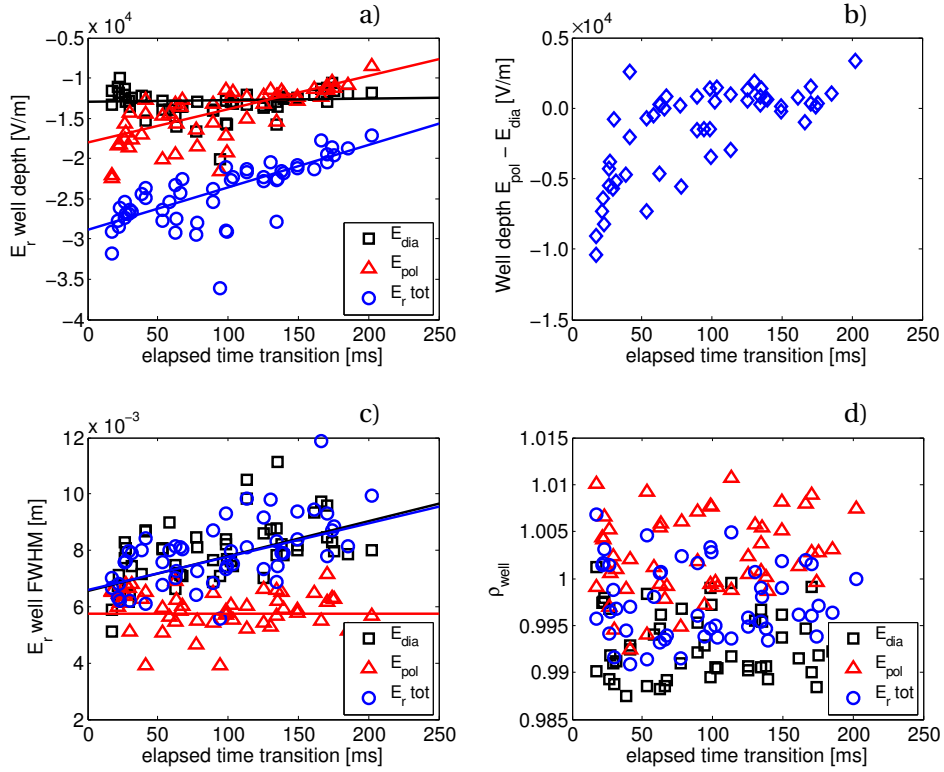
Figure 6.13: Time evolution of the radial electric field well parameters, and its components, in the H-mode phase. (a) depth of the E_r well for the total electric field and its diamagnetic and poloidal velocity components. (b) difference of the well depth of the poloidal velocity and diamagnetic components, the poloidal term dominates after the transition but within 50 ms the difference nullify. (c) FWHM of the well, increases linearly with time for both the total E_r and the diamagnetic component, while is constant for the poloidal term. (d) position in ρ of the well minimum. The minimum of the diamagnetic component is always inside the LCFS, for the poloidal velocity component it is in the SOL, resulting in a minimum just inside the LCFS for the total E_r.
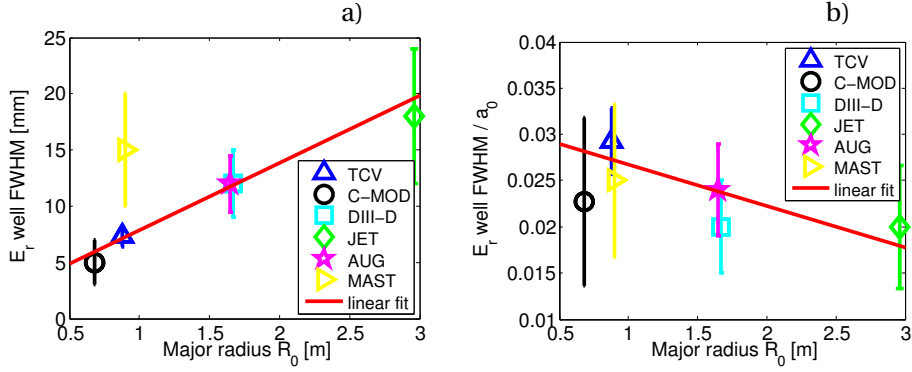
Figure 6.14: E_r well width (FWHM) inter-machine comparison (a) as function of major radius and (b) normalised to the minor radius a_0. The normalisation to a_0 improves the matching with the high aspect ratio tokamaks MAST.

The negative well in the radial electric field that develops in H-mode inside the LCFS is due to both the diamagnetic and the poloidal terms, with the diamagnetic term displaced inwards. The radial electric field well and its components were fitted with Gaussian functions, represented by dashed lines in figure 6.12. The well depth is calculated from the E_r baseline, that is positive in H-mode. The resulting parameters for the reported discharges are shown in figure 6.13 as function of the time elapsed from the transition to ELM-free H-mode. The E_r well averaged parameters calculated for all the selected shots are listed in table 6.4.

The well depth (figure 6.13-a) just after the transition is dominated by the poloidal term, which can be as much as twice the value of the diamagnetic component. The two contributions become comparable (figure 6.13-b) ≥ 50 ms after the transition, due to a decrease of the poloidal component depth, whereas the diamagnetic contribution remains fairly constant after the increase in the initial $\simeq 30$ ms. This is consistent with measurements in C-mod [127] and AUG [93], but contrary that found in MAST, where a diagnostic with similar spatial resolution of the EDGE systems verified that the main contribution to E_r is given solely by the diamagnetic term [131].

The well width (figure 6.13-c) instead is constant for the poloidal term and increases for the diamagnetic term. The resulting total well is larger than the poloidal velocity well, close to the diamagnetic and increases with time. A scaling of the electric well FWHM with machine size was reported in [93, 127], and agrees with the averaged FWHM measured in TCV, as shown in figure 6.14-a, where results from MAST are included [131]. Normalising the well width to the minor radius a_0 (figure 6.14-b), improves the congruence with the spherical tokamak MAST, suggesting that the well size is influenced more by the aspect ratio than just the major radius of the device. This also suggests that the electric field well width is not directly affected by the heating scheme, different for each device (Ohmic in TCV), but determined by the local edge conditions.
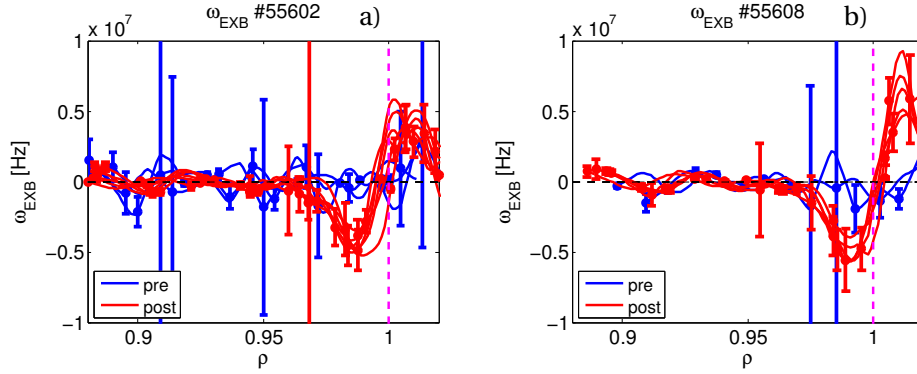
Figure 6.15: **E** × **B** shearing rate across the transition for shot #55602 and #55608. Errorbars are shown for clarity in a reduced set of points.

The two contributions also differ in their profiles, with the diamagnetic term peaking inside the LCFS, at $\rho_{diag} \simeq 0.993$, while the poloidal term is outside the LCFS, at $\rho_{pol} \simeq 1.002$; the total field peaking just inside the LCFS, at $\rho_{E_r} \simeq 0.997$. Note that this difference cannot be ascribed to misalignments with other diagnostics or with the magnetic reconstruction, as it would affect the Carbon pressure and rotation profiles simultaneously. The scatter in the peak positions data masks any possible time dependence.

The shearing rate, calculated from equation 4.24, is shown in figure 6.15 for the representative discharges #55602 and #55608. It is nearly zero in L-modes, but develops a negative well inside the LCFS, with peaking at $\simeq -5$ MHz (comparable to what found in C-mod [127]), balanced by a positive well in the near-SOL, which result in a steep profile at the LCFS, where the shearing rate changes sign. Shearing rates are higher at the beginning of the H-mode, suggesting that they play an important role in the transition [134, 135], as it is known to reduce turbulence, particularly in synergy with magnetic shear [204].

Comparison with the main ion pressure gradient

The radial electric field E_r, although estimated from impurity measurements in most of the fusion devices due to the aforementioned difficulties in measuring directly the main ion parameters (chapter 2), is driven by the main ions. Although the poloidal (and toroidal) flow may differ for each species, as reported in section 4.4, the electric filed must be consistent; by using the E_r calculated from impurities and electron kinetic profiles, main ion parameters can be inferred.

The main ion pressure gradient for example can be estimated from the electron density profile assuming constant dilution d_i [93] and from the Carbon temperature T_C, assuming the species

are thermalised:

$$\frac{\nabla p_i}{n_i} = \frac{\nabla (n_i T_i)}{n_i} \simeq \frac{d_i \nabla n_e}{d_i n_e} T_C + \nabla T_C = \frac{\nabla n_e}{n_e} T_C + \nabla T_C \tag{6.1}$$

From $\frac{\nabla p_i}{n_i}$ and E_r the main ion perpendicular velocity $u_{\perp,i}$ can be estimated by rearranging the term of the radial electric field equation 4.22 expressed for the main ions:

$$u_{\perp,i} = \frac{1}{B}\left(E_r - \frac{1}{e}\left(\frac{\nabla p_i}{n_i}\right)\right) = \frac{1}{B}\left(E_r - \frac{1}{e}\left(\frac{\nabla n_e}{n_e}T_C + \nabla T_C\right)\right) \tag{6.2}$$

while for electrons, the formula for the perpendicular velocity $u_{\perp,e}$ requires only electron parameters and E_r:

$$u_{\perp,e} = \frac{1}{B}\left(E_r + \frac{1}{e}\left(\frac{\nabla n_e}{n_e}T_e + \nabla T_e\right)\right) \tag{6.3}$$

Both the main ion and electron perpendicular velocity profiles are shown in figure 6.16 for a time frame during ELM-free H-mode, together with the main ion diamagnetic velocity $u_{dia,i}$ and the $\mathbf{E} \times \mathbf{B}$ drift. The perpendicular ion velocity is always positive (i.e. plasma rotates in the ion diamagnetic direction) and is close to zero in the edge region, where the E_r well is located. This follows from the ion diamagnetic velocity balancing the $\mathbf{E} \times \mathbf{B}$ flow at the edge, similarly to that described in [93] and [127], suggesting that the main ion pressure gradient is the dominant term establishing the electric field well [224]. Conversely, the electron perpendicular velocity $u_{dia,e}$ is always negative (electron diamagnetic direction) and peaks in the edge region, reaching $u_{dia,e} \leq -40$ km/s. The electrons speed up in the edge region to
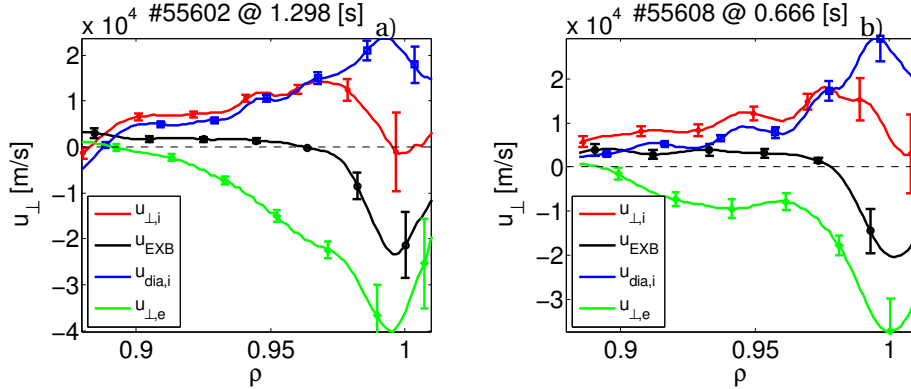
Figure 6.16: Main ion perpendicular velocity $u_{\perp,i}$ (red), diamagnetic velocity $u_{dia,i}$ (blue) and $\mathbf{E} \times \mathbf{B}$ velocity u_{EXB} (black) during ELM-free H-mode in discharges (a) #55602 and (b) #55608. The electron diamagnetic velocity $u_{dia,e}$ is in green. The ion diamagnetic velocity compensates the $\mathbf{E} \times \mathbf{B}$ drift at the edge, resulting in a main ion perpendicular velocity close to zero.

compensate for the missing ion contribution to the current density **j** to the zero order MHD equilibrium equation $\nabla p = \mathbf{j} \times \mathbf{B}$.

6.3.2 Profiles approaching the transition

Shot #55607 provides further insight on the conditions at the transition. Figure 6.17 shows the outline of the shot, there is a phase (phase-a, green) well below the L-H transition threshold, there are 2 phases (phase-b: pink and orange where the plasma conditions are just at the threshold and a phase in ELM-free H-mode (phase-c: blue). Electron density and temperatures are similar in both phases a and b, after the transition n_e increases linearly and the temperature decreases, as observed from both XTe and Thomson. In figure 6.18 the profiles of $u_{\theta,C}, u_{\phi,C}$, T_C and n_C, averaged over a 200 ms time window, are shown for the three phases.

The poloidal velocity well starts developing in phase-b (near the threshold), see figure 6.18-a,
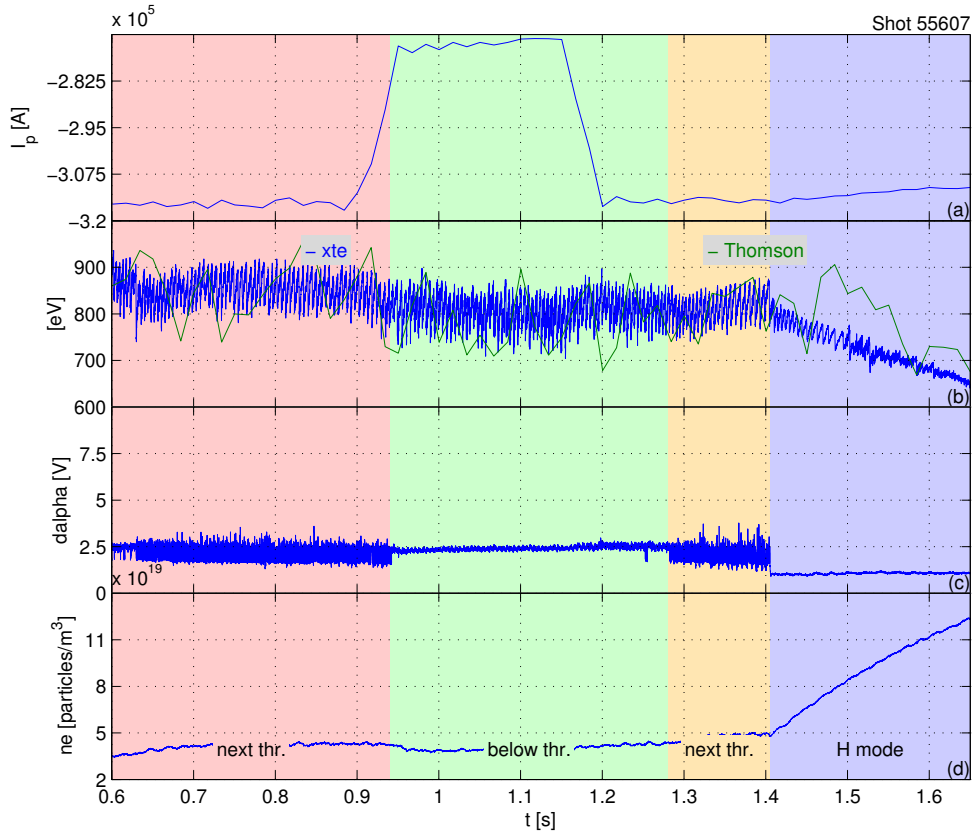
Figure 6.17: Time traces of plasma parameters for discharge #55607: (a) plasma current, (b) electron temperature from XTE and TS, (c) D_α from PM and (d) line integrated electron density from FIR. The discharge is composed of three phases, highlighted in different colours: phase-a in green, phase-b in pink and orange and phase-c in blue.
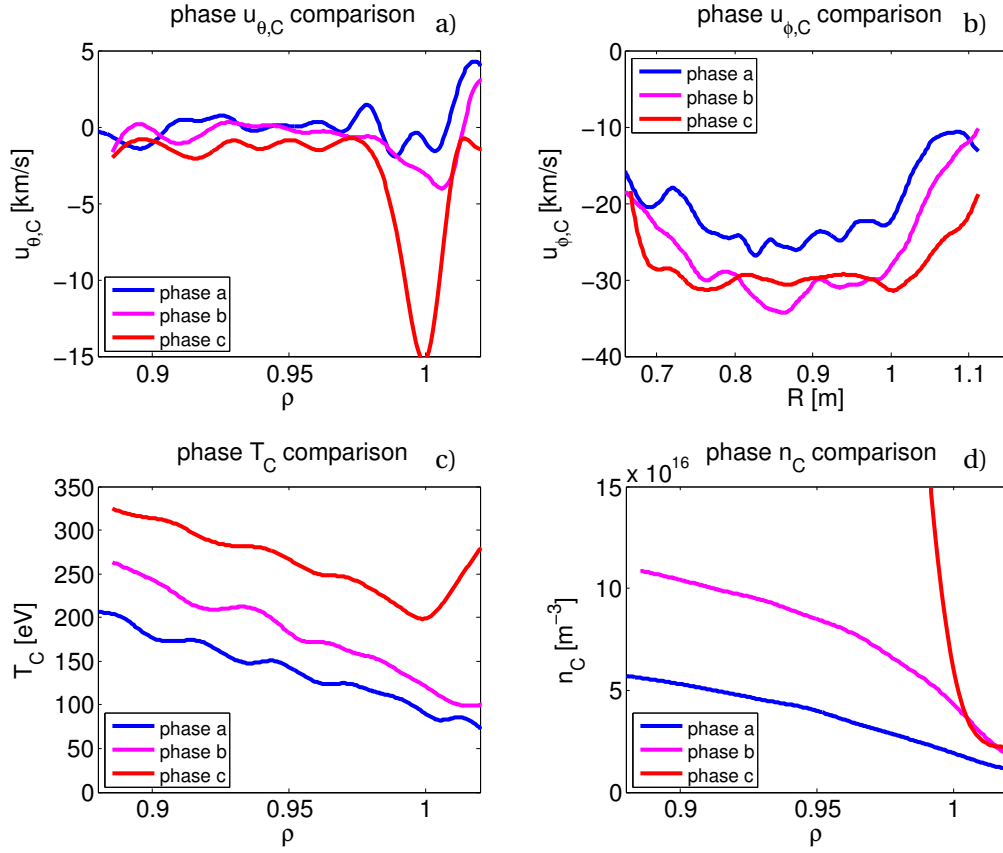
Figure 6.18: Profiles (averaged on a 200 ms time window) comparison in the three phases (a-below the threshold, b-at the threshold, c-during H-mode) of shot #55607 for (a) $u_{\theta,C}$, (b) $u_{\phi,C}$, (c) T_C and (d) n_C.

where it reaches values of $u_{\theta,C} \simeq -4$ km/s, which is still much lower than during phase-c, with typical values of $u_{\theta,C} \simeq -20$ km/s. Towards the core, for $\rho < 0.97$, the poloidal velocity remains negative but close to zero during all three phases.

Changes in the toroidal velocity are also observed (figure 6.18-b). In phase-b the toroidal velocity reaches the values of phase-c in the core (i.e. $u_{\phi,C} \simeq -30$ km/s), but in the edge it retains the conditions of phase-a, with a velocity close to -10 km/s. This shear in the toroidal velocity is also thought to be involved in the triggering of the transition, through its projection on $u_\perp$ [225].

The temperature profiles in phases a and b are linear inside the LCFS. At $\rho = 0.9$ T_i is 50 eV higher in phase-b than phase-a, consistently with the increased ohmic power. Their separation decreases at the LCFS, where their value is close to 100 eV, indicating an increase in the temperature gradient in phase-b. During the H-mode (phase-c), a temperature ≥ 200 eV is observed at the LCFS, while the same gradient as in phase-a is attained.
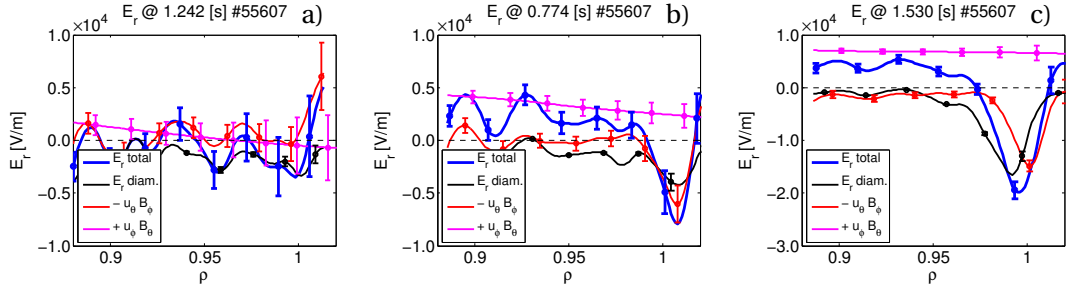
Figure 6.19: E_r profiles and its components (a) below the H-mode threshold, (b) next to the threshold and (c) during H-mode for shot #55607. The development of the electric field well is observed in phase-b.

The Carbon density profile shows the presence of a very small pedestal in phase-b 6.18-d, which is not present in phase-a.

The electric radial field, with its components, calculated from sample profiles, is shown in figure 6.19 for the three phases. The main difference between phase-a and phase-b is the development of a relatively shallow well $|E_r| < 10$ kV/m inside the LCFS, principally from the poloidal rotation term. This suggests that the increase in the electron diamagnetic direction of the poloidal velocity could be component of the trigger for the transition, as the contribution of the diamagnetic term to the radial electric shear is negligible in phase-b.

A possible alternative interpretation of phase-b is that there are rapid transitions to H-mode closely followed by back-transitions to L mode, a.k.a. dithering H-mode [226], with multiple events occurring during the CXRS integration time. The observed profiles would, in this case, suggest that the timescales of poloidal velocity increase are faster than the density pedestal build-up, which is, in turn, faster than the temperature profile increase. This interpretation is still compatible with the triggering mechanism being the increase of poloidal rotation, however a direct causality cannot be inferred unambiguously.

6.4 Comparison with neoclassical predictions

In this section the measured Carbon poloidal rotation is compared with predictions from neoclassical theory in the three phases defined in the previous section 6.3.2 for discharge #55597.

The expected neoclassical rotation is calculated using two different methods: employing the analytical formula of Kim-Diamond 4.28, introduced in chapter 4 and using the neoclassical code NEO (courtesy of Y. Camenen).

The code NEO [227] exploits an Eulerian numerical discretisation scheme, based on a δf expansion, for the solution of the multi-species first-order drift-kinetic-Poisson equations [228].

It provides second order neoclassical transport fluxes and first order flows, enabling a direct comparison with CXRS rotation measurements. The code includes self-consistent cross-species (e^-, ions and impurities) collisional coupling, intrinsically satisfying ambipolarity, allowing calculation of the electrostatic potential. It is therefore particularly suitable for studies of edge flows, and was employed here for this reason.

Both methods required the edge electron density and temperature profiles, that were estimated by fitting the TS experimental profiles with a cubic spline function over a selected time window in each phase, characterised by stable plasma conditions. In phase-a, a time window of 150 ms centered at $t_a = 1.075$ s was selected, in phase-b, the time window was of 300 ms centered at $t_b = 0.75$ s, and in phase-c, a window of 60 ms at 1.4 s was employed. The window in phase-c was smaller due to the strong time evolution of the electron density in ELM-free H-mode. For the Kim-Diamond formula ion species are considered thermalised $T_i = T_C$.

The predictions of the Kim-Diamond formula and the code NEO are shown in figure 6.20 together with the raw experimental CXRS results in the selected time window and a spline fit to the raw data. The experimental impurity measurements are in general in moderate agreement with the neoclassical predictions.

In phase-a and phase-b, the measured poloidal rotation is in excellent agreement with Kim-Diamond predictions, while NEO provides slightly faster flows in the electron diamagnetic direction, that remain, however, compatible with the measurements.

Predictions of the H-mode poloidal rotation (phase-c, figure 6.20-c) seem to be less compatible with the experimental results. In this phase, the analytical formula and NEO provide similar results, differing by less than 2 km/s over the whole profile. The neoclassical predictions are able to describe accurately the inner edge region $0.9 \leq \rho \leq 0.92$ and the rotation value at the LCFS, but fail in the prediction of the poloidal well shape, providing a wider and less steep rotation profile. This effect however can be ascribed to the TS spatial resolution ($\Delta R \simeq 1$ cm, or $\Delta \rho \simeq 0.03$), that was unable to resolve the pedestal features occurring at smaller spatial scales.
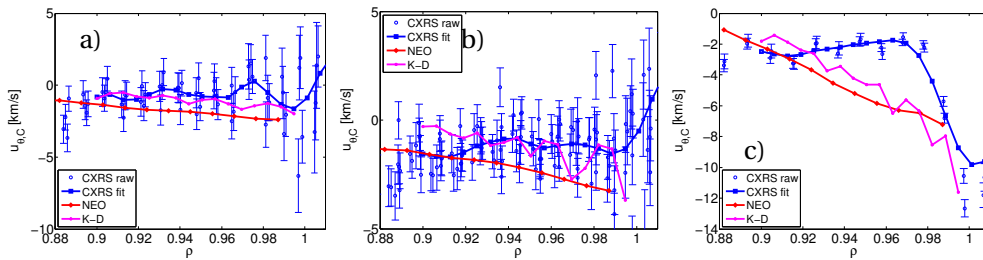
Figure 6.20: Comparison of experimental Carbon $u_{\theta,C}$ profiles with the neoclassical predictions of the NEO code and of Kim-Diamond formula 4.28 in the phases: (a) below the H-mode threshold, (b) next to the threshold and (c) after the transition to ELM-free H-mode, for shot #55597.

Actually the positions where the neoclassical predictions and the CXRS measurements agree, $\rho \simeq 0.93$ and $\rho \simeq 1$, correspond to TS measurements positions, somewhat inward with respect to the pedestal-top and at the bottom of the pedestal respectively (see figure 6.3). The third measurement position of TS in the range $0.9 \le \rho \le 1$ is at the top of the pedestal, influenced by the steep gradients of the region. Conversely, the lack of strong gradients in L-mode can explain the better agreement there. This give us confidence that improving the resolution of the TS diagnostic may result in a better agreement between the neoclassical predictions and the EDGE measurements.

It can be concluded that Carbon impurity flow at the edge of TCV is compatible with neoclassical theory, both in L-mode and H-mode operation regimes. An improvement of the electron pedestal measurement, with a higher spatial resolution TS diagnostic, is desirable to harden these conclusions.

6.5 Conclusions

The new high resolution CXRS EDGE system has permitted, for the first time in TCV, the measurement and characterisation of the Carbon behaviour across the L-H transition at the plasma edge and in the near-SOL. A relatively long integration time $\Delta t_{IT} = 12$ ms together with ELM-free H-mode operation were necessary with this diagnostic-beam based intrinsic rotation measurement, to minimise uncertainties in the Carbon profiles by optimising the photon statistics and reducing spectral perturbations.

The transition to H-mode is characterised by the formation of a narrow ($\simeq 5.5$ mm) and deep ($|u_{\theta,C}| \ge 20$ km/s) poloidal velocity well centered at the LCFS, by the development of a steep, continuously evolving, pedestal in n_C of typical width ≤ 15 mm and by the increase in Carbon temperature of $\Delta T_C \simeq 100$ eV across the whole profile.

The radial electric field was computed from the kinetic Carbon profiles. It is positive and relatively small, $E_{r,L} \ll 10$ kV/m, in L-mode, while a significant negative well ($|E_{r,H}| \le 30$ kV/m) develops just inside the LCFS after the transition to H-mode. The well parameters were computed after fitting by a Gaussian function, showing that the well depth decreases in time while widening, following a drop in the poloidal rotation term. On TCV, this is consistent with the $\mathbf{E} \times \mathbf{B}$ shearing, generated by the poloidal velocity, being the main responsible for the transition.
The averaged total E_r well width on TCV was found to agree with the scaling found from other machines [127].

The main ion perpendicular flow was estimated from E_r, n_e and T_C, showing that, in the E_r well region, the diamagnetic ion velocity balances the $\mathbf{E} \times \mathbf{B}$ drift. This suggests that the main ion pressure gradient is the dominant contributor to the electric field well, as reported in [93, 127].

The measured Carbon poloidal flows were finally compared with neoclassical predictions from the analytical formula of Kim-Diamond 4.28 and the code NEO. Good agreement is found for the L-mode profiles, with impurity rotating slowly, $|u_{\theta,C}| \ll 5$ km/s, in the electron diamagnetic direction. Only a reasonable agreement was obtained in H-mode, where the acceleration in the electron diamagnetic direction is qualitatively reproduced by the models, but with significant discrepancies in the profile shape. This discrepancy could be ascribed to the limited spatial resolution of the electron kinetic measurements, that can be further investigated with the increased resolution of the upgraded TS system (2017, but too late for this thesis).

These results were only obtainable with the periscope aided enhanced poloidal rotation measurements. Here again, the EDGE spectrometer's improved throughput captured the physical changes with a relatively short exposure time. This may be further improved by replacing the EDGE spectrometers' focussing lenses and by using the over a factor of 2 increase in the upgraded Thomson scattering system to resolve sharp features in the H-mode gradients.

TCV's regularly achievable Ohmic-only heated H-mode transition has been analysed for the first time and compares well with other H-mode transitions from other published machine data. The measured plasma rotation, and the deduced electric field, are reliably free of any direct contamination by any auxiliary heating scheme (particularly NBI heating). An increase in the temporal resolution is mandatory to harden these conclusions.
Smearing can be countered employing a shutter synchronised with the camera readout trigger, or by sharing the observation chords over more spectrometers such that the lower intensity chords are not mixed with the inner, much more intense, chords. The new, high intensity, heating beam features a very fast pulsing capability that may also be used to improve the temporal resolution, using the same method as employed on other machines, with the difference that the H-mode transition itself, does not depend on the NBI power, but remains ohmic, alone. These are necessary steps for reaching the temporal resolution limits dictated by the CX cameras of $\Delta t_{IT} \simeq 2$ ms retaining accurate measurements This would improve the constrains on the transition, but it would be insufficient to resolve the changes during the transition. By shading the unused spectral regions and using the "sensor cropped" readout mode, or alternatively the specialised "kinetic-spectral" readout mode, available with these CCD detectors [82], sub-ms measurements are possible, with effectively only photon statistics limiting the IT. CXRS measurements transition-resolved may thus become possible and thus provide a definitive causality between the changes in the poloidal rotation and L-H transition.

This work has, for the first time, achieved one of the main and initial goals of CXRS on TCV over more than a decade in probing the physics around an ohmically heated H-mode transition.

7 Conclusions and outlook

This thesis focussed on the upgrade and then the application of the CXRS diagnostic for studies of rotation and impurity behaviour in the TCV tokamak. The CXRS diagnostics, coupled with a low power diagnostic neutral beam injector in TCV, provides spatial and temporal resolved measurements of impurity intrinsic plasma rotation, usually Carbon, together with its density and temperature, by a spectroscopic analysis of an actively induced CX emission line.

The continuous search in research for better results and understanding results in always increasing challenging problems, that requires a continuous improvement in the diagnostic capabilities. An overview of the TCV legacy CXRS systems permitted to identify the possible upgrades, which culminated in the development of a new CXRS system, devoted to the study of the edge impurity behaviour. The new system attained unprecedented accuracy exploiting a new, in-house designed, high throughput lens spectrometer, by employing numerical-aperture matching optics and by improving the sampling viewing lines. The installation of a periscope with direct view on the DNBI was paramount to reach the target diagnostic space resolution ≤ 3 mm, while preserving the system étendue , in particular for the H-mode pedestal work. Furthermore the hardware optimisation and upgrade of the legacy systems continued during this work, with the replacement of the Acton HFS spectrometer by a SPEX750Mi model (same as LFS), and the upgrade of the VER spectrometer with a copy of the EDGE spectrometer, that improved the system transmission efficiency and the image quality, as well as the measurement accuracy. The transmission and resolution of the two toroidal systems was also improved with an optimised input optical system. These hardware optimisations were supported by improvements in the analysis routines, with a revision of the wavelength calibration function to include non-linear dispersion, improvements in the robustness and reliability of the minimisation spectral fitting algorithm and in the uncertainty estimation, and a complete characterisation of the cameras performance (linearity and saturation).

The upgraded CXRS diagnostic was successfully employed both in the continuation of previous lines of research, obtaining more sophisticated and reliable results, and in the opening of new search roads for spectroscopy at the SPC.

Characterising the absolute emissivity of H and D plasmas produced by a helicon source in RAID, was the first experimental application of the new spectrometer, that demonstrated the designed high optical quality, the great adaptability of the instrument and resulted in a successful commissioning of the EDGE hardware and software packages. The analysis of the measured emissivities through the CR code YACORA, provided the first estimation of the source negative ion production and level of dissociation for this source, which are relevant for applications in reactor-scale negative NBIs [58]. The antenna performance, if found to comply to the presented estimations in an extraction configuration, would allow an increase in the NBI source efficiency of $\simeq$ one order of magnitude, with potentially strong repercussions on the feasibility of a commercial fusion reactor, due to the importance of the heating scheme efficiency in the overall device energy balance.

Another application for the new spectrometer was the measurement of the fast ion D_α emission line by the survey FIDA diagnostic on TCV. The high quality of the measured spectra was used to accurately characterise the fast ion dynamics, that identified an anomalous fast ion transport mechanism and unexpectedly strong CX losses [229]. The high light efficiency and strong immunity to stray light were paramount to a reliable measurement. Following the results of the survey diagnostic, a FIDA system featuring a modified version of the EDGE spectrometer, optimised for the D_α spectral region, with viewing lines across the NBI was commissioned. A new spectrometer was mandatory to obtain active FIDA measurements, as the DNBI LOSs of the survey system had insufficient intensity, highlighting the limits of the active signal strength from the low power diagnostic beam. The design of a more sophisticated FIDA diagnostics is ongoing, with toroidal and poloidal viewing lines on the NBH for a complete characterisation of the fast ions distribution function and is expected to be constructed and installed on TCV in the coming months.

The combination of new spectrometers and/or enhanced measurement techniques was applied to two outstanding problems on TCV.

The study of the effects of ST on the impurity transport strongly benefited from the CXRS diagnostic improvements. Profiles with unprecedented spatial and time resolution were obtained from coherent averaging of the CXRS spectra, resulting in simultaneous profiles of C density, temperature and bulk rotation temporally resolved across the ST cycle. A novel technique that could externally set the ST timing employing ECRH modulation, i.e. ST locking, was developed and proved robustly reproducible over many experimental sessions, permitting a scan in ST period from 8 to 36 ms. The physics of the ST crash itself was used to simultaneously improve the synchronisation with CXRS acquisition, with a huge beneficial effect on the quality of the coherent averaging. The overall effect was to clearly separate the inter-crash to the crash dynamics that could then be compared to "natural" ST by calculating a ST-averaged behaviour for comparison with legacy ST studies. A co-current torque is detected acting in the core at the ST crash, resulting in hollow post-crash rotation profiles. Simultaneously the counter-current core momentum is redistributed to a ring region outside the ST inversion radius. This effect places a limit on the maximum rotation attainable for any particular plasma

conditions, explaining the $1/I_p$ scaling reported from TCV ST-unresolved intrinsic rotation measurements. Reversing the argument, the ST period and inversion radius can be used as actuators for rotation control in the absence of effective direct momentum injectors. This result shows that the internal, intrinsic, plasma rotation can be strongly affected by very fast MHD Tokamak phenomena that, like the electron kinetics, must be included in any model that hopes to predict plasma rotation in any future device.

The absolute calibration of the CXRS system permitted the measurement of the density profile evolution across the ST, with a most interesting event at the crash, where impurities are preferentially removed from the core (more than the main ions). In a reactor scenario this can be exploited for preventing impurity accumulation and for ash removal. Again, a model of impurity confinement that ignore these determinant MHD events (e.g. using turbulent and neoclassical transport alone) can not hope to predict the impurity transport behaviour on future machines.

The performance of the EDGE system was most strongly tested in the extreme conditions of the ELM-free H-mode pedestal. The new system was crucial in the characterisation of the changes in impurity parameters at the onset of H-mode, where a narrow and deep well in the poloidal velocity, that was impossible to observe with the legacy systems, was measured. An improvement in confinement during H-mode is confirmed by the development of a pedestal in the impurity density and the increase in the temperature. The Carbon kinetic profiles were then used to estimate the radial electric field, whose width agrees with the scaling found on other machines. The evolution of the E_r components suggests a strong importance of the poloidal rotation term in triggering the transition, although an increase in the temporal resolution (by a factor of $\simeq 5-10$) is mandatory to confirm this hypothesis. Further improvements in the system transmission, with adoption of single aspherical lenses and the replacement of the periscope window, are relatively simple upgrades that could overcome the current diagnostic resolution time limits for these plasma conditions. A more complicated, but potentially more advantageous, upgrade would be to exploit viewing lines on the NBH and a fast beam modulation. The higher emissivity of the NBI, due to the higher density, despite the reduction in the CX cross section for the 25 keV NBH, would permit a reduction of the diagnostic integration time to scales comparable to the transition, retaining a photon statistics sufficient for the measurement. This experiment would be even more productive with the second planned NBH, that should inject 50 keV neutrals into TCV, close to the optimal energy for the Carbon CX cross section. With fast NBH modulation of the TCV design, and the increased active emission, inter-ELM measurements would became possible, extending the accessible measurement space to ELMy H-mode and to studies on the transition itself.

The design, construction and use of the modular EDGE spectrometer has been demonstrated on TCV and a laboratory plasma device related to auxiliary heating on a fusion reactor. Together with the specialised data analysis techniques and detector optimisations, it represents a new spectroscopic "toolbox" for exciting new experiments on TCV. With increased dispersion, lens changes to extend operation into the UV and new detector modes, many new spectroscopic CXRS challenges can be attempted. Furthermore, following this work, the DNBI power

supplies may be upgraded to allow 1 ms full beam power modulation that can be used to access faster TCV events and further benefit from these increases in diagnostic sensitivity. It is, however, only with a combination of this kind of diagnostic enhancement, together with other diagnostic enhancements (notably the TS improvements), that some of the more speculative results of this thesis work can be hardened and new physics probed.

In the future, when the both 1 MW heating beams will be available on TCV, many new experiments on plasma ion dynamics will become accessible. By continuing to develop the DNBI view lines, together with new diagnostics on the heating beams themselves, the ion profiles can be tracked with and without axillary heating and the relaxation following strong heating can be measured. TCV's heating beams are to be mounted to provide an opposite toroidal torque. The ANDOR detectors used in all CXRS diagnostics feature a CAMLINK real-time output that can be used to extract and process the CXRS data in real time opening up the possibility of toroidal rotation RT control with all the possible effects on MHD modes and their stabilisation that may entail. Furthermore, together with real time control of a set of heating schemes (Ohmic, NBH and ECRH) this can provide a fusion testing device the ability to control the T_i/T_e ratio in addition to the usually implemented observables. This thesis has not only demonstrated that strong MHD events, such as sawteeth, can dominate the ion profiles but has demonstrated methods that resolve these effects in time. The measured profiles must now be modelled by the codes we use to predict future reactor behaviour and the physical processes that cause the observed behaviour identified. Since many other relevant MHD modes are known to affect the plasma behaviour (e.g. NTMs) it is legitimate to speculate that these observations should be extended to cover more of these phenomena. As a final example, fast particle ST-stabilisation, already observed on TCV [230]can be investigated and contrasted with the ECRH stabilisation results presented in this thesis.

A Survey FIDA diagnostic on TCV

Following the restart of TCV at the end of 2015, the intensive use in the MST1 campaign of a newly installed 1 MW NBI provided a strong demand of new diagnostic able to detect and characterise the fast ion population (max injection energy $\simeq 27$ keV) generated by the NBI. A survey FIDA diagnostic was therefore implemented, exploiting the spectrometer designed for SYS4.

A.1 FIDA principles

The fast ion D_α (FIDA) is a CXRS method applied to fast Deuterium ions [231]. The CX reaction of a fast D^+ with neutrals, either provided by NBI or penetrating into the plasma from the edge, provides excited fast ($\mathbf{v}_{D^0} \gg v_{T_i}$) recombined D^0 that emits line radiation.
FIDA exploits the Balmer Alpha emission line D_α ($n = 3 \rightarrow 2$) @ $\lambda_0 = 656.1$ nm to probe the fast ion distribution function, through the modification of the observed wavelength due to the Doppler shift:

$$\Delta\lambda_{D^0} = \frac{\lambda_0}{c}\,\mathbf{v}_{D^0} \cdot \mathbf{e}_{LOS} \tag{A.1}$$

The analysis of the spectrum is complicated by the property of the Doppler formula, which impedes resolved measurements in energy and pitch, since the same value of the projection of a particle velocity on the LOS direction $\mathbf{e}_{LOS}$ can be observed for different combinations of energy and pitch; the latter being defined as the ratio of the particle parallel (to the magnetic field) velocity over the velocity absolute value:

$$\text{pitch} = \frac{v_\parallel}{|v|} \tag{A.2}$$

Note that this degeneracy is irrelevant for CXRS measurements, where the distribution function is assumed to be Gaussian. As in the standard CXRS diagnostics, the radiance can be used to determine the density of the recombining ions, if the density of donor is known or can be estimated.

The interpretation of FIDA spectra is difficult, a direct deconvolution of the signal is not possible due to the unresolved energy-pitch distribution. A method to interpret quantitatively the FIDA spectrum, developed and implemented in [232], is to use a theoretically calculated neoclassical ion distribution function and simulating the corresponding D_α emission (synthetic spectrum), that can then be compared with the experimental measurements.

In the next sections, the first implementation of this diagnostic together with the data interpretation, as reported in [229], are explained.

A.2   FIDA on TCV

The first TCV FIDA survey diagnostic exploited the spectrometer of SYS4 for spectral analysis, using toroidal LOS borrowed from the CXRS LFS system (SYS1), as shown in figure A.1. The
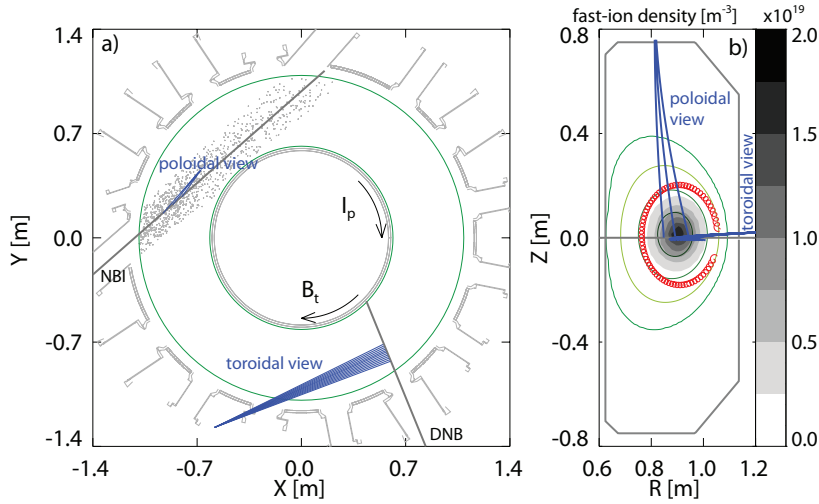
Figure A.1: NBI, DNBI and survey FIDA LOS (toroidal and poloidal) geometry. In red the orbit of a 25 keV ion with a 0.9 pitch.

fast ions are generated by ionisation of the neutrals injected by the NBI, whose geometry is also shown in figure A.1, together with the orbit (in red) of a 25 keV ion with a pitch of 0.9.

The active signal for this system (toroidal), is given by the interaction of the DNBI neutrals and the fast ions. The comparison of the acquired spectra, figure A.2-a, in the NBI ON and OFF phases, showed a strong passive D_α signal, generated by the interaction of the fast ions with the background neutrals, and an extremely weak active signal from the DNBI, as can be deduced by figure A.3-b, that is insufficient for the extraction of spatially resolved information on the fast ions. These considerations led to the installation of a further FIDA diagnostic with LOS intersecting the NBI itself, the poloidal viewing lines of figure A.1, and the construction of yet another dedicated spectrometer, with a design similar to that built for SYS4, but optimized for wavelengths in the D_α region, with a 2000 l/mm grating to improve the étendue at higher

wavelengths.
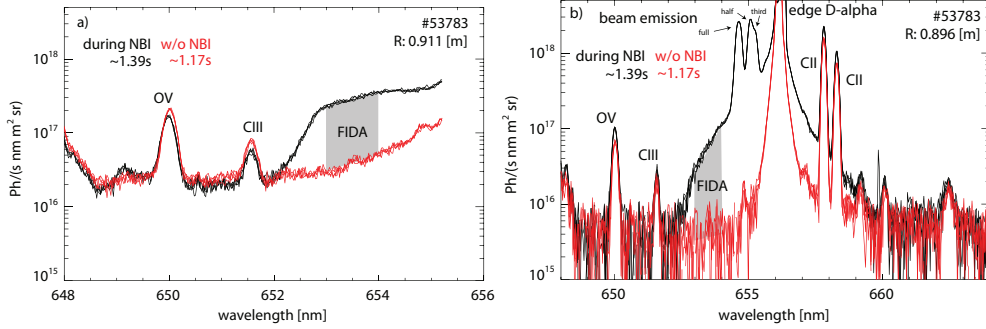
Figure A.2: Measured spectra from a central LOS of (a) the toroidal and (b) the poloidal FIDA systems, in the NBI ON (black) and OFF (red) phases.

Representative spectra of the poloidal FIDA system are shown in figure A.2-b, for both the NBI ON and OFF phases. In this system the active FIDA emission is produced by the NBI itself, while passive emission of the cold edge D_α line is minimised due to the LOS geometry, allowing the observation of the complete D_α spectrum with only a modest sensor saturation at 656.1 nm. This wavelength is avoided in the toroidal system to prevent over-saturation and possible damage to the CCD camera.

The time traces of the integrated FIDA signal, in the wavelength range $653 - 654$ nm, are shown in figure A.3 for both the toroidal and poloidal systems, and are used for a first interpretation of the measurements. As noted above, the radiation observed by the toroidal system is dominated
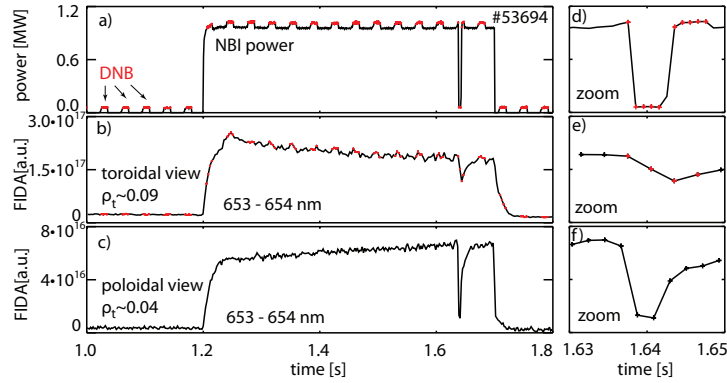
Figure A.3: Time evolution of the integrated ($653 - 654$ nm, in gray in figure A.2) FIDA signal for both (b) toroidal and (c) poloidal systems. (a) sum of the DNBI and NBI power. DNBI ON phases are marked in red.

by the passive FIDA emission. This is deduced from the low correlation of the integrated signal with the DNBI modulation, and from the but modest drop of the signal when the NBI is turned off at 1.63 s, explained by the relatively long slowing down time $\tau_s \simeq 60$ ms of the fast ions,

while the background neutrals (donors for the CX reaction) remain unaltered. The rapid response of the poloidal signal, in contrast, is ascribed to the sudden depleting of the donors from NBI, indicating that the active FIDA signal is the dominant component for this system.

The TRANSP code [233] was used to calculate the neoclassical fast ion distribution function, employing the NUBEAM package for modelling the NBI deposition and TORAY for ECRH-ECCD. A synthetic spectrum is then computed from the resulting distribution function through the Monte Carlo FIDA simulation code FIDASIM [234], accounting for the diagnostic LOS geometry, and then compared to the measurements. The passive FIDA emission is estimated
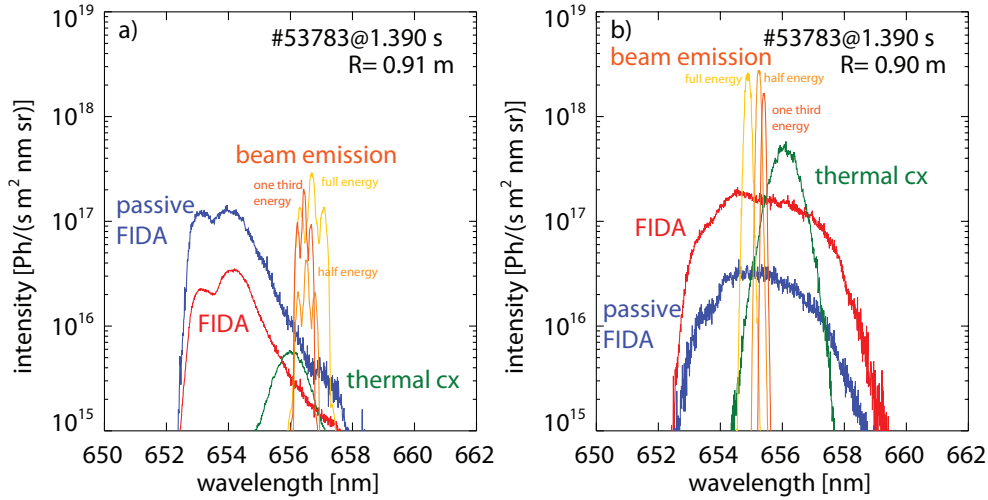
Figure A.4: Synthetic spectra for (a) toroidal-DNBI and (b) poloidal-NBI FIDA systems.

using the background neutral density from the FRANTIC code [235].

The output of FIDASIM for the L-mode, low density $n_e \simeq 2 \cdot 10^{19}$ 1/m^3 and high electron temperature $T_e \leq 4$ keV, discharge #53783 is shown in figure A.4, for the toroidal and poloidal systems. The estimated passive emission (blue) in the toroidal system is clearly dominating the FIDA signal (note the logarithmic scale), the active signal from DNBI (red) being almost one order of magnitude lower. The simulated spectra for the poloidal system, in contrast to the DNBI result, confirms that the active signal from NBI is stronger than the passive, permitting an easier reconstruction of the fast ion distribution profile.

A good match of the synthetic spectrum with measurements is obtained assuming a relatively long particle confinement time $\tau_p \simeq 14$ ms and anomalous fast-ion transport $\chi_a = 0.5$ m^2/s. Using these parameters also the predicted (from TRANSP) toroidal beta and loop voltage agree with the experimental measurements. This leads to an estimated NBI heating efficiency of 15% of the nominal beam power in low density plasmas, ascribed to strong fast-ion CX losses that competes with the fast-ion slowing down at these low plasma densities. These losses are caused by a high background neutral density in TCV, compared to other machines, hypothesis supported by both the toroidal FIDA and the CNPA measurements.

A.3 Conclusions

A survey FIDA system exploiting the spectrometer designed during this thesis, permitted the first FIDA measurements on TCV during the first MST1 campaign. Employing multiple systems, with viewing lines on both the DNBI and NBH, enabled a complete characterisation of the FIDA signal, characterised in TCV by a strong passive component.

A detailed analysis of the FIDA spectra and of CNPA data confirmed the presence of high background neutral densities together with an anomalous fast-ion transport, resulting in substantial CX losses and so in low NBI heating efficiency (at low density and high T_e).

From the results of the survey FIDA systems the design of a more sophisticated FIDA diagnostic is under development, with toroidal and poloidal viewing lines observing the NBI, potentially enabling a phase-space tomographic reconstruction of the fast-ion distribution and a better understanding of the anomalous transport mechanism. Some of the initial data from this work was published at the 2016 IAEA in Japan [236] and on PPCF [229].

B Details on line shapes

This appendix performs a detailed description of the CX emission line shape, explaining the typical approximations used for interpreting the CXRS measurements.

B.1 Emissivity in the coronal model

The spectral emissivity ϵ_λ [ph/s/m^3/sr/Å] due to CX line emission of the impurity ions, described by the distribution function $f_i(\mathbf{x_i}, \mathbf{v_i})$, with a donor $f_d(\mathbf{x_d}, \mathbf{v_d})$ can be calculated, in the coronal approximation (assuming all atoms are in their unexcited ground state), considering that the number of photons emitted (per unit time, volume and solid angle) in the wavelength range $d\lambda$ around λ is:

$$\epsilon_\lambda \, d\lambda = \frac{B_t}{4\pi} \int d\mathbf{v_d} \int d\mathbf{v_{i\perp}} \, f_d(\mathbf{v_d}) \, f_i(\mathbf{v_i}) \, |\mathbf{v_d} - \mathbf{v_i}| \, \sigma_{CX}\left(|\mathbf{v_d} - \mathbf{v_i}|\right) d\nu_{i\parallel} \tag{B.1}$$

where parallel and perpendicular directions for velocities are with respect to the LOS direction, and σ_{CX} [m^2] is the cross section for the CX process that populates the upper level of the emitted line. B_t is the branching ratio for the transition. This is usually stated in coronal models by the equation for the radiant flux per unit volume $I_{i \to k}$ [ph/s/m^3] for the transition $i \to k$:

$$I_{i \to k} = A_{i \to k} \, n^{*i} = \frac{A_{i \to k}}{\sum_j A_{i \to j}} \, n_1 \, n_d \, \langle \sigma_{1i} \, v \rangle = B_{i \to k} \, n_1 \, n_e \, \langle \sigma_{1i} \, v \rangle \tag{B.2}$$

where the excited population density n^{*i} [m^{-3}] is calculated from the ground level population n_1 through the direct CX rate coefficient $q_{1i} = \langle \sigma_{1i} \, v \rangle$. The bracket for a quantity $A(v)$ represent the integral:

$$< A > = \frac{\int A(v) \, f_1(v) \, f_d(v) \, dv^3}{\int f_1(v) \, dv^3 \, \int f_d(v) \, dv^3} \tag{B.3}$$

The branching ratio for the transition $B_{i \to k}$ is simply the contribution to radiative de-excitation

from spontaneous decay, given by the Einstein coefficient $A_{i \to k}$, to the total decay rate considering all the possible transition $\sum_j A_{i \to j}$, i.e. it's the ratio: $B_{i \to k} = A_{i \to k} / \sum_j A_{i \to j}$.

The relation between the parallel velocity and the wavelength is

$$\lambda - \lambda_0 = \frac{\lambda_0}{c} \, v_{i\parallel} \tag{B.4}$$

$$d\lambda = \frac{\lambda_0}{c} \, d v_{i\parallel} \tag{B.5}$$

with λ_0 [Å] the rest wavelength of the considered transition.

If the donors are neutrals of a neutral beam, their distribution function for each energy component can be described by a Dirac delta function in velocity space

$$f_d(\mathbf{x_d}, \mathbf{v_d}) = n_d(\mathbf{x_d}) \delta(\mathbf{v_d} - \mathbf{u_d}) \tag{B.6}$$

and equation B.1 reduces to (for each energy component)

$$\epsilon_\lambda \, d\lambda = \frac{B_t \, n_d}{4\pi} \int d\mathbf{v_{i\perp}} \, f_i(\mathbf{v_i}) \, |\mathbf{u_d} - \mathbf{v_i}| \, \sigma_{CX}(|\mathbf{u_d} - \mathbf{v_i}|) \, d v_{i\parallel} \tag{B.7}$$

Equation B.7 shows that even for the case of a perfectly mono-energetic neutral beam, the line shape (i.e. the spectral emissivity) can significantly deviate form the impurity velocity distribution function if the term $[|\mathbf{v_d} - \mathbf{v_i}| \sigma_{CX}(|\mathbf{v_d} - \mathbf{v_i}|)]$ vary significantly in the range of collision energies. We can express the relative velocity $v_r = |\mathbf{u_d} - \mathbf{v_i}|$ as function of the wavelength:

$$v_r = |\mathbf{u_d} - \mathbf{v_i}| = \sqrt{(\mathbf{v_{i\perp}} - \mathbf{u_{d\perp}})^2 + \left(\frac{c}{\lambda_0}(\lambda - \lambda_0) - \mathbf{u_{d\parallel}} \right)^2} \tag{B.8}$$

and, using the variable λ instead of $v_{i\parallel}$, recast equation B.7 in the form

$$\epsilon_\lambda \, d\lambda = \frac{B_t \, n_d}{4\pi} \int d\mathbf{v_{i\perp}} \, f_i(\mathbf{v_{i\perp}}, \lambda) \, v_r \, \sigma_{CX}(v_r) \, \frac{c}{\lambda_0} d\lambda \tag{B.9}$$

We consider now a thermalised population of impurity, its distribution function follows the Maxwell-Boltzmann velocity distribution function:

$$f_i(\mathbf{v_i}) = \frac{n_i}{\left(2\pi \sigma_i^2\right)^{\frac{3}{2}}} e^{-\frac{(\mathbf{u_i} - \mathbf{v_i})^2}{2\sigma_i^2}} \tag{B.10}$$

with n_i the impurity density, u_i the rotation velocity, or bulk impurity velocity, and σ_i the standard deviation of the Gaussian, that is linked to the impurity temperature by the equation (in SI units)

$$\sigma_i^2 = \frac{k_b \, T_i}{m_i} \tag{B.11}$$

with k_b the Boltzmann constant [J/K], T_i [K] the impurity temperature and m_i [kg] the impurity mass. The condition of small variation of the term $|v_r \sigma_{CX}(v_r)|$ is then met for low enough impurity temperatures. The replacement of the parallel velocity with the wavelength gives:

$$f_i(\mathbf{v_{i\perp}}, \lambda) = \frac{n_i}{\left(2\pi\sigma_i^2\right)^{\frac{3}{2}}} e^{-\frac{(\mathbf{u_{i\perp}} - \mathbf{v_{i\perp}})^2}{2\sigma_i^2}} e^{-\frac{\left(\mathbf{u_{i\parallel}} - \frac{c}{\lambda_0}(\lambda - \lambda_0)\right)^2}{2\sigma_i^2}} \tag{B.12}$$

and using the definitions for the central wavelength λ_1 and spectral standard deviation σ_λ:

$$\lambda_1 = \lambda_0 \left(1 + \frac{u_{i\parallel}}{c}\right) \tag{B.13}$$

$$\sigma_\lambda = \sigma_i \frac{\lambda_0}{c} = \sqrt{\frac{k_b T_i}{m_i}} \frac{\lambda_0}{c} \tag{B.14}$$

form equation B.12 we get:

$$f_i(\mathbf{v_{i\perp}}, \lambda)\frac{c}{\lambda_0} = \frac{n_i}{\left(2\pi\sigma_i^2\right)^{\frac{2}{2}}} e^{-\frac{(\mathbf{u_{i\perp}} - \mathbf{v_{i\perp}})^2}{2\sigma_i^2}} \frac{1}{\left(2\pi\sigma_\lambda^2\right)^{\frac{1}{2}}} e^{-\frac{(\lambda - \lambda_1)^2}{2\sigma_\lambda^2}} \tag{B.15}$$

Equation B.9 can be solved numerically for a generic distribution function $f_i(\mathbf{v_i})$, but usually a Maxwellian distribution (B.12) is assumed and the following approximations are used:

$$v_r = |\mathbf{v_i} - \mathbf{u_d}| \quad \simeq \quad |\mathbf{u_i} - \mathbf{u_d}| = v_{r,app} \tag{B.16}$$

$$\sigma_{CX}(|\mathbf{u_d} - \mathbf{v_i}|) \quad \simeq \quad \sigma_{CX}(v_{r,app}) \tag{B.17}$$

which allow an analytical solution to the integral in the form of a Maxwellian distribution:

$$\epsilon_\lambda(\epsilon_I, \lambda_1, \sigma_\lambda) = \frac{\epsilon_I}{\left(2\pi\sigma_\lambda^2\right)^{\frac{1}{2}}} e^{-\frac{(\lambda - \lambda_1)^2}{2\sigma_\lambda^2}} \tag{B.18}$$

where the constant ϵ_I is the line total emissivity [ph/s/m^3/sr]. Its value depends upon the impurity and donor density and the CX cross section at the beam velocity:

$$\epsilon_I = \frac{B_t}{4\pi} n_i n_d v_{r,app} \sigma_{CX}(v_{r,app}) \tag{B.19}$$

Since the relative velocity is unknown, the additional following approximation is commonly applied:

$$v_{r,app} \simeq |\mathbf{u_d}| \tag{B.20}$$
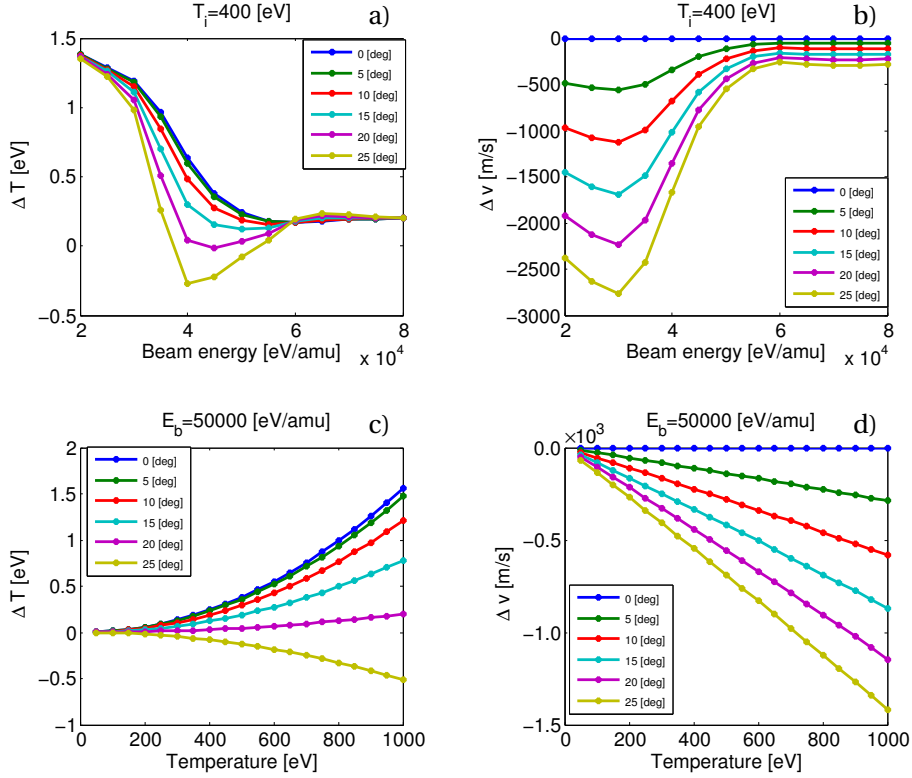
Figure B.1: Errors in the temperature ΔT (a and c) and rotation Δv (b and d) induced by neglecting cross section effects for selected LOS angles to the normal of the NB.

B.2 Cross section effects

The consequence of the approximations B.16 and B.17 were tested by solving numerically equation B.9 and comparing with the analytical solution B.18. Both functions were evaluated and then fitted with Bevington's Gradient Expansion Algorithm [94], i.e. the same algorithm used in the standard CXRS data analysis. The analytical solution is found to converge to the parameters input test value (T_i and v_i) which implies that the difference between the apparent values obtained from B.9 and the input values represent the error in the measurements introduced by the approximations B.16 and B.17.

These errors are termed 'effect due to the energy dependence of cross section' in [61, 76].

Figure B.1 shows the errors in temperature ΔT and rotation Δv induced by the approximations B.16 and B.17. The effect on velocity is present only when the LOS has a non vanishing projection in the beam direction (angle $\neq 0$), while the error in the temperature is always present.
This effect, considering all the LOS geometry of the CXRS systems, is negligible for typical TCV plasma parameters and is therefore neglected in the standard CXRS analysis.
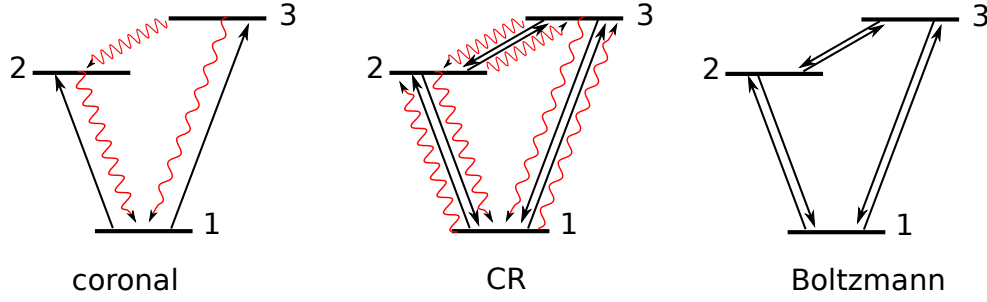
Figure B.2: Graphical representation of the coronal, the CR and the Boltzmann models applied to a 3 energy level atom. Straight lines are used for collisional transitions, wavy lines for radiative transitions.

B.3 Emissivity in the collisional radiative model

The collisional radiative model represents the most comprehensive model available in atomic physics [237]. It takes into account simultaneously all the collisional and radiative excitation and de-excitation processes. A graphical representation of CR model is shown in figure B.2, together with a representation of the coronal and Boltzmann models for comparison. In the coronal model, valid at low collisionality, only direct collisional excitation and radiative de-excitation are considered, while in the Boltzmann model, valid at high collisionality, only collisional processes need to be considered.

A similar derivation as in section B.1 of the emissivity can be performed in the CR model, by substituting the CX direct excitation cross section with the effective cross section calculated by the model. The dominant processes that modify the emission are the redistribution of the energy levels within the n-shell (l-mixing) and the radiative cascade from upper levels. The resulting line shape is still described approximatively by the Gaussian of equation B.18 but with a modified total emissivity ϵ_{I-CR}:

$$\epsilon_{I-CR} = \frac{1}{4\pi} n_i n_d q^{eff}(u_d, n_e, T_e, B) \tag{B.21}$$

where q^{eff} is the effective emission coefficient for the transition, that depends also upon plasma parameters and the background magnetic field.

The description above assumes a single line emission from a transition $n \rightarrow n'$. The L-S coupling removes the energy degeneracy in l developing a fine structure for the atomic levels that leads to multiple transitions ($nl \rightarrow n'l'$) with slightly different wavelength (multiplet emission). The line emission is therefore a sum of Gaussian functions of the form B.18 having different central wavelength $\lambda_{1,l}$ but still the same variance. The fine structure is not resolved by CXRS spectrometers, and since a sum of closely spaced Gaussian functions is approximatively Gaussian, its effect on the line shape is a broadening $\sigma_\lambda \rightarrow \sigma_{\lambda-tot}$ and a shift in the central wavelength $\lambda_1 \rightarrow \lambda_{tot}$ of the total signal, that depends on plasma parameters.

Appendix B. Details on line shapes

Taking into account the different contributions due the donor excited level k for each beam energy component (index b) the total CX emissivity can be written as:

$$\epsilon_{tot} = \sum_k \sum_b \sum_l \epsilon_\lambda(\epsilon_{I-CR,k,b,l}, \lambda_{1,l}, \sigma_\lambda) \tag{B.22}$$

where the emissivity $\epsilon_{I-CR,k,b,l}$ reads:

$$\epsilon_{I-CR,k,b,l} = \frac{1}{4\pi}\, n_i\, n_{d,k,b}\, q^{eff}_{k,l} \tag{B.23}$$

where $n_{d,k,b}$ is the density of donors at level k of beam's energy component b and $q^{eff}_{k,l}$ is the effective emission coefficient for the transition $(nl \rightarrow n'l')$ from donors at excited level k.

The spectral radiance L_{LOS} [ph/s/m^2/sr/Å] measured by a diagnostic LOS is then:

$$L_{LOS}(\lambda) = \int_{LOS} \epsilon_{tot}(\lambda, s)\, ds \tag{B.24}$$

The CXRS analysis in TCV employs equations B.24 and B.22 to calculate the impurity density from radiance measurements, accounting for the four beam energy components $b = (1,2,3,4) \rightarrow [E\ E/2\ E/3\ E/18]$ and for the ground and first exited donor levels $k = (1,2)$.

C Beam excited population

The program ADAS 310 is used to calculate R_{n1} the ratio of excited (level n) to ground ($n = 1$) neutrals of the beam. It calculates the excited population structure by solving the statistical balance equation:

$$
\sum_{n'>n} \left[A_{n'\to n} + N_e q^{(e)}_{n'\to n} + N_p q^{(p)}_{n'\to n} + N^{(imp)} q^{(imp)}_{n'\to n} \right] N_{n'} +
$$

$$
+ \sum_{n''<n} \left[N_e q^{(e)}_{n''\to n} + N_p q^{(p)}_{n''\to n} + N^{(imp)} q^{(imp)}_{n''\to n} \right] N_{n''} +
$$

$$
+ N_e N_+ \alpha^{(r)}_n + N_e^2 N_+ \alpha^{(3)}_n + N_H N_+ \alpha^{(cx)}_n + \int u(\nu) B_{k\to n} dk =
$$

$$
= \left\{ \sum_{n'>n} \left[N_e q^{(e)}_{n\to n'} + N_p q^{(p)}_{n\to n'} + N^{(imp)} q^{(imp)}_{n\to n'} \right] + \right.
$$

$$
+ \sum_{n''<n} \left[A_{n\to n''} + N_e q^{(e)}_{n\to n''} + N_p q^{(p)}_{n\to n''} + N^{(imp)} q^{(imp)}_{n\to n''} \right] +
$$

$$
\left. + N_e q^{(e)}_{n\to \epsilon} + N_p q^{(p)}_{n\to \epsilon} + N^{(imp)} q^{(imp)}_{n\to \epsilon} + \int u(\nu) B_{n\to k} dk \right\} N_n \tag{C.1}
$$

where N_n is the density of the beam's atom in the excited state n, N_e the electron density, N_+ the ionized beam's atoms density, N_p the density of plasma hydrogen nuclei and N_H the density of neutral atoms in the plasma other then the beam's. The collective rate coefficients q are used to include the effects of electron collisional excitation ($q^{(e)}_{n''\to n}$ and $q^{(e)}_{n\to n'}$) and de-excitation ($q^{(e)}_{n'\to n}$ and $q^{(e)}_{n\to n''}$), ion collisional excitation and CX ($q^{(p)}_{n''\to n}$ and $q^{(p)}_{n\to n'}$) and de-excitation ($q^{(p)}_{n'\to n}$ and $q^{(p)}_{n\to n''}$), and similar for the impurity, Carbon in this case, and $q_{n\to \epsilon}$ denotes the rate coefficient for ionization due to electrons $q^{(e)}_{n\to \epsilon}$, ions $q^{(p)}_{n\to \epsilon}$ and impurity $q^{(imp)}_{n\to \epsilon}$. $\alpha^{(r)}_n$, $\alpha^{(3)}_n$ and $\alpha^{(cx)}_n$ are the radiative, three-body and CX rate coefficients respectively. A and B are the Einstein coefficients and $u(\nu)$ the radiation field energy density. Equation C.1 assumes statistical population for the l states within each n state and it is solved with single state resolution up to the level $n = 20$, for higher states a condensed representation is used up to the level $n = 110$. It is also assumed that the ions and electrons are thermalised, $T_i = T_e$.

The output of the program ADAS 310 are the Saha-Boltzmann deviation factors b_n and the

normalized populations α_n, that satisfy the following relationships:

$$N_n = N_n^{(S)} b_n \tag{C.2}$$

$$b_n = F_n^{(1)} \frac{N_1}{N_+} + F_n^{(2)} + F_n^{(3)} \frac{N_H}{N_e} \tag{C.3}$$

$$\alpha_n = \frac{N_n}{b_n N_+} = \frac{N_n^{(S)}}{N_+} \tag{C.4}$$

where $N_n^{(S)}$ is the Saha-Boltzmann population for the level n, $F_n^{(1)}$, $F_n^{(2)}$ and $F_n^{(3)}$ are the contributions to the corrector factor b_n due to excitation processes, free-electron capture and CX respectively. To evaluate the ratio $R_{n1} = \frac{N_n}{N_1}$ of the beam's donors for CXRS, only the $F_n^{(1)}$ contribution is needed, as explained in [238], and enters the equation:

$$R_{n1} = \alpha_n * F_n^{(1)} \tag{C.5}$$

The program ADAS 310 was used to generate a lookup table, with the parameters shown in table C.1, that is used to compute R_{n1} for a plasma within the studied parameter range (and DNBI energies). In figure C.1 the ratio R_{21} is shown as function of the beam energy, T_e, n_e and Z_{eff}. The four main beam energy components, namely full, one half, one third and one eighteenth of the nominal energy $E_{full} = 5.0 \cdot 10^4$ [eV] are shown with dashed lines, with the corresponding averaged value, weighted with the nominal beam energy fraction f_n (expressed as density fraction). The measured beam energy current fraction is $f_c = [0.584\ 0.095\ 0.291\ 0.03]$, and is calculated from the total extracted current J_{tot}:

$$J_{tot} = \sum_k J_k \tag{C.6}$$

with the current value J_k for the energy fraction k given by

$$J_k = f_{ck} J_{tot} = q\, v_k\, n_k \tag{C.7}$$

where q [C] is the fundamental electrical charge, v_k [m/s] the velocity of component k and n_k [m^{-3}] its density. From the relationships

$$f_{ck} J_{tot} = q\, v_k\, n_{tot} f_{nk} \tag{C.8}$$

quantity	range	units
T_e	$10 - 3\ 10^4$	eV
n_e	$10^{10} - 5 \cdot 10^{15}$	cm^{-3}
Z_{eff}	$1 - 5$	-
Beam energy	$10^3 - 5.55 \cdot 10^4$	eV/amu

Table C.1: Parameters used in the program ADAS 310 to generate the lookup table for the estimation of the excitation fraction.
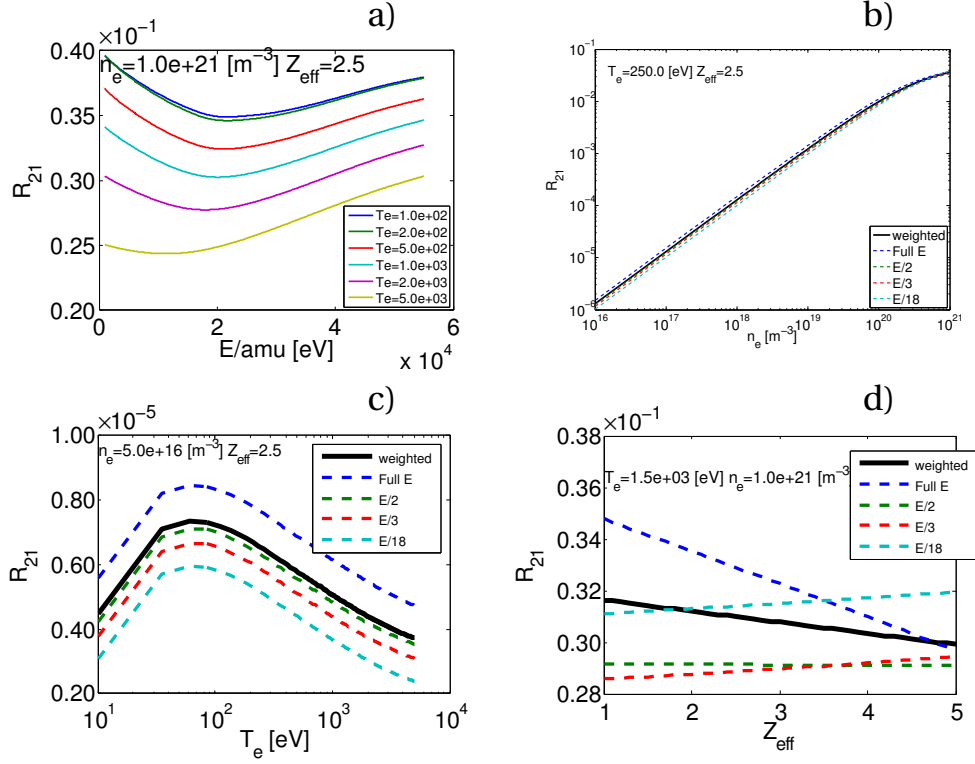
Figure C.1: Ratio R_{21} of excited to ground beam neutrals as function of: (a) neutral beam energy, (b) electron density, (c) electron temperature, (d) Z_{eff} (only Hydrogen and Carbon). The reference full energy is 50 keV/amu.

where f_{nk} is the density fraction for beam energy component k, we can find:

$$f_{nk} = \frac{J_{tot}}{n_{tot}} \frac{1}{q\,v_k} f_{ck} \propto \frac{f_{ck}}{v_k} \tag{C.9}$$

and the beam energy density fractions are $f_n =$ [0.433 0.10 0.373 0.094].

The ratio R_{21} has a maximum for temperature $T_e \simeq 100$ eV and increases with the density, almost following a power law (linear in the logarithmic plot of figure C.1-(b)). The dependence on Z_{eff} is linear, as shown in figure C.1-(d). An insensitivity of the ratio R_{21} to the beam energy is noticeable, the values are close for all the beam energy components, allowing the application of the weighted ratio for all the plasma cross section, and neglecting the differential attenuation of beam energy components (higher at lower energy). The dependence on T_e and n_e is not negligible and local values, from experimental measurements, are necessary to evaluate the population ratio. Notice that the ratio of excited $n = 2$ to ground level neutrals for typical TCV parameters ($T_i = 500$ eV, $n_i = 5 \cdot 10^{19}$ m^{-3}, $Z_{eff} = 2.5$) is $R_{21} \simeq 0.005$.

D Spectrometer description

This appendix is devoted to a theoretical description of the lens spectrometer, with the aim of understanding the performance and transmission properties.

D.1 Equations and conventions

Formulas and conventions used in the description of the spectrometer (and in the functions on the SPC computational cluster LAC) are explained. The angles measured from the grating normal (α_0 incidence optical axis angle, β_0 diffraction optical axis angle and θ scan angle) are shown in figure D.1, with the positive direction defined in the counter-clockwise direction (top-view). In the figure these angles are all negative ($\alpha_0 < 0$, $\beta_0 < 0$, $\theta < 0$ and $|\beta_0| < |\theta| < |\alpha_0|$). The angle ϕ, called half-included angle, is positive defined and is half the angle between the incident direction and diffracted direction. The following relations are easily verified:

$$\theta = \frac{1}{2}(\alpha_0 + \beta_0) \tag{D.1}$$

$$2\phi = \beta_0 - \alpha_0 \tag{D.2}$$

$$\theta = \alpha_0 + \phi = \beta_0 - \phi \tag{D.3}$$

The grating equation is

$$\lambda = \frac{n\,d}{m}\cos\gamma\,(\sin\alpha + \sin\beta) \tag{D.4}$$

where λ is the radiation wavelength [Å], α is the angle of incidence (the subscript 0 refers to the optical axis, without it a generic beam is considered), β is the angle of diffraction, γ is the tilt angle in the vertical direction of the light beam with respect to the optical axis, n is the air refraction index ($n = 1.00027$ is assumed), d is the grating groove spacing (measured in [Å/groove], corresponding to $d = 10^7/G$ for the grating groove density G [groove/mm]) and m

is the diffracting order. The rule to distinguish the sign of the diffracting order is the following

$$\beta \quad > \quad -\alpha \quad \text{positive order: } m > 0 \tag{D.5}$$

$$\beta \quad = \quad -\alpha \quad \text{mirror configuration: } m = 0 \tag{D.6}$$

$$\beta \quad < \quad -\alpha \quad \text{negative order: } m < 0 \tag{D.7}$$

and is shown in figure D.2 for negative α. For the EDGE spectrometer configuration the diffracting order is negative, $m = -1$ (see figure D.1).

The components of a lens-based spectrometer (figure D.3) are:

- Entrance slit;

- Collimating lens;

- Diffraction grating;

- Focusing lens;

- CCD detector.

The collimating lens (a.k.a. first lens, or lens n.1) has a focal length f_1 and a diameter D_1 (both measured in [mm]). Similarly the focusing lens (a.k.a. second lens, or lens n.2) has a focal length f_2 and a diameter D_2.
The commercial SRL Nikon lenses used for the EDGE spectrometer are composed of 12 'simple' lenses and the focal length is defined in the lens specs, $f = 200$ mm (it is measured from the rear nodal point, which is next to the diaphragm). D is then the diameter of the bigger (frontal) lens, $D = 100$ mm, resulting in an f-number $f_\# = \frac{f}{D} = 2$.

A generic point in the object plane (plane of the entrance slit) is represented by the coordinate (x_1, y_1), with the x coordinate in horizontal direction (that is the dispersion direction) and the y coordinate in the vertical direction. Similarly a point in the image plane, where the CCD is located, has coordinate (x_2, y_2). The positive direction for the x coordinate follows by the definition of the angle sign convention, from the relations:

$$\alpha \quad = \quad \alpha_0 + \tan^{-1}\left(\frac{x_1}{f_1}\right) \tag{D.8}$$

$$\beta \quad = \quad \beta_0 + \tan^{-1}\left(\frac{x_2}{f_2}\right) \tag{D.9}$$

and is shown in figure D.4, valid for both the object and image planes. The positive x direction points to the left, as seen from the lens position, or in general as seen by the grating position.
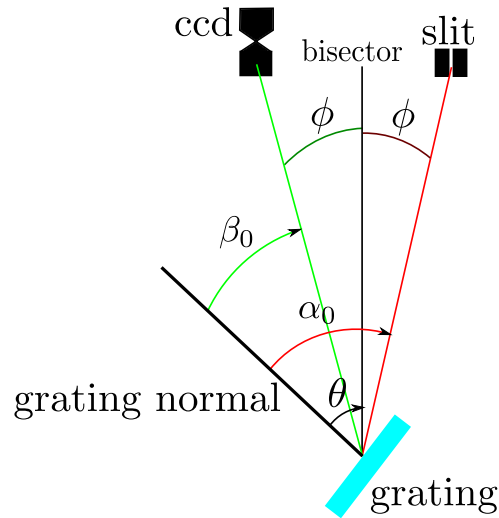
Figure D.1: Angles definition: in red incident optical axis and its angle with the grating normal α_0, in green diffracted optical axis and its angle with the grating normal β_0. The bisector divides the angle between the incident and diffracted optical axis in two equals angles, named half-included angle, ϕ. Also shown is the scan angle θ, the angle between the grating normal and the bisector. The positive direction is counter-clockwise as viewed from the top.
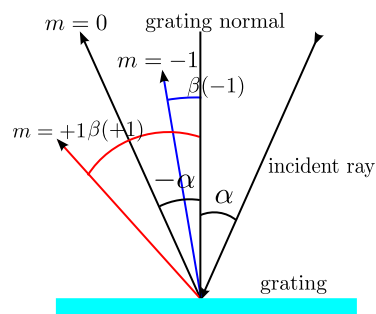
Figure D.2: Diffracting order definition.
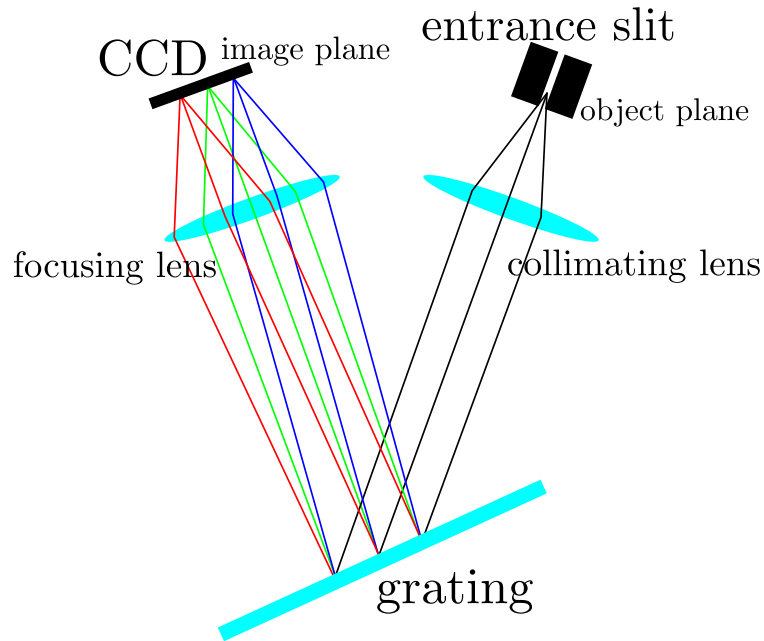
Figure D.3: Spectrometer basic components. The object and image planes are also shown.
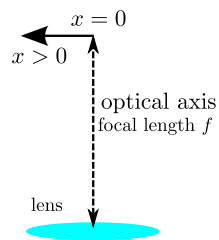
Figure D.4: Positive x direction: pointing to the left both for the object and image planes, as seen from the lens.
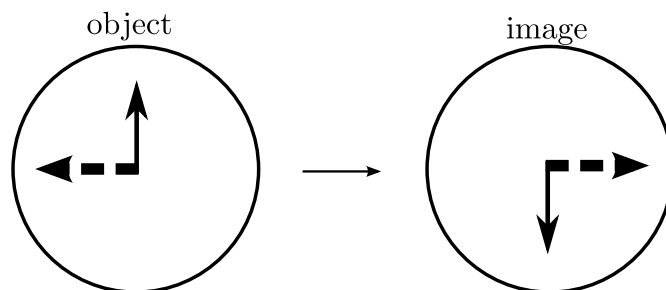
Figure D.5: The image produced by the EDGE spectrometer (see figure D.3) of an object is flipped in both horizontal and vertical directions in the chosen reference system, i.e. image viewed from the last lens towards the screen (or CCD sensor). Notice that with the usual optical reference system (i.e. viewing the image from behind the screen) only the vertical direction would be flipped, due to the grating that behaves as a mirror.

The positive y direction is the ascending vertical direction in both the planes, so that:

$$\tan\gamma = \frac{y_1}{f_1} = \frac{y_2}{f_2} \tag{D.10}$$

Notice that this is not the typical definition of reference system used in optics, since the image of a single lens in this coordinate system is reversed only in the vertical direction, and not in the horizontal one, while in the usual reference system both direction would be flipped.

The main spectrometer parameters are defined as follow:

- Horizontal magnification, relating the entrance slit width W_{slit} [mm] with the width of its image in the image plane (on the CCD) W'_{slit}

$$M_{hor} = \frac{W'_{slit}}{W_{slit}} = \frac{f_2 \, \cos\alpha}{f_1 \, \cos\beta} \tag{D.11}$$

- Vertical magnification, relating the entrance slit height h_{slit} with the height of its image in the image plane (on the CCD) h'_{slit}

$$M_{ver} = \frac{h'_{slit}}{h_{slit}} = \frac{f_2}{f_1} \tag{D.12}$$

- Reciprocal linear dispersion [Å/mm]

$$\frac{\partial\lambda}{\partial x_2} = \frac{d\,n}{m\,f_2}\cos\gamma\,\cos\beta\,\cos^2(\beta - \beta_0) \tag{D.13}$$

which is one of the most important quantities for a spectrometer. It measures how squeezed together the wavelengths are on the sensor;

- Resolving power

$$R = \frac{\lambda}{\delta\lambda} = \frac{n}{\lambda}W_{LUX}\left|\cos\gamma\right|\left|\sin\alpha + \sin\beta\right| \tag{D.14}$$

where $\delta\lambda$ is the smallest difference in wavelengths that can be detected and W_{LUX} is the illuminated width of the grating (it can be smaller than the grating width W_{gr}). This is the theoretical value, but resolution is often limited by diffraction;

- Throughput or étendue [m^2 sr]:

$$G_e = A\Omega \tag{D.15}$$

characterizes the ability of an optical system to accept light. Here A is the area of the limiting element (entrance slit for a spectrometer) and Ω the solid angle of acceptance for an incoming beam. The main purpose of the EDGE spectrometer was to increase

the CXRS system throughput with respect to the legacy systems, to improve the photon statistics. An increase of one order of magnitude in the system étendue permitted the unprecedented accurate measurements presented in this thesis.

- Spectral bandpass (or spectral line-width) [Å], calculated for the central wavelength

$$\Delta\lambda_{line} = \frac{d\,n}{m}\frac{W_{slit}}{f_1}\cos\alpha_0 \qquad\qquad (D.16)$$

which depends on the horizontal magnification and on the dispersion of the instrument. It determines the instrumental function of the spectrometer, since monochromatic light entering the slit forms an image on the sensor having this width. To resolve features of a wavelength size $\Delta\lambda$, the spectral bandpass must be smaller than that: $\Delta\lambda_{line} < \Delta\lambda$. It should be noted that the minimum limit for the spectral bandpass $\delta\lambda$ is set by the resolving power, hence decreasing the entrance slit width to improve (i.e. decrease) the spectral bandpass only works above this value. On the other hand a high resolving power is only possible in conjunction with a small spectral bandpass. This argument encourages the reduction of the slit width, however, reducing the entrance width reduces the system throughput, i.e. the quantity of light transmitted by the spectrometer, that can result in inaccurate measurements. Optimising the measurements usually means to reach a good trade-off between spectral bandpass and throughput.

- Wavelength range on the sensor [Å]

$$\Delta\lambda_{range} = \frac{d\,n}{m}\frac{W_D}{f_2}\cos\beta_0 \qquad\qquad (D.17)$$

with W_D the width of the detector in [mm].

It's worth notice that, with this conventions, the image of an object for the EDGE spectrometer design is flipped both in the horizontal and vertical direction (see figure D.5).

The spectral image of a vertical slit on the sensor is approximatively parabolic, due to the dependence of the dispersion on the tilt angle γ for non axial rays. By expanding the grating equation D.4 for a wavelength λ_c, centered at an angle β_c for $\gamma = 0$, the following equation describing the slit image curvature can be found [93]:

$$\Delta x_2 \simeq \frac{n\,d\,\lambda_c}{2m\,f_2}\frac{\sec^2\left(\beta_c - \beta_0\right)}{\cos\beta_c}(\Delta y_2)^2 \qquad\qquad (D.18)$$

The slit curvature must be considered in the spectrometer wavelength calibration and in the diagnostic design. A strong slit curvature can degrade the instrumental function (IF) quality of the spectrometer when combined with pixel binning. It is possible to design curved slit in order to obtain a straight slit image, but the correction is only exact at a single wavelength, limiting the usability of the spectrometer.

Parameter	Value	Parameter	Value
Angle θ	-40.131 deg	Angle ϕ	10 deg
f_1	200 mm	f_2	200 mm
Grating width W_{gr}	138 mm	Grating height	118 mm
Groove density G	2400 groove/mm	Diffraction order m	-1
Slit width W_{slit}	0.1 mm	Slit height h_{slit}	8 mm
Distance Z_1	380 mm	Distance Z_2	380 mm
Horizontal magnification M_{hor}	0.74	Vertical magnification M_{ver}	1
Resolving power R	$3.312 \ 10^5$	Wavelengths range $\Delta\lambda_{range}$	147 Å
Spectral bandpass $\Delta\lambda_{line}$	1.33 Å	or	4.6 pix
Slit max. curvature	0.083 mm	or	5.2 pix
Reciprocal linear dispersion	18 Å/mm	or	0.288 Å/pix

Table D.1: Edge spectrometer parameters at central wavelength 529 nm.

The wavelength in (x_2, y_2) as function of x_1, y_1, θ, ϕ and all the other spectrometer parameters, as well as the quantities mentioned above, are calculated (on LAC) by the function grating_lambda.m. The results for the EDGE spectrometer configuration are shown in table D.1.

D.2   Spectrometer transmission

It is of fundamental importance studying how the light propagates inside the spectrometer, in order to estimate and maximize the transmission efficiency, particularly at the target working wavelengths. The overall transmission is the product of the lens transmission, the grating transmission and the spectrometer's geometric transmission.

The lens transmission coefficient $T_{lens}(\lambda)$ can be estimated by the number of elements in the lens or measured directly. The diffraction grating transmission coefficient $T_{gra}(\lambda)$ is usually provided by the manufacturer. The following analysis of the geometric transmission $T_G(\lambda)$ of the spectrometer assumes that the losses are engender from the geometrical mismatch of the light ray with the various components (vignetting).

The object is a point source in the position (x_1, y_1) characterised by a numerical aperture NA, so that the cone of light emitted by the object has an half angle $\Psi = \sin^{-1}(NA/n)$. The lenses are represented by a simple thin lens with focal length f_1 and f_2 respectively. The geometric transmission is defined as:

$$T_G(\lambda) = \frac{S_{over-f2}}{S_{tot-f2}} \tag{D.19}$$

where S_{tot-f2} is the area of the light beam, of wavelength λ, projected on the second lens's surface plane without considering any vignetting, and $S_{over-f2}$ is the same quantity, but considering vignetting due to all the spectrometer components.

D.2.1 Lens-grating distance

The distances between the grating centre and the two lenses has to be minimized in order to improve the geometrical transmission, as discussed in the next section. The solution of this simple but tedious geometrical problem is:

$$Z_1 = \frac{1}{4}\frac{1}{\tan\phi}(D_1 + D_2) - \frac{1}{4}\tan\phi\,(D_1 - D_2) \tag{D.20}$$

$$Z_2 = \frac{1}{4}\frac{1}{\tan\phi}(D_1 + D_2) - \frac{1}{4}\tan\phi\,(D_2 - D_1) \tag{D.21}$$

where Z_1 and Z_2 are the requested distances.

These are the closest theoretical positions for optimising transmission, but taking into account the mechanical constrains these distances for any real device are usually longer, and those values should be used for the computation of the transmission.

D.2.2 Beam propagation

To calculate the areas in equation D.19, a coordinate system is defined with the origin in the object plane, at the optical axis. The x coordinate is defined as above in the dispersion direction, positive when pointing towards the left as seen from the grating, the y coordinate in the ascending direction, and the z coordinate coinciding with the optical axis (see Figure D.6 and Figure D.7). We follow the beam propagating in the z direction. The light beam area, i.e. the projection of the beam in the plane perpendicular to the optical axis, will be generically described by an ellipse of equation:

$$\frac{\left[x - x_0(z,\beta)\right]^2}{r_x^2(z,\beta)} + \frac{\left[y - y_0(z)\right]^2}{r_y^2(z)} \leq 1 \tag{D.22}$$

where x_0 and y_0, the coordinate of the centre of the ellipse, depends on the position on the axis z. x_0 is also function of the angle β. r_x and r_y describe the extent of the beam in the x and y directions.

As the beam propagates, 4 zones are identified:

- Zone 1 ($0 < z \leq f_1$): the beam's area is a circle centered at ($x_0 = x_1$, $y_0 = y_1$) and increasing in radius with z, due to the divergence Ψ.

- Zone 2 ($f_1 \leq z < f_1 + Z_{1-mod}$): the circular shape (in the optical axis reference frame) is constant, i.e. perfect beam collimation is assumed. The shape in the beam reference frame is elliptic. The centre translate both in x and y directions.

- Zone 3 ($z = f_1 + Z_{1-mod}$): the beam is "reflected" by the grating (with diffraction angle

β) and is stretched in the x direction (horizontal magnification), becoming elliptic.

- Zone 4 ($f_1 + Z_{1-mod} < z \leq f_1 + Z_{1-mod} + Z_{2-mod}$): the beam's cross section remains elliptic, while the centre translates in the x direction (for light with diffraction angle $\beta \neq \beta_0$) and keep translating in the y direction.

where the quantity Z_{1-mod}, the distance in z direction from the first lens to the point of intersection of the beam with the grating, is different from Z_1 due to the tilt of the beam with respect to the optical axis for a source with initial position $x_1 \neq 0$ (see Figure D.7 and Figure D.8). From Figure D.8 the following equations can be verified:

$$Z_{1-mod} = Z_1 - x_1 \left(1 - \frac{Z_1}{f_1}\right)\cos(\alpha - \alpha_0)\frac{\sin\alpha_0}{\cos\alpha} \tag{D.23}$$

The quantity $x_{0G} = x_0(f_1 + Z_{1-mod})$, the horizontal displacement of the beam calculated at the grating-beam crossing point $z_G = f_1 + Z_{1-mod}$ in the first lens optical axis reference system is:

$$x_{0G} = x_1 \left(1 - \frac{Z_1}{f_1}\right)\cos(\alpha - \alpha_0)\frac{\cos\alpha_0}{\cos\alpha} \tag{D.24}$$

while this distance in the second lens optical axis is:

$$x_{0G\beta_0} = x_1 \left(1 - \frac{Z_1}{f_1}\right)\cos(\alpha - \alpha_0)\frac{\cos\beta_0}{\cos\alpha} \tag{D.25}$$

Similarly for Z_{2-mod} we have:

$$Z_{2-mod} = Z_2 - x_{0G\beta_0} \tan\beta_0 \tag{D.26}$$

The light beam propagating in the spectrometer is then described by the following equations, where any vignetting effect is neglected. In the x direction:

$$x_0(z, \beta) = \begin{cases} x_1 & \text{Zone 1} \\ x_1 - (z - f_1)\frac{x_1}{f_1} & \text{Zone 2} \\ x_{0G\beta_0} + \left[z - (f_1 + Z_{1-mod})\right]\tan(\beta - \beta_0) & \text{Zone 3-4} \end{cases} \tag{D.27}$$

$$r_x(z, \beta) = \begin{cases} z \tan\Psi & \text{Zone 1} \\ f_1 \tan\Psi & \text{Zone 2} \\ f_1 \tan\Psi \frac{\cos(\alpha - \alpha_0)}{\cos\alpha} & \text{Zone 3 (on grating!)} \\ f_1 \tan\Psi \frac{\cos(\alpha - \alpha_0)}{\cos\alpha} \frac{\cos\beta}{\cos(\beta - \beta_0)} & \text{Zone 4} \end{cases} \tag{D.28}$$

183
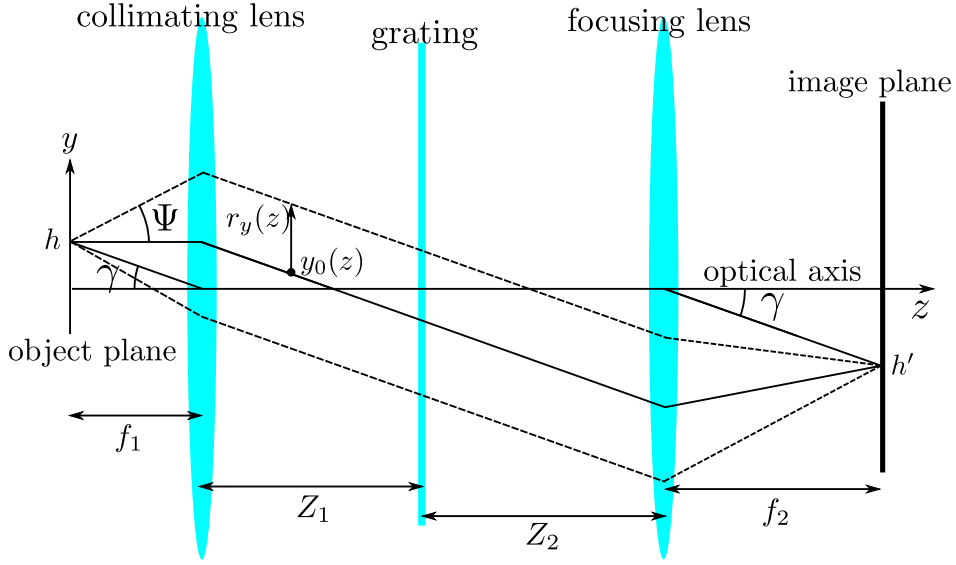
Figure D.6: View of the spectrometer $y - z$ plane for a source point with position $(x_1 = 0, h)$.

in the y direction:

$$y_0(z) = \begin{cases} y_1 & \text{Zone 1} \\ y_1 - (z - f_1)\frac{y_1}{f_1} & \text{Zone 2-3-4} \end{cases} \tag{D.29}$$

$$r_y(z) = \begin{cases} z \tan \Psi & \text{Zone 1} \\ f_1 \tan \Psi & \text{Zone 2} \\ f_1 \tan \Psi & \text{Zone 3 (on grating)} \\ f_1 \tan \Psi & \text{Zone 4} \end{cases} \tag{D.30}$$

The surface of the collimating lens S_{lens1} is described in the optical axis reference system as:

$$S_{lens1} = \left\{ (x, y) : x^2 + y^2 \leq (D_1/2)^2 \right\} \tag{D.31}$$

the surface of the grating S_g, in the optical axis reference system, is:

$$S_g = \left\{ (x, y) : |x| \leq W_{gr}/2 \, \cos \alpha_0, |y| \leq h_{gr}/2 \right\} \tag{D.32}$$

it's worth noting that in this reference system the horizontal extent of the beam is

$$r_{x-oa} = f_1 \tan \Psi$$
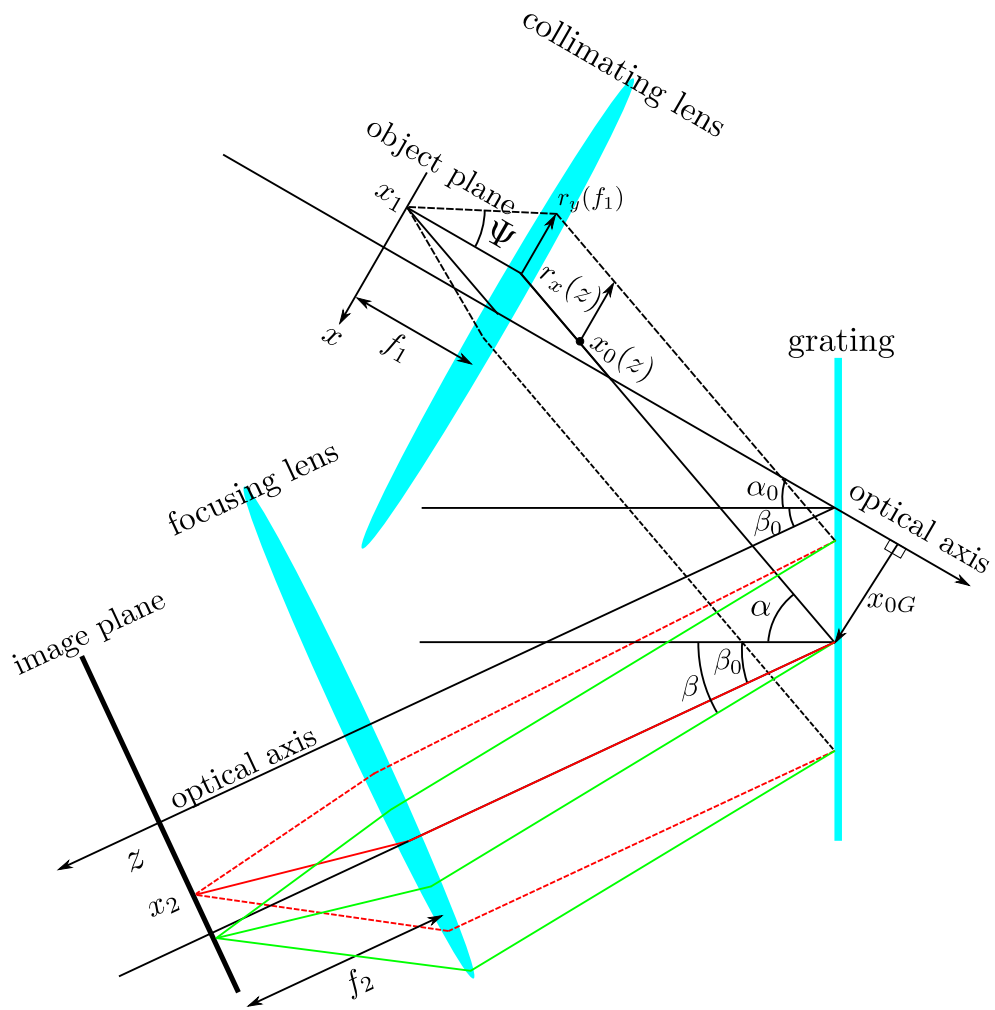
Figure D.7: View of the spectrometer $x - z$ plane for a source point with position $(x_1, h = 0)$.
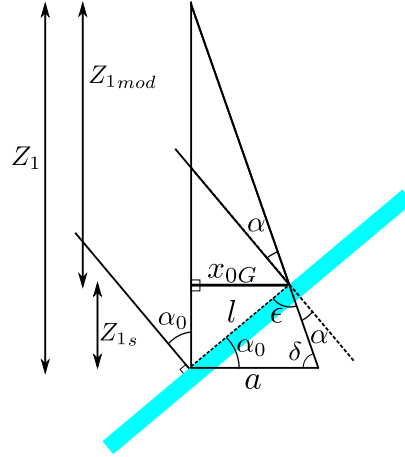
Figure D.8: Sketch for calculating Z_{1-mod}.

that is the one used in the computations, while in the reference system of the beam is

$$r_{x-beam} = f_1 \tan \Psi \cos(\alpha - \alpha_0)$$

and in the reference system of the grating is

$$r_{x-grating} = f_1 \tan \Psi \frac{\cos(\alpha - \alpha_0)}{\cos \alpha}$$

as specified in equation D.28 for Zone 3. The surface of the focusing lens S_{lens2} is

$$S_{lens2} = \left\{ (x, y) : x^2 + y^2 \leq (D_2/2)^2 \right\} \tag{D.33}$$

The surface of the beam passing the collimating lens $S_{over-f1}$ is then:

$$S_{over-f1} = S_{tot-f1} \cap S_{lens1} \tag{D.34}$$

where S_{tot-f1} is the surface of the beam without vignetting at position $z = f_1$, as described by equations D.27, D.28, D.29 and D.30. Then the surface is translated in both x and y directions as the beam reaches the grating, this is the surface S_{vig-g}, that takes into account the vignetting of the first lens. The surface without vignetting is translated to the surface S_{tot-g}. The part of the beam that is reflected by the grating S_{over-g} is:

$$S_{over-g} = S_{vig-g} \cap S_g \tag{D.35}$$

The shape of the diffracted beam is described by the points of S_{over-g} but stretched in the horizontal direction:

$$S_{over-ag}(\beta) = \left\{ (x, y) : \left(x \frac{r_x(\text{Zone 2})}{r_x(\text{Zone 4})}, y \right) \in S_{over-g} \right\} \tag{D.36}$$
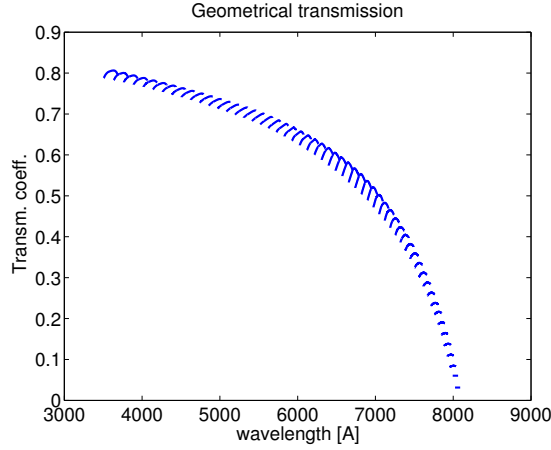
Figure D.9: Theoretical geometrical transmission of the EDGE spectrometer for a scan in the angle θ from $-27°$to $-79°$. The transmission

as described in equation D.28, that explicitly depends on β. Here is where we pass from the first lens optical axis reference system to the second lens one, and that's the reason why the center of the beam passes from x_{0G} to $x_{0G\beta_0}$. The same procedure is applied to S_{tot-g} to obtain $S_{tot-ag}(\beta)$, the beam surface after the grating without considering vignetting. Then both $S_{over-ag}$ and S_{tot-ag} are translated to obtain S_{vig-f2} and S_{tot-f2}, the surfaces at the focusing lens. The part of the beam that passes through the second lens is:

$$S_{over-f2} = S_{vig-f2} \cap S_{lens2} \tag{D.37}$$

which completes all the elements needed to compute T_G from equation D.19.

The program Get_geometrical_transmission.m performs these calculations, the results are shown in Figure D.9 for the EDGE spectrometer (parameters of table D.1), and a scan in the angle θ, from $\theta = -27°$to $\theta = -79°$. The overall tendency for the transmission is to decrease with increasing wavelength (larger angles), due to the grating tilt, effectively limiting the spectrometer operation to wavelengths < 8000 Å. This limit in wavelength depends on the Bragg angle, that is determined by the grating groove density G. This explains why we chose a 2000 l/mm grating for the FIDA optimised spectrometer. The shape of the transmission coefficient at a fixed angle θ, calculated for the spectrometer spectral range, strongly depends on the θ value (see figure D.9) as vignetting of the light beam depends on the details of the propagation path, mostly determined by θ.

D.2.3   Lens transmission

The nikon lens transmission coefficient as function of wavelength $T_{nikon}(\lambda)$ has been experimentally measured, the results are shown in Figure D.10. The blue line is the experimentally
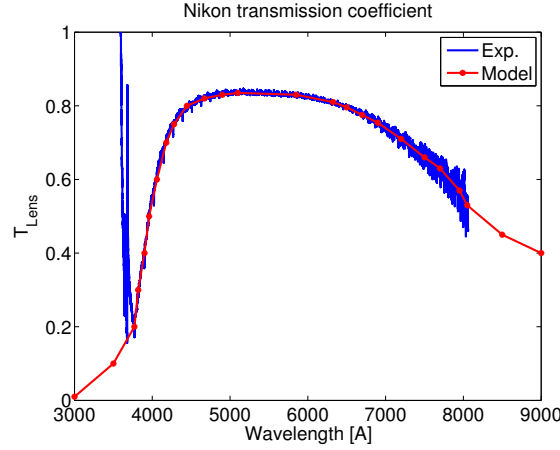
Figure D.10: Nikon lens transmission coefficient as function of wavelength. Experimental results in blue, in red values used in modelling. Discrepancies due to poor photon statistics below 3800 [Å].

measured transmission coefficient, while the values of the red line are used to model the lens transmission. The discrepancies at wavelengths below 3800 Å are due to a strong background-stray light, that invalidates the measured values, the model values are extrapolated values. A transmission coefficient of $\simeq 0.8$ is measured for most of the visible spectrum, which results in a transmission of $\simeq 0.64$ for a lens spectrometer configuration. Aspherical single lenses with anti-reflection coating [239] (typical transmission $\simeq 0.98$) can be employed to further improve the transmission efficiency, if needed, but at the cost of image quality and resilience in spectral scans. This was tested and confirmed in the optimised FIDA spectrometer. Note that the transmission coefficient is measured with low-divergence beams to decouple the effect of vignetting from transmission losses due to reflections and absorption, but in experimental applications vignetting can affect strongly the total light transmission, particularly for objects emitting off-axis (see figure D.6).

D.2.4 Grating transmission

The grating transmission coefficient $T_{grating}(\lambda)$ is shown in Figure D.11, as supplied by the manufacturer.

D.2.5 Theory-experiment comparison

The theoretical predicted values can be compared to the experimental measurements if the spectral radiance of the light source is known. The nominal spectral radiance $L_{source}(\lambda)$ of the calibrated Labsphere source, available at SPC, is shown in Figure D.12.

The theoretical photons rate (number of photons per second N_{ph-Th}) collected by a pixel of
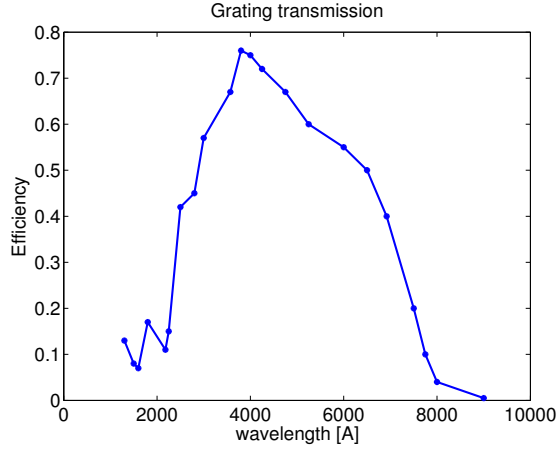
Figure D.11: Grating transmission as function of wavelength.
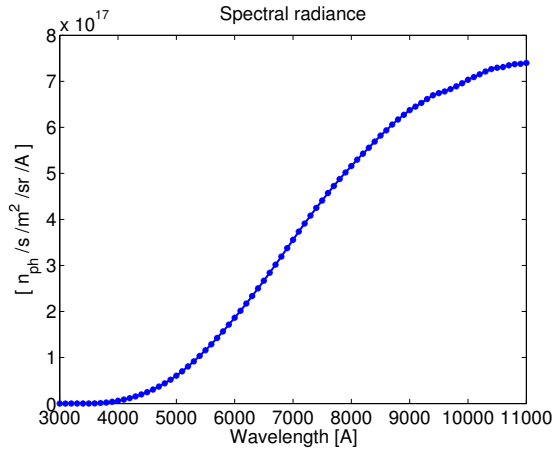
Figure D.12: Labsphere nominal spectral radiance.

the CCD sensor, for an input slit of width equal to the demagnified pixel size, is:

$$N_{ph-Th} = L_{source}(\lambda_{pix}) \, G_{pix} \, \Delta\lambda \, T_G(\lambda_{pix}) \, T_{grating}(\lambda_{pix}) \, T^2_{nikon}(\lambda_{pix}) \tag{D.38}$$

where $\Delta\lambda$ is the wavelength range on the pixel and G_{pix} is its étendue :

$$G_{pix} = \frac{h_{pix}}{M_{ver}} \frac{W_{pix}}{M_{hor}} \, \Omega \tag{D.39}$$

with h_{pix} the pixel height, W_{pix} its width and Ω the solid angle of the incident beam

$$\Omega = \pi \, (NA)^2 \tag{D.40}$$
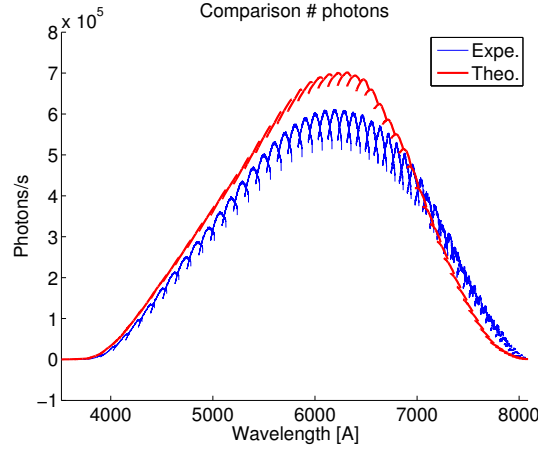
Figure D.13: Comparison between the theoretical predicted photon rate and the observed photon rate.

where $NA = min(NA_{source}, NA_{spectrometer})$ is the smallest numerical aperture between the source and spectrometer. If the input slit is larger than W_{pix}/M_{hor} the light of the neighbour pixels spreads to the considered pixel, increasing the counts proportionally. It is sufficient to divide the experimental number of photons by the input slit size in pixel units to correct for this effect. This procedure is valid for $W_{slit} \gg W_{pix}$, for W_{slit} comparable or smaller than W_{pix} a convolution of the spectrum with the instrumental function is required.

The results are shown in Figure D.13 for a scan in the angle θ, from $\theta = -27°$ to $\theta = -79°$ for the experimental data and the theoretical prediction. The overall transmission is well described by the model, but there is a significant discrepancy in the shape at each fixed scan angle. In the experimental profile the vignetting at the sensor edge is much more pronounced than in the model. This is due to the simple lens assumption of the model, since the real lens vignetting is considerably more complex. Nevertheless the description of the spectrometer transmission is satisfactory and was taken into account for the spectrometer optimisation.

D.3 Conclusions

In this appendix a comprehensive description of the lens-based spectrometer design was reported. The major parameters of interest in spectroscopy are illustrated and the model for the transmission analysis explained. A posteriori comparison of the modelled transmission with experimental measurements validated the procedure as an approximated description, for a detailed transmission analysis a more accurate description of the Nikon lenses is required.

In particular, for the minimum lens' f-number $f_\# = 2$, strong vignetting is observed for external beams, reducing the effective f-number, probably a choice of the constructor to optimise resolution in that region. With the single aspherical lenses this vignetting is strongly reduced

and transmission is flatter and reaches higher values, thanks to the anti-reflection coating. This improves overall transmission at the expense of lower peripheral resolution. Furthermore a single lens cannot be apochromatic, resulting in the need of fine tuning of the spectrometer at each wavelength change. These considerations must be taken into account when designing a spectrometer for any particular purpose.

E Smearing correction and reflections

In this appendix smearing and reflection effects are investigated to better assess the EDGE system performance. Here it is considered smearing only the signal generated by the photo-electrons produced during the frame transfer, and hence erroneously attributed to a different pixel, i.e. frame transfer smearing. There are potentially other smearing mechanisms, the charge transfer smearing and blooming. The former is due to a defective charge transfer, i.e. for CTE<1 (see section 2.2.2), and can minimised with a suitable VSS. The latter consists in charges leaking from one pixel to the neighbours pixels when the potential well limit is reached, but this effect is limited in recent anti-blooming chips and therefore neglected in the following.

E.1 Smearing correction

The data analysis of the legacy CXRS systems neglected CCD smearing effects. Smearing effects increase as the integration time approaches the CCD frame-transfer time and they cannot be neglected when there is a large difference (≥ 1 order of magnitude) among ROIs brightness. The consequence of neglecting this effect were studied repeating three time the same target TCV discharge while changing the EDGE CXRS system setup. The main plasma parameters for these three shots, 56244, 56245 and 56247, are shown in figure E.1. The stronger influence of smearing is expected for the LOS viewing the SOL, where the measured brightness can be orders of magnitude lower than in core LOS and the slit image curvature reach the maximum distance. In shot 56244 core LOS were masked, only the light coming from the 8 outermost LOS could reach the CCD, preventing this source of smearing and allowing an accurate SOL CXRS measurement. In shot 56245 the seven outermost LOS were masked, in order to measure directly the smearing of the core LOS on the masked ROIs. Shot 56247 is used as reference, with the standard CXRS EDGE setup (i.e. no masking).

The result of applying the data analysis without correction is shown in figure E.2 for the L-mode phase and in figure E.3 for the H-mode phase. In L-mode the brightness difference between all the ROIs is less than an order of magnitude, therefore the smearing effects are not expected to be strong. The agreement of measurements for shots 56244 (only SOL LOS) and 56247 (full

Appendix E. Smearing correction and reflections
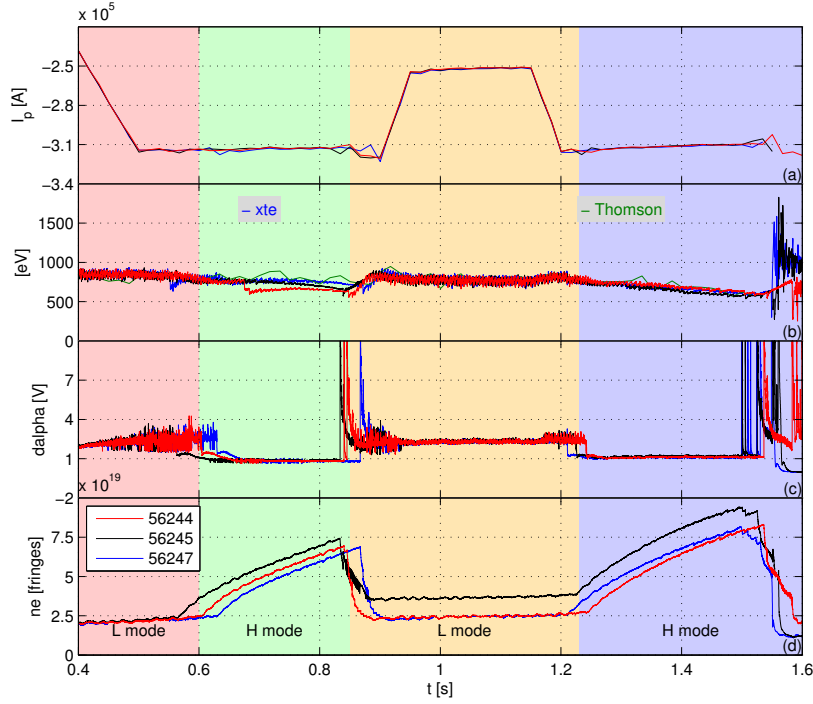
Figure E.1: Comparison of plasma parameters for shots 56244, 56245 and 56247. (a) I_p, (b) T_e, (c) D_α and (d) n_e.

LOS set) confirms this hypothesis. In H-mode the discrepancy of all the systems suggests that
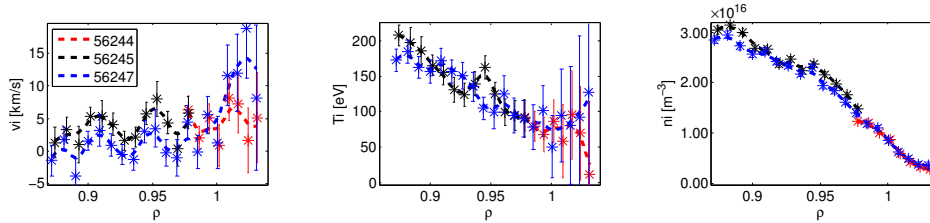
Figure E.2: Comparison of (a) poloidal velocity, (b) T_i and (c) n_i for shots 56244 (red-core LOS masked), 56245 (black-SOL LOS masked) and 56247 (blue-no LOS masked), at time 1.105 s, during L-mode phase. The smearing is negligible and the measurements agree.

the smearing becomes non negligible. There is agreement for shots 56245 and 56247 in the core region, where smearing is expected to be negligible with respect to the actual signal, while all the three shots disagree in the SOL region. The difference in the calculated velocity can be explained by smearing: its increase in shot 56245 with ρ in the SOL, where the signal is purely due to smearing, is due to the curvature of the slit image, that changes the pixel-wavelength relations for each track, while the smearing signal remains at the same horizontal pixel for all the tracks. The velocity calculated for shot 56247, where both the smearing and the actual signal are present, is consistently between the correct (pure) signal of 56244 and the pure

smearing of 56245, weighted by the relative intensity of the two components. The temperature profiles are explained similarly, they are comparable for both the pure signal and smearing (56244 and 56245), while there is an increase of temperature in the SOL for shot 56247 due to the increase in the separation of the two components. There is an intensity ratio (directly related to the calculated density) of $\simeq 2$ between the true signal 56244 and the smearing signal 56245, even though this last shot had a higher density (see figure E.1). The sum of the two components (signal and smearing) measured separately in 56244 and 56245 is consistent with the measurements in 56247.

Figure E.3: Comparison of (a) poloidal velocity,(b) T_i and (c) n_i for shots 56244 (red-core LOS masked), 56245 (black-SOL LOS masked) and 56247 (blue-no LOS masked), at time 0.755 s, during the first H-mode phase. The discrepancy in the outer LOS at $\rho > 1$ is due to smearing effects.

E.1.1 Smearing correction algorithm

It is assumed that the light reaching the CCD is constant in time (stationary source) and that no light is reaching the sensor outside the ROI.

The intensity (or more precisely the radiant flux) $I_{cl}(i)$ [counts/s or ph/s] of light falling on the track (or ROI) i pollutes the other ROIs during the frame transfer, this effect is separate for each column, i.e. it works only in the sensor vertical direction. Since the intensity is assumed constant in time, the contamination of the other ROIs is proportional only to the transfer time and the intensity of the polluting track. The correct (i.e. clean spectra) number of counts (or photons) for the track i is then:

$$C_{cl}(i) = I_{cl}(i)\,\Delta T_{eff}(i) \tag{E.1}$$

where the effective integration time ΔT_{eff} is the time between 2 camera triggers ΔT_{ACQ} corrected by the transfer time. If track l is composed by n_{vp} vertical pixels and the frame shift rate is v_s [s/pix], the transfer time for the track $\Delta T_{shift}(l)$ is:

$$\Delta T_{shift}(l) = n_{vp}(l)\,v_s \tag{E.2}$$

the total transfer time, considering only pixels belonging to a ROI, is then

$$\Delta T_{shift-tot} = \sum_{l=1}^{n_{tr}} \Delta T_{shift}(l) \tag{E.3}$$

and the effective integration time for track i is:

$$\Delta T_{eff}(i) = \Delta T_{ACQ} - \Delta T_{shift-tot} + \Delta T_{shift}(i) \tag{E.4}$$

The total counts $C_{tot}(i)$ for track i obtained from the readout of the sensor, for a fixed horizontal pixel index, are then:

$$C_{tot}(i) = I_{cl}(i) \, \Delta T_{eff}(i) + \sum_{\substack{l=1 \\ l \neq i}}^{n_{tr}} I_{cl}(l) \, \Delta T_{shift}(l) + k_{bg}(i) \tag{E.5}$$

where $k_{bg}(i)$ is the background counts level for track i. In matrix formalism the equation can be written as:

$$\mathbf{C}_{tot-k} = \mathbf{C}_{tot} - \mathbf{k}_{bg} = \mathbf{M}_{tot-k} \, \mathbf{I}_{cl} \tag{E.6}$$

where $\mathbf{C}_{tot-k}$ is the background corrected counts vector. The matrix $\mathbf{M}_{tot-k}$ adds the smearing and performs the time integration to the clean intensity (column) vector $\mathbf{I}_{cl}$ [counts/s]. It is composed by the tracks shift and integration times:

$$\mathbf{M}_{tot-k}(i,j) = \begin{cases} \Delta T_{eff}(i) & \text{if } i = j \\ \Delta T_{shift}(j) & \text{if } i \neq j \end{cases} \tag{E.7}$$

The solution of equation E.6 is simply:

$$\mathbf{I}_{cl} = \mathbf{M}_{tot-k} \backslash \mathbf{C}_{tot-k} \tag{E.8}$$

and the smearing-free clean spectrum in counts (or photons) is:

$$\mathbf{C}_{cl} = \mathbf{I}_{cl} \, \Delta \mathbf{T}_{eff} \tag{E.9}$$

All the parameters entering $\mathbf{M}_{tot-k}$ are known from the camera acquisition parameters, hence from the measured smeared spectrum $\mathbf{C}_{tot-k}$ it is possible to calculate the smearing-free spectrum $\mathbf{C}_{cl}$.

The use of a stationary source is a strong assumption, particularly when the timescales of the phenomenon under study are comparable with the diagnostic integration time, therefore an experimental verification of the algorithm viability is necessary.

E.1.2 Smearing correction test

In order to verify the reliability of the smearing correction algorithm the acquisition setup of the EDGE system was modified for shot TCV 56245 by blocking the light coming from the SOL ROIs (i.e. LOS from 1 to 7). The resulting readout counts of these masked ROIs are then originate from photoelectrons generated by the unobstructed LOS that reached the masked tracks by smearing. The smearing pattern for the CVI line calculated through the algorithm was fitted with a Gaussian function and compared to the fit of the measured data. The comparison is shown in figure E.4 for the fitted line intensity, width and position. The three fitting parameters are in agreement confirming the correctness of the algorithm.
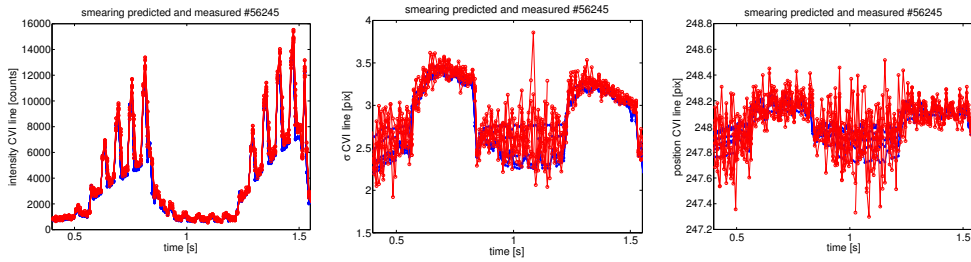
Figure E.4: Comparison of predicted-calculated (blue) and measured (red) smearing effect for the CVI line in TCV shot 56245. The (a) intensity, (b) line width σ and (c) position are in agreement.
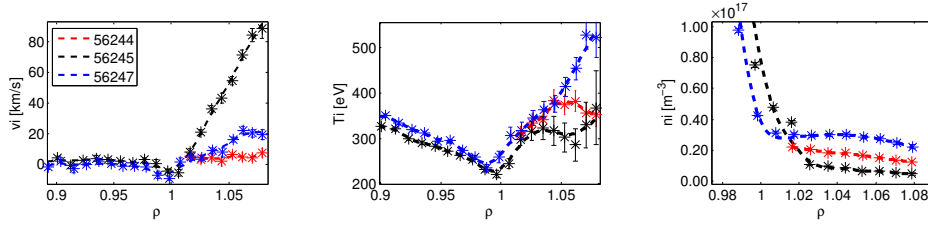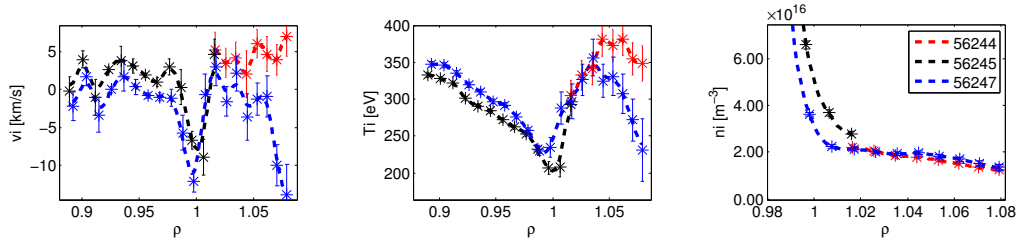

Figure E.5: Comparison of (a) poloidal velocity,(b) T_i and (c) n_i for shots 56244 (red- core LOS masked), 56245 (black - SOL LOS masked) and 56247 (blue - no LOS masked) after the application of the smearing correction algorithm. The profiles are consistent and in agreement for $\rho < 1.05$, confirming the correctness of the algorithm.

The result of the analysis of shots 56244, 56245 and 56247 with smearing correction are shown in figure E.5. The improvement in the profile agreement for the 3 quantities, particularly the density, demonstrates that the previous discrepancies were due to smearing effects and that the correction algorithm is properly implemented. However the smearing subtraction cannot completely correct the signal, if the smearing signal is order of magnitudes higher than the active CX signal, a strong influence of the smearing signal on the measurements remains after the correction, as it is the case for measurements in the far-SOL, $\rho \geq 1.05$. The situation becomes worse as the signal intensity fluctuates during the frame transfer (e.g. for strong fast

events such as ELMs).

The unphysical smearing-free results (see figure E.5) in the SOL temperature profile, that increases with the distance from the LCFS, and in the density profile, that flattened to a constant value, are assessed in the next section.

E.2 Wall reflection

The application of the smearing correction algorithm allowed a consistent profile reconstruction from the similar shots 56244, 56245 and 56247 (figure E.5), but a critical assessment of the physical admissibility of the results reveals important issues. An increase in impurity temperature outside the LCFS and the flattening of the density in the same region was highly unexpected, where an exponential decay of both quantities is usually assumed [18].

Three possible sources of the measured "active" signal were here identified:

1. direct active CX signal due to the interaction of the DNBI with the studied impurity.

2. reflection of the active CX signal (coming from the core region) on the wall tiles and metallic parts that intersect the CXRS system LOS.

3. reflection of the active CX signal in the periscope-input optics.

Considering the unphysical results, the first source has been neglected (on the basis that it is improbable) as the dominant term, leaving the reflection of the active CX signal (from another plasma region than the DNBI-LOS intersection) either by the wall or the input-optics, as the main signal source.

A simple model that assumes Lambertian reflection was used to verify the level of pollution in the EDGE system LOS due to the reflection of the active signal on the wall. The beam is modelled as a cylinder of length L_b and radius $r_d = W_b/2$, where W_b is the DNBI FWHM $\simeq 8$ cm. The emissivity profile of the active signal along the DNBI is estimated from the radiance profile measured by SYS1 and SYS2 divided by the intersection length of the DNBI with the systems LOS. The cross section area of the beam is $A_b = \pi r_d^2$. The radiant flux Φ_{w-in} impinging on an area A_w of the wall is:

$$\Phi_{w-in} = \int_{L_b} \epsilon(R) \, A_b \, \Omega_b(R) \, dR \tag{E.10}$$

where the solid angle Ω_b subtended by the element A_w of the wall is:

$$\Omega_b \simeq \frac{A_w \cos\delta}{r_w^2} \tag{E.11}$$

and the angle δ between the normal to the tile $\hat{n}$ and the distance of the emitting element to the tile $\hat{r_w}$ is $\delta = \theta_b - \gamma$. The angle θ_b is the angle between $\hat{r_w}$ and $\hat{R}$ and γ is the angle of
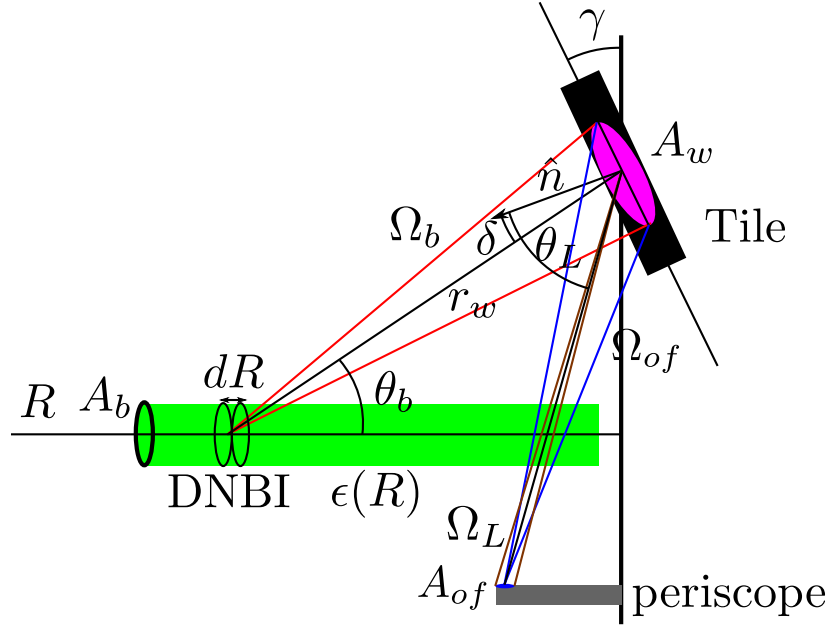
Figure E.6: Sketch of the model used for reflection calculation, with geometrical definitions.

the tile with the vertical. Figure E.6 shows a sketch of this model. The radiant intensity of the reflected light is:

$$I_{out} = \Phi_{w-in} \frac{R_{gr} \cos\theta_L}{\pi} \tag{E.12}$$

with the reflection coefficient of graphite $R_{gr} \simeq 0.3$ [240] and θ_L the angle between $\hat{n}$ and the LOS. The radiant flux Φ_{w-out} of the reflected light collected by the optical fibre of a LOS is

$$\Phi_{w-out} = \int_{\Omega_L} I_{out}\, d\Omega \simeq I_{out}\, \Omega_L \tag{E.13}$$

and the corresponding radiance L_L is

$$L_L = \frac{\Phi_{w-out}}{G_{of}} \tag{E.14}$$

with G_{of} the étendue of the optical fibre. Here we are implicitly using A_w as the area of the wall from which the LOS is collecting the reflected light. The conservation of étendue gives $G_{of} = A_{of}\,\Omega_{of} = A_w\,\Omega_L \cos\theta_L$ and the radiance reads

$$L_L = \frac{R_{gr}}{\pi} A_b \int_{L_b} \epsilon \frac{\cos\delta}{r_w^2}\, dR \tag{E.15}$$

Figure E.7 shows the radiance profile measured by SYS4 in the SOL region (the LCFS is at $R_{LCFS} = 1.1$ m) for both L-mode and H-mode phases. Colours represents different shots for which the periscope insertion depth into the TCV vessel L_p was changed. Shots 56244

and 56247 (blue and cyan) are at the standard (reference) position $L_p = 0$, a displacement towards the plasma core is represented by a positive value. In shot 56443 (green) $L_p = -37.7$ mm (outermost setup), in shot 56432 (yellow) $L_p = -30.7$ mm and in shot 56448 (orange) $L_p = -18.5$ mm. The black profiles are the radiance expected from the model. The expected
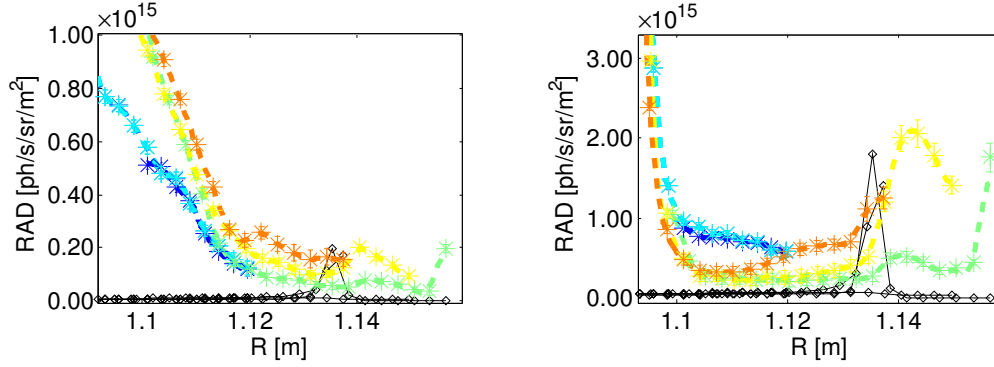
Figure E.7: Radiance of the SOL LOS of SYS4 in (a) L mode and (b) H mode. Shots 56244 and 56247 (blue and cyan) $L_p = 0$, 56443 (green) $L_p = -37.7$ mm ,56432 (yellow) $L_p = -30.7$ mm, 56448 (orange) $L_p = -18.5$ mm. The black profiles are the expected reflected radiance.

radiance is highly sensitive to the position of the reflection area through Ω_b, which is calculated assuming a vessel simplified geometry.

There is a factor ≥ 10 discrepancy in the radiance for the LOSs that have the intersection on the ceiling. The expected radiance is too low, a possible explanation is that for these angles the specular reflection, that is neglected in the model, could be the dominant term on the tile reflection. The expected radiance reaches values comparable with the measured radiance only for LOSs that intersect the external vertical wall close to the DNBI position, corresponding to $R \simeq 1.14$ m in the EDGE mapping (figure E.7).

The measured radiance profiles are characterised by a steep region and a plateau region. The dominant signal of the steep region is the direct active CX signal, while in the plateau region the reflected signal is dominant. The plateau region extends up to the LCFS in H-mode, while in L-mode it's displaced outwards in the SOL. Some radiance profile features are detectable in this region: the spike of the outermost LOS in shots 56443 and the bump at $R = 1.143$ m for shots 56432 56448 and 56443. The position of the bump in the measured radiance is consistent with the maximum of the tile-reflected signal. They are present in both L and H mode, although in H mode they are more distinguishable, as it is expected from a reflected signal coming from the confined region, where the brightness in H mode increases. This is a strong argument in favour of the reflection-origin of the signal in the SOL LOS of SYS4, although a direct experimental verification is not feasible without in-vessel hardware modifications (in the planning).

The radiance base-level in the plateau region may originate from reflections in the input optics.

The vacuum tight window is not anti-reflection coated, resulting in a reflection coefficient (2 air-glass surfaces) $\simeq$ 8%. Considering the amount of light entering the periscope from the aperture, only a fraction of the reflected light is required to explain the plateau base-level, which is only a few % of the core signal. Upgrading the periscope window with an anti-reflection coated glass could confirm or disproof this hypothesis and would, in any case, be an excellent precaution for the future.

Covering the CXRS LOS-tiles intersection surfaces with anti-reflection/absorbing materials and the replacement of the periscope window are two essential steps for reaching the EDGE diagnostic full potential.

Bibliography

[1] A. Einstein. Ist die Trägheit eines Körpers von seinem Energieinhalt abhängig? *Ann. Phys.*, 323(13):639–641, 1905. ISSN 00033804. doi: 10.1002/andp.19053231314. URL http://doi.wiley.com/10.1002/andp.19053231314. 1

[2] Francis F. Chen. *Introduction to Plasma Physics and Controlled Fusion.* Springer US, Boston, MA, 1984. ISBN 978-1-4419-3201-3. doi: 10.1007/978-1-4757-5595-4. URL http://link.springer.com/10.1007/978-1-4757-5595-4. 2, 3, 5, 11, 94, 95

[3] J. Wesson. *Tokamaks.* Oxford, 4 edition, oct 2011. ISBN 9780199592234. URL https://global.oup.com/academic/product/tokamaks-9780199592234?cc=ch{&}lang=en{&}{#}. 2, 3, 4, 5, 6, 7, 8, 9, 105

[4] J.D. Lawson. Some Criteria for a Power producing thermonuclear reactor. Technical report, Atomic Energy Research Establishment, Harwell, Berkshire, U. K., 1955. URL http://stacks.iop.org/0370-1301/70/i=1/a=303. 3

[5] Jeffrey P. Freidberg. *Plasma Physics and Fusion Energy.* Cambridge University Press, Cambridge, 2007. ISBN 9780511755705. doi: 10.1017/CBO9780511755705. URL http://ebooks.cambridge.org/ref/id/CBO9780511755705. 4, 7

[6] F. Wagner, G. Becker, K. Behringer, D. Campbell, A. Eberhagen, W. Engelhardt, G. Fussmann, O. Gehre, J. Gernhardt, G. v. Gierke, G. Haas, M. Huang, F. Karger, M. Keilhacker, O. Klüber, M. Kornherr, K. Lackner, G. Lisitano, G. G. Lister, H. M. Mayer, D. Meisel, E. R. Müller, H. Murmann, H. Niedermeyer, W. Poschenrieder, H. Rapp, H. Röhr, F. Schneider, G. Siller, E. Speth, A. Stäbler, K. H. Steuer, G. Venus, O. Vollmer, and Z. Yü. Regime of Improved Confinement and High Beta in Neutral-Beam-Heated Divertor Discharges of the ASDEX Tokamak. *Phys. Rev. Lett.*, 49(19):1408–1412, nov 1982. ISSN 0031-9007. doi: 10.1103/PhysRevLett.49.1408. URL http://link.aps.org/doi/10.1103/PhysRevLett.49.1408. 4, 22, 24, 131

[7] JET website. URL https://www.euro-fusion.org/jet/. 4

[8] P-H Rebut. The JET preliminary tritium experiment. *Plasma Phys. Control. Fusion*, 34(13):1749–1758, dec 1992. ISSN 0741-3335. doi: 10.1088/0741-3335/34/13/002. URL http://stacks.iop.org/0741-3335/34/i=13/a=002?key=crossref.1a015c7e0b6ecf2cde05140a2d148222. 4

Bibliography

[9] M. Keilhacker and A. Gibson and C. Gormezano and P.J. Lomas and P.R. Thomas and M.L. Watkins and P. Andrew and B. Balet and D., , Borba H.Y., C.D. Challis, I. Coffey, G.A. Cottrell, H.P.L. De Esch, N. Deliyanakis, A. Fasoli, C.W. Gowers, , Guo M.F.F., G.T.A. Huysmans, T.T.C. Jones, W. Kerner, R.W.T. König, M.J. Loughlin, A. Maas, F.B. Marcus, , Nave B.J.D., F.G. Rimini, G.J. Sadler, S.E. Sharapov, G. Sips, P. Smeulders, F.X. Söldner, A. Taroni, Tubbing Team, M.G. von Hellermann, D.J. Ward, and JET. High fusion performance from deuterium-tritium plasmas in JET. *Nucl. Fusion*, 39(2):209, 1999. URL http://stacks.iop.org/0029-5515/39/i=2/a=306. 4

[10] EFDA-ITER website. URL https://web.archive.org/web/20060824071609/http://www.efda.org/. 4

[11] K Ikeda. Progress in the ITER Physics Basis. *Nucl. Fusion*, 47(6), jun 2007. ISSN 0029-5515. doi: 10.1088/0029-5515/47/6/E01. URL http://stacks.iop.org/0029-5515/47/i=6/a=E01?key=crossref.3391a8dabcfa415ae345d3defa8b1c9f. 4, 23

[12] R. Fitzpatrick. *Plasma Physics: An Introduction.* Taylor \& Francis, 2014. ISBN 9781466594265. URL https://books.google.ch/books?id=0RwbBAAAQBAJ. 5

[13] EUROfusion. www.euro-fusion.org. URL https://www.euro-fusion.org/. 6, 17

[14] William Denis D'haeseleer, William Nicholas Guy Hitchon, James D. Callen, and J. Leon Shohet. *Flux Coordinates and Magnetic Field Structure*, volume 31. Springer Berlin Heidelberg, Berlin, Heidelberg, 1991. ISBN 978-3-642-75597-2. doi: 10.1007/978-3-642-75595-8. URL http://doi.wiley.com/10.1002/ctpp.2150310613. 8

[15] J.P. Freidberg. *Ideal MHD.* Cambridge University Press, 2014. ISBN 9781107006256. URL https://books.google.ch/books?id=cjazAwAAQBAJ. 8

[16] F L Hinton and R D Hazeltine. Theory of plasma transport in toroidal confinement systems. *Rev. Mod. Phys.*, 48(2):239–308, apr 1976. ISSN 0034-6861. doi: 10.1103/RevModPhys.48.239. URL https://link.aps.org/doi/10.1103/RevModPhys.48.239. 8, 98, 99

[17] P. Helander and Dieter J. Sigmar. *Collisional transport in magnetized plasmas.* Cambridge University Press, New York, 2002. ISBN 0521807980. URL http://www.cambridge.org/catalogue/catalogue.asp?isbn=9780521807982. 8, 93, 94, 96, 101

[18] P Stangeby. *The Plasma Boundary of Magnetic Fusion Devices.* Series in Plasma Physics. CRC Press, jan 2000. ISBN 978-0-7503-0559-4. doi: 10.1201/9781420033328. URL http://www.crcnetbase.com/doi/book/10.1201/9781420033328. 8, 9, 10, 198

[19] R. J. Hastie. Sawtooth Instability in Tokamak Plasmas. *Astrophys. Space Sci.*, 256(1/2):177–204, 1997. ISSN 0004640X. doi: 10.1023/A:1001728227899. URL http://link.springer.com/10.1023/A:1001728227899. 8, 24, 105, 106

[20] Allen H. Boozer. Physics of magnetically confined plasmas. *Rev. Mod. Phys.*, 76(4): 1071–1141, jan 2005. ISSN 0034-6861. doi: 10.1103/RevModPhys.76.1071. URL http://link.aps.org/doi/10.1103/RevModPhys.76.1071. 8

[21] Y. Camenen. *Etude du tranport d'énergie thermique dans les plasmas du Tokamak à Configuration Variable au moyen de chauffage électronique cyclotronique.* Phd thesis n. 3618, EPFL, 2006. URL https://infoscience.epfl.ch/record/87520. 9

[22] Jing Ou, Guojiang Wu, and Xinxia Li. Effect of the plasma shapes on intrinsic rotation due to collisionless ion orbit loss in the tokamak edge plasmas. *Phys. Plasmas*, 21(7): 072505, jul 2014. ISSN 1070-664X. doi: 10.1063/1.4889898. URL http://aip.scitation.org/doi/10.1063/1.4889898. 9

[23] Robert Goldston and Paul Rutherford. *Introduction to Plasma Physics.* Taylor & Francis, nov 1995. ISBN 978-0-7503-0183-1. doi: 10.1201/9781439822074. URL http://www.crcnetbase.com/doi/book/10.1201/9781439822074. 11, 93, 94, 95

[24] F Hofmann, J B Lister, W Anton, S Barry, R Behn, S Bernel, G Besson, F Buhlmann, R Chavan, M Corboz, M J Dutch, B P Duval, D Fasel, A Favre, S Franke, A Heym, A Hirt, C Hollenstein, P Isoz, B Joye, X Llobet, J C Magnin, B Marletaz, P Marmillod, Y Martin, J M Mayor, J M Moret, C Nieswand, P J Paris, A Perez, Z A Pietrzyk, R A Pitts, A Pochelon, R Rage, O Sauter, G Tonetti, M Q Tran, F Troyon, D J Ward, and H Weisen. Creation and control of variably shaped plasmas in TCV. *Plasma Phys. Control. Fusion*, 36(12B): B277–B287, dec 1994. ISSN 0741-3335. doi: 10.1088/0741-3335/36/12B/023. URL http://stacks.iop.org/0741-3335/36/i=12B/a=023. 12

[25] F. Hofmann, S. Coda, P. Lavanchy, X. Llobet, Ph. Marmillod, Y. Martin, A. Martynov, J. Mlynar, J.-M. Moret, A. Pochelon, and O. Sauter. Extension of the TCV operating space towards higher elongation and higher normalized current. *Nucl. Fusion*, 42(6):312, jun 2002. ISSN 00295515. doi: 10.1088/0029-5515/42/6/312. URL http://stacks.iop.org/0029-5515/42/i=6/a=312?key=crossref.fb680d0071af296b5e6b7014f9d6e792. 14

[26] TCV specifications. URL http://spc.epfl.ch/TCV-technical-data. 14

[27] V. V. Alikaev and V. V. Parail. Current drive by electron cyclotron waves. *Plasma Phys. Control. Fusion*, 33(13):1639–1656, nov 1991. ISSN 0741-3335. doi: 10.1088/0741-3335/33/13/011. URL http://iopscience.iop.org/0741-3335/33/13/011. 16

[28] Alexander N. Karpushov, René Chavan, Stefano Coda, Vladimir I. Davydenko, Frédéric Dolizy, Aleksandr N. Dranitchnikov, Basil P. Duval, Alexander A. Ivanov, Damien Fasel, Ambrogio Fasoli, Vyacheslav V. Kolmogorov, Pierre Lavanchy, Xavier Llobet, Blaise Marlétaz, Philippe Marmillod, Yves Martin, Antoine Merle, Albert Perez, Olivier Sauter, Ugo Siravo, Igor V. Shikhovtsev, Aleksey V. Sorokin, and Matthieu Toussaint. Neutral beam heating on the TCV tokamak. *Fusion Eng. Des.*, 2017. ISSN 09203796. doi: 10.1016/j.fusengdes.2017.02.076. URL http://linkinghub.elsevier.com/retrieve/pii/S0920379617301692. 16

Bibliography

[29] F. Hofmann. FBT - a free-boundary tokamak equilibrium code for highly elongated and shaped plasmas. *Comput. Phys. Commun.*, 48(2):207–221, feb 1988. ISSN 00104655. doi: 10.1016/0010-4655(88)90041-0. URL http://linkinghub.elsevier.com/retrieve/pii/0010465588900410. 18

[30] F. Hofmann and G. Tonetti. Fast identification of plasma boundary and X-points in elongated tokamaks. *Nucl. Fusion*, 28(3):519–522, mar 1988. ISSN 0029-5515. doi: 10.1088/0029-5515/28/3/015. URL http://iopscience.iop.org/0029-5515/28/3/015.

[31] F Hofmann and G Tonetti. Tokamak equilibrium reconstruction using Faraday rotation measurements. *Nucl. Fusion,* 28(10):1871–1878, oct 1988. ISSN 0029-5515. doi: 10.1088/0029-5515/28/10/014. URL http://iopscience.iop.org/0029-5515/28/10/014.

[32] J.-M. Moret, B.P. Duval, H.B. Le, S. Coda, F. Felici, and H. Reimerdes. Tokamak equilibrium reconstruction code LIUQE and its real time implementation. *Fusion Eng. Des.*, 91:1–15, feb 2015. ISSN 09203796. doi: 10.1016/j.fusengdes.2014.09.019. URL http://linkinghub.elsevier.com/retrieve/pii/S0920379614005973. 18

[33] J. Fujita, K. Matsuura, K. Kawahata, S. Fujiwaka, S. Itoh, K. N. Sato, K. Nakamura, H. Zushi, M. Sakamoto, K. Hanada, E. Jotaki, and K. Makino. A rotating coil probe for the magnetic field measurement on a long pulsed tokamak. *Rev. Sci. Instrum.*, 70(1):445–448, jan 1999. ISSN 0034-6748. doi: 10.1063/1.1149281. URL http://aip.scitation.org/doi/10.1063/1.1149281. 18

[34] I. H. Hutchinson. *Principles of Plasma Diagnostics*. Cambridge University Press, Cambridge, 2002. ISBN 9780511613630. doi: 10.1017/CBO9780511613630. URL http://ebooks.cambridge.org/ref/id/CBO9780511613630. 18, 21

[35] R. Behn, J. H. Rommers, R. A. Pitts, Z. A. Pietrzyk, R. Chavan, and B. Marletaz. A Thomson scattering diagnostic for measurements in the divertor region of TCV. *Rev. Sci. Instrum.*, 70(1):768–771, jan 1999. ISSN 0034-6748. doi: 10.1063/1.1149497. URL http://aip.scitation.org/doi/10.1063/1.1149497. 19

[36] Josef Kamleitner. *Suprathermal electron studies in Tokamak plasmas by means of diagnostic measurements and modeling*. Phd thesis n.6523, EPFL, 2015. URL https://infoscience.epfl.ch/record/205095. 19

[37] Paolo Bosshard. *Confinement ionique dans le tokamak TCV mesure par spectroscopie d'echange de charge*. Phd thesis n.2723, EPFL, 2003. URL https://infoscience.epfl.ch/record/33199?ln=en. 20, 31, 40, 45, 65, 71

[38] Alessandro Bortolon. *Plasma Rotation and Momentum Transport Studies in the TCV Tokamak Based on Charge Exchange Spectroscopy Measurements*. Phd thesis n.4569, EPFL, 2009. URL https://infoscience.epfl.ch/record/142212?ln=en. 22, 24, 29, 40, 43, 62, 108, 111, 112, 115

[39] Lucia Isabel Federspiel. *Rotation and Impurity Studies in the presence of MHD activity and Internal Transport Barriers on TCV.* Phd thesis n.6050, EPFL, 2014. URL https://infoscience.epfl.ch/record/199078?ln=en. 20, 23, 24, 40, 41, 108, 112, 115

[40] Christian Schlatter. *Turbulent ion heating in TCV tokamak plasmas.* Phd thesis n.4479, EPFL, Lausanne, 2009. URL https://infoscience.epfl.ch/record/138758?ln=en. 20, 29, 31, 43, 44, 45

[41] Alexander N. Karpushov, Basil P. Duval, Christian Schlatter, Valery I. Afanasyev, and Fedor V. Chernyshev. Neutral particle analyzer diagnostics on the TCV tokamak. *Rev. Sci. Instrum.*, 77(3):033504, mar 2006. ISSN 0034-6748. doi: 10.1063/1.2185151. URL http://aip.scitation.org/doi/10.1063/1.2185151. 21

[42] SPC wiki. URL https://crpplocal.epfl.ch/wiki/Main{_}Page. 21

[43] A. Sushkov, V. Andreev, Y. Camenen, A. Pochelon, I. Klimanov, A. Scarabosio, and H. Weisen. High-resolution multiwire proportional soft x-ray diagnostic measurements on TCV. *Rev. Sci. Instrum.*, 79(2):023506, 2008. ISSN 00346748. doi: 10.1063/1.2833822. URL http://scitation.aip.org/content/aip/journal/rsi/79/2/10.1063/1.2833822. 21

[44] Ivo Furno. *Fast transient transport phenomena measured by soft x-ray emission in TCV tokamak plasmas.* Phd thesis n. 2434, EPFL, 2001. URL https://infoscience.epfl.ch/record/32910. 22

[45] E.J. Doyle, W.A. Houlberg, Y. Kamada, V. Mukhovatov, T.H. Osborne, A. Polevoi, G Bateman, J.W Connor, J.G. Cordey, T Fujita, X Garbet, T.S Hahm, L.D Horton, A.E Hubbard, F Imbeaux, F Jenko, J.E Kinsey, Y Kishimoto, J Li, T.C Luce, Y Martin, M Ossipenko, V Parail, A Peeters, T.L Rhodes, J.E Rice, C.M Roach, V Rozhansky, F Ryter, G Saibene, R Sartori, A.C.C Sips, J.A Snipes, M Sugihara, E.J Synakowski, H Takenaga, T Takizuka, K Thomsen, M.R Wade, H.R Wilson, ITPA Transport Physics Topical Group, ITPA Confinement Database Group, Model, ITPA Pedestal Group, and Edge Topical. Chapter 2: Plasma confinement and transport. *Nucl. Fusion*, 47(6):S18–S127, jun 2007. ISSN 0029-5515. doi: 10.1088/0029-5515/47/6/S02. URL http://stacks.iop.org/0029-5515/47/i=6/a=S02?key=crossref.36e162162f67e92c3a62080002fc7583. 22

[46] a. J. Wootton, B. a. Carreras, H. Matsumoto, K. McGuire, W. a. Peebles, Ch. P. Ritz, P. W. Terry, and S. J. Zweben. Fluctuations and anomalous transport in tokamaks. *Phys. Fluids B Plasma Phys.*, 2(12):2879–2903, dec 1990. ISSN 0899-8221. doi: 10.1063/1.859358. URL http://aip.scitation.org/doi/10.1063/1.859358. 22

[47] P. Manz, M. Ramisch, and U. Stroth. Physical Mechanism behind Zonal-Flow Generation in Drift-Wave Turbulence. *Phys. Rev. Lett.*, 103(16):165004, oct 2009. ISSN 0031-9007. doi: 10.1103/PhysRevLett.103.165004. URL http://link.aps.org/doi/10.1103/PhysRevLett.103.165004. 22

Bibliography

[48] A.M. Garofalo, G.L. Jackson, R.J. La Haye, M. Okabayashi, H. Reimerdes, E.J. Strait, J.R. Ferron, R.J. Groebner, Y. In, M.J. Lanctot, G. Matsunaga, G.A. Navratil, W.M. Solomon, H. Takahashi, M. Takechi, and A.D. Turnbull. Stability and control of resistive wall modes in high beta, low rotation DIII-D plasmas. *Nucl. Fusion*, 47(9):1121–1130, sep 2007. ISSN 0029-5515. doi: 10.1088/0029-5515/47/9/008. URL http://stacks.iop.org/0029-5515/47/i=9/a=008?key=crossref.b9f88c706721411c16ec84e7ef31e8c7. 22

[49] R. J. Buttery, R. J. La Haye, P. Gohil, G. L. Jackson, H. Reimerdes, and E. J. Strait. The influence of rotation on the βN threshold for the 2/1 neoclassical tearing mode in DIII-D. *Phys. Plasmas*, 15(5):056115, may 2008. ISSN 1070-664X. doi: 10.1063/1.2894215. URL http://aip.scitation.org/doi/10.1063/1.2894215. 22

[50] H. Biglari, P. H. Diamond, and P. W. Terry. Influence of sheared poloidal rotation on edge turbulence. *Phys. Fluids B Plasma Phys.*, 2(1):1–4, jan 1990. ISSN 0899-8221. doi: 10.1063/1.859529. URL http://aip.scitation.org/doi/10.1063/1.859529. 22, 97, 131

[51] J.E. Rice, A. Ince-Cushman, J.S. DeGrassie, L.-G. Eriksson, Y. Sakamoto, A. Scarabosio, A. Bortolon, K.H. Burrell, B.P. Duval, C. Fenzi-Bonizec, M.J. Greenwald, R.J. Groebner, G.T. Hoang, Y. Koide, E.S. Marmar, A. Pochelon, and Y. Podpaly. Inter-machine comparison of intrinsic toroidal rotation in tokamaks. *Nucl. Fusion*, 47(11):1618–1624, nov 2007. ISSN 0029-5515. doi: 10.1088/0029-5515/47/11/025. URL http://stacks.iop.org/0029-5515/47/i=11/a=025?key=crossref.28324ceb500ca22140fee82b1a7f5219. 23

[52] W. M. Solomon, K. H. Burrell, A. M. Garofalo, S. M. Kaye, R. E. Bell, A. J. Cole, J. S. DeGrassie, P. H. Diamond, T. S. Hahm, G. L. Jackson, M. J. Lanctot, C. C. Petty, H. Reimerdes, S. A. Sabbagh, E. J. Strait, T. Tala, and R. E. Waltz. Mechanisms for generating toroidal rotation in tokamaks without external momentum input. *Phys. Plasmas*, 17(5):056108, may 2010. ISSN 1070-664X. doi: 10.1063/1.3328521. URL http://aip.scitation.org/doi/10.1063/1.3328521. 23

[53] J.-M Noterdaeme, E. Righi, V. Chan, J DeGrassie, K. Kirov, M. Mantsinen, M.F.F Nave, D. Testa, K.-D Zastrow, R. Budny, R. Cesario, A. Gondhalekar, N. Hawkes, T. Hellsten, Ph Lamalle, F. Meo, F. Nguyen, and EFDA-JET-EFDA Contributors. Spatially resolved toroidal plasma rotation with ICRF on JET. *Nucl. Fusion*, 43(4):274–289, apr 2003. ISSN 0029-5515. doi: 10.1088/0029-5515/43/4/309. URL http://stacks.iop.org/0029-5515/43/i=4/a=309?key=crossref.f05cefbbc6c8c57e425d93863178a7d4. 23

[54] R.M. McDermott, C Angioni, G.D. Conway, R Dux, E Fable, R Fischer, T Pütterich, F Ryter, and E Viezzer. Core intrinsic rotation behaviour in ASDEX Upgrade ohmic L-mode plasmas. *Nucl. Fusion*, 54(4):043009, apr 2014. ISSN 0029-5515. doi: 10.1088/0029-5515/54/4/043009. URL http://stacks.iop.org/0029-5515/54/i=4/a=043009?key=crossref.04ef6f6c7e1445fb03f9a663effdf8b7. 23, 101

[55] EUROFUSION-MST1 campaign. URL https://www.euro-fusion.org/newsletter/first-medium-size-tokamak-campaign-successfully-completed/. 23

[56] RAID device at SPC. URL http://spc.epfl.ch/. 23

[57] D. Wünderlich, S. Dietrich, and U. Fantz. Application of a collisional radiative model to atomic hydrogen for diagnostic purposes. *J. Quant. Spectrosc. Radiat. Transf.*, 110 (1-2):62–71, jan 2009. ISSN 00224073. doi: 10.1016/j.jqsrt.2008.09.015. URL http://linkinghub.elsevier.com/retrieve/pii/S0022407308002082. 23, 86, 87

[58] C. Marini, R. Agnello, B.P. Duval, I. Furno, A.A. Howling, R. Jacquier, A.N. Karpushov, G. Plyushchev, K. Verhaegh, Ph. Guittienne, U. Fantz, D. Wünderlich, S. Béchu, and A. Simonin. Spectroscopic characterization of H 2 and D 2 helicon plasmas generated by a resonant antenna for neutral beam applications in fusion. *Nucl. Fusion*, 57(3):036024, mar 2017. ISSN 0029-5515. doi: 10.1088/1741-4326/aa53eb. URL http://stacks.iop.org/0029-5515/57/i=3/a=036024?key=crossref.b4ba7330f39b0de286823abee1745909. 23, 77, 156

[59] C Angioni, R M McDermott, E Fable, R Fischer, T Pütterich, F Ryter, and G Tardini. Gyrokinetic modelling of electron and boron density profiles of H-mode plasmas in ASDEX Upgrade. *Nucl. Fusion*, 51(2):23006, 2011. ISSN 0029-5515. doi: 10.1088/0029-5515/51/2/023006. URL http://stacks.iop.org/0029-5515/51/i=2/a=023006?key=crossref.aa3d37c129c0fed41cb1f9fc1b90580b. 25

[60] T Nicolas, H. Lütjens, J.-F. Luciani, X Garbet, and R Sabot. Impurity behavior during sawtooth activity in tokamak plasmas. *Phys. Plasmas*, 21(1):012507, jan 2014. ISSN 1070-664X. doi: 10.1063/1.4861859. URL http://aip.scitation.org/doi/10.1063/1.4861859. 25, 108, 124

[61] R. J. Fonck, D. S. Darrow, and K. P. Jaehnig. Determination of plasma-ion velocity distribution via charge-exchange recombination spectroscopy. *Phys. Rev. A*, 29(6): 3288–3309, jun 1984. ISSN 0556-2791. doi: 10.1103/PhysRevA.29.3288. URL https://link.aps.org/doi/10.1103/PhysRevA.29.3288. 28, 33, 34, 36, 72, 168

[62] H P Summers. The ADAS manual, version 2.3. Technical report, University of Strathclyde, 2001. URL http://adas.phys.strath.ac.uk. 28, 30, 33, 73

[63] S.P. Hirshman and D.J. Sigmar. Neoclassical transport of impurities in tokamak plasmas. *Nucl. Fusion*, 21(9):1079–1201, sep 1981. ISSN 0029-5515. doi: 10.1088/0029-5515/21/9/003. URL http://stacks.iop.org/0029-5515/21/i=9/a=003?key=crossref.ce6f9ef543e2d0f66903fdc063d88ec7. 29, 98, 99

[64] B. P. Duval, A. Bortolon, A. Karpushov, R. A. Pitts, A. Pochelon, O. Sauter, A. Scarabosio, and G. Turri. Spontaneous L-mode plasma rotation scaling in the TCV tokamak. *Phys. Plasmas*, 15(5):056113, may 2008. ISSN 1070-664X. doi: 10.1063/1.2841528. URL http://aip.scitation.org/doi/10.1063/1.2841528. 29, 111, 129

[65] R. E. Bell, R. Andre, S. M. Kaye, R. A. Kolesnikov, B. P. LeBlanc, G. Rewoldt, W. X. Wang, and S. A. Sabbagh. Comparison of poloidal velocity measurements to neoclassical

theory on the National Spherical Torus Experiment. *Phys. Plasmas*, 17(8):082507, aug 2010. ISSN 1070-664X. doi: 10.1063/1.3478571. URL http://aip.scitation.org/doi/10.1063/1.3478571. 29, 62, 97

[66] A R Field, J McCone, N J Conway, M Dunstan, S Newton, and M Wisse. Comparison of measured poloidal rotation in MAST spherical tokamak plasmas with neo-classical predictions. *Plasma Phys. Control. Fusion*, 51(10):105002, oct 2009. ISSN 0741-3335. doi: 10.1088/0741-3335/51/10/105002. URL http://stacks.iop.org/0741-3335/51/i=10/a=105002?key=crossref.6b77956c99f27b59b66bb7bdf98925b1.

[67] K D Marr, B Lipschultz, P J Catto, R M McDermott, M L Reinke, and a N Simakov. Comparison of neoclassical predictions with measured flows and evaluation of a poloidal impurity density asymmetry. *Plasma Phys. Control. Fusion*, 52(5):055010, may 2010. ISSN 0741-3335. doi: 10.1088/0741-3335/52/5/055010. URL http://stacks.iop.org/0741-3335/52/i=5/a=055010?key=crossref.283e56c75f0f25657025522543156860.

[68] E Viezzer, T Pütterich, C Angioni, A Bergmann, R Dux, E Fable, R.M. McDermott, U Stroth, and E Wolfrum. Evidence for the neoclassical nature of the radial electric field in the edge transport barrier of ASDEX Upgrade. *Nucl. Fusion*, 54(1):012003, jan 2014. ISSN 0029-5515. doi: 10.1088/0029-5515/54/1/012003. URL http://stacks.iop.org/0029-5515/54/i=1/a=012003?key=crossref.236e707f43703dba058508b9bec226c7. 131, 145

[69] A. Bortolon, Y. Camenen, A.N. Karpushov, B.P. Duval, Y. Andrebe, L. Federspiel, and O. Sauter. Indirect measurement of poloidal rotation using inboard–outboard asymmetry of toroidal rotation and comparison with neoclassical predictions. *Nucl. Fusion*, 53(2):023002, feb 2013. ISSN 0029-5515. doi: 10.1088/0029-5515/53/2/023002. URL http://stacks.iop.org/0029-5515/53/i=2/a=023002?key=crossref.a69a0e8722d6d821715c1f5d2a50d6f6. 29, 56, 85, 96, 97

[70] R. E. Bell, F. M. Levinton, S. H. Batha, E. J. Synakowski, and M. C. Zarnstorff. Poloidal Rotation in TFTR Reversed Shear Plasmas. *Phys. Rev. Lett.*, 81(7):1429–1432, aug 1998. ISSN 0031-9007. doi: 10.1103/PhysRevLett.81.1429. URL http://link.aps.org/doi/10.1103/PhysRevLett.81.1429. 29

[71] T Tala, Y. Andrew, K. Crombé, P.C. de Vries, X Garbet, N Hawkes, H Nordman, K Rantamäki, P Strand, A Thyagaraja, J Weiland, E Asp, Y Baranov, C Challis, G Corrigan, A. Eriksson, C. Giroud, M.-D Hua, I Jenkins, H.C.M Knoops, X Litaudon, P Mantica, V Naulin, V Parail, K.-D Zastrow, and JET-EFDA Contributors. Toroidal and poloidal momentum transport studies in JET. *Nucl. Fusion*, 47(8):1012–1023, aug 2007. ISSN 0029-5515. doi: 10.1088/0029-5515/47/8/036. URL http://stacks.iop.org/0029-5515/47/i=8/a=036?key=crossref.91d49d00d4ff6daf5d8caa97f1cd1127.

[72] K. Crombé, Y. Andrew, M. Brix, C. Giroud, S. Hacquin, N. C. Hawkes, A. Murari, M. F F Nave, J. Ongena, V. Parail, G. Van Oost, I. Voitsekhovitch, and K.-D. Zastrow. Poloidal

Rotation Dynamics, Radial Electric Field, and Neoclassical Theory in the Jet Internal-Transport-Barrier Region. *Phys. Rev. Lett.*, 95(15):155003, oct 2005. ISSN 0031-9007. doi: 10.1103/PhysRevLett.95.155003. URL http://link.aps.org/doi/10.1103/PhysRevLett.95.155003.

[73] W. M. Solomon, K. H. Burrell, R. Andre, L. R. Baylor, R. Budny, P. Gohil, R. J. Groebner, C. T. Holcomb, W. A. Houlberg, and M. R. Wade. Experimental test of the neoclassical theory of impurity poloidal rotation in tokamaks. *Phys. Plasmas*, 13(5):056116, may 2006. ISSN 1070-664X. doi: 10.1063/1.2180728. URL http://aip.scitation.org/doi/10.1063/1.2180728. 29

[74] R C Isler. An Overview Of Charge-Exchange Spectroscopy As A Plasma Diagnostic. *Plasma Phys. Control. Fusion*, 36(2):171–208, 1994. ISSN 0741-3335. doi: 10.1088/0741-3335/36/2/001. URL http://stacks.iop.org/0741-3335/36/i=2/a=001. 34

[75] A Blom and C Jupen. Parametrization of the Zeeman effect for hydrogen-like spectra in high-temperature plasmas. *Plasma Phys. Control. Fusion*, 44(7):312, jul 2002. ISSN 07413335. doi: 10.1088/0741-3335/44/7/312. URL http://stacks.iop.org/0741-3335/44/i=7/a=312?key=crossref.b5cd76c272c144cbfde134eff3b71d10. 34

[76] M von Hellermann, P Breger, J Frieling, R Konig, W Mandl, A Maas, and H P Summers. Analytical approximation of cross-section effects on charge exchange spectra observed in hot fusion plasmas. *Plasma Phys. Control. Fusion*, 37(2):71–94, feb 1995. ISSN 0741-3335. doi: 10.1088/0741-3335/37/2/002. URL http://stacks.iop.org/0741-3335/37/i=2/a=002?key=crossref.bbfd0c7ee9a5f9456530711b340b17ad. 36, 168

[77] R E Bell. New understanding of poloidal rotation measurements in a Tokamak plasma. In *AIP Conf. Proc.*, volume 547, pages 39–52. AIP, 2000. ISBN 1800553684. doi: 10.1063/1.1361778. URL http://aip.scitation.org/doi/abs/10.1063/1.1361778. 37, 38

[78] W M Solomon, K H Burrell, P Gohil, R J Groebner, and L R Baylor. Extraction of poloidal velocity from charge exchange recombination spectroscopy measurements. *Rev. Sci. Instrum.*, 75(10):3481–3486, oct 2004. ISSN 0034-6748. doi: 10.1063/1.1790042. URL http://aip.scitation.org/doi/10.1063/1.1790042. 37

[79] Athina Kappatou. *Investigations of helium transport in ASDEX Upgrade plasmas with charge exchange recombination spectroscopy.* Phd thesis, Technische Universiteit Eindhoven, 2014. URL http://repository.tue.nl/780941. 38, 44, 71, 72

[80] I H Hutchinson. Statistical uncertainty in line shift and width interpretation. *Eur. Phys. J. Plus*, 127(7):81, jul 2012. ISSN 2190-5444. doi: 10.1140/epjp/i2012-12081-3. URL http://www.springerlink.com/index/10.1140/epjp/i2012-12081-3. 39

[81] Ronald E. Bell. Exploiting a transmission grating spectrometer. *Rev. Sci. Instrum.*, 75(10):4158–4161, oct 2004. ISSN 0034-6748. doi: 10.1063/1.1787601. URL http://aip.scitation.org/doi/10.1063/1.1787601. 39

Bibliography

[82] Andor website. URL http://www.andor.com. 42, 154

[83] Alexander N. Karpushov, Yanis Andrebe, Basil P. Duval, and Alessandro Bortolon. The diagnostic neutral beam injector with arc-discharge plasma source on the TCV Tokamak. *Fusion Eng. Des.*, 84(2-6):993–997, jun 2009. ISSN 09203796. doi: 10.1016/j.fusengdes. 2008.12.006. URL http://linkinghub.elsevier.com/retrieve/pii/S0920379608004626. 43

[84] F.L. Hinton and M.N. Rosenbluth. The mechanism for toroidal momentum input to Tokamak plasmas from neutral beams. *Phys. Lett. A*, 259(3-4):267–275, aug 1999. ISSN 03759601. doi: 10.1016/S0375-9601(99)00453-3. URL http://linkinghub.elsevier.com/retrieve/pii/S0375960199004533. 43

[85] H. L. CLAUSING INC. URL http://www.clausing.com. 47

[86] Horiba. Horiba gratings webpage. URL http://www.horiba.com/scientific/products/diffraction-gratings/. 48

[87] Newport. Newport RVS80CC webpage. URL https://www.newport.com/p/RVS80CC. 48

[88] S.K. Madan, B. Bhaumik, and J.M. Vasi. Experimental observation of avalanche multiplication in charge-coupled devices. *IEEE Trans. Electron Devices*, 30(6):694–699, jun 1983. ISSN 0018-9383. doi: 10.1109/T-ED.1983.21191. URL http://ieeexplore.ieee.org/document/1483092/. 51

[89] Andor. EMCCD camera. URL http://www.andor.com/learning-academy/electron-multiplying-ccd-cameras-the-technology-behind-emccds. 51

[90] Robert Nigel Tubbs. *Lucky Exposures: Diffraction limited astronomical imaging through the atmosphere*. PhD thesis, Cambridge University, nov 2003. URL http://www.dspace.cam.ac.uk/handle/1810/224517http://arxiv.org/abs/astro-ph/0311481. 53

[91] IAEA. ALADDIN. URL https://www-amdis.iaea.org/ALADDIN/collision.html. 60

[92] I D Williams, J Geddes, and H B Gilbody. Balmer α emission in collisions of H, H + , H 2 + and H 3 + with H 2. *J. Phys. B At. Mol. Phys.*, 15(9):1377–1389, may 1982. ISSN 0022-3700. doi: 10.1088/0022-3700/15/9/014. URL http://stacks.iop.org/0022-3700/15/i=9/a=014?key=crossref.e79cf382a2e530f5c7ea11cf9cc806c9. 61

[93] E. Viezzer. *Radial electric field studies in the plasma edge of ASDEX Upgrade*. Phd thesis, Ludwig Maximilians Universitat Munchen, 2012. URL http://hdl.handle.net/11858/00-001M-0000-0026-DE35-0. 62, 73, 97, 146, 147, 148, 153, 180

[94] Philip Robinson Bevington, D. Keith Robinson, J. Morris Blair, A. John Mallinckrodt, and Susan McKay. Data Reduction and Error Analysis for the Physical Sciences. *Comput. Phys.*, 7(4):415, 1993. ISSN 08941866. doi: 10.1063/1.4823194. URL http://scitation.aip.org/content/aip/journal/cip/7/4/10.1063/1.4823194. 67, 168

[95] Donald W. Marquardt. An Algorithm for Least-Squares Estimation of Nonlinear Parameters. *J. Soc. Ind. Appl. Math.*, 11(2):431–441, jun 1963. ISSN 0368-4245. doi: 10.1137/0111030. URL http://epubs.siam.org/doi/10.1137/0111030. 67

[96] T Pütterich, E. Wolfrum, R. Dux, and C. F. Maggi. Evidence for Strong Inversed Shear of Toroidal Rotation at the Edge-Transport Barrier in the ASDEX Upgrade. *Phys. Rev. Lett.*, 102(2):025001, jan 2009. ISSN 0031-9007. doi: 10.1103/PhysRevLett.102.025001. URL https://link.aps.org/doi/10.1103/PhysRevLett.102.025001. 71

[97] Manfred G von Hellermann, G Bertschinger, Wolfgang Biel, C Giroud, Roger J E Jaspers, C Jupen, O Marchuk, M G O'Mullane, H P Summers, A Whiteford, K.-D. Zastrow, and M O'. Mullane. Complex Spectra in Fusion Plasmas. *Phys. Scr.*, T120:19–29, 2005. ISSN 0031-8949. doi: 10.1088/0031-8949/2005/T120/003. URL http://stacks.iop.org/1402-4896/2005/i=T120/a=003?key=crossref.c32cd84daf551c2160e1c69aad7b85f6. 72, 73

[98] R. J E Jaspers, M. G. von Hellermann, E. Delabie, J. E. Boom, A. J . H. Donnee, W. Biel, N. C. Hawkes, O. Neubauer, M. Di Maio, S. Sadakov, F. Klinkhamer, B. Snijders, A. Hogenbirk, Giuseppe Gorini, Francesco P. Orsitto, Elio Sindoni, and Marco Tardocchi. The CXRS diagnostic for ITER and the CXRS-Pilot Experiment on TEXTOR. In *AIP Conf. Proc.*, volume 988, pages 209–213. AIP, 2008. ISBN 9780735405073. doi: 10.1063/1.2905069. URL http://aip.scitation.org/doi/abs/10.1063/1.2905069. 72

[99] Athina Kappatou. private communication, 2017. 73

[100] Princeton-Instruments. Princeton Instruments IsoPlane 320 webpage. URL http://www.princetoninstruments.com/products/IsoPlane. 77

[101] G Giruzzi, J F Artaud, M Baruzzo, T Bolzonella, E Fable, L Garzotti, I Ivanova-Stanik, R Kemp, D B King, M Schneider, R Stankiewicz, W Stępniewski, P Vincenzi, D Ward, and R Zagórski. Modelling of pulsed and steady-state DEMO scenarios. *Nucl. Fusion*, 55(7):73002, 2015. ISSN 0029-5515. doi: 10.1088/0029-5515/55/7/073002. URL http://stacks.iop.org/0029-5515/55/i=7/a=073002?key=crossref.a17f63ff9ca973d673434299f4ede2ad. 77

[102] M Bacal and G W Hamilton. H-and D-production in plasmas. *Phys. Rev. Lett.*, 42(1):1538–1540, 1979. URL http://journals.aps.org/prl/abstract/10.1103/PhysRevLett.42.1538. 77, 78

[103] A. Simonin, Jocelyn Achard, K. Achkasov, S. Bechu, C. Baudouin, O. Baulaigue, C. Blondel, J.P. Boeuf, D. Bresteau, G. Cartry, W. Chaibi, C. Drag, H.P.L. de Esch, D. Fiorucci, G. Fubiani, I. Furno, R. Futtersack, P. Garibaldi, A. Gicquel, C. Grand, Ph. Guittienne, G. Hagelaar, A. Howling, R. Jacquier, M.J. Kirkpatrick, D. Lemoine, B. Lepetit, T. Minea, E. Odic, A. Revel, B.A. Soliman, and P. Teste. R&D around a photoneutralizer-based NBI system (Siphore) in view of a DEMO Tokamak steady state fusion reactor. *Nucl. Fusion*, 55(12):123020, nov 2015. ISSN 0029-5515. doi: 10.1088/0029-5515/

Bibliography

55/12/123020. URL http://stacks.iop.org/0029-5515/55/i=12/a=123020?key=crossref. 7dbf406091b84da9fe5d1f9adeaaa8d8. 77, 79, 80

[104] T Inoue, M Taniguchi, T Morishita, M Dairaku, M Hanada, T Imai, M Kashiwagi, K Sakamoto, T Seki, and K Watanabe. R&D on a high energy accelerator and a large negative ion source for ITER. *Nucl. Fusion*, 45(8):790–795, aug 2005. ISSN 0029-5515. doi: 10.1088/0029-5515/45/8/004. URL http://stacks.iop.org/0029-5515/45/i=8/a=004? key=crossref.2352702e33336171f2c137cd4126ac20. 78

[105] E Speth, H D Falter, P Franzen, U Fantz, M Bandyopadhyay, S Christ, A Encheva, M Fröschle, D Holtum, B Heinemann, W Kraus, A Lorenz, Ch. Martens, P McNeely, S Obermayer, R Riedl, R Süss, A Tanga, R Wilhelm, and D Wünderlich. Overview of the RF source development programme at IPP Garching. *Nucl. Fusion*, 46(6):S220, 2006. ISSN 0029-5515. doi: 10.1088/0029-5515/46/6/S03. URL http://stacks.iop.org/ 0029-5515/46/i=6/a=S03. 78, 92

[106] M D Carter, F W Baity, G C Barber, R H Goulding, Y Mori, D O Sparks, K F White, E F Jaeger, F. R. Chang-Diaz, and J P Squire. Comparing experiments with modeling for light ion helicon plasma sources. *Phys. Plasmas*, 9(12):5097–5110, dec 2002. ISSN 1070-664X. doi: 10.1063/1.1519539. URL http://aip.scitation.org/doi/10.1063/1.1519539. 78, 80

[107] D Rapp, T. E. Sharp, and D. D. Briglia. Large isotope effect in the formation of H- or D- by electron impact on H2, HD, and D2. *Phys. Rev. Lett.*, 14(14):533–535, apr 1965. ISSN 0031-9007. doi: 10.1103/PhysRevLett.14.533. URL http://link.aps.org/doi/10.1103/ PhysRevLett.14.533. 78

[108] George J Schulz. Resonances in Electron Impact on Diatomic Molecules. *Rev. Mod. Phys.*, 45(3):423–486, jul 1973. ISSN 0034-6861. doi: 10.1103/RevModPhys.45.423. URL http://link.aps.org/doi/10.1103/RevModPhys.45.423. 78

[109] D. S. Walton, B. Peart, and K. T. Dolder. A measurement of cross sections for detachment from H - by a method employing inclined ion and electron beams. *J. Phys. B At. Mol. Phys.*, 4(10):1343–1348, oct 1971. ISSN 0022-3700. doi: 10.1088/ 0022-3700/4/10/019. URL http://stacks.iop.org/0022-3700/4/i=10/a=019?key=crossref. 4584dfe17be1035568f36fb29c4fc5bd. 78

[110] V A Godyak, R B Piejak, and B M Alexandrovich. Measurement of electron energy distribution in low-pressure RF discharges. *Plasma Sources Sci. Technol.*, 1(1):36–58, mar 1992. ISSN 0963-0252. doi: 10.1088/0963-0252/1/1/006. URL http://stacks.iop.org/ 0963-0252/1/i=1/a=006?key=crossref.af4b2f08ac404ea642620308825e9c4c. 78

[111] M Umair Siddiqui, Justin F Kim, Cory D Jackson, and Noah Hershkowitz. Presheath and boundary effects on helicon discharge equilibria. *Plasma Sources Sci. Technol.*, 24(1):015022, dec 2014. ISSN 0963-0252. doi: 10.1088/0963-0252/24/1/015022. URL http://dx.doi.org/10.1088/0963-0252/24/1/015022. 78

[112] Francis F Chen. Helicon Plasma Sources. In Oleg A. Popov, editor, *High Density Plasma Sources*, chapter 1 Helicon, pages 1–75. Elsevier, Park Ridge, NJ, 1995. doi: 10.1016/B978-081551377-3.50003-7. URL http://linkinghub.elsevier.com/retrieve/pii/B9780815513773500037. 80

[113] Ph Guittienne, E. Chevalier, and Ch Hollenstein. Towards an optimal antenna for helicon waves excitation. *J. Appl. Phys.*, 98(8):083304, oct 2005. ISSN 0021-8979. doi: 10.1063/1.2081107. URL http://aip.scitation.org/doi/10.1063/1.2081107. 80

[114] G.H. Dieke. *DiekeThe Hydrogen Molecule Wavelength Tables of Gerhard Heinrich Dieke*. The Johns Hopkins University Wiley-Interscience, New York, 1972. 83

[115] Boris P Lavrov and Ivan S Umrikhin. Atlas and wavenumber tables for the visible part of the electronic-vibro-rotational D2 spectrum emitted by low-temperature plasma. *J. Quant. Spectrosc. Radiat. Transf.*, 182:180–192, oct 2016. ISSN 00224073. doi: 10.1016/j.jqsrt.2016.05.026. URL http://linkinghub.elsevier.com/retrieve/pii/S0022407315303058. 83

[116] D.R. Farley, D.P. Stotler, D.P. Lundberg, and S.A. Cohen. Modeling of hydrogen ground state rotational and vibrational temperatures in kinetic plasmas. *J. Quant. Spectrosc. Radiat. Transf.*, 112(5):800–819, mar 2011. ISSN 00224073. doi: 10.1016/j.jqsrt.2010.10.015. URL http://linkinghub.elsevier.com/retrieve/pii/S0022407310004012. 83

[117] C. S. Carey, I. Furno, H. Weisen, R. Behn, E. Fable, and C. Angioni. Application of the singular value decomposition method for inversion of interferometer measurements in fusion plasmas. *Rev. Sci. Instrum.*, 75(10):3411–3413, oct 2004. ISSN 0034-6748. doi: 10.1063/1.1779613. URL http://aip.scitation.org/doi/10.1063/1.1779613. 84

[118] I Furno, C Angioni, F Porcelli, H Weisen, R Behn, T.P Goodman, M.A Henderson, Z.A Pietrzyk, A Pochelon, H Reimerdes, and E Rossi. Understanding sawtooth activity during intense electron cyclotron heating experiments on TCV. *Nucl. Fusion*, 41(4):403–420, apr 2001. ISSN 0029-5515. doi: 10.1088/0029-5515/41/4/306. URL http://stacks.iop.org/0029-5515/41/i=4/a=306http://stacks.iop.org/0029-5515/41/i=4/a=306?key=crossref.b326795f626b9bb0e41e51bab909f531. 84, 106

[119] M Anton, H Weisen, M Dutch, P Marmillod, and P Paris. X-ray tomography on the TCV tokamak. *Plasma Phys. Control. Fusion*, 38(38):1849–1878, 1996. ISSN 0741-3335. doi: 10.1088/0741-3335/38/11/001. URL http://iopscience.iop.org/0741-3335/38/11/001. 84

[120] K Behringer and U Fantz. The influence of opacity on hydrogen excited-state population and applications to low-temperature plasmas. *New J. Phys.*, 2:23, sep 2000. ISSN 1367-2630. doi: 10.1088/1367-2630/2/1/323. URL http://stacks.iop.org/1367-2630/2/i=1/a=323?key=crossref.2ac8f3fe26ac98a6b1b2a008c0a5800f. 87

Bibliography

[121] U. Fantz and D. Wünderlich. A novel diagnostic technique for H- (D-) densities in negative hydrogen ion sources. *New J. Phys.*, 8(12):301–301, dec 2006. ISSN 1367-2630. doi: 10.1088/1367-2630/8/12/301. URL http://stacks.iop.org/1367-2630/8/i=12/a=301?key=crossref.0f040596b412cad5387b13e4dcbc7d85. 87

[122] Cameron M Samuell and Cormac S Corr. Atomic and molecular hydrogen gas temperatures in a low-pressure helicon plasma. *Plasma Sources Sci. Technol.*, 24(4):045003, jun 2015. ISSN 0963-0252. doi: 10.1088/0963-0252/24/4/045003. URL http://stacks.iop.org/0963-0252/24/i=4/a=045003?key=crossref.82aaed5b2fbe702e34a7c0b9e0a3f13b. 89

[123] S. ̃I. Braginskii. Transport Processes in a Plasma. *Rev. Plasma Phys.*, 1:205, 1965. URL http://adsabs.harvard.edu/abs/1965RvPP....1..205B. 93

[124] James D. Callen. Plasma Descriptions I : Kinetic , Two-Fluid. In *Fundam. Plasma Phys.*, chapter 5. Madison, Wisconsin, draft edition, 2006. URL http://homepages.cae.wisc.edu/{~}Callen/book.html. 93, 95, 96

[125] John David Jackson. *Classical electrodynamics (3rd ed.)*. Wiley, New York. ISBN 978-0-471-30932-1. 93

[126] R. D. Hazeltine. Rotation of a toroidally confined, collisional plasma. *Phys. Fluids*, 17 (5):961, 1974. ISSN 00319171. doi: 10.1063/1.1694838. URL http://scitation.aip.org/content/aip/journal/pof1/17/5/10.1063/1.1694838. 96

[127] R. M. McDermott, B. Lipschultz, J. W. Hughes, P. J. Catto, A. E. Hubbard, I. H. Hutchinson, R. S. Granetz, M. Greenwald, B. LaBombard, K. Marr, M. L. Reinke, J. E. Rice, and D. Whyte. Edge radial electric field structure and its connections to H-mode confinement in Alcator C-Mod plasmas. *Phys. Plasmas*, 16(5):056103, may 2009. ISSN 1070-664X. doi: 10.1063/1.3080721. URL http://aip.scitation.org/doi/10.1063/1.3080721. 97, 131, 139, 145, 146, 147, 148, 153

[128] P Gohil, K.H Burrell, E.J Doyle, R.J Groebner, J Kim, and R.P Seraydarian. The phenomenology of the L-H transition in the DIII-D tokamak. *Nucl. Fusion*, 34(8):1057–1068, aug 1994. ISSN 0029-5515. doi: 10.1088/0029-5515/34/8/I01. URL http://stacks.iop.org/0029-5515/34/i=8/a=I01?key=crossref.92d09020b6077711bb25d2aab5db0de8. 97

[129] Y Andrew, N C Hawkes, T Biewer, K Crombe, D Keeling, E de la Luna, C Giroud, A Korotkov, A Meigs, A Murari, I Nunes, R Sartori, and T Tala. Evolution of the radial electric field in a JET H-mode plasma. *EPL (Europhysics Lett.*, 83(1):15003, jul 2008. ISSN 0295-5075. doi: 10.1209/0295-5075/83/15003. URL http://stacks.iop.org/0295-5075/83/i=1/a=15003?key=crossref.294feb1a3d817d84aa6e625972fc1e83. 97, 132

[130] K. Ida, S. Hidekuma, M. Kojima, Y. Miura, S. Tsuji, K. Hoshino, M. Mori, N. Suzuki, and T. Yamauchi. Edge poloidal rotation profiles of H-mode plasmas in the JFT-2M tokamak. *Phys. Fluids B Plasma Phys.*, 4(8):2552–2559, aug 1992. ISSN 0899-8221. doi: 10.1063/1.860486. URL http://aip.scitation.org/doi/10.1063/1.860486. 97

[131] H Meyer, C Bunting, P G Carolan, N J Conway, M R Dunstan, A Kirk, R Scannell, D Temple, M Walsh, the MAST Teams, and NBI. The structure, evolution and role of the radial edge electric field in H-mode and L-mode on MAST. *J. Phys. Conf. Ser.*, 123:012005, jul 2008. ISSN 1742-6596. doi: 10.1088/1742-6596/123/1/012005. URL http://stacks.iop.org/1742-6596/123/i=1/a=012005?key=crossref.0d29a752301a6c4272a59c34f44f0e14. 97, 132, 145, 146

[132] Thomas H Stix. Decay of poloidal rotation in a tokamak plasma. *Phys. Fluids*, 16(8):1260, 1973. ISSN 00319171. doi: 10.1063/1.1694506. URL http://scitation.aip.org/content/aip/journal/pof1/16/8/10.1063/1.1694506. 97, 99, 100, 103

[133] U Stroth, P Manz, and M Ramisch. On the interaction of turbulence and flows in toroidal plasmas. *Plasma Phys. Control. Fusion*, 53(2):024006, feb 2011. ISSN 0741-3335. doi: 10.1088/0741-3335/53/2/024006. URL http://stacks.iop.org/0741-3335/53/i=2/a=024006?key=crossref.2e643655a16ba8539e0638569dd59396. 97

[134] T S Hahm. Rotation shear induced fluctuation decorrelation in a toroidal plasma. *Phys. Plasmas*, 1(9):2940–2944, sep 1994. ISSN 1070-664X. doi: 10.1063/1.870534. URL http://aip.scitation.org/doi/10.1063/1.870534. 98, 147

[135] T S Hahm and K H Burrell. Role of flow shear in enhanced core confinement regimes. *Plasma Phys. Control. Fusion*, 38(8):1427, 1996. ISSN 07413335. doi: 10.1088/0741-3335/38/8/049. URL http://stacks.iop.org/0741-3335/38/i=8/a=049. 98, 147

[136] P. W. Terry. Suppression of turbulence and transport by sheared flow. *Rev. Mod. Phys.*, 72(1):109–165, jan 2000. ISSN 0034-6861. doi: 10.1103/RevModPhys.72.109. URL https://link.aps.org/doi/10.1103/RevModPhys.72.109. 98

[137] R B White. *Theory of tokamak plasmas.* North-Holland, 1989. ISBN 9780444874757. URL http://www.sciencedirect.com/science/book/9780444874757. 99

[138] T Pütterich, R Dux, M.A. Janzer, and R.M. McDermott. ELM flushing and impurity transport in the H-mode edge barrier in ASDEX Upgrade. *J. Nucl. Mater.*, 415(1):S334–S339, aug 2011. ISSN 00223115. doi: 10.1016/j.jnucmat.2010.09.052. URL http://linkinghub.elsevier.com/retrieve/pii/S0022311510005623. 99

[139] Y.B. B Kim, P.H. H Diamond, and R.J. J Groebner. Neoclassical poloidal and toroidal rotation in tokamaks. *Phys. Fluids B Plasma Phys.*, 3(8):2050–2060, aug 1991. ISSN 0899-8221. doi: 10.1063/1.859671. URL http://aip.scitation.org/doi/10.1063/1.859671. 99, 100

[140] F L Hinton, J. Kim, Y.-B. Kim, A Brizard, and K H Burrell. Poloidal rotation near the edge of a tokamak plasma in H mode. *Phys. Rev. Lett.*, 72(8):1216–1219, feb 1994. ISSN 0031-9007. doi: 10.1103/PhysRevLett.72.1216. URL https://link.aps.org/doi/10.1103/PhysRevLett.72.1216. 99

Bibliography

[141] J. M. Berger, W. A. Newcomb, J. M. Dawson, E. A. Frieman, R. M. Kulsrud, and A. Lenard. Heating of a Confined Plasma by Oscillating Electromagnetic Fields. *Phys. Fluids*, 1 (4):301, 1958. ISSN 00319171. doi: 10.1063/1.1705888. URL http://scitation.aip.org/content/aip/journal/pof1/1/4/10.1063/1.1705888. 99

[142] John M. Dawson and Myron F. Uman. Heating a plasma by means of magnetic pumping. *Nucl. Fusion*, 5(3):242–248, sep 1965. ISSN 0029-5515. doi: 10.1088/0029-5515/5/3/009. URL http://stacks.iop.org/0029-5515/5/i=3/a=009?key=crossref.ed474cd4a675dd97c98cbb4f883ee8cb.

[143] Adil B Hassam and Russell M Kulsrud. Time evolution of mass flows in a collisional tokamak. *Phys. Fluids*, 21(12):2271, 1978. ISSN 00319171. doi: 10.1063/1.862166. URL http://aip.scitation.org/doi/abs/10.1063/1.862166. 99

[144] D Testa, C Giroud, A Fasoli, and K.-D. Zastrow. On the measurement of toroidal rotation for the impurity and the main ion species on the Joint European Torus. *Phys. Plasmas*, 9 (1):243–250, jan 2002. ISSN 1070-664X. doi: 10.1063/1.1427727. URL http://aip.scitation.org/doi/10.1063/1.1427727. 101

[145] F. L. Hinton and S. K. Wong. Neoclassical ion transport in rotating axisymmetric plasmas. *Phys. Fluids*, 28(10):3082, 1985. ISSN 00319171. doi: 10.1063/1.865350. URL http://scitation.aip.org/content/aip/journal/pof1/28/10/10.1063/1.865350. 101

[146] A. Bortolon, B. P. Duval, A. Pochelon, and A. Scarabosio. Observation of Spontaneous Toroidal Rotation Inversion in Ohmically Heated Tokamak Plasmas. *Phys. Rev. Lett.*, 97(23):235003, dec 2006. ISSN 0031-9007. doi: 10.1103/PhysRevLett.97.235003. URL https://link.aps.org/doi/10.1103/PhysRevLett.97.235003. 101

[147] J E Rice, a C Ince-Cushman, M L Reinke, Y Podpaly, M J Greenwald, B LaBombard, and E S Marmar. Spontaneous core toroidal rotation in Alcator C-Mod L-mode, H-mode and ITB plasmas. *Plasma Phys. Control. Fusion*, 50(12):124042, dec 2008. ISSN 0741-3335. doi: 10.1088/0741-3335/50/12/124042. URL http://stacks.iop.org/0741-3335/50/i=12/a=124042?key=crossref.914376f41bbbf8be28530fc85905f200. 101, 131

[148] Felix I Parra and Michael Barnes. Intrinsic rotation in tokamaks: theory. *Plasma Phys. Control. Fusion*, 57(4):045002, apr 2015. ISSN 0741-3335. doi: 10.1088/0741-3335/57/4/045002. URL http://stacks.iop.org/0741-3335/57/i=4/a=045002?key=crossref.4aae68333c11be380fb621050a6b489a. 101

[149] K.-D Zastrow, W.G.F Core, L.-G Eriksson, M.G. Von Hellermann, A.C Howman, and R.W.T König. Transfer rates of toroidal angular momentum during neutral beam injection. *Nucl. Fusion*, 38(2):257–263, feb 1998. ISSN 0029-5515. doi: 10.1088/0029-5515/38/2/309. URL http://stacks.iop.org/0029-5515/38/i=2/a=309?key=crossref.bb1759703c7eb161f1d0a3095b3f0e33. 102

[150] A. G. Peeters, C. Angioni, and D. Strintzi. Toroidal Momentum Pinch Velocity due to the Coriolis Drift Effect on Small Scale Instabilities in a Toroidal Plasma. *Phys. Rev. Lett.*, 98(26):265003, jun 2007. ISSN 0031-9007. doi: 10.1103/PhysRevLett.98.265003. URL https://link.aps.org/doi/10.1103/PhysRevLett.98.265003. 102

[151] Y. Camenen, A. Bortolon, B. P. Duval, L. Federspiel, A. G. Peeters, F. J. Casson, W. A. Hornsby, A. N. Karpushov, F. Piras, O. Sauter, A. P. Snodin, and G. Szepesi. Experimental Evidence of Momentum Transport Induced by an Up-Down Asymmetric Magnetic Equilibrium in Toroidal Plasmas. *Phys. Rev. Lett.*, 105(13):135003, sep 2010. ISSN 0031-9007. doi: 10.1103/PhysRevLett.105.135003. URL https://link.aps.org/doi/10.1103/PhysRevLett.105.135003. 102

[152] Y. Camenen, A. G. Peeters, C. Angioni, F. J. Casson, W. A. Hornsby, A. P. Snodin, and D. Strintzi. Transport of Parallel Momentum Induced by Current-Symmetry Breaking in Toroidal Plasmas. *Phys. Rev. Lett.*, 102(12):125001, mar 2009. ISSN 0031-9007. doi: 10.1103/PhysRevLett.102.125001. URL https://link.aps.org/doi/10.1103/PhysRevLett.102.125001.

[153] Y. Camenen, A. G. Peeters, C. Angioni, F. J. Casson, W. A. Hornsby, A. P. Snodin, and D. Strintzi. Impact of the background toroidal rotation on particle and heat turbulent transport in tokamak plasmas. *Phys. Plasmas*, 16(1):012503, jan 2009. ISSN 1070-664X. doi: 10.1063/1.3057356. URL http://aip.scitation.org/doi/10.1063/1.3057356. 102

[154] Felix I Parra and Peter J Catto. Turbulent transport of toroidal angular momentum in low flow gyrokinetics. *Plasma Phys. Control. Fusion*, 52(5):059801–059801, may 2010. ISSN 0741-3335. doi: 10.1088/0741-3335/52/5/059801. URL http://stacks.iop.org/0741-3335/52/i=5/a=059801?key=crossref.98ec9f8d6d0509f720f8755d5df52d06. 102, 103

[155] R. E. Waltz, G. M. Staebler, and W. M. Solomon. Gyrokinetic simulation of momentum transport with residual stress from diamagnetic level velocity shears. *Phys. Plasmas*, 18(4):042504, apr 2011. ISSN 1070-664X. doi: 10.1063/1.3579481. URL http://aip.scitation.org/doi/10.1063/1.3579481. 102

[156] Ian H Hutchinson. Spontaneous tokamak rotation: observations turbulent momentum transport has to explain, 2010. URL http://arxiv.org/abs/0904.4003{%}0A. 102

[157] Bruno Coppi. Accretion theory of 'spontaneous' rotation in toroidal plasmas. *Nucl. Fusion*, 42(1):1–4, jan 2002. ISSN 0029-5515. doi: 10.1088/0029-5515/42/1/301. URL http://stacks.iop.org/0029-5515/42/i=1/a=301?key=crossref.f0e8c1b587282cf1e1ba938c622f74d5. 102

[158] P Monier-Garbet, K.H Burrell, F.L Hinton, J Kim, X Garbet, and R.J Groebner. Effects of neutrals on plasma rotation in DIII-D. *Nucl. Fusion*, 37(3):403–412, mar 1997. ISSN 0029-5515. doi: 10.1088/0029-5515/37/3/I09. URL http://stacks.iop.org/0029-5515/37/i=3/a=I09?key=crossref.e429d0daaf2825221224ca750bf07cdb. 102

Bibliography

[159] J. D. Callen, A. J. Cole, and C. C. Hegna. Toroidal flow and radial particle flux in tokamak plasmas. *Phys. Plasmas*, 16(8):082504, aug 2009. ISSN 1070-664X. doi: 10.1063/1. 3206976. URL http://aip.scitation.org/doi/10.1063/1.3206976. 102

[160] W M Solomon, K H Burrell, J S DeGrassie, R Budny, R J Groebner, J E Kinsey, G J Kramer, T C Luce, M a Makowski, D Mikkelsen, R Nazikian, C C Petty, P a Politzer, S D Scott, M A Van Zeeland, and M C Zarnstorff. Momentum confinement at low torque. *Plasma Phys. Control. Fusion*, 49(12B):B313—-B324, 2007. ISSN 0741-3335. doi: 10.1088/0741-3335/49/12B/S29. URL http://stacks.iop.org/0741-3335/49/i=12B/a=S29?key=crossref.76eb210540b7061b788d3760028a69ab{%}7B{%}25{%}7D5Cnhttp://iopscience.iop.org/article/10.1088/0741-3335/49/12B/S29. 102

[161] W.M. Solomon, K.H. Burrell, A.M. Garofalo, A.J. Cole, R.V. Budny, J.S. DeGrassie, W.W. Heidbrink, G.L. Jackson, M.J. Lanctot, R. Nazikian, H. Reimerdes, E.J. Strait, and M.a. Van Zeeland. Advances in understanding the generation and evolution of the toroidal rotation profile on DIII-D. *Nucl. Fusion*, 49(8):085005, aug 2009. ISSN 0029-5515. doi: 10.1088/0029-5515/49/8/085005. URL http://stacks.iop.org/0029-5515/49/i=8/a=085005?key=crossref.201405c4d073c013385bea2e4a51e5f0.

[162] S. Suckewer, H.P. Eubank, R.J. Goldston, J. McEnerney, N.R. Sauthoff, and H.H. Towner. Toroidal plasma rotation in the PLT tokamak with neutral-beam injection. *Nucl. Fusion*, 21(10):1301–1309, oct 1981. ISSN 0029-5515. doi: 10.1088/0029-5515/21/10/009. URL http://stacks.iop.org/0029-5515/21/i=10/a=009?key=crossref.5ebc6032ea5f03477a8615eafbdedf09.

[163] D. Nishijima, A. Kallenbach, S. Günter, M. Kaufmann, K. Lackner, C. F. Maggi, A. G. Peeters, G. V. Pereverzev, B. Zaniol, and the ASDEX Upgrade Team. Experimental studies of toroidal momentum transport in ASDEX Upgrade. *Plasma Phys. Control. Fusion*, 47(1):89–115, jan 2005. ISSN 0741-3335. doi: 10.1088/0741-3335/47/1/006. URL http://stacks.iop.org/0741-3335/47/i=1/a=006?key=crossref.99c6f7119003c22d0ca4866bc0ac0529. 102

[164] S. D. Scott, P. H. Diamond, R. J. Fonck, R. J. Goldston, R. B. Howell, K. P. Jaehnig, G. Schilling, E. J. Synakowski, M. C. Zarnstorff, C. E. Bush, E. Fredrickson, K. W. Hill, A. C. Janos, D. K. Mansfield, D. K. Owens, H. Park, G. Pautasso, A. T. Ramsey, J. Schivell, G. D. Tait, W. M. Tang, and G. Taylor. Local measurements of correlated momentum and heat transport in the TFTR tokamak. *Phys. Rev. Lett.*, 64 (5):531–534, jan 1990. ISSN 0031-9007. doi: 10.1103/PhysRevLett.64.531. URL https://link.aps.org/doi/10.1103/PhysRevLett.64.531. 102

[165] P C de Vries, K M Rantamäki, C Giroud, E Asp, G Corrigan, A Eriksson, M de Greef, I Jenkins, H C M Knoops, P Mantica, H Nordman, P Strand, T Tala, J Weiland, K-D Zastrow, and JET EFDA Contributors. Plasma rotation and momentum transport studies at JET. *Plasma Phys. Control. Fusion*, 48(12):1693–1708, 2006. ISSN 0741-3335. doi:

10.1088/0741-3335/48/12/001. URL http://stacks.iop.org/0741-3335/48/i=12/a=001?key=crossref.9e6f8181a092aba899fbd7d26e80c9de.

[166] T. Tala, K.-D. Zastrow, J. Ferreira, P. Mantica, V. Naulin, A. G. Peeters, G. Tardini, M. Brix, G. Corrigan, C. Giroud, and D. Strintzi. Evidence of Inward Toroidal Momentum Convection in the JET Tokamak. *Phys. Rev. Lett.*, 102(7):075001, feb 2009. ISSN 0031-9007. doi: 10.1103/PhysRevLett.102.075001. URL https://link.aps.org/doi/10.1103/PhysRevLett.102.075001. 102

[167] S. K. Wong and V. S. Chan. The neoclassical angular momentum flux in the large aspect ratio limit. *Phys. Plasmas*, 12(9):092513, sep 2005. ISSN 1070-664X. doi: 10.1063/1.2048027. URL http://aip.scitation.org/doi/10.1063/1.2048027. 102

[168] J.S DeGrassie, D.R Baker, K.H Burrell, P Gohil, C.M Greenfield, R.J Groebner, and D.M Thomas. Toroidal rotation in neutral beam heated discharges in DIII-D. *Nucl. Fusion*, 43(2):142–156, 2003. ISSN 0029-5515. doi: 10.1088/0029-5515/43/2/307. URL http://stacks.iop.org/0029-5515/43/i=2/a=307?key=crossref.9e1c9732785fb3232ce87196de8b9ce9. 103

[169] G. Tardini, J. Ferreira, P. Mantica, A. G. Peeters, T. Tala, K. D. Zastrow, M. Brix, C. Giroud, G. V. Pereverzev, and Jet-Efda Contributors. Angular momentum studies with NBI modulation in JET. *Nucl. Fusion*, 49(8):085010, 2009. ISSN 0029-5515. doi: 10.1088/0029-5515/49/8/085010. URL http://iopscience.iop.org/0029-5515/49/8/085010{%}5Cnhttp://iopscience.iop.org/0029-5515/49/8/085010/{%}5Cnhttp://iopscience.iop.org/0029-5515/49/8/085010/pdf/0029-5515{_}49{_}8{_}085010.pdf. 103

[170] V. Rozhansky and M. Tendler. Reviews of Plasma Physics- Plasma rotation in tokamaks. In B.B. Kadomtsev, editor, *vol 19*, chapter 3, page 147. Consultants Bureau, New York - London, 1996. 103

[171] S. von Goeler, W. Stodiek, and N. Sauthoff. Studies of Internal Disruptions and m=1 Oscillations in Tokamak Discharges with Soft-X-Ray Tecniques. *Phys. Rev. Lett.*, 33(20):1201–1203, nov 1974. ISSN 0031-9007. doi: 10.1103/PhysRevLett.33.1201. URL https://link.aps.org/doi/10.1103/PhysRevLett.33.1201. 105

[172] H. Reimerdes, I. Furno, F. Hofmann, An Martynov, A. Pochelon, and O. Sauter. Sawtooth behaviour in highly elongated TCV plasmas. *Plasma Phys. Control. Fusion*, 48(11):1621–1632, nov 2006. ISSN 0741-3335. doi: 10.1088/0741-3335/48/11/004. URL http://stacks.iop.org/0741-3335/48/i=11/a=004?key=crossref.3d977fc5af2053a74e6c55b71b08fadd. 106, 112

[173] T. P. Goodman, F. Felici, O. Sauter, and J. P. Graves. Sawtooth Pacing by Real-Time Auxiliary Power Control in a Tokamak Plasma. *Phys. Rev. Lett.*, 106(24):245002, jun 2011. ISSN 0031-9007. doi: 10.1103/PhysRevLett.106.245002. URL https://link.aps.org/doi/10.1103/PhysRevLett.106.245002. 106, 112

Bibliography

[174] G P Canal, B Duval, F Felici, T Goodman, J Graves, A Pochelon, H Reimerdes, O Sauter, D Testa, and the TCV Team. Fast Seeding of Neoclassical Tearing Modes by Sawtooth Crashes in TCV. In *EPS/ICPP 2012, 39th EPS Conf. Plasma Phys. 16th Int. Congr. Plasma Phys.*, volume 1, pages 3–6, 2012. ISBN 9781622769810. URL https://infoscience.epfl.ch/record/179934. 106

[175] Menno Lauret, F. Felici, Gert Witvoet, T.P. Goodman, G. Vandersteen, O. Sauter, and M.R. de Baar. Demonstration of sawtooth period locking with power modulation in TCV plasmas. *Nucl. Fusion*, 52(6):062002, jun 2012. ISSN 0029-5515. doi: 10.1088/0029-5515/52/6/062002. URL http://stacks.iop.org/0029-5515/52/i=6/a=062002?key=crossref.bf5f01b2bc222714923ac968d016a6a1. 106, 112

[176] A. W. Edwards, D. J. Campbell, W. W. Engelhardt, H. U. Fahrbach, R. D. Gill, R. S. Granetz, S. Tsuji, B. J D Tubbing, A. Weller, J. Wesson, and D. Zasche. Rapid Collapse of a Plasma Sawtooth Oscillation in the JET Tokamak. *Phys. Rev. Lett.*, 57(2):210–213, jul 1986. ISSN 0031-9007. doi: 10.1103/PhysRevLett.57.210. URL https://link.aps.org/doi/10.1103/PhysRevLett.57.210. 106, 108

[177] B B Kadomtsev. Disruptive instability in tokamaks. *Sov. J. Plasma Phys.*, 1(5):389, 1975. 106, 107

[178] F. M. Levinton, S. H. Batha, M. Yamada, and M. C. Zarnstorff. q-profile measurements in the Tokamak Fusion Test Reactor. *Phys. Fluids B Plasma Phys.*, 5(7):2554, 1993. ISSN 08998221. doi: 10.1063/1.860743. URL http://scitation.aip.org/content/aip/journal/pofb/5/7/10.1063/1.860743. 108

[179] F. Porcelli, D. Boucher, and M. N. Rosenbluth. Model for the sawtooth period and amplitude. *Plasma Phys. Control. Fusion*, 38(12):2163–2186, dec 1996. ISSN 0741-3335. doi: 10.1088/0741-3335/38/12/010. URL http://stacks.iop.org/0741-3335/38/i=12/a=010?key=crossref.ccf614f38c2c183df54b01d6933e4f65. 108

[180] C G Gimblett and R J Hastie. Calculation of the post-crash state and 1 1/2 D simulation of sawtooth cycles. *Plasma Phys. Control. Fusion*, 36(9):1439–1455, sep 1994. ISSN 0741-3335. doi: 10.1088/0741-3335/36/9/005. URL http://stacks.iop.org/0741-3335/36/i=9/a=005?key=crossref.8cc70d2b41197fd8bebc3a7f0ac27c31. 108

[181] M. F F Nave, H. R. Koslowski, S. Coda, J. Graves, M. Brix, R. Buttery, C. Challis, C. Giroud, M. Stamp, and P. de Vries. Exploring a small sawtooth regime in Joint European Torus plasmas with counterinjected neutral beams. *Phys. Plasmas*, 13(1):014503, jan 2006. ISSN 1070-664X. doi: 10.1063/1.2162528. URL http://aip.scitation.org/doi/10.1063/1.2162528. 111

[182] I.T Chapman, T.C Hender, S Saarelma, S.E Sharapov, R.J Akers, N.J Conway, and the MAST Team. The effect of toroidal plasma rotation on sawteeth in MAST. *Nucl. Fusion*, 46(12):1009–1016, 2006. ISSN 0029-5515. doi: 10.1088/

0029-5515/46/12/004. URL http://stacks.iop.org/0029-5515/46/i=12/a=004?key=crossref.c9b46d08a94406944d723a8069971e31. 111

[183] I. T. Chapman, M. F. de Bock, S. D. Pinches, M. R. Turnyanskiy, V. G. Igochine, M. Maraschek, and G. Tardini. The effect of off-axis neutral beam injection on sawtooth stability in ASDEX Upgrade and Mega-Ampere Spherical Tokamak. *Phys. Plasmas*, 16(7):072506, jul 2009. ISSN 1070-664X. doi: 10.1063/1.3187905. URL http://aip.scitation.org/doi/10.1063/1.3187905. 111

[184] I.T. Chapman, S.D. Pinches, H.R. Koslowski, Y. Liang, A. Krämer-Flecken, and M. de Bock. Sawtooth stability in neutral beam heated plasmas in TEXTOR. *Nucl. Fusion*, 48(3):035004, 2008. ISSN 0029-5515. doi: 10.1088/0029-5515/48/3/035004. URL http://stacks.iop.org/0029-5515/48/i=3/a=035004?key=crossref.b3338f1f2d919c1e63911971cb52808c. 111

[185] C. Angioni, A. Pochelon, N. N. Gorelenkov, K. G. McClements, O. Sauter, R. V. Budny, P. C. De Vries, D. F. Howell, M. Mantsinen, M. F. F. Nave, S. E. Sharapov, and Contributors To the Efda-Jet Workprogramme. Neutral beam stabilization of sawtooth oscillations in JET. *Plasma Phys. Control. Fusion*, 44(2):205–222, feb 2002. ISSN 0741-3335. doi: 10.1088/0741-3335/44/2/305. URL http://stacks.iop.org/0741-3335/44/i=2/a=305?key=crossref.bc28c0533148cf7055b93ff9dfb7b959. 112

[186] J P Graves, C Angioni, R V Budny, R J Buttery, S Coda, L-G Eriksson, C G Gimblett, T P Goodman, R J Hastie, M A Henderson, H R Koslowski, M J Mantsinen, An Martynov, M-L Mayoral, A Mück, M F F Nave, O Sauter, E Westerhof, and JET–EFDA Contributors. Sawtooth control in fusion plasmas. *Plasma Phys. Control. Fusion*, 47(12B):B121–B133, dec 2005. ISSN 0741-3335. doi: 10.1088/0741-3335/47/12B/S10. URL http://stacks.iop.org/0741-3335/47/i=12B/a=S10?key=crossref.c90c50b9d15883f70dba92e03d3bda56. 112, 113

[187] I.T. T Chapman, J P Graves, T Johnson, O Asunta, P Bonoli, M Choi, E F Jaeger, Martin Jucker, and O Sauter. Sawtooth control in ITER using ion cyclotron resonance heating. *Plasma Phys. Control. Fusion*, 53(12):124003, dec 2011. ISSN 0741-3335. doi: 10.1088/0741-3335/53/12/124003. URL http://stacks.iop.org/0741-3335/53/i=12/a=124003?key=crossref.fb669aa224b6fa3577d24c0b70cd80e9. 112

[188] I.T. Chapman, R.J. La Haye, R.J. Buttery, W.W. Heidbrink, G.L. Jackson, C.M. Muscatello, C.C. Petty, R.I. Pinsker, B.J. Tobias, and F Turco. Sawtooth control using electron cyclotron current drive in ITER demonstration plasmas in DIII-D. *Nucl. Fusion*, 52(6):063006, jun 2012. ISSN 0029-5515. doi: 10.1088/0029-5515/52/6/063006. URL http://stacks.iop.org/0029-5515/52/i=6/a=063006?key=crossref.9335a19d42b475bf7f5aed718090ff82.

[189] F Felici, T.P. Goodman, O Sauter, G Canal, S Coda, B.P. Duval, and J.X. Rossel. Integrated real-time control of MHD instabilities using multi-beam ECRH/ECCD systems on TCV. *Nucl. Fusion*, 52(7):074001, jul 2012. ISSN 0029-5515. doi: 10.1088/

0029-5515/52/7/074001. URL http://stacks.iop.org/0029-5515/52/i=7/a=074001?key=crossref.d3101d38dcee6b7c03d9aa2ba4fc4ffe.

[190] G.P. Canal, B.P. Duval, F. Felici, T.P. Goodman, J.P. Graves, A. Pochelon, H. Reimerdes, O. Sauter, and D. Testa. Fast seeding of NTMs by sawtooth crashes in TCV and their preemption using ECRH. *Nucl. Fusion*, 53(11):113026, nov 2013. ISSN 0029-5515. doi: 10.1088/0029-5515/53/11/113026. URL http://stacks.iop.org/0029-5515/53/i=11/a=113026?key=crossref.839a210045a56cf305a33defd68fc4be.

[191] Paganini Canal. *Sawtooth Generated Magnetic Islands and the Properties of the Snowflake Divertor*. PhD thesis, EPFL, 2014. URL https://infoscience.epfl.ch/record/200481/files/EPFL{_}TH6272.pdf. 112

[192] J I Paley, F Felici, S Coda, T P Goodman, and F Piras. Real time control of the sawtooth period using EC launchers. *Plasma Phys. Control. Fusion*, 51(5):055010, may 2009. ISSN 0741-3335. doi: 10.1088/0741-3335/51/5/055010. URL http://stacks.iop.org/0741-3335/51/i=5/a=055010?key=crossref.b0eefa9c1c981e7a18bd76197fc698ff. 112

[193] K. Matsuda. Ray tracing study of the electron cyclotron current drive in DIII-D using 60 GHz. *IEEE Trans. Plasma Sci.*, 17(1):6–11, 1989. ISSN 00933813. doi: 10.1109/27.21664. URL http://ieeexplore.ieee.org/document/21664/. 113

[194] P. Helander. On ion flow caused by the inductive electric field in a tokamak. *Phys. Plasmas*, 8(10):4700–4703, oct 2001. ISSN 1070-664X. doi: 10.1063/1.1402172. URL http://aip.scitation.org/doi/10.1063/1.1402172. 124, 126

[195] B P Duval, A Bortolon, A Karpushov, R A Pitts, A Pochelon, and A Scarabosio. Bulk plasma rotation in the TCV tokamak in the absence of external momentum input. *Plasma Phys. Control. Fusion*, 49(12B):B195–B209, dec 2007. ISSN 0741-3335. doi: 10.1088/0741-3335/49/12B/S18. URL http://stacks.iop.org/0741-3335/49/i=12B/a=S18?key=crossref.8f52cca05727c8323a1dbc4be6d63d9d. 125

[196] F. I. Parra, M. F F Nave, A. A. Schekochihin, C. Giroud, J. S. de Grassie, J. H F Severo, P. de Vries, and K.-D. Zastrow. Scaling of Spontaneous Rotation with Temperature and Plasma Current in Tokamaks. *Phys. Rev. Lett.*, 108(9):095001, feb 2012. ISSN 0031-9007. doi: 10.1103/PhysRevLett.108.095001. URL https://link.aps.org/doi/10.1103/PhysRevLett.108.095001. 129

[197] K.H. Burrell. Summary of experimental progress and suggestions for future work (H mode confinement). *Plasma Phys. Control. Fusion*, 36:A291–A306, 1994. URL http://iopscience.iop.org/0741-3335/36/7A/043. 131

[198] ITER Physics Expert Groups on Confinement and Traspor, ITER Physics Expert Group on Confinement Modelling and Database, and ITER Physics Basis Editors. Chapter 2: Plasma confinement and transport. *Nucl. Fusion*, 39(12):2175, 1999. URL http://stacks.iop.org/0029-5515/39/i=12/a=302. 131

[199] R.J Groebner, D.R Baker, K.H Burrell, T.N Carlstrom, J.R Ferron, P. Gohil, L.L Lao, T.H Osborne, D.M Thomas, W.P West, J.A Boedo, R.A Moyer, G.R McKee, R.D Deranian, E.J Doyle, C.L Rettig, T.L Rhodes, and J.C Rost. Progress in quantifying the edge physics of the H mode regime in DIII-D. *Nucl. Fusion*, 41(12):1789–1802, dec 2001. ISSN 0029-5515. doi: 10.1088/0029-5515/41/12/306. URL http://stacks.iop.org/0029-5515/41/i=12/a=306?key=crossref.7ff3da61b77224868a942195235c1a00. 131

[200] O. Sauter, S. Brunner, D. Kim, G. Merlo, R. Behn, Y. Camenen, S. Coda, B. P. Duval, L. Federspiel, T. P. Goodman, A. Karpushov, A. Merle, and Tcv Team. On the non-stiffness of edge transport in L-mode tokamak plasmas. *Phys. Plasmas*, 21(5):055906, may 2014. ISSN 1070-664X. doi: 10.1063/1.4876612. URL http://aip.scitation.org/doi/10.1063/1.4876612. 131

[201] K H Burrell, T N Carlstrom, S. Coda, E J Doyle, P. Gohil, R J Groebner, J Kim, R A Moyer, W A Peebles, C L Rettig, T L Rhodes, and D M Thomas. Constraints on theories provided by fast time response measurements across the L to H transition on DIII-D. *Plasma Phys. Control. Fusion*, 38(8):1313–1318, aug 1996. ISSN 0741-3335. doi: 10.1088/0741-3335/38/8/028. URL http://stacks.iop.org/0741-3335/38/i=8/a=028?key=crossref.18c5c1baa1f6262cdc8b5543a3e52249. 131

[202] J.E Rice, W.D Lee, E.S Marmar, P.T Bonoli, R.S Granetz, M.J Greenwald, A.E Hubbard, I.H Hutchinson, J.H Irby, Y Lin, D Mossessian, J.A Snipes, S.M Wolfe, and S.J Wukitch. Observations of anomalous momentum transport in Alcator C-Mod plasmas with no momentum input. *Nucl. Fusion*, 44(3):379–386, mar 2004. ISSN 0029-5515. doi: 10.1088/0029-5515/44/3/001. URL http://stacks.iop.org/0029-5515/44/i=3/a=001?key=crossref.70e4079a01f1976a1e574c6fb72db847. 131

[203] B LaBombard, J.E Rice, A.E Hubbard, J.W Hughes, M Greenwald, J Irby, Y Lin, B Lipschultz, E.S Marmar, C.S Pitcher, N Smick, S.M Wolfe, S.J Wukitch, and the Alcator Group. Transport-driven Scrape-Off-Layer flows and the boundary conditions imposed at the magnetic separatrix in a tokamak plasma. *Nucl. Fusion*, 44(10):1047–1066, oct 2004. ISSN 0029-5515. doi: 10.1088/0029-5515/44/10/001. URL http://stacks.iop.org/0029-5515/44/i=10/a=001?key=crossref.633fd3b0a6b1832035bd6b54ff9e8195. 131

[204] K. H. Burrell. Effects of E×B velocity shear and magnetic shear on turbulence and transport in magnetic confinement devices. *Phys. Plasmas*, 4(5):1499–1518, may 1997. ISSN 1070-664X. doi: 10.1063/1.872367. URL http://aip.scitation.org/doi/10.1063/1.872367. 131, 147

[205] P Gohil, K.H Burrell, and T.N Carlstrom. Parametric dependence of the edge radial electric field in the DIII-D tokamak. *Nucl. Fusion*, 38(1):93–102, jan 1998. ISSN 0029-5515. doi: 10.1088/0029-5515/38/1/308. URL http://stacks.iop.org/0029-5515/38/i=1/a=308?key=crossref.f0f2365d60cfb4618d0f2b44bef613de. 132, 145

[206] N C Hawkes, D V Bartlett, D J Campbell, N Deliyanakis, R M Giannella, P J Lomas, N J Peacock, L Porte, A Rookes, and P R Thomas. Evolution of edge electric field at the L

to H transition in JET. *Plasma Phys. Control. Fusion*, 38(8):1261–1266, aug 1996. ISSN 0741-3335. doi: 10.1088/0741-3335/38/8/019. URL http://stacks.iop.org/0741-3335/38/i=8/a=019?key=crossref.48570ea1d26236c1a02e36183ecf9e26. 132

[207] Sykes A., R.J. Akers, L.C. Appel, E.R. Arends, P.G. Carolan, N.J. Conway, G.F. Counsell, G. Cunningham, Dnestrovskij A., Yu.N. Dnestrovskij, A.R. Field, S.J. Fielding, M.P. Gryaznevich E., S. Korsholm, E. Laird, Martin R., M.P.S. Nightingale, C.M. Roach, M.R. Tournianski, M.J. Walsh, C.D. Warrick, H.R. Wilson, S. You, the MAST Teams, and NBI. First results from MAST. *Nucl. Fusion*, 41(10):1423, 2001. URL http://stacks.iop.org/0029-5515/41/i=10/a=310. 132

[208] J.A Snipes, R.S Granetz, M Greenwald, O.J.W.F Kardaun, A Kus, F Ryter, U Stroth, J Kollermeyer, S.J Fielding, M Valovic, J.C DeBoo, T.N Carlstrom, D.P Schissel, K Thomsen, D.J Campbell, J.P Christiansen, J.G Cordey, E Righi, Y Miura, N Suzuki, M Mori, T Matsuda, H Tamai, T Fukuda, Y Kamada, T Matsuda, M Sato, T Takizuka, K Tsuchiya, and S.M Kaye. H mode power threshold database for ITER. *Nucl. Fusion*, 36(9):1217–1264, sep 1996. ISSN 0029-5515. doi: 10.1088/0029-5515/36/9/I11. URL http://stacks.iop.org/0029-5515/36/i=9/a=I11?key=crossref.3687d4625c49b29442c1b93a884ca86f. 132, 133

[209] F Ryter, L Barrera Orte, B Kurzan, R M McDermott, G Tardini, E Viezzer, M Bernert, R Fischer, The ASDEX Upgrade Team, Biglari H et Al, Groebner R J et Al, Burrell K.H., Wagner F., Stroth U et Al, Sauter P et Al, Hinton F L et Al, McDermott R M et Al, Viezzer E et Al, Kim E J et Al, Moyer R A et Al, Colchin R J et Al, Punzmann H et Al, Conway G D et Al, Estrada T et Al, Schmitz L et Al, Ryter F et Al, Martin Y R et Al, Ryter F et Al, Ryter F et Al, Ma Y et Al, Maggi C et Al, Ryter F et Al, Fielding S J et Al, Fukuda T et Al, Andrew Y et Al, McDermott R M et Al, Viezzer E et Al, Pankin A et Al, Willensdorfer M et Al, Gohil P et Al, Viezzer E et Al, Kaye S et Al, Ryter F et Al, Polevoi A et Al, and Righi E et Al. Experimental evidence for the key role of the ion heat channel in the physics of the L–H transition. *Nucl. Fusion*, 54(8):83003, 2014. ISSN 0029-5515. doi: 10.1088/0029-5515/54/8/083003. URL http://stacks.iop.org/0029-5515/54/i=8/a=083003?key=crossref.41680f22a6f479cd738eae57cf14edfd. 132, 133

[210] T Ozeki, MS Chu, LL Lao, TS Taylor, M.S. Chance, S. Kinoshita, K.H. Burrell, and R.D. Stambaugh. Plasma shaping, edge ballooning stability and ELM behaviour in DIII-D. *Nucl. Fusion*, 30(8):1425–1432, aug 1990. ISSN 0029-5515. doi: 10.1088/0029-5515/30/8/003. URL http://iopscience.iop.org/0029-5515/30/8/003. 132

[211] H Zohm. Edge localized modes (ELMs). *Plasma Phys. Control. Fusion*, 38(2):105–128, feb 1996. ISSN 0741-3335. doi: 10.1088/0741-3335/38/2/001. URL http://stacks.iop.org/0741-3335/38/i=2/a=001?key=crossref.f28892e44e8eadadb5c7b755b5fc53e6. 132

[212] J W Connor. Edge-localized modes - physics and theory. *Plasma Phys. Control. Fusion*, 40(5):531–542, may 1998. ISSN 0741-3335. doi: 10.1088/0741-3335/40/5/002. URL http://stacks.iop.org/0741-3335/40/i=5/a=002?key=crossref.3cc5541a95d14269089e873a201c51ec. 132

[213] S. Devaux, T. Eich, G. Arnoux, W. Fundamenski, and H. Thomsen. Type-I ELM filamentary substructure on the JET divertor target. *J. Nucl. Mater.*, 415(1):S865–S868, aug 2011. ISSN 00223115. doi: 10.1016/j.jnucmat.2011.01.050. URL http://linkinghub.elsevier.com/retrieve/pii/S0022311511000821. 132

[214] T. Eich, A. Herrmann, and J. Neuhauser. Nonaxisymmetric Energy Deposition Pattern on ASDEX Upgrade Divertor Target Plates during Type-I Edge-Localized Modes. *Phys. Rev. Lett.*, 91(19):195003, nov 2003. ISSN 0031-9007. doi: 10.1103/PhysRevLett.91.195003. URL https://link.aps.org/doi/10.1103/PhysRevLett.91.195003. 132

[215] T. Eich, B. Sieglin, A.J. Thornton, M. Faitsch, A. Kirk, A. Herrmann, and W. Suttrop. ELM divertor peak energy fluence scaling to ITER with data from JET, MAST and ASDEX upgrade. *Nucl. Mater. Energy*, 0:1–7, may 2017. ISSN 23521791. doi: 10.1016/j.nme.2017.04.014. URL http://linkinghub.elsevier.com/retrieve/pii/S2352179116302927. 132

[216] J. Linke, T. Loewenhoff, V. Massaut, G. Pintsuk, G. Ritz, M. Rödig, A. Schmidt, C. Thomser, I. Uytdenhouwen, V. Vasechko, and M. Wirtz. Performance of different tungsten grades under transient thermal loads. *Nucl. Fusion*, 51(7):073017, jul 2011. ISSN 0029-5515. doi: 10.1088/0029-5515/51/7/073017. URL http://stacks.iop.org/0029-5515/51/i=7/a=073017?key=crossref.6cc38f09500f7468bf3dbfe40fa6eb9f. 132

[217] M Greenwald, R.L Boivin, F Bombarda, P.T Bonoli, C.L Fiore, D Garnier, J.a Goetz, S.N Golovato, M.a Graf, R.S Granetz, S Horne, A Hubbard, I.H Hutchinson, J.H Irby, B LaBombard, B Lipschultz, E.S Marmar, M.J May, G.M McCracken, P O'Shea, J.E Rice, J Schachter, J.a Snipes, P.C Stek, Y Takase, J.L Terry, Y Wang, R Watterson, B Welch, and S.M Wolfe. H mode confinement in Alcator C-Mod. *Nucl. Fusion*, 37(6):793–807, jun 1997. ISSN 0029-5515. doi: 10.1088/0029-5515/37/6/I07. URL http://stacks.iop.org/0029-5515/37/i=6/a=I07?key=crossref.fd155a72f131bf4d2c2047d42042ae41. 133

[218] K H Burrell, W P West, E J Doyle, M E Austin, J S DeGrassie, P Gohil, C M Greenfield, R J Groebner, R Jayakumar, D H Kaplan, L L Lao, A W Leonard, M A Makowski, G R McKee, W M Solomon, D M Thomas, T L Rhodes, M R Wade, G Wang, J G Watkins, and L Zeng. Edge radial electric field structure in quiescent H-mode plasmas in the DIII-D tokamak. *Plasma Phys. Control. Fusion*, 46(5A):A165–A178, may 2004. ISSN 0741-3335. doi: 10.1088/0741-3335/46/5A/018. URL http://stacks.iop.org/0741-3335/46/i=5A/a=018?key=crossref.ccb8c3ef4d1da355ba0686401a69eedd. 133

[219] M Shimada, D.J Campbell, V Mukhovatov, M Fujiwara, N Kirneva, K Lackner, M Nagami, V.D Pustovitov, N Uckan, J Wesley, N Asakura, A.E Costley, A.J.H Donné, E.J Doyle, A Fasoli, C Gormezano, Y Gribov, O Gruber, T.C Hender, W Houlberg, S Ide, Y Kamada, A Leonard, B Lipschultz, A Loarte, K Miyamoto, V Mukhovatov, T.H Osborne, A Polevoi, and A.C.C Sips. Chapter 1: Overview and summary. *Nucl. Fusion*, 47(6):S1–S17, jun 2007. ISSN 0029-5515. doi: 10.1088/0029-5515/47/6/S01. URL http://stacks.iop.org/0029-5515/47/i=6/a=S01?key=crossref.9f5018b333c98316af6e827446ba6d15. 133

Bibliography

[220] E.J. Doyle, W.A. Houlberg, Y. Kamada, V. Mukhovatov, T.H. Osborne, A. Polevoi, G Bateman, J.W Connor, J.G. Cordey, T Fujita, X Garbet, T.S Hahm, L.D Horton, A.E Hubbard, F Imbeaux, F Jenko, J.E Kinsey, Y Kishimoto, J Li, T.C Luce, Y Martin, M Ossipenko, V Parail, A Peeters, T.L Rhodes, J.E Rice, C.M Roach, V Rozhansky, F Ryter, G Saibene, R Sartori, A.C.C Sips, J.A Snipes, M Sugihara, E.J Synakowski, H Takenaga, T Takizuka, K Thomsen, M.R Wade, H.R Wilson, ITPA Transport Physics Topical Group, ITPA Confinement Database Group, Model, ITPA Pedestal Group, and Edge Topical. Chapter 2: Plasma confinement and transport. *Nucl. Fusion*, 47(6):S18–S127, jun 2007. ISSN 0029-5515. doi: 10.1088/0029-5515/47/6/S02. URL http://eprints.whiterose.ac.uk/58147/{%}5Cnhttp://stacks.iop.org/0029-5515/47/i=6/a=S02?key=crossref.36e162162f67e92c3a62080002fc7583. 133

[221] D Kalupin, M Z Tokar, B Unterberg, X Loozen, D Pilipenko, R Zagorski, and TEXTOR Contributors. On the difference of H-mode power threshold in divertor and limiter tokamaks. *Plasma Phys. Control. Fusion*, 48(5A):A309–A317, may 2006. ISSN 0741-3335. doi: 10.1088/0741-3335/48/5A/S30. URL http://stacks.iop.org/0741-3335/48/i=5A/a=S30?key=crossref.ce3664a028a823ddd3d3164463b23bcc. 133

[222] H Weisen, F Hofmann, M J Dutch, Y Martin, A Pochelon, J-M Moret, B P Duval, A Hirt, J B Lister, Ch Nieswand, R A Pitts, Z A Pietrzyk, M Anton, R Behn, G Besson, F Bühlmann, R Chavan, D Fasel, A Favre, S Franke, P Isoz, P Lavanchy, B Joye, X Llobet, P Mandrin, B Marletaz, Ph Marmillod, J C Magnin, J-M Mayor, P J Paris, A Perez, O Sauter, W van Toledo, G Tonetti, M Q Tran, F Troyon, and D J Ward. Ohmic H-modes in the TCV tokamak. *Plasma Phys. Control. Fusion*, 38(8):1137, 1996. URL http://stacks.iop.org/0741-3335/38/i=8/a=006. 133

[223] Martin Greenwald. Density limits in toroidal plasmas. *Plasma Phys. Control. Fusion*, 44(8):201, aug 2002. ISSN 07413335. doi: 10.1088/0741-3335/44/8/201. URL http://stacks.iop.org/0741-3335/44/i=8/a=201?key=crossref.10b223c9bfedf85db5ed007f2fdae8a5. 134

[224] Grigory Kagan and Peter J. Catto. Arbitrary poloidal gyroradius effects in tokamak pedestals and transport barriers. *Plasma Phys. Control. Fusion*, 50(8):085010, aug 2008. ISSN 0741-3335. doi: 10.1088/0741-3335/50/8/085010. URL http://stacks.iop.org/0741-3335/50/i=8/a=085010?key=crossref.669fb578d20d8346a0b790047bf20807. 148

[225] R J Groebner, K H Burrell, and R P Seraydarian. Role of edge electric field and poloidal rotation in the L - H transition. *Phys. Rev. Lett.*, 64(25):3015–3018, jun 1990. ISSN 0031-9007. doi: 10.1103/PhysRevLett.64.3015. URL https://link.aps.org/doi/10.1103/PhysRevLett.64.3015. 150

[226] H. Zohm. Dynamic behavior of the L - H transition. *Phys. Rev. Lett.*, 72(2):222–225, jan 1994. ISSN 0031-9007. doi: 10.1103/PhysRevLett.72.222. URL https://link.aps.org/doi/10.1103/PhysRevLett.72.222. 151

[227] E A Belli and J Candy. Kinetic calculation of neoclassical transport including self-consistent electron and impurity dynamics. *Plasma Phys. Control. Fusion*, 50(9):095010, sep 2008. ISSN 0741-3335. doi: 10.1088/0741-3335/50/9/095010. URL http://stacks.iop.org/0741-3335/50/i=9/a=095010?key=crossref.24354c43f2072562b80dc7e3b3c68def. 151

[228] E A Belli and J Candy. An Eulerian method for the solution of the multi-species drift-kinetic equation. *Plasma Phys. Control. Fusion*, 51(7):075018, jul 2009. ISSN 0741-3335. doi: 10.1088/0741-3335/51/7/075018. URL http://stacks.iop.org/0741-3335/51/i=7/a=075018?key=crossref.f5b5014981aa2b4454d0132400a8567c. 151

[229] B. Geiger, A. N. Karpushov, B.P. Duval, C. Marini, O. Sauter, Y. Andrebe, D. Testa, M. Marascheck, M. Salewski, P.A. Schneider, the TCV Team, and the EUROFusion MST1 Team. Fast-ion transport in low density L-mode plasmas at TCV using FIDA spectroscopy and the TRANSP code. *Plasma Phys. Control. Fusion*, 59(11):115002, 2017. URL http://stacks.iop.org/0741-3335/59/i=11/a=115002. 156, 160, 163

[230] B. P. Duval and A. N. Karpushov. Neutral Beam Heating on the TCV Tokamak. In *26th IAEA Fusion Energy Conf. (FEC 2016)*, kyoto, Japan, 2016. URL https://conferences.iaea.org/indico/event/98/session/32/contribution/703. 158

[231] Y. Luo, W. W. Heidbrink, K. H. Burrell, D. H. Kaplan, and P. Gohil. Measurement of the Dα spectrum produced by fast ions in DIII-D. *Rev. Sci. Instrum.*, 78(3):033505, mar 2007. ISSN 0034-6748. doi: 10.1063/1.2712806. URL http://aip.scitation.org/doi/10.1063/1.2712806. 159

[232] B. Geiger. *Fast-ion transport studies using FIDA spectroscopy at the ASDEX Upgrade tokamak*. Ph.d. thesis, LMU Munich, 2012. URL https://edoc.ub.uni-muenchen.de/15367/1/Geiger{_}Benedikt.pdf. 160

[233] RJ Hawryluk. An empirical approach to tokamak transport. *Phys. plasmas close to Thermonucl. Cond.*, 1:19–46, 1980. URL http://w3.pppl.gov/{~}pshare/transp/papers/Hawryluk.pdf. 162

[234] W. W. Heidbrink, D. Liu, Y. Luo, E. Ruskov, and B. Geiger. A Code that Simulates Fast-Ion Dα and Neutral Particle Measurements. *Commun. Comput. Phys.*, 10(03):716–741, sep 2011. ISSN 1815-2406. doi: 10.4208/cicp.190810.080211a. URL http://www.journals.cambridge.org/abstract{_}S1815240600001754. 162

[235] S. Tamor. ANTIC: A code for calculation of neutral transport in cylindrical plasmas. *J. Comput. Phys.*, 40(1):104–119, mar 1981. ISSN 00219991. doi: 10.1016/0021-9991(81)90202-3. URL http://linkinghub.elsevier.com/retrieve/pii/0021999181902023. 162

[236] B. Geiger, A. Karpushov, B. Duval, C. Marini, D. Testa, and R. Di Campli. Study of the Fast-Ion Distribution Function in the TCV Tokamak based on FIDA Spectroscopy and the TRANSP Code. In *26th IAEA Fusion Energy Conf. (FEC 2016)*, Kyoto, 2016. URL http://hdl.handle.net/11858/00-001M-0000-002C-8443-E. 163

Bibliography

[237] H P Summers, W J Dickson, M G O'Mullane, N R Badnell, A D Whiteford, D H Brooks, J Lang, S D Loch, and D C Griffin. Ionization state, excited populations and emission of impurities in dynamic finite density plasmas: I. The generalized collisional–radiative model for light elements. *Plasma Phys. Control. Fusion*, 48(2):263–293, feb 2006. ISSN 0741-3335. doi: 10.1088/0741-3335/48/2/007. URL http://stacks.iop.org/0741-3335/48/i=2/a=007?key=crossref.f88c8fb59bc0bbcf9fc671f91cd4d8bd. 169

[238] H. Anderson, M. G. von Hellermann, R. Hoekstra, L D Horton, A. C. Howman, R. W. T. Konig, R. Martin, R E Olson, and H. P. Summers. Neutral beam stopping and emission in fusion plasmas I: deuterium beams. *Plasma Phys. Control. Fusion*, 42(7):781–806, jul 2000. ISSN 0741-3335. doi: 10.1088/0741-3335/42/7/304. URL http://stacks.iop.org/0741-3335/42/i=7/a=304?key=crossref.17eac2d118d45a567dda91d744d122f2. 172

[239] Asphericon website. URL https://www.asphericon.com/en/. 188

[240] K.-D. Zastrow, S. R. Keatings, L. Marot, M. G. O'Mullane, and G. de Temmerman. Modeling the effect of reflection from metallic walls on spectroscopic measurements. *Rev. Sci. Instrum.*, 79(10):10F527, oct 2008. ISSN 0034-6748. doi: 10.1063/1.2955856. URL http://aip.scitation.org/doi/10.1063/1.2955856. 199

Acknowledgements

I would like to express my gratitude to all the people that supported me during this five extraordinary years at SPC, without your help this thesis would not have been possible.

First of all, I would like to thank my supervisor Basil Duval, for entrusting me with complete freedom in my research project, for encouraging me to strengthen my critical spirit and for all the support and advices, not only professional, he gave me during these years. Thank you also for trying to minimise the number of violations I often commit against the English language and for your ...British humour I got accustomed to enjoy.

I am thankful to my co-supervisor Alexander Karpushov, that despite the huge workload for the NBH upgrade he was charged with, has always found time to help me, particularly with the frequent IT problems. Thank you also for keeping the DNBI in good shape, which is another exhausting task, that permitted the measurements reported in this thesis.

I am obliged to Ivo Furno, that played the role of a third supervisor, by giving me the important task of characterising the spectral emission of RAID. Grazie mille per avermi dato la possibilità di lavorare su RAID, per l'aiuto morale e materiale e per la carica positiva che infondi ad ogni incontro. E' stato un piacere lavorare con te!

I would also like to express my deep gratitude to the SPC direction, in particular to Prof. Ambrogio Fasoli, who gave me the opportunity to work in such a wonderful environment, and to Prof. Minh Quang Tran, it was a pleasure to be an assistant for your classes.

I am also thankful to the seniors that contributed to my development as researcher with discussions and collaborations, in particular to Howling Alan, Sauter Olivier, Testa Duccio and Ricci Paolo. I also would like to thank the experts of my thesis committee, Dr. Neil Conway, Dr. Yann Camenen, Dr. Jonathan Graves and Prof. Frédéric Mila, for carefully reading my thesis and for the constructive comments.

Je suis particulièrement reconnaissant à Yanis Andrebe pour son aide prècieuse dans la conception et la mise en œuvre des instruments optiques, ainsi que pour l'aide dans le laboratoire. Merci également aux concepteurs du bureau technique, en particulier Guy Pochon, Robert Bertizzolo et Matthieu Toussaint, et aux travailleurs de l'atelier, qui construit la plupart des composants de mon spectromètre. Merci aussi a Conti Pascal et Raggi Claude pour le travail sur TCV, Moura Christian pour le travail sur RAID et Llobet Xavier et Joan Decker pour le indispensable support informatique. Et il ne faut pas oublier les secrétaires du SPC, en particulier Edith Grueter, pour la disponibilité dans la résolution de toutes les tâches bureaucratiques.

Acknowledgements

I am thankful to Dr. Benedikt Geiger for the great enthusiasm he inspired in every situation, particularly while working on the new FIDA diagnostics in TCV. Our efforts finally have been rewarded!

I am also grateful to Dr. Rachael McDermott for giving me the opportunity to work at AUG and expanding my knowledge on CXRS and spectroscopy.

I am obliged to Prof. Ursel Fantz and to Dr. Dirk Wünderlich for the inestimable help with the interpretation of RAID spectra. I would also like to thank the members of the RAID group, Rémy, Riccardo, Philippe and Gennady, for the nice environment and their fundamental assistance during my spectroscopic measurements. We really gave RAID a hard time with my requests!

Special thanks are in order for the DDJ-ninjas, Kevin and Pedro, the former for doing mostly all the hard work (and for his expertise in spectroscopy and beers), the latter for his constant overflow of ideas for improvements.

However, though it may seem strange, there is more than physics in a life of a PhD, and I ought to be grateful for finding so many amazing people here.

Thanks to my colleagues for the nice and merry environment, particularly to the "old guys": Lucia, Silvano, Matteo, Annamaria, Umar, Fabio (R. and A.), Oulfa, Kevin, Josef, Falk, Paola, Christoph, Julien, Himank and Joyeeta, for all the good times we had playing sports, swimming at lunch break, hiking, drinking at Sat or doing BBQ. I'm also glad to leave knowing that the fresh Italian students, Francesco "pizzaiolo", Federico "Pesa" and Lorenzo "stip", will keep up the level of "italianity" of the lab.

Thanks to my late officemates, Andreas and Samuel, for the every-day short-nice-chats and serious working-silence for the remainder of the day; also thank you Samuel for taking care of our office cooling system, it really helped a lot during the writing of this thesis.

Thank you Carrie for reinvigorating my passion for climbing and running, it was nice to have some training sessions together, although I was usually struggling to reach the end.

A special thank to Lucia for introducing me to the wonders of CXRS and entrusting me with the precious diagnostics, other than for organising the famous banana split evenings.

Finally a thank to all the person I meet, more or less randomly, and had good time with, in this years: Camille, Marina, Abhik, Nataliya, Andrew and Alina; it's nice to find friends among the non-physicists.

I would like to express my deepest gratitude to Valya for all the adventures and amazing time we spent together. I wish you all the happiness in your life.

Dedico questa tesi ai miei genitori, Giusi e Angelo, ed a mia sorella Elisa, che mi hanno sempre incoraggiato durante questa avventura quinquennale e che, nonostante la distanza fisica, ho sempre sentito vicini. Ritornare a casa e trovare il vostro affetto (oltre ai pasti squisiti che mi preparate) e il sapere di poter sempre contare su di voi, mi ha aiutato a superare i momenti piú difficili.

Un grazie di cuore ai miei amici italiani, in particolare a Diego, Elisa, Manu, Mara, Pippo,

Benzo, Sbalú, Signo e Pezzo, per tutti i bei momenti che mi regalate durante i miei fugaci rientri in Italia.

Un sentito ringraziamento va ai miei colleghi Fisici "Plasmonici" di Milano, Daniele e Alberto, che fato volle rincontrassi in territorio elvetico, per le argute discussioni sui sommi principi, oltre che sulla fiisica e la botanica.

E come non ringraziare Gabriele e Federico, compagni di grandi baldorie, oltre che amici fidati, se questi anni sono passati in un attimo e' anche colpa vostra!

Lausanne, 23 July 2017   Claudio

Claudio Marini

22 Rue Valentin
Lausanne, CH 1004,
Switzerland

Phone : +41 78 897 27 42
E-mail 1 : claudio.marini.j@gmail.com
E-mail 2 : claudio.marini@epfl.ch
Born: 21/01/1984
Nationality: Italian
Status: single

Curriculum Vitae

Education

05/2012-07/2017	**PhD** in plasma physics at the Swiss Plasma Center (SPC), EPFL, Lausanne, Switzerland. Supervisors: Dr. (MER) B.P. Duval, Dr. A.N. Karpushov. "Poloidal CX visible light plasma rotation diagnostics in TCV".
6/04/2011	**Master degree** in physics at Universitá degli Studi di Milano, Milano, Italy. Curriculum "Physics of matter", 120 ECTS degree course. Experimental Thesis about the development of a diagnostic system for an electron bunch in the Malmberg-Penning trap ELTRAP, based on Thomson scattering. Supervisors: Prof. M. Romé, Dr. B. Paroli, Dr. G. Maero. Final grade: 110/110 cum laude.
13/12/2007	**Bachelor degree** in physics at Universitá degli Studi di Milano, Milano, Italy. Curriculum "General physics", 180 ECTS degree course. Computational Thesis on the Fermi Pasta Ulam problem in the presence of a magnetic field. Supervisor: Prof. A. Carati. Final grade: 110/110 cum laude.

Research collaborations

September-October 2015:	**Momentum and impurity redistribution in sawtoothing plasmas at ASDEX-Upgrade** , IPP, Garching, Germany . CXRS data analysis and interpretation for AUG discharges featuring sawtooth activity.

Publications

Papers in international journal

C.Marini et al., *Spectroscopic characterisation of H_2 and D_2 helicon plasmas generated by a resonant antenna for neutral beam applications in fusion*, Nuclear Fusion, **57** 036024 (2017), doi:10.1088/1741-4326/aa53eb.

B. Paroli, including C. Marini, *Thomson backscattering diagnostic set-up for the study of nanosecond electron bunches in high space-charge regime*, Journal of instrumentation, **7**

P01008 (2012), 10.1088/1748-0221/7/01/P01008.

A. Simonin, including C. Marini, *Negative ion source development for a photoneutraliza-tion based neutral beam system for future fusion reactors*, New Journal of Physics, **18** 125005 (2016), 10.1088/1367-2630/18/12/125005.

K. Verhaegh, including C. Marini, *Spectroscopic investigations of divertor detachment in TCV*, Nuclear Materials and Energy, **0** 1-7 (2016), 10.1016/j.nme.2017.01.004.

B. Geiger, including C. Marini, *Fast-ion transport in low density L-mode plasmas at TCV using FIDA spectroscopy and the TRANSP code*, submitted to Plasma Physics and Controlled Fusion, (2017).

Papers in conference proceedings

I. Furno, including C. Marini, *A novel helicon plasma source for negative ion beams for fusion* 5th International Symposium on Negative Ions, Beams and Sources (NIBS'16), Sep. 2016, Oxford, United Kingdom.

Posters (selection)

C. Marini et al., *Impurity density and momentum transport during the sawtooth cycle*, EPS, Berlin, Germany, June 2014.

C. Marini et al., *Spectroscopic measurements for hydrogen dissociation degree in a helicon plasma*, APS, Savannah, Georgia, November 2015.

C. Marini et al., *Spectroscopic measurements of hydrogen dissociation degree and H^- pro-duction in resonant antenna-generated helicon plasmas*, EPS, Leuven, Belgium, July 2016.

R. McDermott, including C. Marini, *Effect of sawteeth on low-Z impurity particle and mo-mentum transport investigated in ASDEX Upgrade*, 21st Joint EU-US Transport Task Force Meeting, Leysin, Switzerland, September 2016.

B. Geiger, including C. Marini, *Study of the fast-ion distribution function in the TCV toka-mak based on FIDA spectroscopy and the TRANSP code*, IAEA, Kyoto, Japan, October 2016.

Seminars (selection)

C. Marini et al., *Impurity density and momentum transport during the sawtooth cycle*, SPS Annual Meeting, Fribourg 30 June - 2 July 2014.

Languages

Italian: Native
English: Fluent C2
French: Intermediate B2

Relevant activities and skills

Teaching assistant:
Responsible for preparation of exercises and solutions and assisting during exercise sessions for EPFL classes:
Analysis III (MATH-201), fall 2012.
Analysis IV (MATH-206), spring 2013.
General Physics III (PHYS-201(d)), fall 2013, fall 2015.
General Physics II (PHYS-106(f)), spring 2014, spring 2015, spring 2016.

Administrator:
Responsible of the schedule for the TCV diagnosticians (DDJ), overseeing a team of ≥ 25 people involved in TCV daily operation.
Coordinating and working in the team for the maintenance and upgrade of the DDJ tools (DDJ-ninjas).

Guide for visitors:
Guide for groups visiting the Swiss Plasma Center, introducing concepts on plasma physics and nuclear fusion, tour of TCV and TORPEX. Presentation given in English, Italian and French.

Computer skills:
Matlab, C++, $\LaTeX 2_\varepsilon$, Linux, HTML-CSS.

Technical skills:
Expert in spectrometry and in the design and installation of optical devices, their calibration, testing and integration in complex systems. Data analysis and interpretation. Accustomed to work with high power lasers.

Extra-curricular activities

Sports:
Competitive level runner and swimmer. Enjoy climbing and hiking. Trained in karate and boxing.